

Two-way Coupled Multiscale Tsunami Modelling from Generation to Coastal Zone Hydrodynamics

William James PRINGLE

2016

To Mum and Dad,
my wonderful parents,
for your unconditional love, support and patience

and

To Hitomi
for always being by my side
providing love and encouragement

ABSTRACT

Tsunami motion covers a wide range of length scales and physical phenomena. It propagates in the open ocean from its source towards the coastal zone where it interacts with the complex geometries of bays and coastal structures before possibly inundating the coast; damaging infrastructure, carrying debris, and causing erosion and deposition of sediment. To overcome the physical and numerical constraints of the problem this study introduces a two-way coupled multiscale tsunami model combining the shallow water equations with the Reynolds-averaged Navier-Stokes equations. The shallow water model can simulate wide-scale tsunami propagation and the basic inundation mechanism while the Navier-Stokes model is able to consider complex hydrodynamics upon wave breaking and interaction with structures.

The model was verified for solitary wave transformation and breaking on a plane beach. Various offshore wave heights and slopes were tested. The two-way coupling algorithm was found to be sufficiently robust particularly if the local wave height and slope are sufficiently small, and the coupling depths are sufficiently large. In contrast to the Navier-Stokes model the shallow water model could not replicate the rapid rate of shoaling required late in the shoaling process. An equation was derived to determine the location where the shallow water model breaks down and thus the optimal depth for coupling to the Navier-Stokes model. The resulting transformation and breaking characteristics described by the coupled model were compared with theoretical reference shoaling rates, physical experiments and a fully nonlinear potential flow model. Good overall agreement was found with possible improvements to the equations derived from the potential model for certain conditions. In contrast to the potential flow model, a Navier-Stokes model is able to simulate post-breaking turbulent behaviour such as touchdown of the plunging jet and splashup which were qualitatively in good agreement with snapshots from experiments.

The coupled model was further investigated through an application to a real-scale tsunami problem on Japan's Tohoku coast. During the 2011 Tohoku-oki Earthquake Tsunami the 63 m deep Kamaishi Bay offshore tsunami breakwater was partially damaged, but the tsunami height was still attenuated with estimates in the 40-50% range. The coupled model was used to investigate the hydrodynamics around the submerged section of the breakwater during the tsunami. Coupling was mostly robustly achieved due to the large Navier-Stokes domain. As a result, it was found that inundation heights and volume fluxes through the submerged section are not largely affected by the introduction of the Navier-Stokes model into the shallow water one. However, pressures much different to hydrostatic ones develop over the submerged breakwater caissons leading to a pressure force that reaches as low as a factor of safety of 0.77 which likely led to the sliding of the caissons. Due to vertical accelerations over the submerged section, the momentum jet angles downwards to the bed. The effect of this is to induce large horizontal velocities found to be considerably greater than those calculated in the shallow water model in an extended region up to 1.3 km from the breakwater. The resultant bed shear stresses have the potential to cause substantial erosion and deposition of sediment in the bay.

ACKNOWLEDGEMENTS

Although individual endeavours such as a PhD study require hard work and dedication on the part of the protagonist, they almost always require an initial and continuing base of support to work from. This is most certainly the case for myself where at times I feel simply just fortunate. Fortunate that I was born into such a loving family which allowed me to grow and achieve something that is really of interest and value to me.

For this, my first and foremost thanks and appreciation goes to my beloved parents, Julia and Bill, who this thesis is primarily dedicated to. You have always supported me in whatever I have chosen to do; including coming to Japan for the last five years! Your tolerance and patience *knows no bounds*, as you (Dad) would put it. I love you both very much.

Secondly, I have an immense amount of gratitude towards my advisor Nozomu Yoneyama sensei for first accepting me to come into the lab and not only advising me on my studies but also looking after me for these five years. His kind support and great guidance is much appreciated. It is thanks to him that I could write this thesis with the freedom and quality I had hoped for. I hope we can continue our collaboration together into the future. Much thanks also goes to my co-advisor Nobuhito Mori sensei for his refreshing attitude and great knowledge on a wide range of topics. His comments and discussion are always extremely helpful. I also hope that we continue a strong working relationship into the future, and look forward to tasting more Sake together. Finally, the assistance from Akira Igarashi sensei in the latter part of my studies is greatly appreciated. Your comments and suggestions are always on point and I am extremely lucky to have had your valued input into this thesis to improve its quality.

Much appreciation is also reserved for Poppa and my late Nanny for providing me with both financial and loving support during my education. I will always have great memories of my trips up north each year to meet you and travel to the beach house together. This is where I caught my first fish, we built a bench and fence together, played board games and badminton, “surfed”, kayaked, and “just chilled”. Thank you to Uncle Jonathan and Aunty Debbie for often providing great Xmas dinners, and Uncle Michael for being a great companion to laze with on the beach or in the sea.

Not least, my deepest love and thanks goes out to my late grandparents, Nana and Granddad who I had been fortunate enough to visit on a regular basis during most of my life in Christchurch. The memories of Tilford St will always stay with me. It was unfortunate that Nana and her youngest daughter; my amazing (No.1 favourite!) Aunty Clare passed away during my studies here. They will both be sorely missed. My love and wishes go out to all the rest of my extended family who have had to deal with such big losses in recent times. A special mention is reserved for my cousin and great pal Madeline and our time spent together in our younger years.

I also have much thanks and admiration for my younger sister, Sophie. Thanks to you for helping me to improve my sporting and wrestling skills when we were younger, and thanks for your refreshing bluntness and humour particularly in recent times (it was annoying before now).

I am so pleased that you had the determination to travel and experience the world, and I hope you continue to do what you love in your future.

My heartfelt love and thanks goes out to my dearest Hitomi Imai, who I have also decided to dedicate this thesis to. You have always been by my side during this endeavour and have provided me with much encouragement and happiness throughout. Thank you for working hard in your job while I studied, travelling to my home from Osaka at least every weekend, being a great travelling buddy, cooking delightful meals and bentos to keep me going and even much more delightful ones on special occasions, and most importantly for your smile. You have become a great companion and I am very much looking forward to a wonderful future with you. From Kiwiland with love.

My life would never have been the same without my best friend Mike Couling who had much influence on me, introducing me to table tennis and also to the scholarship that enabled me to come here to Japan. Thanks for everything bro in good times and bad. Cheers Toby Cartwright/an unlistable number of nicknames, for your friendship and all the enjoyment at Shirley, Uni, the mint flat and most importantly D'Lair. Those times will always be some of my most cherished and hilarious. Thanks to Chengy Liu, Victor Ganescu and Scrath Flavell too for their great friendship and company over the years. Thank you to Paul Connor-Woodley for being my greatest academic rival and otherwise genuine GC. An extra thanks to countless others who have crossed my path in my NZ life.

My time in Japan has been made unquantifiably better thanks to the great friendship of Yosuke Kozakai, Meshkati Shahmirzadi, Vova Fedoroff, Christian Auel, Josko Yoshiko, and many others. The times playing futsal, discussing life and science, or just chilling together in Tacobar have been my most treasured during my stay. On that note, a big mention is reserved for Master-san. He is one of the most genuine guys I have ever known with an immense amount of kindness, openness and generosity. You have made my life in Japan and those of countless other foreign students extra-special. The Tacobar legacy will always remain. I want to also give thanks to my laboratory colleagues for their assistance and discussions over the years, especially Masaki Miwa, Takeshi Fujiki, Hiroshi Nagashima, Yutaka Tanaka, and Xue Kai (Ross).

A final big thanks is left to my first academic mentor, Dr. Roger Nokes. He has been a huge inspiration for me to engage in fluid dynamics related studies. His passion and knowledge for the subject is peerless, and you can really tell the effort he puts in to enable his students to learn and understand.

Lastly, my sincerest appreciation goes to the Monbukagakusho: Ministry of Education, Culture, Sports, Science, and Technology (MEXT) for continued financial support throughout my studies. I would not have been able to come and study here if it wasn't for the great scholarship on offer by the Japanese Government.

TABLE OF CONTENTS

	Page
List of Tables	xi
List of Figures	xiii
Nomenclature	xxiv
1 Introduction	1
1.1 Background	2
1.1.1 Tsunami Disasters	2
1.1.2 Countermeasures for Tsunami Disasters	6
1.1.3 Numerical Analysis for Tsunami Hazard Mitigation	8
1.2 Research Problem and Objectives	10
1.3 Thesis Outline	11
2 Theory and Literature Review	13
2.1 Basic Equations and Theory	14
2.1.1 Incompressible Navier-Stokes Equations	14
2.1.2 Potential Flow Theory	17
2.1.3 Long Wave Theory	20
2.2 Numerical Modelling of Tsunami Hydrodynamics	24
2.2.1 Past and Present	24
2.2.2 To the Future and Study Motivation	29
3 Numerical Methodology	31
3.1 Introduction	32
3.2 Shallow Water Model	36
3.2.1 Governing Equations	36
3.2.2 Discretization Scheme	37
3.2.3 Special Considerations	40
3.2.4 Lateral Boundary Conditions	45
3.2.5 Initial Conditions	48

TABLE OF CONTENTS

3.3	Two-way Multi-grid Nesting	51
3.3.1	Spatial Nesting	52
3.3.2	Temporal Nesting	57
3.4	Reynolds-Averaged Navier-Stokes Equations Model	61
3.4.1	Governing Equations	61
3.4.2	Numerical Procedure	62
3.4.3	Discretization Scheme	64
3.4.4	Free Surface Model	66
3.4.5	Turbulence Model	75
3.4.6	Temporal Stability	78
3.4.7	Boundary Conditions	79
3.4.8	Initial Conditions	85
3.4.9	Variable Grid Construction	86
3.5	Two-way Multiscale Coupling	88
3.5.1	Shallow Water to RANS Exchange	90
3.5.2	RANS to Shallow Water Exchange	93
3.5.3	Temporal Coupling	94
4	Solitary Wave Transformation and Breaking on a Plane Beach	99
4.1	Introduction	100
4.2	Problem Setup and Model Conditions	103
4.2.1	Canonical Problem Definition and Dimensionless Variables	103
4.2.2	Model Conditions	105
4.2.3	Permanent Form Solutions	108
4.2.4	Range of Variables Investigated	109
4.3	Comparisons of Solitary Wave Shoaling on a Plane Beach for Individual Models	111
4.3.1	Basic Model Comparisons	111
4.3.2	Optimisation of the Coupling Position	113
4.4	Solitary Wave Shoaling and Breaking on a Plane Beach using 2CLOWNS	116
4.4.1	Basic Evaluation of 2CLOWNS Coupled Model	116
4.4.2	Pre-breaking shoaling performance	130
4.4.3	Wave Breaking Characteristics	133
4.4.4	Post-breaking Behaviour and Wave Shape	135
4.4.5	Velocity profiles	136
4.5	Conclusions	139
5	Flow Hydrodynamics near the Kamaishi Bay Offshore Tsunami Breakwater during the 2011 Tohoku-oki Earthquake Tsunami	141
5.1	Introduction	142

5.2	Model Conditions and Setup for Application	145
5.2.1	Kamaishi Bay and Offshore Tsunami Breakwater	145
5.2.2	Bathymetry/Tsunami Source Data and Computational Grids	145
5.2.3	Model Conditions	150
5.3	Validation of Tsunami Height and Inundation Measurements	152
5.3.1	Wave Buoy Measurements	152
5.3.2	Maximum Inundation Heights and Inundation Area	152
5.4	Flow Hydrodynamics Onshore of Breakwater	162
5.4.1	Velocity Comparisons with 2DH NSWE Simulation	162
5.4.2	Horizontal Distribution of the Hydrodynamics	165
5.4.3	Vertical Distribution of the Hydrodynamics	169
5.4.4	Bed Shear Stresses	173
5.4.5	Summary	176
5.5	Hydrodynamic Forces on the Submerged Breakwater Section	178
5.5.1	Comparisons with 2DH NSWE Simulation	178
5.5.2	Comparisons with Critical Values	179
5.6	Conclusions	183
6	Conclusions and Recommendations	185
6.1	Conclusions	186
6.2	Recommendations for Future Work	191
A	Multi-grid Temporal Nesting Subroutine - Numerical Code	193
B	Finite-differences in RANS Model	195
C	RANS Model Grid Convergence and Accuracy for Solitary Wave Transformation	199
D	Extra Figures for Chapter 5: 2CLOWNS-3D Simulation in Kamaishi Bay	205
	References	217

LIST OF TABLES

TABLE	Page
3.1 Example setup with three nested layers and their attributes	57
4.1 Coefficients to transfer desired solitary wave height into required input wave height and the average number of wavelengths of propagation to obtain the permanent waveform	108
4.2 Matrix of slopes and offshore wave heights investigated in this study. The values in the cells indicate the value of S_0 and hence breaker types as written underneath . . .	110
4.3 Computational time taken for wave to travel from $x' = -X'_g$ to $h' = 0.10$ depending on RANS or 2CLOWNS simulations each conducted using six OpenMP threads	117
4.4 Test combinations used to investigate two-way coupling and the effects of the RANS velocity boundary condition	118

LIST OF FIGURES

FIGURE	Page
1.1 Steel-framed building in Minami-Sanriku, Miyagi Prefecture, Japan ravaged by the 2011 Tohoku-oki Earthquake Tsunami and left as a memorial	1
1.2 Aftermath of the 2004 Indian Ocean Tsunami in Aceh, Indonesia 2005 (source: AusAID, retrieved from; https://www.flickr.com/photos/dfataustralianaid/10730863873/)	4
1.3 Surveyed inundation and runup heights along the Pacific coast of Japan resulting from the 2011 Tohoku-oki Earthquake Tsunami (source: The 2011 Tohoku Earthquake Tsunami Joint Survey (TTJS) Group, retrieved from; http://www.coastal.jp/tsunami2011/)	5
1.4 View of Kamaishi Bay (left) and Ofunato Bay (right), Iwate Prefecture, seen before the 2011 Tohoku-oki tsunami. Note the large scale breakwaters at the bay mouths (source: Iwate Prefecture Government, retrieved from; http://www.pref.iwate.jp/kouwankuukou/kouwan/)	7
2.1 Visual representation of instantaneous quantities that exhibit turbulent fluctuations and a corresponding time-averaged quantity at a certain location in space	16
2.2 Problem definition sketch for a free surface wave above an arbitrary sea bed	18
3.1 Finite-difference stencil of the staggered leap-frog method, in the $x - t$ (analogous to $y - t$ plane) and $x - y$ planes. In the $x - y$ plane the stencil is shown specifically for the calculation of the flux, $Q_{x(i+1/2,j)}$	38
3.2 Illustration of the situation at the shoreline (interface between wet and dry cells) when considering inundation	42
3.3 Illustration of the consideration of thin seawalls, breakwaters or river banks that are defined on cell boundaries	44
3.4 Illustration of the prescribed variables at the lateral boundaries	46
3.5 Different gridding approaches to deal with the change in spatial scales as a tsunami propagates towards the coastal zone	51
3.6 Example schematic of multi-grid nesting where a fine grid (layer), $L2$ has been placed in the centre of a coarse grid (layer), $L1$	53

3.7	Illustration of the exchange of volume fluxes from the coarse grid, $L1$, to the fine grid, $L2$	54
3.8	Illustration of the exchange of the free surface volume fluxes from the fine grid, $L2$ to the coarse grid, $L1$	56
3.9	Example flowchart of the calculation order for temporal nesting of three layers where $\Delta t_{ratio} = 2$ between two adjacent layers. The arrows show the exchange of information where the horizontal position of the ends of the arrows indicate the time step of the exchanged data	59
3.10	Finite-difference stencil of the RANS method in the $x - y/z$ plane, shown specifically for the calculation of u_c with positive velocity. Analogous stencils exist for finding v_c and w_c	65
3.11	Illustration of fluid volume fractions (shown by the numbers) used to describe the free surface (drawn by the black line) which is of bore-like behaviour in this figure	67
3.12	Illustration of the cell flags NF used to indicate their status and construct the free surface correctly. The surface orientation, NFB is also included for free surface cells (where $NF = 2$)	69
3.13	Illustration of the centre of gravity of the free surfaces and the vectors between the adjacent cells used to find the free surface normal vector at cell c , \vec{n}_c	70
3.14	Illustration of the reconstructed free surface using an arbitrary free surface normal	71
3.15	Illustration of both an object and fluid within a computational cell which may be accounted for by the improved FAVOR method used in this study	72
3.16	Illustration of the fluid surface cutting through the object. The bold line indicates the actual free surface plane to be solved and the dashed lines indicate the initial guesses	73
3.17	Illustration of the fluxes on the boundary to cell c that are calculated using the PLIC method when updating F_c	74
3.18	Linear interpolation/extrapolation of the pressure from the fluid cell to the centre of the surface cell. The case where $NFB = -3$ is drawn.	80
3.19	Pressure in a surface cell centre with $ NFB = 3$ when it is directly above an object cell	80
3.20	Velocities that need to be determined at the interface between fluid cells and air cells (shown by the white arrows) via the tangential stress boundary condition and continuity. Black arrows indicate velocities that are calculated normally through momentum and the Poisson Pressure equation	82
3.21	Velocity u_b tangential to and within the boundary, and the turbulent quantities, k_b and ϵ_b that may be applied as ghost cell values when evaluating the finite-difference approximation of the bed shear stress. However, if the wall function approximation is adopted, the shear stress on the boundary is directly calculated based on the value of u_c to get u_τ . Similarly, k_c and ϵ_c are directly inserted based on this calculation. The wall function approach assumes that u_c , k_c and ϵ_c fall within the log-law region	83

3.22	Sketch of the power law variation in cell size between two prescribed locations	87
3.23	Interface region between the 2DH NSWE and 3D RANS models in the $x - z$ plane (above) and $x - y$ plane (below). The necessary variables required for two-way coupling are indicated. Some arrows and cell centre circles have been omitted for legibility . .	89
3.24	Illustration of the arbitrary velocity profile based on no-gradient of the fluctuation, u'' from the depth-averaged component, U	91
3.25	Example flowchart of the calculation order for temporal coupling with three layers ($L3$ is a RANS model layer) where $\Delta t_{ratio} = 2$ between two adjacent layers. The arrows show the exchange of information where the horizontal position of the ends of the arrows indicate the time step of the exchanged data. ϕ in the $L3$ block is a dummy variable to indicate all scalar and vector quantities in the RANS model	96
4.1	Sketch of the canonical problem definition for solitary wave propagation, transformation and breaking on a plane beach	103
4.2	Illustration of suitable grid setup for the RANS model. The gradual shoaling and rapid shoaling interface may be estimated from Eqn.(4.12). The variation in grid sizes can be achieved using the power law technique described in §3.4.9	107
4.3	Comparison of the offshore permanent waveform centred at $x' = -X'_s$ between the NSWE and FNBM models for the full range of offshore wave heights ($0.05 \leq A'_0 \leq 0.30$) investigated in this study	109
4.4	Selected solitary wave transformation of the local wave height, A' versus h_0/h comparing: NSWE, FNBM, RANS models, Green's law and Synolakis (1986) experiments in (e). (a) $A'_0 = 0.05$, $s = 1/100$, (b) $A'_0 = 0.10$, $s = 1/60$, (c) $A'_0 = 0.15$, $s = 1/35$, (d) $A'_0 = 0.20$, $s = 1/35$, (e) $A'_0 = 0.30$, $s = 1/20$	112
4.5	Solitary wave transformation of the local wave height, A' versus h_0/h until breaking on various slopes for $A'_0 = 0.05, 0.10, 0.15, 0.20, 0.25$ and 0.30 using NSWE and FNBM models. (a) $s = 1/20$, (b) $s = 1/35$, (c) $s = 1/60$, (d) $s = 1/100$. Filled triangles indicate the water depth, h'_c where divergence of the NSWE and FNBM models is estimated through Eqn. (4.12)	114
4.6	Illustration of the usual setup of the 2CLOWNS model with appropriate grid sizes indicated. The suitable location for coupling (approximation of interface between gradual and rapid shoaling) may be estimated from Eqn.(4.12)	117
4.7	Snapshots of the wave profile of incident waves and waves reflected off the vertical wall on the right, comparing the singular RANS simulation with 2CLOWNS ones (coupling takes place at $x' = 5$) where two types of coupling boundary conditions for the velocity profiles are used. (a) $A'_0 = 0.05$, (b) $A'_0 = 0.15$, (i) incident waves, (ii) reflected waves.	119

4.8 Testing of one-way and two-way coupling (at $h_0/h_c = 3.03$), and the velocity boundary condition type for $A'_0 = 0.15$ on $s = 1/20$ as summarised in Table 4.4. Plots show differences between 2CLOWNS simulations and the singular RANS one; (a) difference in the local wave height, A' normalised by A'_0 versus h_0/h , (b) difference in the potential energy of the entire computational domain, Ep' versus t' , (c) difference in the the free surface level, η' at the coupling interface ($h_0/h_c = 3.03$) versus t' , (d) difference in the the volume fluxes, Q' at the coupling interface ($h_0/h_c = 3.03$) versus t' 120

4.9 Velocity profiles (u' on the left and w' on the right) measured at the coupling interface ($h_0/h_c = 3.03$) at three snapshots in time for the $A'_0 = 0.15$ on $s = 1/20$ case comparing the singular RANS simulation result with 2CLOWNS simulations 123

4.10 Difference in the local wave height, A' normalised by A'_0 between 2CLOWNS NN and singular RANS simulations until wave breaking. Coupling at three different depths for each slope (positions indicated by the vertical lines) are conducted where the middle depth is derived from Eqn. (4.12) and the other two coupling depths are in between this location and; the toe of the slope and breaking point respectively. (a) $A'_0 = 0.15$ on $s = 1/20$, (b) $A'_0 = 0.15$ on $s = 1/35$, (c) $A'_0 = 0.15$ on $s = 1/60$, (d) (c) $A'_0 = 0.05$ on $s = 1/100$ 125

4.11 Snapshots of selected solitary waves on $s = 1/35$ centred on the 2CLOWNS coupling position calculated using Eqn. (4.12). Shaded area indicates RANS domain in 2CLOWNS simulation. (a) $A'_0 = 0.05$, (b) $A'_0 = 0.15$, (c) $A'_0 = 0.30$ 127

4.12 Snapshots of solitary waves with $A'_0 = 0.15$ on various slopes centred on the 2CLOWNS coupling position calculated using Eqn. (4.12). Shaded area indicates RANS domain in 2CLOWNS simulation. (a) $s = 1/20$, (b) $s = 1/60$, (c) $s = 1/100$ 128

4.13 Solitary wave transformation of the local wave height, A' versus h_0/h until breaking on various slopes for $A'_0 = 0.05, 0.10, 0.15, 0.20, 0.25$ and 0.30 comparing 2CLOWNS NN with FNBM simulations. (a) $s = 1/20$, (b) $s = 1/35$, (c) $s = 1/60$, (d) $s = 1/100$. Filled triangles indicate the water depth, h'_c where coupling in 2CLOWNS occurs calculated using Eqn. (4.12) 129

4.14 The total error of $(A'_{2CLOWNS} - A'_{FNBM})/A'_{FNBM}$ denoted, A_{RE} around the coupling interface for all 2CLOWNS NN simulations with best fit line (Eqn. (4.14)) included . . . 130

4.15 Evolution of the local wave height of a solitary wave ($A'_0 = 0.05$) on a $1/60$ slope comparing 2CLOWNS NN, FNBM, NSWE models with theoretical reference shoaling rates (Synolakis and Skjelbreia, 1993) included 131

4.16 Selected solitary wave transformation of the local wave height, A' versus h_0/h comparing: RANS and 2CLOWNS models, Green's law and Synolakis (1986) experiments in (e). (a) $A'_0 = 0.05, s = 1/100$, (b) $A'_0 = 0.10, s = 1/60$, (c) $A'_0 = 0.15, s = 1/35$, (d) $A'_0 = 0.20, s = 1/35$, (e) $A'_0 = 0.30, s = 1/20$ 132

4.17	Breaking criteria calculated in 2CLOWNS NN for all wave cases in this study with best fit curves compared to those calculated in Grilli et al. (1997): (a) water depth at breaking, h'_b versus S_0/A'_0 with Eqn. (4.17) - this study and Eqn. (4.15) - (Grilli et al., 1997); (b) wave breaking index, A_b/h_b versus S_0 with Eqn. (4.18) - this study and Eqn. (4.16) - (Grilli et al., 1997)	134
4.18	Breaking wave shape and kinematic quantities (velocity magnitude, u' and turbulent kinetic energy, k') for $A'_0 = 0.20$ on $s = 1/35$: (a) prior to breaking (u'), (b) at the onset of wave breaking (u'), (c) formation of the plunging jet (u'), (d) touchdown of the plunging jet (u'), (e) wave splashup (u'), (f) touchdown of the plunging jet (k'), (g) wave splashup (k')	136
4.19	Velocity profiles (i) u' on left, (ii) w' on right) under the wave crest of a solitary wave ($A_0 = 0.05$) on a 1/60 slope at four separate locations comparing 2CLOWNS NN, NSWE, and FNBM simulations; (a) $h/h_b = 2.1$, (b) $h/h_b = 1.2$, (c) $h/h_b = 0.93$, (d) $h/h_b = 0.68$	137
5.1	Sketch of Kamaishi Bay breakwater with the damaged caissons shaded red and yellow. Front on view and cross-section of the submerged section; adapted from: Arikawa et al. (2012); Port and Airport Research Institute of Japan (2011b)	146
5.2	Contour plot of the bathymetry (water depth from T.P. (m)) data (Kotani et al., 1998) in five layers of resolution and the position of the Port and Airport Research Institute of Japan (2011a) GPS wave buoys (#801 - #807). Dashed rectangle indicates the location of the next layer. (a) 1350 m resolution, (b) 450 m resolution, (c) 150 m resolution with contours omitted below -100 m depth, (d) 50 m resolution with contours omitted below -100 m depth, (e) 10 m resolution (no offshore breakwater) with contours omitted below -100 m depth	147
5.3	Colour plots of the 10 m mesh later for the three offshore breakwater conditions. (a) no offshore breakwater, (b) post-tsunami partially damaged breakwater, (c) pre-tsunami undamaged breakwater	148
5.4	Schematic of the 3D RANS mesh with range of grid sizes indicated. (a) Plane view of the mesh where the shading indicates initial water depths (T.P.), (b) $x - z$ cross-section of the mesh along the $y = 4,345,150$ m northing	150
5.5	Water level time series at three Port and Airport Research Institute of Japan (2011a) GPS wave buoys closest to Kamaishi Bay, comparing simulation results in this study using the Tohoku University version1.2 source (Imamura et al., 2012) with the measured water levels	153

5.6	Colour plots of the maximum recorded free surfaces, η_{max} using the NSW model for three conditions of the offshore tsunami breakwater, with a comparison to TTJS survey measurements (Mori et al., 2012) (indicated by filled circles). (a) No offshore breakwater, (b) Post-tsunami damaged breakwater, (c) Pre-tsunami undamaged breakwater	154
5.7	Effect of the offshore tsunami breakwater on inundation heights and area for 2 hours of simulation with the NSW model. (a) Difference in maximum inundation heights between TTJS survey measurements and simulated ones at locations ordered in a clockwise direction around the coast with least-squares lines of regression (lsline) also plotted, (b) Time series of the inundation area with estimate of actual maximum area (in the greater Kamaishi City region larger than our computational domain) shown for comparison	155
5.8	Time series of the measured volume flux per unit width, Q (averaged in the north-south direction) for 90 minutes of simulation comparing the 2DH NSW and 2CLOWNS-3D simulations. Positive indicates flow in the onshore direction (east to west). (a) east boundary of the RANS domain, (b) submerged section of the breakwater	157
5.9	Difference in maximum recorded free surfaces, η_{max} between the 2CLOWNS-3D and 2DH NSW simulation - $(\eta_{max})_{2CLOWNS} - (\eta_{max})_{NSW}$ - for 2 hours of simulation. Dashed black rectangle indicates the location of the 3D RANS domain	159
5.10	Difference in inundation between the 2CLOWNS-3D and 2DH NSW model simulations. (a) Difference in maximum inundation heights between TTJS survey measurements and simulated ones at locations ordered in a clockwise direction around the coast with least-squares lines of regression (lsline) also plotted, (b) Time series of the inundation area with estimate of actual maximum area (in the greater Kamaishi City region larger than our computational domain) shown for comparison	160
5.11	Map of the maximum recorded magnitudes of the depth-averaged velocities, U_{max} during the 2DH NSW and 2CLOWNS-3D model simulations for 2 hours of simulation on the 10 m 2DH NSW mesh. (a) 2DH NSW simulation, (b) 2CLOWNS-3D simulation - dashed black rectangle indicates the location of the 3D RANS domain . .	163
5.12	Colourplot of the magnitudes of the depth-averaged velocities, U during the 2DH NSW and 2CLOWNS-3D model simulations on the 10 m 2DH NSW mesh at $t = 1740$ s after the earthquake rupture. (a) 2DH NSW simulation, (b) 2CLOWNS-3D simulation - dashed white rectangle indicates the location of the 3D RANS domain .	164
5.13	Horizontal distribution of the velocity and colour plots of various scalar indicators of the hydrodynamics on the $z = -20.8$ m contour within the 3D RANS domain for the 2CLOWNS-3D model simulation at $t = 1740$ s after the earthquake rupture: (a) horizontal velocity magnitude, V , (b) horizontal vorticities, ω , and (c) turbulent kinetic energy, k	166

5.14	Horizontal distribution of the velocity and colour plots of various scalar indicators of the hydrodynamics on the $z = -20.8$ m contour within the 3D RANS domain for the 2CLOWNS-3D model simulation at $t = 2340$ s after the earthquake rupture: (a) horizontal velocity magnitude, V , (b) horizontal vorticities, ω , and (c) turbulent kinetic energy, k	167
5.15	Vertical distribution of the velocity and colour plots of various scalar indicators of the hydrodynamics along the $y = 4,345,175$ m northing cross-section of the 3D RANS domain for the 2CLOWNS-3D model simulation at $t = 1740$ s after the earthquake rupture: (a) velocity magnitude in $x - z$ plane, W , (b) vertical vorticities, ω , and (c) turbulent kinetic energy, k	169
5.16	Vertical distribution of the velocity and colour plots of various scalar indicators of the hydrodynamics along the $y = 4,345,175$ m northing cross-section of the 3D RANS domain for the 2CLOWNS-3D model simulation at $t = 2340$ s after the earthquake rupture: (a) velocity magnitude in $x - z$ plane, W , (b) vertical vorticities, ω , and (c) turbulent kinetic energy, k	170
5.17	Vertical profiles of, (a) the horizontal velocity, u , (b) vertical velocity, w and, (c) the dynamic pressure (difference from hydrostatic), p_d along the $y = 4,345,175$ m northing coordinate within the 3D RANS domain for the 2CLOWNS-3D model simulation at $t = 1740$ s after the earthquake rupture. The direction of u is given by its position from the dotted line that indicates the location of the profile measurement. For w and p_d a positive value is right (east) of the dotted line	171
5.18	Vertical profiles of, (a) the horizontal velocity, u , (b) vertical velocity, w and, (c) the dynamic pressure (difference from hydrostatic), p_d along the $y = 4,345,175$ m northing coordinate within the 3D RANS domain for the 2CLOWNS-3D model simulation at $t = 2340$ s after the earthquake rupture. The direction of u is given by its position from the dotted line that indicates the location of the profile measurement. For w and p_d a positive value is right (east) of the dotted line	172
5.19	Colour plot of the maximum dimensionless bed shear stress, τ_b^* within the 3D RANS domain comparing the 2DH NSWE and 2CLOWNS-3D simulations. A uniform grain size, $D_{50} = 1$ mm is assumed. (a) 2DH NSWE simulation, shear stress calculated from depth-averaged velocity, (b) 2CLOWNS-3D simulation, shear stress calculated from depth-averaged velocity, (c) 2CLOWNS-3D simulation, shear stress calculated through wall function based on the velocity just above the sea bed	174
5.20	Time series of the envelopes of the free surface/pressure difference over the submerged caissons in the 2CLOWNS-3D and 2DH NSWE model simulations due to the incoming tsunami - blue shaded region: 2CLOWNS-3D pressure difference converted to equivalent hydrostatic free surface difference, black shaded region: 2CLOWNS-3D free surface difference, red shaded region: 2DH NSWE free surface difference	179

5.21	Location dependent envelopes of, (a) drag force per unit width, F_D , (b) overturning moment per unit width about the caisson heel, M_D , and (c) punching pressure on the rubble mound, P_e on the submerged caissons and rubble mound due to the incoming tsunami as calculated by 2CLOWNS-3D and compared with critical values - blue shaded region: simulated results, black shaded region: simulated hydrostatic component, red shaded region: critical resistance values, red line: design pressure, red dashed line: critical pressure	181
6.1	The Lone Miracle Pine located in Rikuzentakata City, Iwate Prefecture now stands as a symbol of hope for the region after surviving the 2011 Tohoku-oki Earthquake Tsunami (photo: courtesy of my colleague, Hiroshi Nagashima)	185
C.1	Effect of horizontal grid size, $\Delta x'$ for solitary wave transformation on slope, $s = 1/35$ with offshore wave height, $A'_0 = 0.30$. The local wave height, A' and snapshots of the waveform are shown at four different values of t' . Green's law and the BP in the FNPF of Grilli et al. (1997) is included for comparison	200
C.2	Effect of gradually varying the horizontal grid size, $\Delta x'$ offshore of $x' = 20$ for solitary wave transformation on slope, $s = 1/35$ with offshore wave height, $A'_0 = 0.30$. The local wave height, A' and snapshots of the waveform are shown at four different values of t' . Green's law and the BP in the FNPF of Grilli et al. (1997) is included for comparison	201
C.3	Effect of vertical grid size, $\Delta z'$ for solitary wave transformation on slope, $s = 1/35$ with offshore wave height, $A'_0 = 0.30$. The local wave height, A' and snapshots of the waveform are shown at four different values of t' . Green's law and the BP in the FNPF of Grilli et al. (1997) is included for comparison	202
C.4	Effect of gradually varying vertical grid size, $\Delta z'$ from the bed to just below the free surface for solitary wave transformation on slope, $s = 1/35$ with offshore wave height, $A'_0 = 0.30$. The local wave height, A' and snapshots of the waveform are shown at four different values of t' . Green's law and the BP in the FNPF of Grilli et al. (1997) is included for comparison	203
C.5	Performance of RANS model for shoaling and prediction of breaking point versus the FNPF model (Grilli et al., 1997) on a slope, $s = 1/35$ using the optimised grid setup (c.f. Figure 4.2)	204
D.1	Colour plot of the magnitudes of the depth-averaged velocities, U and the vector field during 2CLOWNS-3D model simulations on the 10 m 2DH NSWE mesh at various snapshots for $1000 < t < 2000$ s after the earthquake rupture. White dashed rectangle indicates location of the 3D RANS domain	206

D.2	Colour plot of the magnitudes of the depth-averaged velocities, U and the vector field during 2CLOWNS-3D model simulations on the 10 m 2DH NSWE mesh at various snapshots for $2000 < t \leq 3000$ s after the earthquake rupture. White dashed rectangle indicates location of the 3D RANS domain	207
D.3	Colour plot of the magnitudes of the depth-averaged velocities, U and the vector field during 2CLOWNS-3D model simulations on the 10 m 2DH NSWE mesh at various snapshots for $3000 < t \leq 4500$ s after the earthquake rupture. White dashed rectangle indicates location of the 3D RANS domain	208
D.4	Colour plot of the magnitudes of the horizontal velocities, V and the vector field in the 3D RANS domain during 2CLOWNS-3D model simulations on the $z = -20.8$ m contour at various times ($1740 \leq t \leq 4500$ s) after the earthquake rupture	209
D.5	Colour plot of the vorticities, ω and the vector field in the 3D RANS domain during 2CLOWNS-3D model simulations on the $z = -20.8$ m contour at various times ($1740 \leq t \leq 4500$ s) after the earthquake rupture	210
D.6	Colour plot of the turbulent kinetic energy, k and the vector field in the 3D RANS domain during 2CLOWNS-3D model simulations on the $z = -20.8$ m contour at various times ($1740 \leq t \leq 4500$ s) after the earthquake rupture	211
D.7	Colour plot of the turbulent viscosity, ν_t and the vector field in the 3D RANS domain during 2CLOWNS-3D model simulations on the $z = -20.8$ m contour at various times ($1740 \leq t \leq 4500$ s) after the earthquake rupture	212
D.8	Colour plot of the magnitudes of the velocities in the $x - z$ plane, W and the vector field in the 3D RANS domain during 2CLOWNS-3D model simulations along the $y = 4, 345, 175$ m northing cross-section at various times ($1740 \leq t \leq 4500$ s) after the earthquake rupture	213
D.9	Colour plot of the magnitudes of the vorticities in the $x - z$ plane, ω and the vector field in the 3D RANS domain during 2CLOWNS-3D model simulations along the $y = 4, 345, 175$ m northing cross-section at various times ($1740 \leq t \leq 4500$ s) after the earthquake rupture	214
D.10	Colour plot of the magnitudes of the turbulent kinetic energy, k and the vector field in the $x - z$ plane of the 3D RANS domain during 2CLOWNS-3D model simulations along the $y = 4, 345, 175$ m northing cross-section at various times ($1740 \leq t \leq 4500$ s) after the earthquake rupture	215
D.11	Colour plot of the magnitudes of the turbulent viscosity, ν_t and the vector field in the $x - z$ plane of the 3D RANS domain during 2CLOWNS-3D model simulations along the $y = 4, 345, 175$ m northing cross-section at various times ($1740 \leq t \leq 4500$ s) after the earthquake rupture	216

Symbol	Description
a	length of tsunami source
A	wave amplitude from the initial undisturbed water level (equal to the wave height for solitary waves)
A_0	offshore wave height
A_b	wave height at wave breaking
A_c	coefficient of the Poisson pressure equation at cell, c
ADV_ϕ	advection term of k or ϵ
B	width of caisson
c	wave speed
c_i	truncation error correction coefficients in shallow water model
C_f	bed roughness coefficient
C_w	weir discharge coefficient; = 0.35
C_μ	empirical constant for turbulent viscosity in $k - \epsilon$ model; = 0.09
$C_{\epsilon 1}$	empirical constant for production of ϵ in $k - \epsilon$ model; = 1.44
$C_{\epsilon 2}$	empirical constant for dissipation of ϵ in $k - \epsilon$ model; = 1.92
C^+	constant of integration in log-law (function of k_s^+)
CI_{re}	maximum relative error around coupling interface during coupling
Cr	overall Courant number of the grid; = $\sqrt{gh_{max}}\Delta t/\Delta x$
Cr_i	local Courant number in the i direction; = $\sqrt{gh}\Delta t/\Delta x_i$
d	free parameter of the plane equation
D_c	correction coefficient to avoid negative depths in the shallow water model
D_{50}	median sediment grain size
$DIFF_\phi$	diffusion term of k or ϵ
E_{re}	relative error of wave energy
g	acceleration due to gravity in the negative z direction; $\approx 9.81 \text{ ms}^{-2}$
g_i	the body force term in the i direction
f	Darcy friction factor
f_i	finite-difference of the sum of the pressure gradient and nonlinear advection terms in shallow water model for the i component of the volume flux
F	volume fraction associated with the Volume-of-Fluid method
F_i	discretization of the bottom friction terms in the shallow water model
F_D	drag force
F_{Dcrit}	critical drag force for sliding
F_L	lift force

Symbol	Description
h	initial undisturbed water depth
h_0	offshore initial undisturbed water depth
h_b	initial undisturbed water depth at wave breaking
h_c	initial undisturbed water depth at coupling
h_i	ratio of the initial undisturbed water depth to the horizontal grid size; $= h/\Delta x_i$
h_{max}	maximum initial water depth in the grid
h_o	original undisturbed water depth before tsunami source is initiated
H	total water depth; $= h + \eta$
i	used to indicate cell number in the x direction
$is2$	first cell number inside fine grid layer in x direction
j	used to indicate cell number in the y direction
$js2$	first cell number inside fine grid layer in y direction
k	turbulent kinetic energy; $\equiv \frac{1}{2} \overline{u'_i u'_i}$
k_s	equivalent sand roughness height
k_s^+	non-dimensional boundary layer equivalent sand roughness height
ke	total number of vertical cells
l	turbulent length scale
L	representative length scale
L_0	offshore wavelength
L_s	offshore wavelength between the maximum slope on the solitary wave
$L\#$	grid layer number #
$L(r)$	limiter function of r
m_c	mass of concrete caisson
M_D	overturning moment
M_{Dcrit}	critical overturning moment about caisson heel
n	Manning's roughness coefficient
\vec{n}	outward unit normal vector of the free surface
\vec{n}_{temp}	outward normal vector of the free surface
NF	flag to indicate the cell type (boundary, fluid, air, or free surface)
NFB	flag to indicate the orientation of free surface cells
p	instantaneous pressure
\bar{p}	Reynolds-averaged pressure
\tilde{p}	pseudo-pressure used as first guess in momentum equation
\mathbf{p}	arbitrary point on a plane
p_{atm}	atmospheric pressure
p_a	frequency dispersion importance parameter for tsunamis
p_d	dynamic pressure
P_k	turbulent production term

NOMENCLATURE

Symbol	Description
Q_i	horizontal volume flux in the i direction
\tilde{Q}_i	horizontal volume flux in the i direction in the position of the volume flux perpendicular to it
r_d	distance from centre of mass of caisson to its heel
r_e	distance from resultant vertical force to caisson heel
r_i	ratio of time step to grid size in i direction; $= \Delta t / \Delta x_i$
r^+	ratio of the differences in advected quantities across cells in direction of positive velocity
r^-	ratio of the differences in advected quantities across cells in direction of negative velocity
R	distance from tsunami source
Re	Reynolds number; $= \frac{VL}{\nu}$
s	slope (rise over run)
S	magnitude of the mean strain rate tensor
S_0	dimensionless slope parameter
S_{ij}	mean strain rate tensor of the Reynold-averaged velocities
$(SA_{object})_i$	surface area of an object on a computational cell boundary perpendicular to the i direction
t	temporal dimension
T	wave period
u	horizontal velocity component (x direction)
u_i	instantaneous velocity component in the i direction
\bar{u}_i	Reynolds-averaged velocity component in the i direction
u'_i	fluctuating velocity component from the Reynolds-averaged one in the i direction
u_i^*	intermediate velocity calculated from momentum equations in the i direction
u_t	representative turbulent velocity magnitude
u_α	horizontal velocity component in Nwogu (1993) type Boussinesq models defined at arbitrary elevation
u_τ	magnitude of shear velocity
$u_{\tau i}$	shear velocity in the i direction
U_i	depth-averaged velocity component in the i direction (horizontal only)
U_{max}	maximum horizontal depth-averaged velocity magnitudes for simulation
(UF)	volume flux at the cell boundary in the x direction
v	horizontal velocity component (y direction)
V	horizontal velocity magnitude
V_{fluid}	volume of fluid within a computational cell
V_{object}	volume of an object within a computational cell

Symbol	Description
(VF)	volume flux at the cell boundary in the y direction
w	vertical velocity component (z direction)
W	$x - z$ plane velocity magnitude
(WF)	volume flux at the cell boundary in the z direction
x	horizontal (left to right) Cartesian Coordinate axis
$x_{\#}$	distance number $\#$ in the x direction used for interpolation in multi-grid nesting
x_i	the i^{th} Cartesian Coordinate axis
X_s	initial position of the solitary wave offshore
y	horizontal (top to bottom) Cartesian Coordinate axis
$y_{\#}$	distance number $\#$ in the y direction used for interpolation in multi-grid nesting
y_k	roughness length in log-law
y_p	distance from the boundary to the nearest computed velocity
y_p^+	non-dimensional boundary layer distance from the boundary to the nearest computed velocity
z	vertical Cartesian Coordinate axis
z_{α}	arbitrary elevation of horizontal velocity component defined in Nwogu (1993) type Boussinesq models
z_{wall}	elevation of a seawall, breakwater or levee crest

Greek Symbol	Description
α	multiplication coefficient for variable grid construction
γ	linear dispersion tuning coefficient
γ_i^{α}	aperture ratio at the cell boundary perpendicular to the i axis
γ^v	void ratio of the computational cell
δ_0	coefficient of initial turbulent kinetic energy
δ_v	wall layer thickness
Δp	change in pressure between the pseudo-pressure and correct pressure due to the divergence free condition
Δt	step size in the temporal direction
Δt_{ratio}	time step size ratio between a coarse grid layer, $k - 1$ and a fine grid layer, k ; $= \Delta t_{k-1}/\Delta t_k$
Δx	grid size in the x direction
Δx_i	grid size in the i direction
Δy	grid size in the y direction
Δz	grid size in the z direction
ϵ	the turbulent kinetic energy dissipation rate; $\equiv \overline{v u'_{ij} u'_{ij}}$

Greek Symbol	Description
ϵ_{ijk}	the Levi-Civita tensor; = $\begin{cases} +1 & \text{if } (i, j, k) \text{ is } (1, 2, 3) \text{ or } (2, 3, 1) \text{ or } (3, 1, 2) \\ -1 & \text{if } (i, j, k) \text{ is } (3, 2, 1) \text{ or } (1, 3, 2) \text{ or } (2, 1, 3) \\ 0 & \text{if } i = j \text{ or } i = k \text{ or } j = k \end{cases}$
ϵ_D	error of continuity
ϵ^F	error of volume fraction in plane equation iteration guess
ϵ	nonlinearity ratio of wave in intermediate/shallow water; = A/h
ζ_0	coefficient of initial turbulent viscosity
η	free surface elevation
η^{cg}	centre of gravity of the free surface
η_{max}	maximum free surface levels for simulation
Θ_i	representation of advection and viscous terms for the momentum equation in the i direction
κ	wave number; = $2\pi/\lambda$
κ_v	von Kármán constant; = 0.41
λ	wavelength
μ	frequency dispersion parameter; = h/λ
μ_0	offshore frequency dispersion parameter; = h_0/L_0
μ_s	frequency dispersion parameter for use in slope parameter; = h_0/L_s
ν	kinematic viscosity; $\approx 1.00 \times 10^{-6} \text{ m}^2\text{s}^{-1}$ for water at 20°C
ν_f	coefficient of friction
ν_n	numerical viscosity
ν_t	turbulent viscosity
π	the ratio of circumference of a circle to its diameter; $\approx \frac{22}{7}$
ρ	density (of a fluid); $\approx 1025 \text{ kgm}^{-3}$ for standard sea water
ρ_s	density of sediment; $\approx 2065 \text{ kgm}^{-3}$ for standard sediment
σ_k	turbulent Prandtl number in $k - \epsilon$ model; = 1.0
σ_ϵ	dissipative Prandtl number in $k - \epsilon$ model; = 1.3
τ_{ij}	viscous stresses in the momentum equation
τ_{bi}	bed stress in the i direction (only horizontal)
τ_b^*	dimensionless bed shear stress
ϕ	velocity potential
ϕ_c	dummy variable for any scalar quantity defined at the centre of cell, c
Φ_c	value of k or ϵ interpolated onto the c cell boundary in an upwind TVD sense
ψ	dispersion potential function
ω	angular frequency; = $2\pi/T$, or vorticity

INTRODUCTION

This study focusses on numerical modelling of tsunamis using a novel technique to couple together models with different governing equations. Most readers will have a clear idea of the devastation tsunamis can induce (see Figure 1.1), not least those in Japan where I have spent my years on this study since the 2011 disaster. Tsunamis are characterised by their large length scales in comparison to the water depth which can be true even at the deepest parts of the ocean for large seismically induced ones. This allows for special considerations when numerical modelling is performed. However, we will see that these considerations lose validity when the waves start to interact with the very coastal structures and landforms that engineers hope to analyse with numerical models.



Figure 1.1: Steel-framed building in Minami-Sanriku, Miyagi Prefecture, Japan ravaged by the 2011 Tohoku-oki Earthquake Tsunami and left as a memorial

1.1 Background

This section begins by introducing the tsunamis and their related disasters in §1.1.1. Engineering countermeasures for these are disasters described in §1.1.2. Finally, §1.1.3 discusses the numerical analysis of tsunamis and how it may be used for hazard mitigation measures.

1.1.1 Tsunami Disasters

Tsunamis are superficially well known examples of extreme disasters throughout the world. The word “tsunami” though is aptly borrowed from the Japanese term - a country more which than any other knows the potential dangers of tsunamis - that literally translates to “harbour wave”. It may at first appear a strange description however tsunamis are indeed commonly enhanced due to resonance and other effects within bays causing disruption to harbours for many hours after their generation. In fact, the influence from the continental shelf and coastal topography are one of the most important factors that turn fascinating geophysical phenomena into devastating disasters. But what initially makes the geophysics of the tsunami different from “ordinary” waves? While, ordinary waves are generated by disturbances on or near the free surface (e.g. wind and vessels), tsunamis are associated with a *large* displacement of water by some external action. Thus, there are many potential sources of tsunamis such as: displacement of the seabed due to seismic action, submarine landslides, submarine volcanic eruptions, subaerial landslides, collapse of sectors of volcanic edifices, and falling extraterrestrial bodies. The huge energy of the external action induces vertical displacement of the water. In other words, the kinetic energy of the external motion has been converted into potential energy of the water body. The pressure difference between vertical water columns due to the presence of the free surface carry that energy in the form of a very long wave potentially over entire oceans. Hence, a tsunami can be viewed simply as an energy transmitting mechanism. As a tsunami propagates, the energy is dispersed so its potential for damage is much larger closer to its source, but may still be significant for far-field locations if the initial energy of the source is sufficiently large.

In terms of the hydrodynamics, the length scales of tsunamis play an important role for the propagation of tsunamis. Picture an undersea megathrust earthquake in a subduction zone where vertical displacement of the seabed has occurred over a length scale on the order of ~ 100 km. It is not hard to imagine the induced tsunami to be of a similar scale, i.e. the wavelength of the tsunami. In comparison the water depths in deep ocean are better measured on orders of ~ 1 km, and those on the continental shelf of orders less. It is usually fair to assume that in the case of some arbitrary wave that the influence of the wave on water particles will decay to zero at depths on the order of the wavelength. However, for tsunamis the ratio of water depth to the wavelength of tsunamis is relatively small, hence water particles in the entire water column must “feel” the influence of the wave. Moreover, the horizontal motion of the particles will almost be the same between the free surface and the seabed as there is relatively little water depth for

decay to occur. It is easy to imagine how a phenomena that can induce the non-trivial motion of entire water bodies (including oceans) may have such devastating effects. Additionally, the length scales of tsunamis have important consequences in terms of the physics of fluid motion which will be explained in more detail in Chapter 2. To summarise here, the wave speed of these long waves becomes essentially independent of their wavelength and almost entirely dependent on the water depth. Thus, the (simple) estimation of tsunami motion becomes fairly straightforward. However, there are a number of other behaviours that need to be considered for tsunami motion related to the local bathymetry and topography that generally exist for all water wave motion: diffraction, refraction, shoaling, reflection, resonance, and trapping (Murata et al., 2009). Such effects make tsunami behaviour far more complex in the coastal zone than in the open ocean. Different combinations of these effects lead to either the amplification or attenuation of the tsunami depending on the local topography.

Tsunamis become disasters when the height of the wave becomes large enough to inundate the coast, and/or strong currents in harbours cause damage to vessels, and port infrastructure. The former (and the latter) is most likely to occur from near-field or regional-field type tsunamis (those where the source is fairly close to the coast) and are the most dangerous type of tsunami disaster. Possible near-field/regional-field tsunami sources include large subduction zones of the coasts of countries such as: the Japan trench off the northeast coast of Honshu Island, Japan, the Cascadian subduction zone along the west coast of USA, Hikurangi-Kermadec trench off the east coast of the North Island, New Zealand, the Chile-Peru trench along the west coast of Peru and Chile, and the Sunda trench off the southwest coasts of the Indonesian Islands, Sumatra and Java. In recent times, the latter and the former have been associated with two of the largest natural disasters to have occurred in modern times: the 2004 Indian Ocean Tsunami, and the 2011 Tohoku-oki Earthquake Tsunami respectively. These two examples will be explained in more detail below. Numerous other near-field sources are possible: collapse of sections of volcanic edifices into bays, landslides on steep slopes surrounding fjords or tidal inlets, submarine landslides, and underwater volcanic eruptions. Notable examples of these include: the collapse of the eastern flank due to the volcanic activities of Mt. Unzen in 1792 causing a large tsunami in Shimabara Bay resulting in 15,000 fatalities (Ogawa, 1924), the 1998 tsunami in Papua New Guinea generated by a submarine landslide due to seismic action with an average of 10 m wave heights killing 2,100 people (Synolakis et al., 2002), and the 1958 Lituya Bay rockslide triggered by an 8.3 magnitude earthquake that recorded an extraordinary maximum runup of 524 m (Fritz et al., 2001). The major difference between these near-field sources and those generated by large subduction zone fault-slips is that they tend to be very localised and extremely devastating in the area close to the source but have relatively little effect outside the near-field region due to their smaller length scales.

The 26th December 2004 Indian Ocean Tsunami was generated by the Sumatra-Andaman earthquake, the largest to be recorded since 1964 with a seismic moment magnitude of $M_w =$



Figure 1.2: Aftermath of the 2004 Indian Ocean Tsunami in Aceh, Indonesia 2005 (source: AusAID, retrieved from; <https://www.flickr.com/photos/dfataustralianaid/10730863873/>)

9.1 - 9.3, and a so called tsunami moment magnitude of $M_t = 9.1$ (Kanamori, 2006; Lay et al., 2005). The rupture occurred along 1,200 - 1,300 km of the fault boundary between the Indo-Australian plate and the southeastern portion of the Eurasian plate, with peak slip displacements of ~ 15 m (Kanamori, 2006; Ammon et al., 2005; Lay et al., 2005). The tsunami resulting from this earthquake had enormous effects in the near-field and regional-field, most significantly in: Indonesia, Sri Lanka, India, and Thailand. The total number of fatalities is estimated at 227,000 while about 1.8 million people were displaced (Athukorala, 2012). Economic losses in those countries have been estimated at US\$9.4bn (Abe and Thangavelu, 2012). The largest destruction by the tsunami occurred nearest to the epicentre in the Aceh region (see Figure 1.2) with a maximum runup of 30 m and flow depths > 9 m (Borrero et al., 2006; Synolakis and Kong, 2006). While the earthquake and tsunami were considerably large events, the extent of the humanitarian crisis was particularly extreme due to: the high density of populations living near the coast, the relative poverty of the affected areas, and the lack of tsunami education, preparedness and disaster mitigation measures. A huge global humanitarian aid effort resulted with over US\$14bn pledged by the international community to help in the relief and reconstruction phases of the recovery process (Athukorala, 2012).

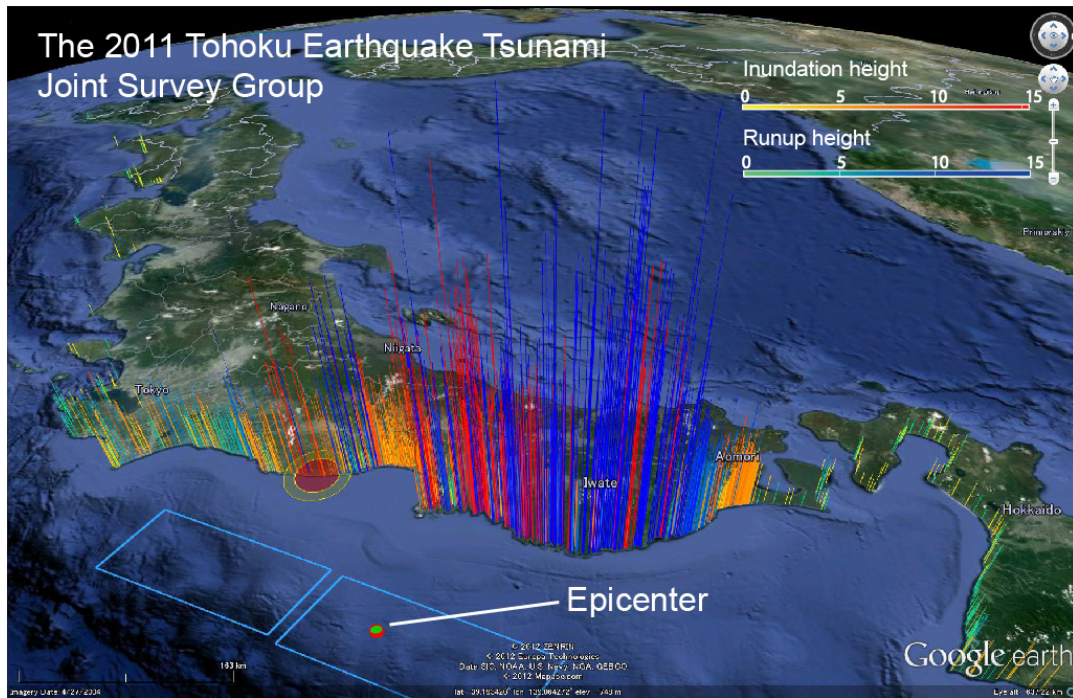


Figure 1.3: Surveyed inundation and runup heights along the Pacific coast of Japan resulting from the 2011 Tohoku-oki Earthquake Tsunami (source: The 2011 Tohoku Earthquake Tsunami Joint Survey (TTJS) Group, retrieved from; <http://www.coastal.jp/tsunami2011/>)

On March 11, 2011 a magnitude $M_w = 9.0$ earthquake occurred off the northeast coast of Honshu Island, Japan. It was the most powerful earthquake recorded since the Sumatra-Andaman earthquake one just over six years prior. The earthquake is assumed to have occurred over a rupture area of 450×200 km (Mori et al., 2011) at a depth of 30 km (United States Geological Survey, 2011). The uplift of the seabed has been estimated to be over 10 m near the trench axis and ~ 5 m near the epicentre with subsidence up to 2 m near the coastline (Fujii et al., 2011). This dramatic change in the seabed induced the gigantic Tohoku-oki tsunami that reached the nearest coastline in 20 min and affected over 2000 km of Japan's pacific coast concentrated in the Tohoku region (see Figure 1.3) (Mori et al., 2011). The tsunami caused 15,892 fatalities with an additional 2,574 missing. In total, 124,663 buildings fully collapsed, 274,638 buildings partially collapsed and 116 bridges were damaged as of July 10, 2015 (National Police Agency of Japan, 2015). The direct economic damage has been estimated at US\$183bn while costs for recovery might reach US\$122bn (Norio et al., 2011). However, the perceived risk for a tsunami in the region was high (with the similarly large Meiji Sanriku earthquake tsunami ($M_w = 8.2-8.5$) in 1896 and smaller ones every 10-50 years (Mori et al., 2011)), the public were comparatively well educated about tsunamis, and preparedness was high particularly in terms of hard (structural) protection measures such as breakwaters, seawalls, tsunami gates, and forest barriers (Suppasri

et al., 2013). This is in stark contrast to the conditions on the Sumatra coast during 2004 Indian Ocean Tsunami. However, immense damages and casualties still resulted in the Tohoku region. Suppasri et al. (2013) has commented on the performance of the hard protection measures and warns of their overreliance in place of soft measures such as evacuation strategies, evacuation shelters, warnings, and town planning.

Tsunamis may also affect places in the far-field in addition to the near-field and region-field. For example the 2004 Indian Ocean tsunami travelled across the Indian Ocean affecting the Arabian Peninsula and large portions of Africa's east coast. Similarly, the 2011 Tohoku-oki tsunami travelled across the Pacific Ocean affecting places as far away as Chile, California, and New Zealand. In this case, inundation and destruction of towns is typically not as severe compared with near-field tsunamis or often inundation does not occur at all. However, tsunami currents may still be significant and can cause damage to vessels and port infrastructure, sediment erosion and deposition, and disruption to port operations. For example in the Port of Salalah, Oman, 90 minutes after the arrival of the 2004 Indian Ocean tsunami strong currents broke all the mooring lines of a large freighter that got caught up in system of eddies and could not be brought under control (Lynett et al., 2014). During the 2011 Tohoku-oki tsunami significant damages were recorded in California ports with over US\$50mn of damage to two dozen harbours (Wilson et al., 2012). Thus, tsunamis are significant events in particular for countries with coastlines facing the Pacific and Indian Oceans. Even if the source of large tsunamis that occur are not nearby, disruptions and damage can arise. It is important that suitable mitigation measures and strategies are developed for these regions.

1.1.2 Countermeasures for Tsunami Disasters

A number of countermeasures are available for prevention and mitigation of tsunami disasters. Some discussion has already been mentioned in the previous section on the division of hard and soft measures. Hard measures are mainly structural ones where coastal structures such as breakwater and seawalls are constructed in bays and on coastlines. Such measures have the explicit goal of attenuating the wave energy in the bay and preferably preventing the wave from inundating coastal cities. Other structural measures include tsunami gates at river mouths, natural barriers such as forests and mangroves (which may be intentionally or unintentionally adopted), and river banks.

The 2011 Tohoku-oki tsunami has allowed for the best case study on the performance of various hard measures possible because the pacific coast of Japan is probably the most "protected" coast against tsunamis in the entire world. For example, many large breakwaters are present along the Sanriku coast including the deepest breakwater in the world (63 m) at the entrance to Kamaishi bay, and another large breakwater at the entrance to Ofunato bay (38 m deep) (see Figure 1.4). Unfortunately, despite their size the tsunami wave was even larger and overtopped the structures, causing significant damage to them while attenuating some of the tsunami energy



Figure 1.4: View of Kamaishi Bay (left) and Ofunato Bay (right), Iwate Prefecture, seen before the 2011 Tohoku-oki tsunami. Note the large scale breakwaters at the bay mouths (source: Iwate Prefecture Government, retrieved from; <http://www.pref.iwate.jp/kouwankuukou/kouwan/>)

before inundating the cities in behind. Moreover, seawalls are ubiquitous along the entire coast of Japan. Many are designed simply for protection from large waves and storm surges, however some were specifically designed against tsunamis (Suppasri et al., 2013). An example is Taro town, that had ~2.4 km of seawall length which had been successful against the 1960 Chilean tsunami but was overtopped and damaged during the 2011 Tohoku-oki tsunami (Suppasri et al., 2013). In addition forest barriers were present in Rikuzentakata City, Natori, and Ishinomaki with indications of spectacular failure in the former cases (all the trees except one were left standing and may have contributed to further damage on the city by debris impacts in Rikuzentakata City) and success in the latter case (helped to reduce the damage to houses in behind). The reasons for the difference in success is likely due to the relative size of the tsunami in the different locations where the tsunami height was ~6 m in Ishinomaki but > 10 m in the other two locations (Suppasri et al., 2013).

Other measures available against tsunamis are soft ones that are important to consider even for highly developed regions. For example, various stories of success (few) and failure (many) of the hard structural measures exist in the 2011 Tohoku-oki tsunami case (see Suppasri et al. (2013) for an in-depth review). It is clear that for an extremely large event it becomes essentially impossible and disingenuous to design against the tsunami to achieve complete prevention of the disaster under reasonable economical and social constraints. This has led to the slight change of tact in the Japanese case: design to *prevent* damage against frequent smaller, ~10-100 year events, termed Level 1 events (through hard measures), but only to *mitigate* the damage in the case of very large ~1000+ year events, termed Level 2 events (Shibayama et al., 2013). Soft measures are a key component of disaster mitigation. The main goal of soft measures are to save lives, which in terms of tsunamis generally revolve around evacuation strategies, shelters and

warning systems. It is common not only in Japan, but for many towns with coasts on the Pacific to now have tsunami inundation hazard maps, evacuation routes, and designated evacuation buildings. A large majority of consultancy and local government work on tsunami mitigation deals with the development of these aspects. Furthermore, the Pacific Tsunami Warning Center located in Hawaii was explicitly founded to forecast expected tsunami heights and currents in the Pacific Ocean after major earthquake events and issue warnings to the pertinent regions. In general, these measures of course do not protect property and other damages, unless one considers town planning and the movement of property and residents to higher ground a soft measure. However, living and working near the coast can be extremely important for people's everyday lives (fishing, trade and recreation) and it is mostly undesirable to sacrifice this for disaster prevention means.

1.1.3 Numerical Analysis for Tsunami Hazard Mitigation

In order to deduce the potential tsunami threat (forecasting), conduct a real-time assessment of the tsunami magnitude (nowcasting), and to analyse past tsunami impacts (hindcasting), numerical analyses are commonly performed. Numerical analysis is particularly important in the field of tsunami hazard mitigation because: the true length and time scales of the phenomenon are unattainable in the laboratory so that the Reynolds number will always be much smaller than in real scale flows, i.e. dynamic similarity will be impossible to attain (Nokes, R., personal communication, Nov 26, 2015), local topography and bathymetry are the most important parameters for consideration of the tsunami behaviour (also difficult to represent in the laboratory), tsunami propagation in general is well predicted by simple analytical equations easy to implement in numerical models, significant events are rare which means that field data is relatively scarce, and tsunamis affect particularly large areas resulting in sparse and costly field data. However, experimental and field data are still extremely important in order to better understand fundamental aspects, assess impacts, and verify numerical models. The post-event survey of the 2011 Tohoku-oki tsunami (Mori et al., 2012) has resulted in a large mass of data at more than 5,200 locations available for this purpose.

As mentioned, tsunami propagation can in general be adequately described by relatively simple analytical equations. These are known as the (nonlinear) shallow water equations (NSWE) that result from the consideration of the length scales of the phenomenon, which is described in detail in §2.1.3. Thus, it is straightforward to describe tsunami motion from the source towards the coast. Once the tsunami reaches the coastal zone, it transforms significantly where most of these effects may also be accounted for by the NSWE. Technically, however the tsunami becomes more flow-like as inundation occurs and the wave equations should break down. But flood inundation analysis is often achieved using the NSWE (e.g. Liang, 2010) because the motion is still mostly gravity and advection-driven. Indeed it has been shown that those equations can also perform relatively well for tsunami runup and inundation analyses (e.g. Kanoglu, 2004;

Titov and Synolakis, 1998; Shuto et al., 1986). Hence in general, for basic hazard assessments of tsunamis, e.g. computing the tsunami from the source to the coast and predicting the likely extent and depth of inundation, these equations are extremely useful and suitable. A large proportion of numerical analyses of tsunamis do indeed conduct this type of simulation in order to design tsunami hazard maps, and evacuation strategies. Moreover, the NSWE may also provide information on the basic performance of hard measures such as breakwaters, seawalls, and river banks.

However, there are many effects related to tsunami behaviour that may not be well captured by the NSWE model such as: frequency dispersive effects that are important for tsunami propagation over very long distances, landslide-induced tsunamis, and the formation of undular bores (e.g. Løvholt et al., 2008; Lynett, 2005), detailed formation of jets and coherent turbulent structures in harbours (e.g. Lynett et al., 2012), three-dimensional velocity structure and its relation to sediment transport in the coastal zone (e.g. Kihara et al., 2012), macro-roughness effects during inundation (Park et al., 2013), hydrodynamic response with coastal structures and infrastructure on land (Lynett and Liu, 2011), and complex tsunami-driven debris motion (e.g. Yoneyama et al., 2012). However, these effects are important for better tsunami hazard predictions and evaluations. For example, when the Pacific Tsunami Warning Center issues warnings across the Pacific Ocean, the arrival times are usually provided but these may not be accurate using the non-dispersive NSWE model for far-field coastal regions. Furthermore, the tsunami current hazard is significant even for ports in those far-field locations. The potential for damage to vessels, piers, docks and costs related to tsunami induced erosion and deposition of sediment should be considered by port operators. Moreover, during the tsunami decisions should be made whether to temporarily halt port operations, where to keep boats docked or whether or not to take them offshore. In addition, the design of coastal structures, infrastructure, and buildings, their locations and potential for damage is important knowledge for ports and coastal cities to adequately prevent and mitigate the disaster. Knowledge of the detailed hydrodynamic response of the structures with the tsunami, including the potential for impacts with tsunami-driven debris, can be extremely helpful to achieve these means effectively. Hence, numerical analyses are extremely useful for tsunami hazard mitigation means but it is also important to use the best model to correctly describe the phenomena to the accuracy desired.

1.2 Research Problem and Objectives

Tsunami disasters are real and significant hazards for many coastal communities. Evaluation of the potential risks and impacts, and developing engineering countermeasures for disaster prevention and mitigation is essential for these communities in order to properly manage the hazard. One particularly important tool to achieve this is the numerical analysis of tsunami behaviour as discussed in §1.1.3.

There are many relevant scales and physical processes involved in the entire description of the tsunami lifecycle. However, it is unlikely that any one set of equations (numerical model) can simulate the whole problem efficiently and accurately. For example, although the Navier-Stokes (N-S) equations may be used to approximate any phenomena relating to incompressible fluid flow (c.f. §2.1.1), they are impossible to actually physically apply over the full range of length scales present due to computational constraints. Thus, certain assumptions and techniques are required in order to reduce the problem to an accurately computable one.

This thesis introduces one possible technique to consider the efficient but potentially very detailed and accurate computation of tsunami behaviour. The method revolves around *two-way* multiscale coupling. This term refers to the coupling of different grid resolutions and equations at specified regions in the flow domain where information is passed in both directions between them. This technique enables the coupled model to potentially simulate the tsunami beginning from the earthquake source, propagating towards the coastal zone before modelling the complex hydrodynamics in a fine region of interest, for example around coastal structures, buildings and infrastructure. The method assumes that each model is the most suitable (balance of efficiency and accuracy) to that specific region, and at the point of coupling the physics may be equally well described by both models. Hence, in addition to the development of the multiscale coupling method it is also important to know the following, which may be considered to be the objectives of this study in addition to the detailing of the adopted models, and multiscale coupling algorithms:

1. The most suitable boundary conditions for coupling
2. Range of applicability of the coupled model and robustness of the coupling
3. Location where each model should be defined and coupled together
4. Potential for application to real-scale tsunami problems

1.3 Thesis Outline

This dissertation concerns the development, applicability assessment, and an example of the real-world application of a numerical tool to allow for the in-depth calculation of tsunamis in specified regions while still computing the general tsunami behaviour over a wide-scale. The thesis is divided up into six chapters as follows:

Chapter 1 Presents background on tsunami disasters and countermeasures for disaster prevention and mitigation. Introduces the use of numerical analysis for hazard assessments and the design of suitable countermeasures. Outlines some of the problems encountered in numerical modelling and the objectives of this thesis to address these issues.

Chapter 2 Introduces the basic range of theories available to model tsunami phenomena. Discusses previous studies and the chronological development of numerical modelling of tsunami hydrodynamics. Outlines the current state-of-the-art and the probable direction of research in the near future including the motivation for this thesis.

Chapter 3 Describes the numerical methods of the individual shallow water equation and Reynolds-averaged Navier-Stokes equation models that are chosen to simulate the tsunami behaviour. Details the adopted techniques for two-way multiscale coupling that includes: nesting the horizontal grids, nesting in the temporal space, and converting depth-averaged information to vertically varying quantities (and vice-versa).

Chapter 4 A study on solitary wave transformation and breaking on a plane beach used to investigate: the basic performance of the two-way multiscale coupling technique, locations where it is best to couple the models, the range of conditions where the coupled model is expected to perform well, expected errors at the coupling interface, and ability of the coupled model to describe physical processes that would otherwise be difficult without coupling.

Chapter 5 Application of the coupled model to simulate the hydrodynamics around a breakwater in a real-scale tsunami problem. Illustrates the ability of the model to be used in real-world problems and discusses new findings that were made possible using the coupled model.

Chapter 6 Concludes the study highlighting the results of the study in addition to areas where gaps still exist and hence possible future research directions.

THEORY AND LITERATURE REVIEW

Numerical modelling of tsunami hydrodynamics covers a wide range of scales and physical behaviour as will be discussed in this chapter. §2.1 starts by introducing the most basic of equations for fluid flow before applying assumptions that simplify the theory for water waves and eventually for very long water waves in particular, e.g. tsunamis. Lastly, the common theory and numerical techniques used throughout the history of tsunami modelling is introduced in §2.2, leading up to the present day and where this thesis fits into the scheme of things.

2.1 Basic Equations and Theory

This section begins by introducing the governing equations and a short discussion of the relevant theory for this thesis. §2.1.1 starts with the most complete set of equations for wave motion and incompressible fluid flow in general - the incompressible Navier-Stokes (N-S) equations. A special case of the N-S equations is the Reynolds-averaged Navier-Stokes (RANS) equations and this is introduced in §2.1.1. By applying the inviscid and irrotational assumption to the N-S equations we get the often used velocity potential formulation for wave motion in §2.1.2. A further assumption to potential flow is that the water depth is very small compared to the wave length - the long wave assumption. Taking the assumption to the first-order results in the shallow water equations presented in §2.1.3. The shallow water equations are widely used in a number of problems including open channel flow, tidal motion, inertial waves and gravity waves including tsunami propagation and inundation as found in this thesis. Additionally, taking a more general approach to the long wave assumption (to higher-order) results in the Boussinesq equations which is briefly presented in §2.1.3. Note, that this section (§2.1) will be short on proofs and will basically introduce the theory and equations as they can be found in a vast number of textbook or lecture notes on the subject. On that note the author of this thesis would like to acknowledge the following resources for the compilation of this section: Nokes (2008a) in §2.1.1 and §2.1.2; Nokes (2008b) in §2.1.1; Dawson and Mirabito (2008) and Chanson (1999) in §2.1.3; and Wei et al. (1995); Nwogu (1993); Madsen et al. (1991); Peregrine (1967) for §2.1.3.

2.1.1 Incompressible Navier-Stokes Equations

Fluid motion is assumed be a continuum phenomenon, that is we can think of the fluid flowing in and out of a control volume - that it completely occupies - without needing to model the individual movement of molecules. Through this assumption governing equations for fluid motion can be found by considering the conservation of certain universals in the control volume such as mass and momentum. Furthermore, many environmental fluid problems that for example just involve water and air, experience small changes in pressure in comparison to their bulk modulus of elasticity. That means that the changes of density in time and space are negligible with pressure, called the incompressible assumption. Note that technically this does not imply that the density is necessarily constant as density indeed changes depending on temperature and salinity in the ocean.

With these assumptions in mind, the conservation of mass or continuity equation can be written simply as:

$$\frac{\partial u_i}{\partial x_i} = 0 \quad (2.1)$$

where u_i is the velocity component in the i direction. x_i indicates the i^{th} Cartesian Coordinate axis. Note that Einstein's summation index notation is used in Eqn. (2.1) above and throughout this thesis as it is a convenient way to write tensor equations. In three-dimensions, i can be chosen

to be 1, 2, and 3 which in this thesis nominally refers to the x , y , and z Cartesian Coordinate axes respectively.

The next and last governing equation for fluid flow is the conservation of momentum or in fact the incompressible Navier-Stokes equations:

$$\frac{\partial u_i}{\partial t} + u_j \frac{\partial u_i}{\partial x_j} = -\frac{1}{\rho} \frac{\partial p}{\partial x_i} + g_i + \nu \frac{\partial^2 u_i}{\partial x_j \partial x_j} \quad (2.2)$$

where t is the time axis, ρ is the fluid density, p is the pressure, g_i is the body force in the i direction, and ν is the kinematic viscosity of the fluid. The entire body of incompressible fluid flow is said to be governed by combination of Eqn. (2.1) and (2.2). It is useful to name each of the terms in the Navier-Stokes equations to help understand their separate functions: the terms on the left are inertial ones and they are called the local acceleration and advective acceleration terms respectively. The first on the left is called the local acceleration term because it tells us how the velocity of the fluid at a certain location is changing with time. The advective acceleration term describes how fluid is moved from one point to another by the flow. The first term on the right is the pressure gradient term, and the middle one is the body force term. These are dominant forces for waves in the ocean, in particular long waves which are the focus of this thesis. The last term on the right is the viscous term and corresponds to the dissipation of energy. For most of the life of an ocean wave this is an almost negligible term which is useful for deriving simplified governing equations as presented in the following sections.

Lastly, the only boundary condition that we can be guaranteed of in a real fluid flow is the no-slip boundary condition which states that all fluid in contact with the solid boundary can only move with the velocity of the boundary (which can usually be approximated to be zero for the sea bed). However, we will find in §2.1.2 that through the inviscid assumption this boundary condition will in fact disappear to be replaced by a different one.

Reynolds-Averaged Navier-Stokes Equations

In environmental fluid problems the flow often becomes turbulent. This happens when the Reynolds number, $Re = \frac{VL}{\nu}$, a measure of the ratio of inertial to viscous forces becomes large. Here, V and L are some representative velocity magnitude and length scale respectively of the problem. In such a case, if one were to measure u_i and p at a particular point in time one would find a distribution similar to the solid line in Figure 2.1. The quantities essentially vary randomly with time and the same is also true in space. Thus, it is very difficult to make sense of the data in its raw form. One method to simplify the analysis is to take an ‘‘average’’ of the quantities, u_i and p as first proposed by Reynolds (1895). The ‘‘average’’ technically should be achieved through an ensemble average, i.e. by running many experiments and averaging the results from all of the experiments. This may be quite difficult to fully achieve in practice hence the average can also be estimated through time-averaging since turbulent fluctuations happen on small time scales compared with the time scales of the effects we are usually interested in. A visual representation

of the time-average is shown by the dashed line in Figure 2.1. Note that the mean (time-averaged) quantity may vary in time due to the previous argument.

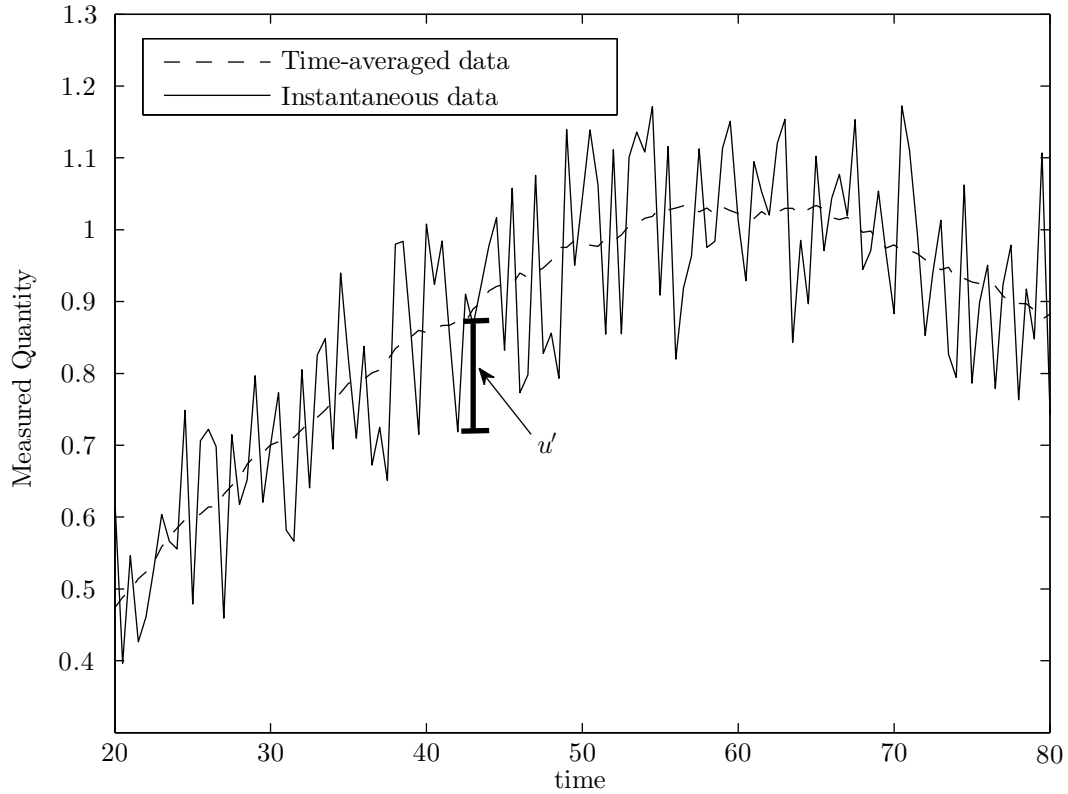


Figure 2.1: Visual representation of instantaneous quantities that exhibit turbulent fluctuations and a corresponding time-averaged quantity at a certain location in space

To perform the analysis in the form of this averaged quantity, which we call the Reynolds-average, we decompose u_i and p into the mean (time-averaged) and fluctuating components:

$$u_i = \bar{u}_i + u'_i \quad p = \bar{p} + p' \quad (2.3)$$

where $\bar{\cdot}$ indicates the Reynolds-averaged quantity and $'$ is the fluctuating component. We then use this decomposed form from Eqn. (2.3) to re-evaluate the incompressible Navier-Stokes equations, (2.1) and (2.2). Since that by definition the fluctuating component has zero mean Eqn.(2.1) simply reduces to:

$$\frac{\partial \bar{u}_i}{\partial x_i} = 0 \quad (2.4)$$

This implies that the fluctuating components play no role in the conservation of mass. The analysis is more complex for the conservation of momentum, Eqn. (2.2), but will reduce to:

$$\frac{\partial \bar{u}_i}{\partial t} + \bar{u}_j \frac{\partial \bar{u}_i}{\partial x_j} = -\frac{1}{\rho} \frac{\partial \bar{p}}{\partial x_i} + g_i + \frac{\partial}{\partial x_j} \left(\nu \frac{\partial \bar{u}_i}{\partial x_j} - \overline{u'_i u'_j} \right) \quad (2.5)$$

where the extra term on the RHS, $\overline{u'_i u'_j}$ is called the Reynolds-stress term (when multiplied by ρ) and has arisen due to the averaging of the nonlinear advection term. It is the Reynolds-stress terms which make turbulent flow complex since their effect can be significant even though the viscous stresses, $\nu \frac{\partial \bar{u}_i}{\partial x_j}$ in the high Re limit are negligible. In order to use the Reynolds-averaged Navier-Stokes (RANS) equations given by Eqns. (2.4) and (2.5), one needs to introduce some sort of model to approximate the Reynolds-stresses in order to “close” the equations. A common approach is to relate the stresses to a turbulent viscosity through Boussinesq’s assumption. To get a time and position dependent turbulent viscosity involves modelling the transport of other time-averaged turbulent quantities such as turbulent kinetic energy and the rate at which that dissipates. One common form of this is the $k - \epsilon$ model which is adopted in this thesis and introduced in §3.4.5. Assuming this turbulence closure model works well, the N-S equations are now significantly simpler to model in the form of the RANS equations because the fluctuating components that act on very small time and spatial scales may be ignored and only the transport of the mean quantities need to be considered. In other words spatial grid and temporal step sizes need not be prescribed at prohibitively small scales.

2.1.2 Potential Flow Theory

We begin with Eqns. (2.1) and (2.2) for incompressible flow introduced in §2.1.1. The first assumption we can make due to a scale analysis is that waves can generally be assumed inviscid. That is, the viscous stress term is assumed to be very small in comparison to all the other terms and is neglected. The flow state where $Re \gg 1$ indicates an inviscid assumption is a suitable one. For a typical coastal engineering problem this is easily satisfied since the characteristic length and velocity scales are far larger than the kinematic viscosity of water. Following from this assumption for a fluid body initially at rest (no rotation), Kelvin’s circulation theorem guarantees that the flow will be irrotational for all time. Irrotationality refers to the curl of the velocity vector becoming zero:

$$\epsilon_{ijk} \frac{\partial u_k}{\partial x_j} = 0 \quad (2.6)$$

where ϵ_{ijk} is the Levi-Civita tensor. Since the curl of a scalar gradient is always zero, the irrotational assumption of the flow mathematically leads to the convenient consequence that the velocity field can be expressed as the gradient of a scalar field called the velocity potential, ϕ :

$$u_i = \frac{\partial \phi}{\partial x_i} \quad (2.7)$$

Expressing the continuity Eqn. (2.1) in terms of the velocity potential yields what is known as Laplace’s equation:

$$\frac{\partial^2 \phi}{\partial x_i \partial x_i} = 0 \quad (2.8)$$

Laplace's equation can be solved subject to appropriate boundary conditions to give the velocity field. Furthermore, to find the pressure one can introduce the velocity potential into the momentum Eqn. (2.2) - sans the viscous stress term - and integrate to obtain the Bernoulli equation:

$$\frac{\partial \phi}{\partial t} + \frac{1}{2} \left(\frac{\partial \phi}{\partial x_i} \right)^2 + \frac{p - p_{atm}}{\rho} - g_i x_i = 0 \quad (2.9)$$

where p_{atm} is the atmospheric pressure. To find solutions to Eqns. (2.8) and (2.9) boundary conditions are required. Firstly, a suitable problem definition is required to simplify the problem. In our case we can consider a body of water with some initial free surface level (M.S.L), above an arbitrary sea bed so that the local water depth, h becomes a function of the horizontal dimensions (assuming it does not change with time), disturbed so that waves form on the free surface, with a local elevation, η above the initial free surface level, amplitude, A and wavelength, λ as illustrated in Figure 2.2.

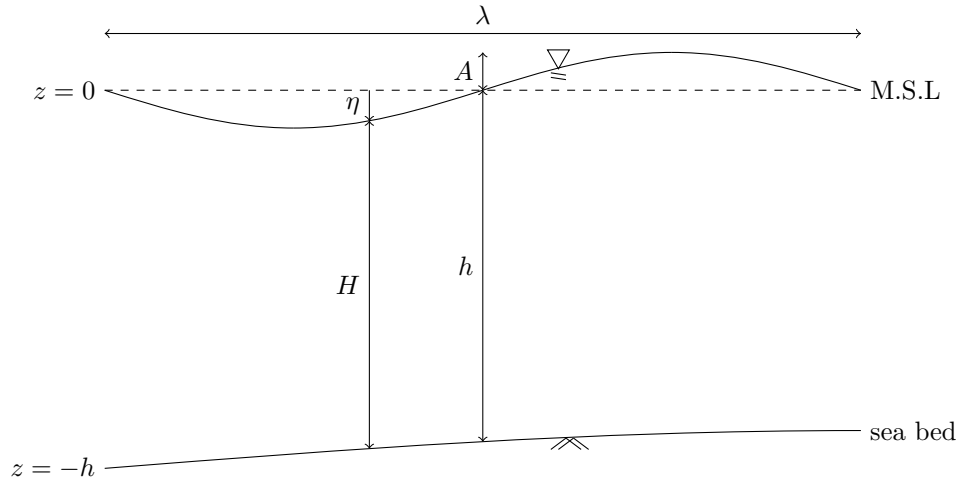


Figure 2.2: Problem definition sketch for a free surface wave above an arbitrary sea bed

Notice that the problem has been transformed so that obvious boundaries exist at the top and bottom in the z direction but none exist at the horizontal boundaries, which is of course due to the gravity force. This necessarily distinguishes the horizontal and vertical directions so that hereafter in §2.1, z will be used independently and i in Einstein's index notation will indicate only 1 and 2 (the x and y directions). Furthermore, the body force term will be assumed only to be that of the acceleration due to gravity in the negative z direction (ignoring Coriolis and other effects), denoted g .

Considering the bottom boundary, since the flow is inviscid there is no viscosity to enforce the no-slip boundary condition. However, flow is still not able to pass through normal to the boundary which leads to the following kinematic boundary condition:

$$\frac{\partial \phi}{\partial z} = - \frac{\partial \phi}{\partial x_i} \frac{\partial h}{\partial x_i} \quad \text{on } z = -h(x_i) \quad (2.10)$$

For a flat sea bed this would mean that the vertical velocity, $w = \frac{\partial \phi}{\partial z}$ is equal to zero here. At the free surface there are two boundary conditions. The first is a dynamic one that simply says that the pressure must be equal to the atmospheric pressure, p_{atm} at the free surface:

$$p = p_{atm} \quad \text{on } z = \eta(x_i, t) \quad (2.11)$$

The second is a kinematic one which states that a fluid particle on the free surface moves with the free surface. This is equivalent to the material derivative of the surface, $z - \eta(x_i, t) = 0$ being equal to zero and simplifies to:

$$\frac{\partial \phi}{\partial z} = \frac{\partial \eta}{\partial t} + \frac{\partial \phi}{\partial x_i} \frac{\partial \eta}{\partial x_i} \quad \text{on } z = \eta(x_i, t) \quad (2.12)$$

Finally, by differentiating Bernoulli's Eqn. (2.9) with respect to t we can combine the two free surface boundary conditions Eqn. (2.11) and (2.12) into one to obtain:

$$\frac{\partial^2 \phi}{\partial t^2} + \frac{\partial \phi}{\partial x_i} \frac{\partial^2 \phi}{\partial x_i \partial t} + g \left(\frac{\partial \phi}{\partial z} - \frac{\partial \phi}{\partial x_i} \frac{\partial \eta}{\partial x_i} \right) = 0 \quad \text{on } z = \eta(x_i, t) \quad (2.13)$$

In terms of an inviscid and irrotational flow for the problem definition in Figure 2.2, Eqns. (2.8), Eqns. (2.9), (2.10), and (2.13) are exact equations without any assumptions as to the length scales involved. However, the equations are very complicated to solve as is. A common assumption applied is that the wave amplitude is much smaller than the water depth i.e. the nonlinearity ratio, $\varepsilon = A/h \ll 1$. This simplifies Bernoulli's equation and the boundary condition at the free surface considerably. For a flat bed of constant depth it leads to what is known as Airy's wave theory (linear wave theory). Although simple, it is often surprisingly accurate and the first go to tool for estimating a wave's property. One of the main outcomes of Airy's theory is the so called linear dispersion relation:

$$\omega^2 = g\kappa \tanh \kappa h \quad (2.14)$$

which has been given in terms of the angular frequency, ω and wave number, κ . By definition the wave speed is equal to, $c = \omega/\kappa$. In terms of c the dispersion relationship may be written as:

$$c = \sqrt{\frac{g \tanh \kappa h}{\kappa}} \quad (2.15)$$

which says that the wave speed depends on both κ (λ) and h . There are two limits which one may consider. The first is the deep water limit where the water depth is much larger than the wavelength i.e. $\kappa h \gg 1$, and thus the wave speed approaches, $c = \sqrt{g/\kappa}$. Here, the wave speed only depends on κ . The other is the shallow water limit, when the wavelength is much larger than the depth i.e. $\kappa h \rightarrow 0$, and the wave speed approaches, $c = \sqrt{gh}$. Here, the only parameter that matters when determining the wave speed is the water depth, h !

2.1.3 Long Wave Theory

In §2.1.2 the linear dispersion relation was introduced. For so called shallow water waves where the frequency dispersion parameter, $\mu = h/\lambda \ll 1$, the wave speed was shown to only depend on the water depth. It is thus straightforward to make a back of the envelope calculation to determine say a tsunami's wave speed and to obtain a rough estimate of its arrival time. The only problem of course is that the water depth is a function of the horizontal axes (a non-flat bed) in a real geophysical problem which makes any accurate solution to the problem invariably more difficult to obtain. Furthermore, as tsunamis approach the shoreline the depth decreases so that ε may become significant reducing the accuracy of the linear assumption.

Thus, we seek a simplified version of the full potential theory shown in §2.1.2 applying the long wave assumption - $\mu \ll 1$ plus the finite-amplitude assumption, $\varepsilon \sim O(1)$ - on an arbitrary seabed. The first thing to do is to go back to the incompressible Navier-Stokes equations and investigate the relative scales. For example the inviscid momentum equation in the z -direction is ($i = 1, 2$ only in Einstein's index notation):

$$\frac{\partial w}{\partial t} + u_i \frac{\partial w}{\partial x_i} + w \frac{\partial w}{\partial z} = -\frac{1}{\rho} \frac{\partial p}{\partial z} - g \quad (2.16)$$

Suitable scales for each term are then listed below:

$$\frac{\partial}{\partial t} \sim \frac{c}{\lambda} \quad \frac{\partial}{\partial x_i} \sim \frac{1}{\lambda} \quad \frac{\partial}{\partial z} \sim \frac{1}{h} \quad w \sim \varepsilon \mu c \quad u_i \sim \varepsilon c \quad p \sim \rho g h \quad (2.17)$$

This leads to the following order of magnitude estimate:

$$O \quad \frac{\varepsilon \mu c^2}{\lambda} \quad \frac{\mu \varepsilon^2 c^2}{\lambda} \quad \frac{\mu^2 \varepsilon^2 c^2}{h} \quad \sim \quad \frac{\rho g h}{\rho h} \quad g \quad (2.18)$$

If the wave speed is then assumed to be proportional to the long wave one ($c = \sqrt{gh}$), Eqn (2.18) reduces to:

$$O \quad \mu^2 \varepsilon g \quad \mu^2 \varepsilon^2 g \quad \mu^2 \varepsilon^2 g \quad \sim \quad g \quad g \quad (2.19)$$

Thus, all terms on the left hand side are of order μ^2 , and since $\mu \ll 1$ they can be neglected which leaves us with:

$$\frac{\partial p}{\partial z} = -\rho g \quad (2.20)$$

which is just the hydrostatic pressure distribution that implies, $p = \rho g(\eta - z) + p_{atm}$. Differentiating this by the horizontal direction gives the following relation:

$$\frac{\partial p}{\partial x_i} = \rho g \frac{\partial \eta}{\partial x_i} \quad (2.21)$$

Applying a similar scaling approach for the horizontal momentum equations in order to remove the dependence on w and inserting Eqn. (2.21) yields:

$$\frac{\partial u_i}{\partial t} + u_j \frac{\partial u_i}{\partial x_j} + g \frac{\partial \eta}{\partial x_i} = 0 \quad (2.22)$$

The second step is to integrate the continuity Eqn. (2.1) with respect to z from the seabed to the free surface ($-h$ to η). Note that since h and η depend on x_i and t the Leibniz integral rule is used:

$$\frac{\partial}{\partial x_i} \int_{-h}^{\eta} u_i dz + u_i(-h) \frac{\partial h}{\partial x_i} - u_i(\eta) \frac{\partial \eta}{\partial x_i} + w(\eta) - w(-h) = 0 \quad (2.23)$$

It so happens that the boundary conditions on the free surface and the seabed in Eqns. (2.12) and (2.10) respectively simplify Eqn. (2.23) considerably to give:

$$\frac{\partial \eta}{\partial t} + \frac{\partial Q_i}{\partial x_i} = 0 \quad (2.24)$$

where the horizontal volume flux, $Q_i \equiv \int_{-h}^{\eta} u_i dz$ has been introduced.

Since, Eqns. (2.22) and (2.24) are independent of the vertical direction those equations can be integrated and depth-averaged so that one only needs to model a single layer of flow. The depth-averaged velocity, $U_i = Q_i/H$ is introduced, where $H \equiv \eta - h$ is the total depth. The equations then become:

$$\frac{\partial \eta}{\partial t} + \frac{\partial(U_i H)}{\partial x_i} = 0 \quad (2.25)$$

$$\frac{\partial U_i}{\partial t} + U_j \frac{\partial U_i}{\partial x_j} + g \frac{\partial \eta}{\partial x_i} = 0 \quad (2.26)$$

Eqns. (2.25) and (2.26) are the set of equations called the horizontal two-dimensional (nonlinear) shallow water equations (2DH NSWE). The term “nonlinear” is often used particularly in the tsunami community to differentiate from the linearised (assumes $\varepsilon \ll 1$) form since for the propagation of tsunamis in the open ocean away from the coast the linearised equations may be used to good effect. Hence the “N” in the NSWE abbreviation. Just to clarify, the linearised form (LSWE), ignores the second term in Eqn. (2.26), the advection term, to give what is otherwise known as the classic wave equation:

$$\frac{\partial U_i}{\partial t} + g \frac{\partial \eta}{\partial x_i} = 0 \quad (2.27)$$

A common addition to the NSWE are the consideration of the viscous effects from the sea bed. Although, the inviscid assumption was made in our formulation of the equations which helped to eliminate the z dependence on the flow, an averaged effect on the depth-averaged layer of fluid can be helpful to approximate the real world conditions more accurately. This is often introduced as a bed stress term and simply added onto the LHS of Eqn. (2.26):

$$\frac{\partial U_i}{\partial t} + U_j \frac{\partial U_i}{\partial x_j} + g \frac{\partial \eta}{\partial x_i} + \frac{\tau_{bi}}{\rho H} = 0 \quad (2.28)$$

where the bed stress, τ_{bi} can be given in the quadratic form:

$$\tau_{bi} = \rho C_f \frac{U_i \sqrt{U_j U_j}}{2} \quad (2.29)$$

C_f is a bed roughness or drag coefficient which can be approximated a number of ways. Perhaps most accurately and satisfyingly for fluid mechanics scientists it can be related to the Darcy-Weisbach friction factor, f which was originally developed for pipe flow:

$$C_f = \frac{f}{4} \quad (2.30)$$

The Colebrook-White formula which is valid for turbulent flows can then be used to determine f based on Re , H and an equivalent bed roughness height, k_s using an iterative process. Another common method familiar with engineers but controversial among the fluid mechanics community however, is the Gauckler-Manning approximation:

$$C_f = 2 \frac{gn^2}{H^{1/3}} \quad (2.31)$$

where n is Gauckler-Manning's roughness coefficient. Tabulated values of n are widely available for different land uses and surfaces. This helps to explain its ubiquity particularly in tsunami modelling despite that fact that it is empirical, n is not dimensionless, and the formula is only valid for steady, uniform equilibrium or gradually varied, fully rough turbulent flows of clear water (Chanson, 1999).

High-Order Long Wave Theory: Boussinesq Equations

All long wave theories are based on the assumption, $\mu \ll 1$. The literal application of this leads to the shallow water equations as demonstrated in §2.1.3. The main idea of Boussinesq theory is to set a perturbation from the literal long wave theory. For example, u_i is expanded in terms of ε :

$$u_i = u_{i0} + \varepsilon u_{i1} + \varepsilon^2 u_{i2} + \dots \quad (2.32)$$

p , η and Q_i are also expanded in the same way. w is further multiplied by μ like in Eqn. (2.17):

$$w = \mu(w_0 + \varepsilon w_1 + \dots) \quad (2.33)$$

These are inserted into the governing equations (potential flow theory) to reduce the equations to 2DH and obtain the Boussinesq equations to the desired order of accuracy. It is common to first non-dimensionalize the potential flow equations so that terms of orders in μ and ε can be appropriately dropped as desired. For example, in order to balance the linear frequency dispersive effects, μ^2 and the nonlinear amplitude dispersive effects, ε , the condition that, $\mu^2 \sim \varepsilon \ll 1$ should be applied. This is the one used to derive the weakly nonlinear Boussinesq equations. In this case terms higher than $O(\mu^2)$ and terms of $O(\varepsilon)$ in $O(\mu^2)$ are neglected. If a fully nonlinear Boussinesq formulation is required then terms like $O(\varepsilon\mu^2)$ and $O(\varepsilon^2\mu^2)$ are instead retained.

One important issue relates to the dispersive characteristics of the equations. One set of equations derived by Peregrine (1967) known as the "standard" Boussinesq equations is defined in terms of the depth-averaged velocity:

$$\frac{\partial \eta}{\partial t} + \frac{\partial(U_i H)}{\partial x_i} = 0 \quad (2.34)$$

$$\frac{\partial U_i}{\partial t} + U_j \frac{\partial U_i}{\partial x_j} + g \frac{\partial \eta}{\partial x_i} = \frac{h}{2} \frac{\partial^3 (U_j h)}{\partial x_i x_j t} - \frac{h^2}{6} \frac{\partial^3 U_j}{\partial x_i x_j t} \quad (2.35)$$

One may notice that only the RHS of Eqn. (2.35) is different to the NSWE. However, the equations have already become rather complicated including derivatives up to the third-order as shown. Relative to the linear wave speed these equations are accurate up to $\mu \approx 0.13$ (Madsen et al., 1991). This is in comparison to the NSWE which are often said to be practically suitable for $\mu < 0.05$. Additionally, it so happens that the dispersive characteristics of Boussinesq equations are related to the elevation of the horizontal velocity that appears in the equations. Knowing this, Nwogu (1993) derived the Boussinesq equations in terms of a horizontal velocity, $u_{\alpha i}$ at an arbitrary elevation, z_α :

$$\frac{\partial \eta}{\partial t} + \frac{\partial (u_{\alpha i} H)}{\partial x_i} + \frac{\partial}{\partial x_j} \left[\left(\frac{z_\alpha^2}{2} - \frac{h^2}{6} \right) h \frac{\partial^2 u_{\alpha j}}{\partial x_i x_j} + \left(z_\alpha + \frac{h}{2} \right) h \frac{\partial^2 (u_{\alpha j} h)}{\partial x_i x_j} \right] = 0 \quad (2.36)$$

$$\frac{\partial u_{\alpha i}}{\partial t} + u_{\alpha j} \frac{\partial u_{\alpha i}}{\partial x_j} + g \frac{\partial \eta}{\partial x_i} = -z_\alpha \frac{\partial^3 (u_{\alpha j} h)}{\partial x_i x_j t} - \frac{z_\alpha^2}{2} \frac{\partial^3 u_{\alpha j}}{\partial x_i x_j t} \quad (2.37)$$

In this case, while Eqn. (2.37) is similar to Eqn. (2.35), a number of complicated terms have appeared in the continuity Eqn. (2.36). The benefit from the additional terms is the improvement in the linear dispersion relation. It turns out that by setting $z_\alpha = -0.53h$, the model matches the linear wave speed up to approximately $\mu \approx 0.5$ (Nwogu, 1993). Other methods of derivation such as that by Madsen et al. (1991) have also been able to improve the linear dispersion relation up to a similar level. Finally, it should be mentioned that the two sets of Boussinesq equations shown here are both weakly nonlinear. A fully nonlinear version of the Nwogu (1993) type equations was derived by Wei et al. (1995), that inevitably contains a few additional terms. Fully nonlinear equation models will perform better when nonlinear effects which otherwise restrict the validity of the frequency dispersion relation in the weakly nonlinear equations appear.

2.2 Numerical Modelling of Tsunami Hydrodynamics

As §2.1 has shown, because of the length scales of tsunamis, governing equations for their flow can often be greatly simplified in comparison to the full N-S and potential flow equations. Still, a great variety of long wave theories and numerical techniques have been employed to solve tsunami flow each with their own subtle or not so subtle differences. There is thus no real global consensus on a “good” model but various benchmark tests and workshops (e.g. Synolakis et al., 2009, 2007) have been created to ensure that they meet some standard, at least if they are to be used for non-academic purposes. §2.2.1 first describes the development of tsunami modelling towards theory and methods that are commonly used today. This is followed by a look to the future, whereby new considerations in tsunami assessment are outlined in §2.2.2. Possible numerical techniques and ideas to facilitate such considerations, and thus the motivation of this dissertation are put forward.

2.2.1 Past and Present

Initially, analytical models for “tsunami” waves generated by a vertical dislocation of the ground were widely investigated. The models mainly focussed on linear wave theory and could describe the temporal and spatial evolution over uniform depth (e.g Hammack, 1973; Moimoi, 1964; Kajiura, 1963; Ichiye, 1958). The results were useful to determine the behaviour of the waves near the source region and the expected decay of leading waves. This lead Kajiura (1963) to propose conditions when frequency dispersion effects would become important for propagation, that is when, $p_a < 3$:

$$p_a = \left(\frac{6h}{R} \right)^{1/3} \frac{a}{h} \quad (2.38)$$

where R is the distance from the source, a is the length of the tsunami source, and h is the water depth. Additionally, Hammack (1973) investigated the importance of the nonlinear effects by comparison of the linear solution with the KdV equation. It was found that assuming that the linear solution was valid near the source, it would be reasonable for propagation only for some finite distance (about 20 depths) before nonlinear effects become important. But there are severe restrictions by assuming uniform depth. For example, the importance of nonlinear effects may be eased if the depth is increased from the one at the source (e.g. from continental shelf to deep ocean).

Numerical modelling thus became an important consideration in order to simulate tsunami propagation with variable water depths. Despite the warning by Hammack (1973), the linear assumption has been commonly adopted for tsunami propagation due to length scale considerations for long waves in the open ocean. An early example was Aida (1969) who used a finite-difference (FDM) form of the LSWE to compute the propagation of the 1964 Niigata Tsunami and the 1968 Tokachi-oki Tsunami with 10 km and 20 km grid spacing respectively. An initial free surface displacement based on an estimation of the crustal movement and the origin of the tsunami was

determined by an inverse refraction diagram. Similarly, Hwang and Divoky (1970) computed the propagation of the 1964 Alaskan Good Friday tsunami using a FDM formulation of the NSWE on a 16.1 km grid spacing and time steps of 100 s. The details of the spatial and temporal grid spacings are important because one of the major differences in numerical modelling of tsunami propagation today is simply our increase in computational power. Note that by using the LSWE or NSWE with variable depth, the effects of frequency dispersion were lost, but as long as the relative distances of travel were short, and source lengths large (Eqn. (2.38)), both LSWE and NSWE could be considered suitable approximations to the problem. Following these studies other early examples of tsunami propagation using similar FDM formulations of the LSWE include; Chen (1986); Nakamura (1984, 1983); Hwang et al. (1972). Nakamura (1983) mentioned that there was only a 1% difference in the height of the leading tsunami wave compared with a NSWE model that included bottom friction and Coriolis effects. Later, Shuto (1991) was able to summarise that the LSWE can give satisfactory results for tsunamis in water depths greater than approximately 50 m. Accordingly the LSWE were shown to be useful for tsunami propagation outside of the coastal zone.

The next step for researchers was to start looking at the evolution of tsunamis in the coastal zone leading to runup and inundation. Prior, reflection conditions at the coastlines were used which prevented runup calculations. Conveniently however, using Bessel functions as a solution to the NSWE for a solitary waves on a plane beach, Synolakis (1987) found that the maximum height at the shoreline from the LSWE solutions (that could not be solved for evolution beyond the initial shoreline) actually equals the maximum runup from the NSWE solutions as long as the linear assumption is valid offshore. This is despite different wave behaviours in the surf zone. However, many unknowns still remained since two-dimensional effects, real bathymetries that may be different from a plane beach, and bottom friction effects were not taken into account. This is in addition to the question of the adequacy of solitary waves as an approximation of tsunami waves (c.f. Madsen and Schaffer, 2010). One of the first major breakthroughs for numerically computing the evolution of the shoreline was made by Hibberd and Peregrine (1979) with their FDM formulation of the NSWE for runup of a bore on a plane beach by giving a provisional water level estimated from the extrapolation of the free surface and calculating the flux based on that water level and depth. Moreover, around the same time in Japan two other seminal studies had successfully used an inundation algorithm for tsunamis (Iwasaki and Mano, 1979; Aida, 1977) again for FDM formulations of the NSWE.

The studies of Shuto (1991); Shuto et al. (1986); Goto and Shuto (1983) which more carefully analysed the different numerical techniques and effects on propagation and inundation, developed into the widely used model now known as TUNAMI-N2 (Goto et al., 1997). It utilises the explicit leap-frog scheme and was shown to have relatively small truncation errors in comparison to other explicit schemes (Imamura and Goto, 1988). Zelt (1991) showed a different approach for runup of calculations of solitary waves in 1DH. He used a Lagrangian Boussinesq finite-element

(FEM) wave model to track the shoreline that was applicable for both non-breaking and breaking waves, where the latter generally require frequency dispersion effects. The only major drawback was the necessity to calibrate the bottom friction and artificial viscosity terms. The next major breakthrough for inundation modelling was the VTCS-2 model used to analyse solitary wave runup in 1DH (Titov and Synolakis, 1995). It reverted back to using a FDM approximation of the NSWE but adopted a novel technique of a variable grid formulation that did not require bottom friction or other ad-hoc effects to reproduce the wave runup. This developed into a 2DH model called VTCS-3 (Titov and Synolakis, 1998; Titov and González, 1997) which became known as MOST (Method of Splitting Tsunami), a model that is still widely used today. Around the same time, another model similar to TUNAMI-N2 based on the explicit leap-frog scheme for the NSWE was presented (Liu et al., 1995, 1998). It became known as COMCOT (Cornell Multi-grid Coupled Tsunami Model).

What has not been yet mentioned is that the three models; TUNAMI-N2, MOST, and COMCOT had developed into codes capable of multi-grid nesting. The techniques allowed for down-scaling from a large grid that may cover an entire ocean basin on the order of kilometres, gradually down to a fine resolution in the nearshore region. This technique became an important consideration for computation from the tsunami source towards the coastal zone if one desired high resolution in specific regions for inundation assessments (on the order of tens of metres or even metres). High resolution in the coastal zone would still be a heavy burden to compute even now if one had to use that high resolution everywhere in the geophysical domain. Furthermore, although all three models are based on the NSWE, and dispersive effects had largely been ignored in the modelling community after Kajiura (1963) identified his criteria for judging their importance, Shuto (1991); Imamura et al. (1990) identified the possibility of utilising the inherent numerical dispersion contained within the models. By equating the discretized form of the LSWE with the linear Boussinesq equations one could match the numerical dispersion to physical dispersion by correctly adjusting the cell size depending on the water depth. The method was then improved to include propagation in the diagonal direction (Cho and Yoon, 1998) and hence the propagation of tsunamis over long distances could now be more robustly considered without resorting to a more computationally intensive model such as the Boussinesq equations.

However as long wave theory, numerical methods and computing power improved the use of more computationally intensive models that could start to describe more complicated flow conditions started to appear. In terms of the theory, although 25 years prior, Peregrine (1967) had generalised the derivation of higher-order long wave equations based on the depth-averaged velocity, dispersive characteristics were still limited to fairly small values of μ . Firstly, Madsen et al. (1991); Madsen and Sorensen (1992) and then Nwogu (1993) suddenly introduced a new paradigm to the Boussinesq equations by matching the wave speeds with the (2,2) Padé approximation of the linear wave speed (Witting, 1984) to improve performance up to $\mu \approx 0.5$ (Madsen and Sorensen, 1992). Sato (1996) was able to show that by using the Madsen and Sorensen (1992)

model, improved runup heights could be obtained in particularly steep regions on the Okushiri coastline during the 1993 Hokkaido Tsunami compared with the standard NSWE. Following this the Nwogu (1993) type weakly nonlinear equations were further extended to a fully nonlinear version in Wei et al. (1995). That is, whilst deriving the equations the terms of $O(\epsilon)$ in $O(\mu^2)$ that are ignored in the original Nwogu (1993) equations are instead retained. Greater accuracy in the prediction of solitary wave shoaling on plane slopes was shown for a great range of offshore wave heights (Wei et al., 1995). The derivation of even higher-order Boussinesq equations to any desired accuracy was since generalised by Madsen and Schaffer (1998).

Regarding numerical methods, in order to robustly consider higher-order Boussinesq models, state-of-the-art numerical integration techniques were required. Wei et al. (1995) introduced a fourth-order Adams-Bashforth-Moulton predictor-corrector scheme, that would allow for the numerical dispersion to be much smaller than the physical dispersion included in the theory, and this was also adopted by Lynett et al. (2002) in an early version of his model COULWAVE (Cornell University Long and Intermediate Wave Modeling Package), and was applied to simulate a theoretical setup of landslide induced tsunamis (Lynett, 2005). Fuhrman and Madsen (2009) similarly adopted a fourth-order Runge-Kutta integration scheme and successfully applied their model to both earthquake and landslide induced tsunami verification experiments. Note that all three of these high-order models still adopted FDMs. But due to the high-order derivatives it became quite cumbersome to model runup and inundation, as ad-hoc techniques such as extrapolation at the boundary to the shoreline (Fuhrman and Madsen, 2009; Lynett, 2005; Lynett et al., 2002) or the “slot-technique” (Madsen, 1997) would be necessary. In addition to FEMs (e.g. Zelt, 1991), a good alternative to FDMS are finite-volume (FVM) ones.

FVMs were already making much headway for discretization of the hyperbolic NSW equations in general free surface flow problems. The idea was that shallow water equations actually allow for discontinuities or shocks e.g. tsunami bores and wet/dry fronts (Toro, 2001). Shocks presented a challenge for numerical modelling because unphysical spurious oscillations often develop in their vicinity. In fact Godunov’s theorem (Godunov, 1959) guaranteed that oscillations would develop if linear discretization methods are used with order of accuracy greater than one. Godunov’s method (Godunov, 1959) was then applied to solve the Riemann problem at the interface of two finite-volumes to resolve the shocks, by using the first-order upwind formulation. But the inaccuracies of the first-order discretization were greater than desired and higher-order methods were developed. Sweby (1984); Harten (1983); Roe (1983) developed what is known as Total Variation Diminishing (TVD) methods that allow for high-order discretizations over smooth regions but tend to first-order ones in the shock region thus satisfying Godunov’s theorem - termed shock capturing. Toro (2001) presented a seminal book on the subject of FVM, shock-capturing, and TVD methods. The FVM-TVD schemes allowed for Boussinesq models to be more easily and naturally applied to compute wave runup and model bore fronts. The techniques have been included into a number of currently relevant models (e.g. Kazolea and Delis, 2013; Shi et al.,

2012a; Roeber et al., 2010; Kim et al., 2009; Tonelli and Petti, 2009). Other more sophisticated and less commonly adopted shock-capturing methods include the UNO (uniformly non-oscillatory) (Harten and Osher, 1987), ENO (essentially non-oscillatory) (Harten et al., 1987) and WENO (weighted essentially non-oscillatory) (Liu et al., 1994) schemes that retain the high-order of accuracy even in shock regions. The WENO scheme was successfully used in Li and Raichlen (2002) to accurately simulate non-breaking and breaking solitary wave runup.

Modern models based on Boussinesq equations commonly used in tsunami applications include COULWAVE (Kim et al., 2009), FUNWAVE-TVD (Shi et al., 2012a) and BOSZ (Roeber et al., 2010). For example, COULWAVE has been used in studies; Lynett et al. (2014); Park et al. (2013); Lynett et al. (2012); Lynett and Liu (2011); Son et al. (2011) to consider tsunami currents and eddy formation in harbours and ports, tsunami inundation and their velocities in an idealized town with buildings, and has been nested with the COMCOT model to improve its computational efficiency for tsunami simulation from the source to the coastal zone. FUNWAVE-TVD was applied to investigate the sensitivity to a transient co-seismic source of the 2011 Tohoku-oki Earthquake Tsunami (Grilli et al., 2012) in comparison to the typical instantaneous assumptions of source models. All three models appeared in the latest (2015) mapping and modelling benchmark workshop of the National (United States of America) Tsunami Hazard Mitigation Program on tsunami currents (National Tsunami Hazard Mitigation Program, 2015). Since tsunami currents have rarely been touched on in past research efforts, it is not known whether the common NSWE models can correctly reproduce their effects. This is one area where Boussinesq models may have an advantage (Lynett et al., 2014).

In addition to Boussinesq models, there are a number of different wave theories and approaches beyond the basic depth-averaged NSWE that have also been applied to tsunami simulations in recent times. One example is Yamazaki et al. (2011a, 2009) whose model NEOWAVE (Non-Hydrostatic Evolution of Ocean WAVE) is a FDM “depth-integrated non-hydrostatic” model that uniquely computes the bottom non-hydrostatic pressure to yield dispersive characteristics slightly less accurate than the Madsen and Sorensen (1992) scheme but which it makes up for through model stability, simple multi-grid nesting formulation, and accurate runup/inundation performance. Another is SELFE (Zhang and Baptista, 2008) that computes the *three-dimensional* NSWE on unstructured FEM grids. Although it cannot consider dispersive effects it can consider vertical ones such as vertical mixing. The numerical method is especially suited to inundation modelling due to the use of unstructured grids. Similarly the quasi-3D Regional Ocean Modelling System (ROMS) in non-hydrostatic mode (NSWE) has also been used for tsunami inundation analysis (Mori et al., 2015). Perhaps one of the most sophisticated models applied to real-scale tsunami propagation according to the author’s knowledge is NHWAVE (Non-Hydrostatic WAVE model) (Ma et al., 2012). It solves the N-S equations using free surface and terrain following coordinates (i.e. it assumes a single free-surface and sea bed). A Godunov type FVM is employed and a Smagorinsky turbulent viscosity model is adopted for turbulent closure. Its particular

strength lies in its ability to accurately consider transient ground movements e.g. fault slips (Grilli et al., 2012) and landslide induced tsunamis (Shi et al., 2012b; Tehranirad et al., 2012). Thus, the nonlinear interaction of the ground motion and the full 3D nonlinear, dispersive wave motion near the source can be accurately taken into account. Moreover, even more sophisticated RANS models have been applied in a limited number of cases to simulate tsunami motion and runup in detail. For example, Lin et al. (1999) simulated solitary wave runup and rundown on plane slopes. Furthermore, locally high tsunami runup from 1993 Hokkaido Nansei-oki tsunami was computed with good agreement to scaled experiments and field observations (Yoneyama et al., 2002). A similar study was also conducted by Choi et al. (2007) for runup around an idealised conical island verifiable with laboratory experiments. Moreover, Yoneyama et al. (2012) developed a RANS model for simulating tsunami driftage that was tested against laboratory experiments and found to roughly estimate the overall three-dimensional motion of the floating objects. The use of RANS type models are however mostly restricted to use on laboratory scales or in very small real-scale regions due to their numerical and computational restraints.

2.2.2 To the Future and Study Motivation

Over the years tsunami models have come a long way. Energized by the the exponential increase of computing power, better numerical methods to more sophisticated wave theories have been adopted. But the major focus has so often been simply a macro-assessment of tsunami runup and inundation, and most models - even the simplest ones - are already rather adept at estimating that. However, a new paradigm is evolving in the current environment; focus is slowly widening to include consideration of tsunami currents and eddies (e.g. National Tsunami Hazard Mitigation Program, 2015; Lynett et al., 2014; Fritz et al., 2012), hydrodynamic forces on structures (e.g. Palermo et al., 2013; Fujima et al., 2009; Yeh, 2006), sophisticated transient fault models (e.g. Grilli et al., 2012), sediment transport (e.g. Kihara et al., 2012; Wilson et al., 2012; Tonkin et al., 2003), debris impacts (e.g. Rueben et al., 2014; Naito et al., 2014), and detailed inundation behaviour (e.g. Park et al., 2013). In addition, this also crucially requires better field measurements and experiments for verification of numerical models and a detailed understanding of the underlying physics.

In order to facilitate the computation of these considerations listed above, it is often the case that a single model cannot do everything required of it to the desired level of accuracy or computational efficiency (which are often working against each other). For example, NHWAVE can consider the nonlinear interaction between waves and the bed movement close to the source and hence should be very accurate in comparison to most other models. But if one wanted to compute wave propagation to the shoreline, it would be extremely computationally expensive. Moreover, it has been shown that dispersive and nonlinear effects for tsunami propagation in the open ocean are often very small, and a simple NSWE model could likely do the same job in a fraction of the time. Extending that example, as the waves approach the coastal zone and

interact with coastal structures, the NSWE models may start to underperform in their prediction of tsunami currents, eddies, shear stresses for sediment transport, wave breaking processes and most definitely hydrodynamic impacts on the structures. In these regions Boussinesq models, 3D models, and particularly for hydrodynamic simulations with structures, N-S based models will do better a job (Lynett and Liu, 2011).

One of the obvious solutions to this problem is to appreciate the individual strengths and weaknesses of each model, and use them only in their regions of strength while avoiding their weaknesses. In this case, to facilitate the seamless calculation of the entire problem requires coupling the different models together. Model coupling is not a completely new idea and there are examples of it already in tsunami modelling. For example, one of the earliest examples was in the studies by Fujima et al. (2002); Fujima (2006) where a N-S model (similar to NHWAVE) was coupled with the NSWE to model an experiment of tsunami flow through a breakwater. Later, Sitanggang and Lynett (2010) extended that to couple the Boussinesq model, COULWAVE with a (Reynolds-averaged Navier-Stokes) RANS model and validated it with theory and experiments in 1DH/2DV (vertical 2D). Concerning applications to full scale scenarios, Son et al. (2011) coupled COULWAVE with COMCOT in the nearshore area, and NHWAVE was coupled with FUNWAVE-TVD beyond the source region (Grilli et al., 2012). However, model coupling for tsunami applications is still in its infancy and various factors are still unknown. For example, it is not clear where exactly the models are best coupled, the best choice of boundary conditions e.g. vertical velocity distributions, when coupling will or will not perform well, or if the coupled models can perform to the level it is conceptually designed to do at all.

The previously mentioned issues and incompleteness of the topic are the main motivation of this dissertation to formally investigate model coupling - namely two-way multiscale coupling - for tsunami applications. Multiscale refers to the inclusion of multiple physical behaviour that occur at disparate scales. This requires the coupling of different resolutions and model equations. Two-way coupling refers to the passing of information between models in both directions, for example free surfaces and depth-averaged velocities in a NSWE model to a Boussinesq one *as well as* the feedback from the Boussinesq back to the NSWE model. This is to avoid the situation where the boundary conditions become too poorly matched after some length of calculation, in addition to the obvious practical benefits of projecting better resolved results between models.

NUMERICAL METHODOLOGY

The numerical techniques adopted and developed in this study are detailed in this chapter. Following §2.2 it was identified that a possible approach to improve the overall ability of tsunami models is to consider a multiscale coupling approach. As briefly mentioned in Chapter 1, the type that is adopted in this study is one where a shallow water model propagates the tsunami wave over a large region - which may include multiple nested grids of various grid resolutions - towards a complex model defined in a comparatively extremely small region with fine grid resolution. Thus, this chapter follows a similar direction to the coupled model itself: §3.2 outlines the basic numerical scheme of the shallow water model; §3.3 details how different length and temporal scales are nested together to form a cohesive model; §3.4 describes the numerical method adopted in the RANS model; finally, §3.5 combines those models and techniques to illustrate how the two-way coupled multiscale model is formed. The numerical methods described in this chapter form an important part of the work of this thesis; the shallow water model (numerical scheme is mainly borrowed from previous studies), multi-grid nesting (c.f. Nagashima et al., 2015), and the two-way multiscale coupling (c.f. Pringle and Yoneyama, 2014, 2013; Pringle et al., submitted) have been almost entirely single-handedly coded and developed by the author. The RANS model is based on that by Yoneyama and Moriya (1995); Yoneyama et al. (2002, 2012). Improvements in the code and theory described in this chapter have been achieved through collaboration and guidance of Nozomu Yoneyama.

3.1 Introduction

There are a number of methods available to model tsunamis as outlined Chapter 2. The major concern of this thesis is to develop a coupled model capable of: (1) simulating the propagation of a tsunami wave from the source to the coastal zone, (2) simulating inundation and the basic effects of friction, (3) considering the basic effects of seawalls and breakwaters on inundation, (4) simulating the turbulent details of tsunamis including wave breaking, jets and coherent turbulent structures, and (5) detailing the hydrodynamic response of coastal structures, infrastructure and buildings. The first three points may be adequately described by a simpler wave equation based model because the effects are generally horizontal two-dimensional (2DH) or quasi-three-dimensional (Q3D) and are only very weakly affected by non-hydrostatic and turbulent aspects. The last two points require a more complex flow solver to adequately perform the task where the effects are generally highly three-dimensional, rotational and non-hydrostatic.

With regards to the wave equation based model, the exact choice of theory is the first step. Traditionally, the 2DH shallow water equations (NSWE) have been widely used. Other choices include higher-order long wave theories such as Boussinesq type equations or depth-integrated non-hydrostatic models. All of these theories are 2DH where only one layer of fluid is modelled. The difference being that the NSWE are hydrostatic and have no vertical variation of velocity while high-order theories are weakly non-hydrostatic and may consider a prescribed vertical profile of horizontal velocities. One may also consider Q3D variations of these theories where an arbitrary number of layers is considered. Consideration of layers can improve dispersive characteristics (e.g. Lynett, 2005), and vertical mixing aspects (e.g. Zhang and Baptista, 2008). Firstly, considering the requirements, a Q3D model is probably unnecessary given the explicit assumption that mixing aspects will be generally negligible in the calculation domain of the wave based equation model. Furthermore, in this thesis the main applications will be to seismically induced tsunamis where dispersive effects are generally very small (compared with landslide-induced tsunamis) except for very long distances of propagation. Moreover, for long distances of propagation a basic correction to the linear frequency dispersion characteristics (of the NSWE) is generally only required rather than a complex high-order solution (Pedersen and Løvholt, 2008). With these considerations in mind, a NSWE based model will generally be adequate for this study. In case dispersive effects become slightly non-trivial the correction to the linear frequency dispersion effects can be achieved numerically by matching numerical dispersion to physical dispersion or by actually solving weakly nonlinear dispersive Boussinesq wave theories which are generally just small modifications to the NSWE (c.f. §2.1.3).

The next step is to choose the numerical method for the NSWE based model. The evolution of methods and the current state-of-the-art have been described in §2.2.1. Most models have been based on finite-difference methods which have a long history of success in tsunami modelling. More sophisticated modern methods generally look to employ finite-volume methods (FVMs) for high-resolution of the advection term and shock-capturing, or finite-element (FEM) ones on

unstructured grids. Both these methods are attractive ones but should be carefully designed. The author in general would suggest the use of a FVM with some high-resolution scheme such as a MUSCL (Monotone Upstream-Centered Schemes for Conservation Laws) or WENO (Weighted Essentially Non-Oscillatory) approach to accurately model: advection aspects to high-order, shocks and inundation. In contrast, it may be difficult for finite-difference methods (FDMs) to consider advection to high-order without instabilities particularly upon inundation and in the regions of shocks. However, finite-difference methods are simple to construct, computationally fast, and are generally appropriate to describe most of the tsunami behaviour even if advection is not considered to high-order. Thus, for the purposes of this thesis a FDM approach is adopted for simplicity since the multiscale coupling approach is the major focus. In the tsunami community it has been common to use the leap-frog FDM, e.g. COMCOT (Liu et al., 1998) and TUNAMI-N2 (Imamura et al., 2006). The reason is that it is computationally extremely fast but second-order accurate in time and space except for the advection term. Additionally, it has been straightforward to match numerical dispersion to physical dispersion (Cho and Yoon, 1998) or to actually model weakly nonlinear dispersive Boussinesq wave theories (Shigihara and Fujima, 2007) in the leap-frog approach. Finally, the low-order finite-difference aspect of the model allows for the simple consideration of inundation and multi-scale nesting. Thus, the leap-frog FDM is adopted in this thesis given its ubiquity, versatility and simplicity. The model is developed and coded by the author of this study for full control over the coupling aspects.

Within the NSWEE based model, it is necessary to consider some method to simulate over a range of grid scales. This is because as the tsunami approaches the coastal zone the details of the local bathymetry and coastline become gradually more important to correctly consider various physical behaviour at a specified bay and coastal community. However, those details are similarly relatively unimportant further offshore. For efficiency it is best to have fairly coarse grids offshore and fine grids near the coast and when the wave is present. There are a number of approaches including unstructured grids, local/adaptive mesh refinement and multi-grid nesting to achieve these means which are described in detail in §3.3. In short, the multi-grid nesting technique is adopted in this thesis because: it is simple to formulate and implement, effective for zooming into a specified region which is relevant for this study, and is still highly computationally efficient in comparison to a system without nesting.

A choice of theory for the more complex flow solver is now required. A weakly rotational and turbulent depth-integrated model such as a fully nonlinear Boussinesq model (FNBM) (Kim et al., 2009) may be able to consider some of the effects that are required such as great details of the horizontal aspects of tsunami currents and coherent turbulent structures in ports and harbours. But it cannot simulate vertical acceleration effects, wave overturning, and the hydrodynamic response of structures in any detail. To consider wave motion in general, with full non-linearities, dispersive, and three-dimensional effects, potential flow theory is most appropriate (c.f. §2.1.2). Unfortunately the model is inviscid and neglects rotational, turbulent

effects. To consider rotational and turbulent effects, the Navier-Stokes equations should be considered. However in general, the Navier-Stokes equations are unrealistic to directly simulate (DNS) because of the tiny size of the Kolmogorov length scales in comparison to the overall domain size. Thus, some variation on the Navier-Stokes equations should be considered. Two main variations are the Reynolds-averaged Navier-Stokes (RANS) equations and Large-Eddy Simulation (LES). The former has been introduced in §2.1.1. It can be considered the most appropriate variation to simulate the range of effects required in this study without extremely long computational times associated with LES due to the scale of problem.

A numerical method is now required to model the RANS equations. Similar to the NSWE model, finite-difference methods have been commonly used (e.g. Lara et al., 2010; Sitanggang and Lynett, 2010; Yoneyama et al., 2002; Isobe et al., 1999; Lin et al., 1999; Lin and Liu, 1998). Other more modern common choices include finite-volume methods (e.g. Higuera et al., 2013; del Jesus et al., 2012; Versteeg and Malalasekera, 2007). In general much success has been achieved for wave modelling by finite-difference means on staggered grids. Furthermore, since the NSWE model also uses the finite-difference method on a staggered grid it makes sense to adopt the same form for the RANS equations. In general, staggering is used to avoid issues associated with the pressure-velocity coupling and for simplicity of the derivation of the finite-differences. In addition, the temporal integration also requires a method to deal with the pressure-velocity coupling issue. Various choices are available such as projection methods (Chorin, 1968), SMAC (Amsden and Harlow, 1970), SIMPLE (Patankar and Spalding, 1972), and PISO (Issa, 1986). The non-iterative projection and SMAC methods are typically regarded as being accurate for unsteady flows (e.g. Kim and Benson, 1992), hence SMAC is adopted here. In order to model the free surface - aside from the 2DH assumption of a single free surface - the most commonly used and effective approach is the Volume-of-Fluid (VOF) method (Hirt and Nichols, 1981), because it does not require much memory, is computationally efficient, and it can model the movement of fluid volumes in order to describe almost any complex phenomenon such as wave overturning and splash-up. Lastly, a method is required to estimate the Reynolds stresses resulting from the Reynolds-averaging. The turbulent viscosity approach combined with the commonly used $k - \epsilon$ method (Launder and Spalding, 1974) is adopted in this thesis.

Finally, the two-way multiscale coupling technique should be devised. Studies that are closely related to the present one include; Son et al. (2011); Kim et al. (2010); Sitanggang and Lynett (2010); Fujima (2006); Fujima et al. (2002), which have been mostly introduced in §2.2.2. These studies may be used to help formulate the basic coupling technique. One of the most similar coupled models is that by Fujima et al. (2002) where a NSWE model was coupled with a single free surface RANS model. The major differences being that the RANS model in that study could not model overturning effects and a simplified zero-equation turbulence model was considered. Despite this, considering just the coupling aspects the similarities with this study are large (NSWE coupled to RANS). However, the studies Fujima (2006); Fujima et al. (2002) only

considered one application to an experimental study around a breakwater and it had yet to be applied to the real-scale scenario. The study Son et al. (2011) coupled two wave models - NSW E and FNBM (COULWAVE) - together in a real-scale scenario. Sitanggang and Lynett (2010) used COULWAVE as the wave model and a RANS-VOF model to consider complex flow in vertical two-dimensions. On that note it might in fact be superior to consider the coupling between more than two models, e.g. NSW E \rightarrow FNBM \rightarrow RANS. In this scenario it may be easier to match the physics between each model as there is a steady decrease from hydrostatic/irrotational \rightarrow weakly non-hydrostatic/rotational \rightarrow fully non-hydrostatic/rotational. In this study the jump is from hydrostatic/irrotational (NSWE) to fully non-hydrostatic/rotational (RANS). However, for this thesis it is simpler to focus on the coupling of just two models, which if coupled correctly still has the capability to adequately simulate a wide range of phenomena. Thus, one of the main issues with the coupling in this thesis is dealing with the matching of the vastly different physical assumptions of the models at the interface. It can be hypothesised that an appropriate location for coupling is hence a large key to success.

3.2 Shallow Water Model

3.2.1 Governing Equations

Governing equations to the 2DH NSWE were presented in §2.1.3 by Eqns. (2.25) and (2.28) in terms of the depth-averaged velocity. The model used in this paper is a FDM one discretized on an Arakawa C-grid - this will be explained in detail in §3.2.2. Unfortunately discretizing Eqn. (2.25) in this way may be inaccurate at times since U_i and H are defined at different locations (Goto et al., 1997). A better equation is actually the conservative form of the continuity equation (Eqn. (2.24)) that is defined in terms of the volume flux per unit width, $Q_i \equiv U_i H$, so that discretization is only of a single variable. It is printed again here for completion:

$$\frac{\partial \eta}{\partial t} + \frac{\partial Q_i}{\partial x_i} = 0 \quad (3.1)$$

In addition, primarily for the purposes of calculating solitary wave propagation in Chapter 4, linear frequency dispersive effects are required to balance with the amplitude dispersion effects already included. These come in the form of additional terms on the RHS of Eqn. (2.28) like those found in the Peregrine (1967) standard Boussinesq equations shown in Eqn. (2.35). Finally, Eqn. (2.28) with the frequency dispersion terms included is integrated over the depth to get it in terms of Q_i in order to be consistent with the continuity Eqn. (2.24):

$$\frac{\partial Q_i}{\partial t} + \frac{\partial}{\partial x_j} \left(\frac{Q_j Q_i}{H} \right) + gH \frac{\partial \eta}{\partial x_i} + \frac{\tau_{bi}}{\rho} = h \frac{\partial \psi}{\partial x_i} \quad (3.2)$$

the additional term, ψ on the RHS is the dispersion potential function defined as:

$$\psi = \left(\gamma + \frac{1}{3} \right) h \frac{\partial^2 Q_j}{\partial x_j \partial t} + \gamma g h^2 \frac{\partial^2 \eta}{\partial x_j \partial x_j} \quad (3.3)$$

the γ coefficient is a free value that can be tuned to improve linear dispersion characteristics from the Peregrine (1967) version (which is equivalent to $\gamma = 0$). Following Shigihara and Fujima (2007), $\gamma = 1/15$ corresponds to linear dispersion characteristics equivalent to the Madsen et al. (1991) scheme (valid up to $\mu \approx 0.5$), which we adopt here.

Different formulations of the bed stress term were introduced in §2.1.3, which can be related to a Darcy-Weisbach friction factor or a Gauckler-Manning roughness coefficient among others. Despite our arguments put forward there the Gauckler-Manning formulation is used in this thesis since it is the common approach in tsunami modelling and roughness data is often provided along with bathymetry data in terms of Gauckler-Manning roughness coefficients (however it would be equally as straightforward to use a general drag coefficient if one desired). In terms of Q_i , the bed stress term becomes:

$$\tau_{bi} = \rho \frac{gn^2}{H^{7/3}} Q_i \sqrt{Q_j Q_j} \quad (3.4)$$

3.2.2 Discretization Scheme

The finite-difference staggered leap-frog scheme is used to discretize Eqns. (3.1) and (3.2). It is the scheme adopted in the widely used tsunami models, TUNAMI-N2 (Goto et al., 1997) and COMCOT (Liu et al., 1998). It is characterized by the “staggering” of the two main variables, η and Q_i in both space and time. The space staggering is achieved by placing the main variables on an Arakawa C-grid. This entails defining Q_i on the centres of the cell boundaries that are perpendicular to the i direction, and the scalar variables, in particular η on cell centres. In the temporal space, η and Q_i are defined at different half time-steps. To illustrate this visually the finite-difference stencils are shown in Figure 3.1.

Notice that the fluxes in the x direction, Q_x are centred on the east-west cell boundaries and those in the y direction, Q_y are centred on the north-south boundaries. The \tilde{Q}_y , fluxes represent an average of the surrounding Q_y fluxes at the position of the Q_x flux which will be required later. The following two sections will present the discretized formulae and the procedures for solving the explicit scheme and the implicit scheme (used when the linear frequency dispersion terms are considered).

Explicit Procedure

The explicit leap-frog scheme is used to solve the traditional non-dispersive shallow water equations given where the RHS of Eqn. (3.2) is zero. Initially say, at a time point in time, $t = n$, the flux, Q_i^n and the free surface, $\eta^{n-1/2}$ at every point on the grid is known. Through continuity Eqn. (3.1), a new free surface, $\eta^{n+1/2}$ at the cell centre, (i, j) , may be calculated by the following operation:

$$\eta_{(i,j)}^{n+1/2} = \eta_{(i,j)}^{n-1/2} - r_x \left(Q_{x(i+1/2,j)}^n - Q_{x(i-1/2,j)}^n \right) - r_y \left(Q_{y(i,j+1/2)}^n - Q_{y(i,j-1/2)}^n \right) \quad (3.5)$$

where $r_x = \Delta t / \Delta x$ and $r_y = \Delta t / \Delta y$. This is a second-order accurate discretization based on the Taylor expansion about the cell centre, (i, j) and time, $t = n$. This discretized form of the continuity equations above is one of the strengths of this scheme due to its simplicity and accuracy. Figure 3.1 illustrates the continuity equation visually using dashed arrows in the $x - t$ plane. To obtain $\eta_{(i,j)}^{n+1/2}$, the variables $\eta_{(i,j)}^{n-1/2}$, $Q_{x(i-1/2,j)}^n$, and $Q_{x(i+1/2,j)}^n$ are required. A plot of the $y - t$ plane would also show something similar where the fluxes, $Q_{y(i,j-1/2)}^n$, and $Q_{y(i,j+1/2)}^n$ are required. The new free surface, $\eta^{n+1/2}$ is used to evaluate the momentum equation to get a new flux, Q_i^{n+1} . For example to obtain the flux, $Q_{x(i+1/2,j)}^{n+1}$ the following operation is performed:

$$Q_{x(i+1/2,j)}^{n+1} = \frac{1}{1 + F_x \Delta t} \left[(1 - F_x \Delta t) Q_{x(i+1/2,j)}^n - f_{x(i+1/2,j)} \right] \quad (3.6)$$

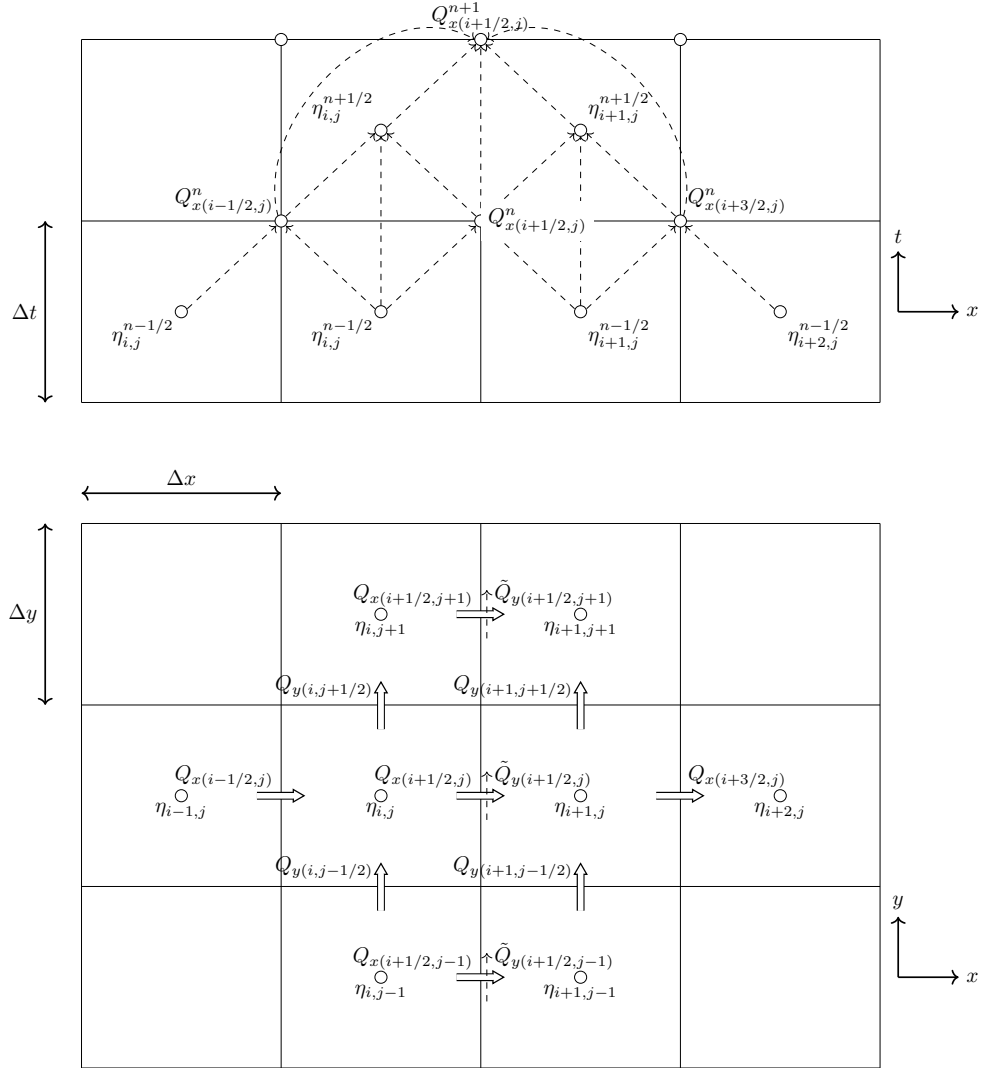


Figure 3.1: Finite-difference stencil of the staggered leap-frog method, in the $x-t$ (analogous to $y-t$ plane) and $x-y$ planes. In the $x-y$ plane the stencil is shown specifically for the calculation of the flux, $Q_{x(i+1/2, j)}$

where $f_{x(i+1/2, j)}$ is given as:

$$\begin{aligned}
 f_{x(i+1/2, j)} &= r_x g H_{(i+1/2, j)}^{n+1/2} \left(\eta_{(i+1, j)}^{n+1/2} - \eta_{(i, j)}^{n+1/2} \right) \\
 &+ r_x \left(\lambda_{x1} \frac{\left(Q_{x(i-1/2, j)}^n \right)^2}{H_{(i-1/2, j)}^n} + \lambda_{x2} \frac{\left(Q_{x(i+1/2, j)}^n \right)^2}{H_{(i+1/2, j)}^n} + \lambda_{x3} \frac{\left(Q_{x(i+3/2, j)}^n \right)^2}{H_{(i+3/2, j)}^n} \right) \\
 &+ r_y \left(\tilde{\lambda}_{y1} \frac{\left(Q_x \tilde{Q}_y \right)_{(i+1/2, j-1)}^n}{H_{(i+1/2, j-1)}^n} + \tilde{\lambda}_{y2} \frac{\left(Q_x \tilde{Q}_y \right)_{(i+1/2, j)}^n}{H_{(i+1/2, j)}^n} + \tilde{\lambda}_{y3} \frac{\left(Q_x \tilde{Q}_y \right)_{(i+1/2, j+1)}^n}{H_{(i+1/2, j+1)}^n} \right)
 \end{aligned} \tag{3.7}$$

Figure 3.1 also illustrates the $x - t$ part of the momentum equation visually using dashed arrows in the $x - t$ plane. Eqn. (3.6) is a second-order accurate discretization based on the Taylor expansion about $(i + 1/2, j)$ and time, $t = n + 1/2$. Furthermore, in the evaluation of $f_{x(i+1/2,j)}$, the first line in Eqn. (3.7) corresponding to the hydrostatic pressure gradient is also a second-order accurate central difference discretization about $(i + 1/2, j)$. However, the last two lines correspond to the discretization of the nonlinear advection terms and are only first-order accurate upwind differences about $(i + 1/2, j)$. Thus, if they were ignored (LSWE), the entire scheme is second-order, but with their addition the scheme is just first-order. The coefficients in the first-order upwind scheme are given by:

$$\begin{cases} \lambda_{x1} = -1, & \lambda_{x2} = 1, & \lambda_{x3} = 0, & \text{if } Q_{x(i+1/2,j)}^n \geq 0, \\ \lambda_{x1} = 0, & \lambda_{x2} = -1, & \lambda_{x3} = 1, & \text{if } Q_{x(i+1/2,j)}^n < 0 \end{cases} \quad (3.8)$$

$$\begin{cases} \tilde{\lambda}_{y1} = -1, & \tilde{\lambda}_{y2} = 1, & \tilde{\lambda}_{y3} = 0, & \text{if } \tilde{Q}_{y(i+1/2,j)}^n \geq 0, \\ \tilde{\lambda}_{y1} = 0, & \tilde{\lambda}_{y2} = -1, & \tilde{\lambda}_{y3} = 1, & \text{if } \tilde{Q}_{y(i+1/2,j)}^n < 0 \end{cases} \quad (3.9)$$

The term, F_x corresponds to the discretization of the bottom friction terms which are semi-implicitly calculated:

$$\tau_{bx} = F_x \left(Q_{x(i+1/2,j)}^{n+1} + Q_{x(i+1/2,j)}^n \right) \quad (3.10)$$

where, F_x is defined as:

$$F_x = \frac{1}{2} \frac{gn^2}{\left(H_{(i+1/2,j)}^n \right)^{7/3}} \sqrt{\left(Q_{x(i+1/2,j)}^n \right)^2 + \left(\tilde{Q}_{y(i+1/2,j)}^n \right)^2} \quad (3.11)$$

The last thing to consider is how to get the total water depths, H (that are defined at cell centres and half time-steps like η) at the cell boundaries as well as \tilde{Q}_i from the surrounding values. Given the order of the scheme in general they are just found from linear averages:

$$h_{(i+1/2,j)} = 0.5 \left(h_{(i+1,j)} + h_{(i,j)} \right) \quad (3.12)$$

$$H_{(i+1/2,j)}^{n+1/2} = 0.5 \left(\eta_{(i+1,j)}^{n+1/2} + \eta_{(i,j)}^{n+1/2} \right) + h_{(i+1/2,j)} \quad (3.13)$$

$$H_{(i+1/2,j)}^n = 0.25 \left(\eta_{(i+1,j)}^{n+1/2} + \eta_{(i,j)}^{n+1/2} + \eta_{(i+1,j)}^{n-1/2} + \eta_{(i,j)}^{n-1/2} \right) + h_{(i+1/2,j)} \quad (3.14)$$

$$\tilde{Q}_{y(i+1/2,j)}^n = 0.25 \left(Q_{y(i+1,j-1/2)}^n + Q_{y(i,j-1/2)}^n + Q_{y(i+1,j+1/2)}^n + Q_{y(i,j+1/2)}^n \right) \quad (3.15)$$

Note that the initial water depths, h are defined on the cell centres and are simply a function of the bathymetry and topography, that is assumed to be steady in time. A positive h indicates ocean, and a negative one indicates land.

A formulation for the calculation of the fluxes in the y direction, $Q_{y(i,j+1/2)}$ may also be similarly derived by replacing i with j and x with y in the above equations.

Implicit Dispersion Correction

In case the linear dispersion terms are considered - RHS of Eqn. (3.2) is non-zero - an implicit scheme is required for stability. The dispersive characteristics of this scheme and its procedure has been outlined precisely by Shigihara and Fujima (2007). The procedure basically ends up working like a correction to the explicit scheme described in the previous section. In fact the continuity equation is the same as before (Eqn. (3.5)), but the momentum equation now becomes:

$$\mathbf{Q}_{x(i+1/2,j)}^{n+1} = \frac{1}{1 + F_x \Delta t} \left[(1 - F_x \Delta t) \mathbf{Q}_{x(i+1/2,j)}^n - f_{x(i+1/2,j)} + r_x h_{(i+1/2,j)} \left(\psi_{(i+1,j)}^{n+1/2} - \psi_{(i,j)}^{n+1/2} \right) \right] \quad (3.16)$$

The difficulty then arises from the determination of $\psi^{n+1/2}$. It must be found from the following Poisson-type system of equations:

$$\begin{aligned} & \left(\gamma + \frac{1}{3} \right) \left[h_x^2 \left(\psi_{(i+1,j)}^{n+1/2} + \psi_{(i-1,j)}^{n+1/2} \right) + h_y^2 \left(\psi_{(i,j+1)}^{n+1/2} + \psi_{(i,j-1)}^{n+1/2} \right) \right] - \left[1 + 2 \left(\gamma + \frac{1}{3} \right) \left(h_x^2 + h_y^2 \right) \right] \psi_{(i,j)}^{n+1/2} \\ & = \left(\gamma + \frac{1}{3} \right) \left[h_x \left(f_{x(i+1/2,j)} - f_{x(i-1/2,j)} \right) + h_y \left(f_{y(i,j+1/2)} - f_{y(i,j-1/2)} \right) \right] \\ & - \gamma g \left[h_x^2 \left(\eta_{(i-1,j)}^{n+1/2} - 2\eta_{(i,j)}^{n+1/2} + \eta_{(i+1,j)}^{n+1/2} \right) + h_y^2 \left(\eta_{(i,j-1)}^{n+1/2} - 2\eta_{(i,j)}^{n+1/2} + \eta_{(i,j+1)}^{n+1/2} \right) \right] \end{aligned} \quad (3.17)$$

where $h_x = h_{(i,j)}/\Delta x$ and $h_y = h_{(i,j)}/\Delta y$. Thus, the procedure is as follows:

1. f_x and f_y are evaluated as prescribed in the explicit procedure (Eqn. (3.7))
2. The system of equations, Eqn. (3.17) is solved for $\psi^{n+1/2}$ using a suitable matrix solver such as the biconjugate gradient stabilized (BiCGSTAB) method that is adopted in this study and suggested by Shigihara and Fujima (2007)
3. \mathbf{Q}_i^{n+1} is evaluated in Eqn. (3.16).

Note that the explicit procedure follows the same process except step 2) is ignored with $\psi^{n+1/2}$ zero everywhere. Unfortunately, step 2) is the most time consuming part of the scheme due to the matrix inversion. For example, Shigihara and Fujima (2007) mentioned that the implicit procedure would be take roughly 10 times as long to compute as the explicit procedure (using the BiCGSTAB method). However, if the precise propagation of waves with non-trivial frequency dispersion effects are required it is a useful scheme. For example, the scheme will be used to accurately propagate solitary waves in Chapter 4. On the other hand, frequency dispersion for tsunami waves in the regional and near field is generally negligible, hence the faster explicit procedure will be adopted in Chapter 5.

3.2.3 Special Considerations

Various special considerations are necessary in order to consider for example inundation which must employ some technique to deal with the wet/dry cell interface. Other techniques may also be adopted to avoid negative depths, consider seawalls and breakwaters whose widths are sub-grid

scales, and to avoid excessive numerical diffusion in the nonlinear advection scheme. These techniques are described in this section.

Inundation Algorithm

The inundation algorithm refers to the method used to consider the wet/dry cell interface which defines the shoreline. On land, h is negative, and if it is a dry cell, η is equal to $-h$ so that the total water depth, $H = \eta + h$ is zero. If a flux, Q_i calculated through the momentum equation, becomes non-zero (directed into the cell) at one or any of the cell boundaries then through the continuity equation η may become larger than $-h$ so that, H is non-zero and hence it becomes a wet cell. In practice a very small H in a wet cell can lead to numerical difficulties since the nonlinear advection terms and the bottom friction terms include division by H which may lead to unphysical fluxes. Thus, a cutoff depth, H_c is introduced to avoid this issue. Here, a cell is considered dry until the depth H becomes larger than H_c . Note that η is conserved until this happens, i.e. η is *not* reset to $-h$ each time step if $0 < H < H_c$. Using this method, only one cell may become inundated in series each time step.

The question then becomes, under what conditions does the flux at the cell boundary become non-zero, and when will it stay zero. Essentially, by assuming that the bathymetry is composed of discrete values of h - like a staircase - then the following conditions are set (c.f. Figure 3.2):

$$\begin{cases} H_{shore} = 0 & \text{if } \eta_{wet} + h_{dry} \leq H_c, \\ H_{shore} = \eta_{wet} + h_{dry} & \text{if } \eta_{wet} + h_{dry} > H_c \end{cases} \quad (3.18)$$

where $_{wet}$ and $_{dry}$ subscripts refer to the wet and dry cell centres respectively, and $_{shore}$ refers to the shoreline, i.e. at the cell boundary between wet and dry cells. Notice that it is different to the usual formulation that uses an average of the adjacent cell depths to get the depth at the boundary. When $H_{shore} = 0$ then in the momentum equation everything becomes zero so that Q_{shore} also remains zero. On the other hand, when $H_{shore} > 0$, this depth is used to evaluate the momentum flux as usual to obtain a non-zero flux at the shoreline. The dry cell may then become flooded through the continuity equation.

Avoiding Negative Depths

Sometimes due to unavoidable numerical errors such as discretization ones, η may become less than $-h$ when a wet cell is emptied indicating a negative depth. This doesn't necessarily pose us many issues as it can simply be classed as a dry cell and the value of η can be preserved to conserve mass. But in the momentum equation the gradient of η is required and physically the value of η in the dry cell should be equal to $-h$ (rather than $< -h$). Moreover, the negative depth represents a mistake in the calculation of the flux, hence if the flux was adjusted to give zero depth rather than a negative one the flow overall may be improved. A method to do just that has

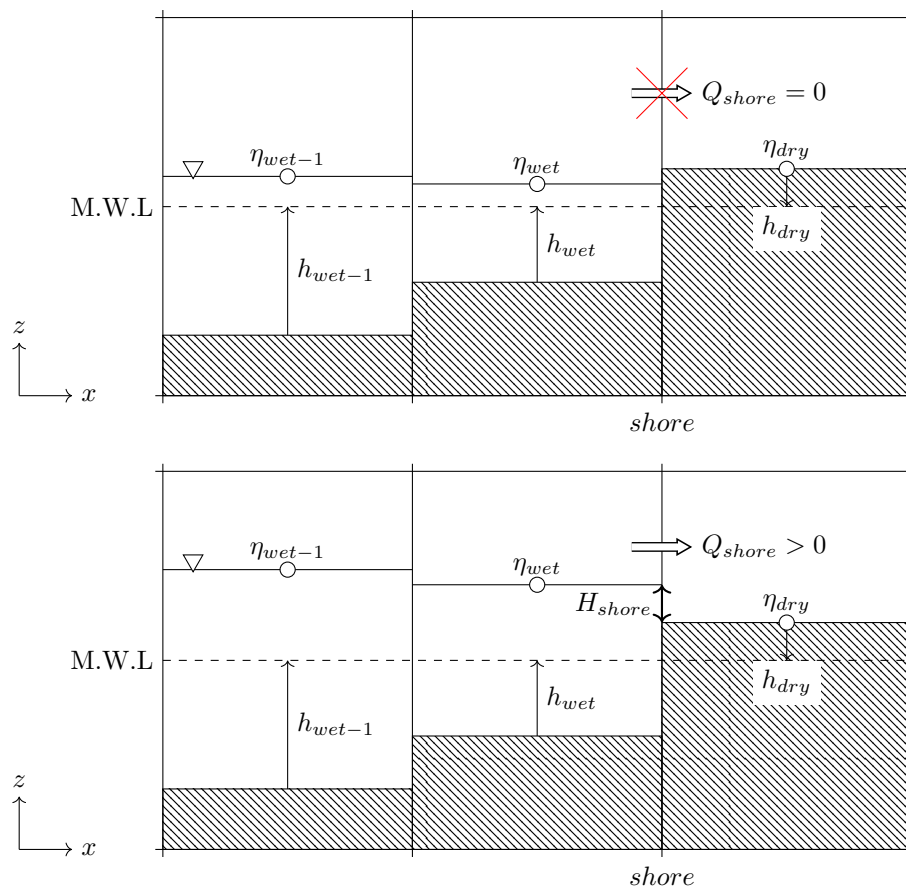


Figure 3.2: Illustration of the situation at the shoreline (interface between wet and dry cells) when considering inundation

been outlined in Fukazawa and Tosaka (2014). It involves a calculation of a correction coefficient, D_c as:

$$D_c = \frac{H^n \Delta x \Delta y + Q_{in} \Delta t}{Q_{out} \Delta t} \quad \text{for cell where } H^{n+1} < 0 \quad (3.19)$$

where Q_{out} and Q_{in} are the sum of the outgoing and ingoing volume fluxes (the usual values of Q_i need to be multiplied by the grid width tangential to its direction) respectively. Each individual outgoing flux is multiplied by D_c and continuity is recalculated so that η is guaranteed to become equal to $-h$ as the cell empties.

Sub-grid Scale Walls

Walls such as seawalls, breakwaters and river banks are important structures that can help to prevent or mitigate inundation. When tsunami modelling is conducted, for a realistic calculation their presence should be taken into account. Additionally, it is useful to know what the effect would be with and without those structures (in case of failure or removal). Usually bathymetric

and topographic data is provided such that buildings and infrastructure are absent. However, crest heights of walls may be included in separate files. This is because the widths of the walls are usually of sub-grid scales so they may not be easily included in the raw ground level data. In such a case, a special method is required to consider the presence of these walls. A common approach is to define the wall data on the cell boundaries so that the general bathymetric data is unaffected and a special equation that replaces the usual momentum one is then specified when calculating the flux, Q_{wall} at this cell boundary. One such equation is Honma's empirical weir overflow equation (Honma, 1940) which may be written as (c.f. Figure 3.3):

$$Q_{wall} = \begin{cases} 0 & \text{if } H_L \leq 0 \\ C_w H_L \sqrt{2gH_L} & \text{if } H_L \leq 2/3H_R \\ 3/2 C_w H_R \sqrt{6g(H_L - H_R)} & \text{if } H_L > 2/3H_R \end{cases} \quad (3.20)$$

where, $H_L (= \eta_L - z_{wall})$ and $H_R (= \eta_R - z_{wall})$ are equal to the equivalent water depths left and right of the wall on the cell boundary respectively ($H_L > H_R$), z_{wall} is the elevation of the wall crest, and $C_w (= 0.35)$ is the weir discharge coefficient. The three cases in Eqn. (3.20) refer to: no overtopping, complete overtopping, and submerged overtopping respectively as illustrated in Figure 3.3.

Nonlinear Advection Truncation Error Correction

One of the main weaknesses of the staggered leapfrog scheme is the fact that the nonlinear advection terms must be specified by a first-order upwind method, thus introducing considerable numerical diffusion. This is related to the truncation error of the discretization (for $Q_c < 0$):

$$\frac{\partial}{\partial x} \left(\frac{Q_c^2}{H} \right) = \frac{(Q^2/H)_c - (Q^2/H)_u}{\Delta x} + 0.5(1 - Cr)\Delta x \frac{\partial^2}{\partial x^2} \left(\frac{Q_c^2}{H} \right) \quad (3.21)$$

where the subscript c and u represent the centre and upwind cell boundaries respectively, and Cr is equal to the local Courant number which may be defined in terms of the wave speed as, $Cr = \sqrt{gh_c} \Delta t / \Delta x$. The truncation error which is the last term on the RHS of Eqn. (3.21) will be small in the case where $Cr \rightarrow 1$ and/or the second-order derivative of Q_c^2/H approaches zero. In general, with variable depths it is not possible to have Cr close to 1 for every cell and furthermore in the two-dimensional case Cr is theoretically limited to $Cr = \sqrt{2}/2$ for stability. On the other hand, for very long waves the curvature of Q_c^2/H may approach zero. Thus, typically for tsunami propagation in the ocean, the truncation error may not be significant. However, if the wave becomes shorter and curvature increases the numerical diffusion may become non-trivial. One example is solitary wave propagation where it is important that linear frequency dispersion effects are balanced with the amplitude dispersion ones. In the case that solitary waves become short so that $\mu > 0.05$, linear frequency dispersion should be included using the implicit dispersion correction procedure. However, at the same time the curvature of the wave becomes large so

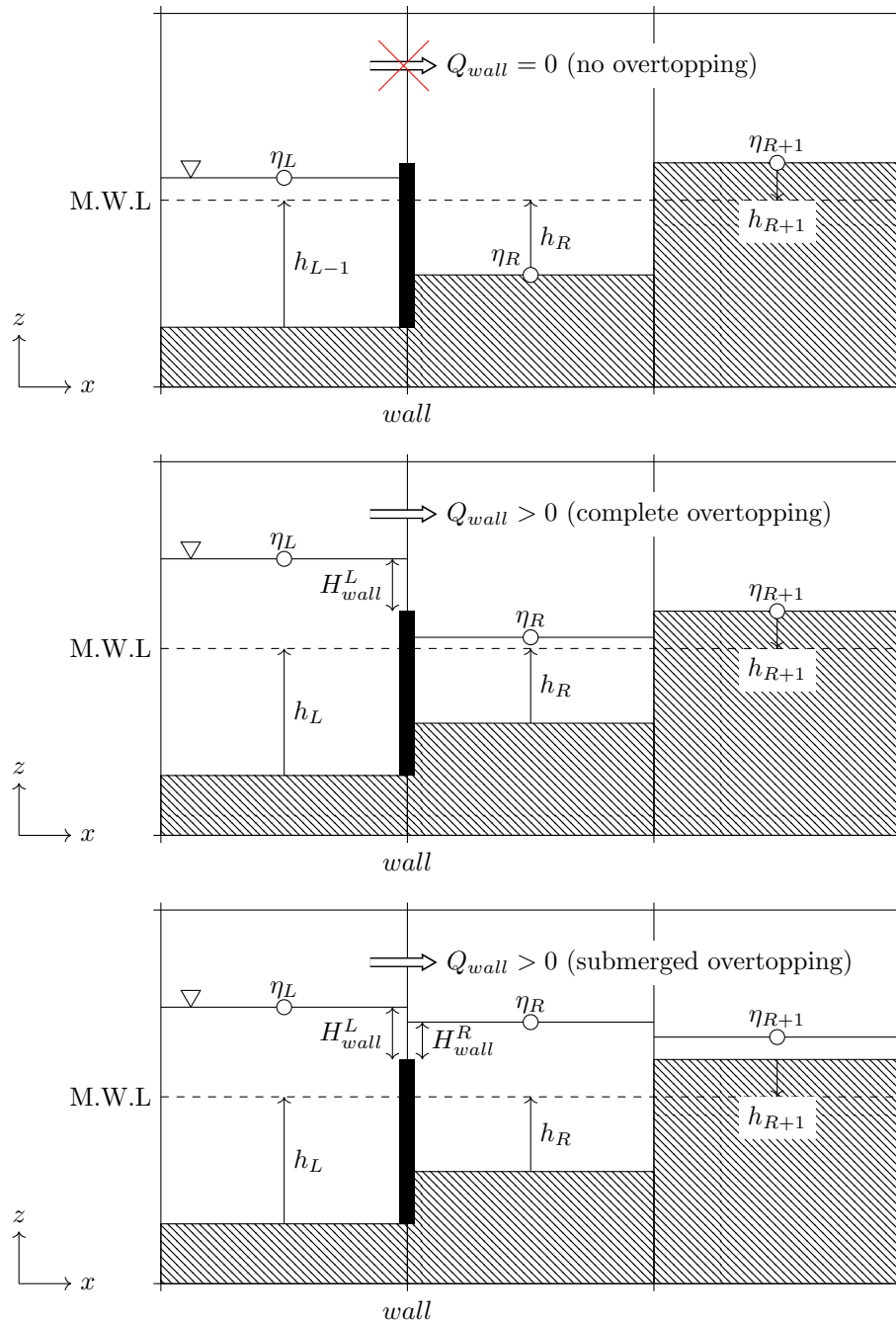


Figure 3.3: Illustration of the consideration of thin seawalls, breakwaters or river banks that are defined on cell boundaries

that the nonlinear advection terms are poorly evaluated by the upwind scheme and the wave will rapidly decay with distance. In order to account for this one can simply discretize and back-substitute the truncation errors in when evaluating the first-order upwind difference. This can be achieved by a second-order central-difference to evaluate the curvature of Q_c^2/H . Note that

since this is a central-difference it is really only stable for the implicit scheme. In the code, if the implicit scheme is chosen, back-substitution of the truncation errors will automatically take place. In the case of the explicit scheme it is assumed that the curvature of Q_c^2/H is small and the truncation errors are ignored. In equation form, when back-substitution of the truncation errors are considered, the coefficients in the upwind scheme become:

$$\begin{cases} \lambda_{x1} = -1 + c_x, & \lambda_{x2} = 1 - 2c_x, & \lambda_{x3} = c_x, & \text{if } Q_{x(i+1/2,j)}^n \geq 0, \\ \lambda_{x1} = -c_x, & \lambda_{x2} = -1 + 2c_x, & \lambda_{x3} = 1 - c_x, & \text{if } Q_{x(i+1/2,j)}^n < 0 \end{cases} \quad (3.22)$$

$$\begin{cases} \tilde{\lambda}_{y1} = -1 + c_y, & \tilde{\lambda}_{y2} = 1 - 2c_y, & \tilde{\lambda}_{y3} = c_y, & \text{if } \tilde{Q}_{y(i+1/2,j)}^n \geq 0, \\ \tilde{\lambda}_{y1} = -c_y, & \tilde{\lambda}_{y2} = -1 + 2c_y, & \tilde{\lambda}_{y3} = 1 - c_y, & \text{if } \tilde{Q}_{y(i+1/2,j)}^n < 0 \end{cases} \quad (3.23)$$

where $c_x = 0.5(1 - Cr_x)$, and $c_y = 0.5(1 - Cr_y)$ are the contributions in the truncation error in terms of the Courant number in the x and y directions respectively. $Cr_x = \sqrt{gh_{(i+1/2,j)}}\Delta t/\Delta x$, and $Cr_y = \sqrt{gh_{(i+1/2,j)}}\Delta t/\Delta y$. This technique is adopted in Chapter 4 which demonstrates its effectiveness.

3.2.4 Lateral Boundary Conditions

Boundary conditions are an important part of any numerical model. In fact, without appropriate boundary conditions nothing of any importance would ever be calculated. Note that the seabed and free surface boundary conditions are already included in the governing equations. Thus, this section refers to the lateral boundary conditions that surround the domain in the horizontal plane. There are two main types of lateral boundary conditions. One is termed an active boundary condition. These are responsible for creating input flow conditions, for example, propagating waves from the boundary. In this section, the propagation of solitary waves, and an arbitrary wave shape is described. The other type is a passive boundary condition. These boundary conditions just respond to what is happening in the calculation domain. One obvious example of this is a wall type boundary which just reflects the information at the boundary. A contrasting example is an open boundary which allows the information from the domain to propagate freely out without (or with minimal) reflections. These two types are also described in this section.

In order to implement the lateral boundary conditions in the model, the normal flux at the actual boundary, $Q_{n(b,j)}$, the tangential flux at the cell boundary adjacent to the last calculation cell (a ghost cell), $Q_{t(b-1/2,j-1/2)}$, and the free surface at the cell centre adjacent to the last calculation cell (a ghost cell), $\eta_{(b-1/2,j)}$ are prescribed. This configuration is illustrated in Figure 3.4. In all our lateral boundary conditions in this model the tangential flux in the ghost cell is set equal to the tangential flux in the last calculation cell on the boundary (no gradient), i.e. $Q_{t(b-1/2,j-1/2)} = Q_{t(b+1/2,j-1/2)}$. This corresponds to a frictionless lateral boundary. The other two boundary variables are prescribed differently depending on the case.

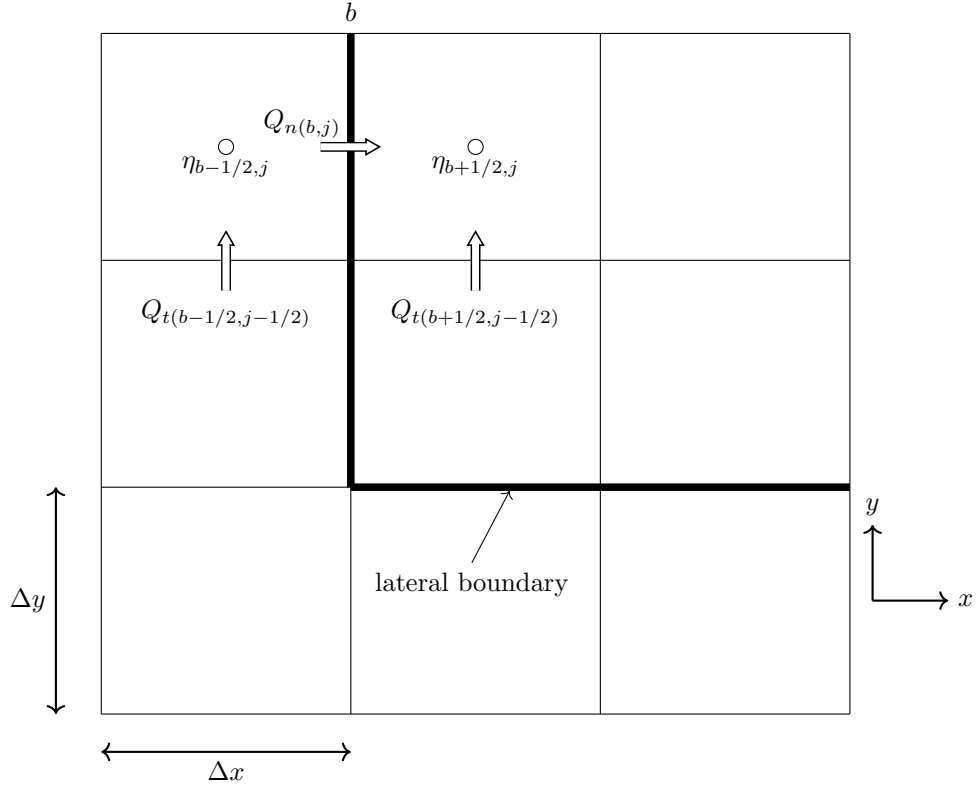


Figure 3.4: Illustration of the prescribed variables at the lateral boundaries

Solitary Wave

There are numerous solitary wave theories available. However, since the numerical model is of low-order, a low-order theory is reasonable. One such first approximation is based on the expansion of the velocity potential in a power series and retaining the first two terms, as described in Munk (1949). The solitary wave shape resulting from this theory known as Boussinesq's first approximation is equal to:

$$\eta(x, t) = A \operatorname{sech}^2(\kappa(x - ct)) \quad (3.24)$$

where A is the amplitude of the wave, $\kappa (= \sqrt{3A/4h^3})$ is the wavenumber and $c (= \sqrt{g(A+h)})$ is the wave speed. Furthermore, the depth-averaged velocity, U can be found from the following equation:

$$U(x, t) = c \frac{\eta(x, t)}{\eta(x, t) + h} \quad (3.25)$$

In order to use these equations as boundary conditions in the model, $Q_{n(b,j)}$ and $\eta_{(b-1/2,j)}$ are prescribed. Firstly, $\eta_{(b-1/2,j)}(t + 1/2)$ is set to equal to $\eta(-\Delta x/2, t + 1/2)$ in Eqn. (3.24) at time, $t + 1/2$ and a fixed x position of $-\Delta x/2$ (the distance from the actual boundary to the cell centre). Secondly, $Q_{n(b,j)}$ is set equal to:

$$Q_{n(b,j)}(t) = U(0, t)(\eta(0, t) + h_{(b,j)}) \quad (3.26)$$

where $U(0, t)$ is found from Eqn. (3.25) and $\eta(0, t)$ is found from Eqn. (3.24), with $x = 0$ at time, t .

Arbitrary Wave Shape

Sometimes from experiments or field data, the time series of a measured wave profile is available. In such a case it is useful to be able to input this wave profile on the lateral boundary. To do this, firstly the time series of the wave profile, $\eta(t)$ is input at the ghost cell: $\eta_{(b-1/2,j)}(t+1/2) = \eta(t+1/2)$. Secondly, the flux data must be inserted. In some fortunate cases the time series of the depth-averaged velocities, $U(t)$ may also have been measured. In such a case one can input the normal flux on the boundary as:

$$Q_{n(b,j)}(t) = U(t)(\eta(t) + h_{(b,j)}) \quad (3.27)$$

assuming that the distance $\Delta x/2$ is trivial in comparison to the measurement correlation errors between $U(t)$ and $\eta(t)$. In many situations however, the velocity data is not available. To get the flux on the boundary requires assuming a wave theory. This simplest one that is compatible with the governing equations is LSWE theory. Using this theory the new normal flux on the boundary is calculated as:

$$Q_{n(b,j)}^{n+1} = Q_{n(b,j)}^n - r_x g H_{n(b,j)}^{n+1/2} \left(\eta_{(b+1/2,j)}^{n+1/2} - \eta(t+1/2) \right) \quad (3.28)$$

Wall Boundaries

It is often necessary in experimental situations and otherwise for simplicity to specify a wall lateral boundary condition. What this physically entails is that the flux normal to the boundary is zero:

$$Q_{n(b,j)} = 0 \quad (3.29)$$

In addition the no gradient condition on the free surface, $\eta_{(b-1/2,j)} = \eta_{(b+1/2,j)}$ may be employed in case it is required. However this is not normally the case since the term, $Q_{(b,j)}^2/H_{(b,j)}$ needed in the nonlinear advection difference will always be zero independent of $H_{(b,j)}$ (which is found from $\eta_{(b-1/2,j)}$ and $\eta_{(b+1/2,j)}$).

Open Boundaries

When a tsunami simulation is conducted under real conditions, unless the lateral boundary is consumed by land, open boundaries that allow the flow conditions to freely leave the domain (out into the open ocean) should be set. By a method of characteristics it is possible to determine the free surface on the boundary as (Bradford, 2005; Sanders, 2002):

$$\eta_{(b-1/2,j)} = \frac{1}{16g} \left(4\sqrt{g(\eta(t+1/2) + h_{(b,j)})} - 2\sqrt{gh_{(b,j)}} + 2\sqrt{gH_{(b+1/2,j)}^{n+1/2}} - \frac{Q_{n(b,j)}^n}{H_{(b,j)}^n} \right)^2 - h_{(b,j)} \quad (3.30)$$

where $Q_{n(b,j)}^n$ is positive for the direction towards the boundary. $\eta(t+1/2)$ is the free surface that is given by one of our forced boundary conditions, e.g. the solitary wave or arbitrary wave shape

described in the previous sections. In this case reflections can pass out through the domain as well as become prescribed at the boundary. Therefore, Eqn.(3.30) works like a correction to the initially prescribed free surface on the boundary. In the case where we have just a passive open boundary, $\eta(t+1/2) = -h_{(b,j)}$ is set in Eqn.(3.30) so that the first term on the left in the parenthesis vanishes. Following the calculation of $\eta_{(b-1/2,j)}$, the flux normal to the boundary may be found by the LSWE assumption presented in Eqn.(3.28) in the case of either of the forced open or passive open boundary situations.

3.2.5 Initial Conditions

Initial conditions particularly for tsunami calculations are important. Such initial conditions can include tide levels and the water level on land. These two conditions are often coupled together since if the tide level is increased then more land may be flooded at the initial stage. In addition, land elevation may be defined below the tide level but is not flooded in reality because it is surrounded by walls or land elevations that are greater than the tide level in between that location and the coast. In the numerical code a user may specify an initial tide level, which is followed by a special algorithm that ensures that only cells that have an elevation lower than the tide level *and* have a flooded connection to the coast are flooded. The initial free surface in a dry land cell is set equal to $-h$ of that cell. Other initial conditions concern the shape of the free surface and velocities used to initiate, for example, a solitary wave or tsunami wave train. Both of these cases are described in this section.

Solitary Wave

The forcing of a solitary wave through a lateral boundary has been described in §3.2.4. Another method for creating solitary waves is to define it as an initial condition within the computational domain. For example, the wave shape and velocities as defined by the first approximation of solitary wave in §3.2.4 can be prescribed as a function of x at $t = 0$. However, in the case that the linear frequency dispersion terms are included then the model satisfies weakly nonlinear dispersive theory. An exact solitary wave (permanent form) solution of this theory in terms of the depth-averaged velocity was proposed by Schember (1982). In this theory the wave speed is the same as the first approximation, that is:

$$c = \sqrt{g(A+h)} \quad (3.31)$$

However, the wave profile becomes slightly more complicated:

$$\eta(x) = \frac{1}{g} (A_u(c - A_u)\text{sech}^2(\kappa(x - x_0)) + A_u^2\text{sech}^4(\kappa(x - x_0))) \quad (3.32)$$

where, κ , is a measure of the wavenumber defined as:

$$\kappa^2 = \frac{3A_u}{4ch^2} \quad (3.33)$$

in which A_u is an amplitude variable equal to:

$$A_u = c \left(1 - \frac{gh}{c^2} \right) \quad (3.34)$$

As an initial condition the wave profile from Eqn. (3.32) may set centred around the location, $x = x_0$. If no initial velocities are specified then the soliton will split into two solitons travelling in opposite directions of roughly half the specified wave height as the calculation is commenced. However usually only one soliton travelling in a specified direction is desired. To achieve this the depth-averaged velocities must also be defined as:

$$U(x) = A_u \operatorname{sech}^2(\kappa(x - x_0)) \quad (3.35)$$

In order to get the flux as necessary for the numerical model, $U(x)$ and $\eta(x)$ are combined:

$$Q(x) = U(x)(\eta(x) + h(x)) \quad (3.36)$$

The values of $\eta(x)$ in Eqn. (3.32) and $Q(x)$ in Eqn. (3.36) may be specified on every cell in the computational domain as an initial condition. Practically, it is useful to employ a cutoff distance from $x = x_0$ where $\eta(x)$ and $Q(x)$ are set to zero to avoid very small values. In the current model, $\eta(x)$ and $Q(x)$ are limited to 1×10^{-10} m so any value below this is ignored and set to zero.

Tsunami Source

For real applications the tsunami source is an integral part of the simulation that directly affects the overall accuracy. A number of models termed “fault models” exist that provide information on the time evolution of the ground elevation as a function of a number of earthquake fault parameters, such as strike, dip, rake angle, fault area, depth of source, and slip. The most common of such models is based on the idealised formulation by Okada (1985); Mansinha and Smylie (1971) which assume that the Earth’s crust is a homogeneous elastic material (Behrens and Dias, 2015). On the other hand, a more sophisticated version based on a FEM model that may account for inhomogeneous material properties in the subduction zone has been used in Grilli et al. (2012) to better approximate the transient source of the 2011 Tohoku-oki earthquake tsunami. Furthermore, in hindcast simulations the slip distribution of the earthquake may found by inverting measured waveform data (e.g. Fujii et al., 2011). However, it is not the purpose of the thesis to deal with the source characteristics. Often, source data may be obtained from third-parties. The data should contain the change in seabed elevation over the computational domain (final or transient evolution) which may be used for the hydrodynamic tsunami simulations. This is the case in Chapter 5 where the data has been provided by an outside source.

In the hydrodynamics tsunami simulation, a common assumption made is that the maximum ground movement occurs instantaneously over the source area. This is especially true if the source area is relatively small and the earthquake event is short since the transient effects would

be unlikely to have a significant effect on the tsunami waveform in this case. This assumption will be made here since it becomes much easier to implement the source as an initial condition before commencing the tsunami simulation with a now rigid bed. Studies like those by Grilli et al. (2012) that consider the transient movement may provide more accurate descriptions of the source, but as long the simulated waveform near our region of interest is within fair agreement to the measured one we can be generally satisfied with the setup.

Under the instantaneous maximum ground movement assumption, data for the maximum change in initial water depth, Δh (from the original bathymetry data) at each computational cell should be collated. As the calculation is initiated, h in each computational cell is suddenly changed to $h_o + \Delta h$, where h_o is the original initial water depth. Due to the conservation of mass, the free surface level becomes, $-\Delta h$ (assuming that the initial free surface level is zero everywhere). Initial conditions for the horizontal velocities are assumed to be zero. Due to the new free surface distribution, the calculation may proceed like dam-break flow and the tsunami propagates out in the ocean and its energy is dispersed.

3.3 Two-way Multi-grid Nesting

Conducting a tsunami simulation from the source region to a specific location in the coastal zone requires that various spatial and temporal scales are navigated. For example, as the tsunami wave propagates in the open ocean it covers an extremely large area while in comparison to its size, small perturbations in the seabed are unimportant. In this case it is often sufficient to use grids on the order of ~ 1 km. However, as the tsunami crosses over the continental shelf where the depth becomes smaller and nonlinear effects play a role, the details of the seabed become increasingly important perhaps on the order of ~ 100 m. When the tsunami makes it way to the nearshore area, with respect to the harbour or bay, details on the order of ~ 10 m may be important. Finally, for detailed inundation of a town or even the performance of a single coastal structure, then the geometries of infrastructure, buildings, the coastal structure may be significant down to the order of metres. Thus, in order to navigate these scales efficiently a tsunami model that can seamlessly couple grids of different scales together is required.

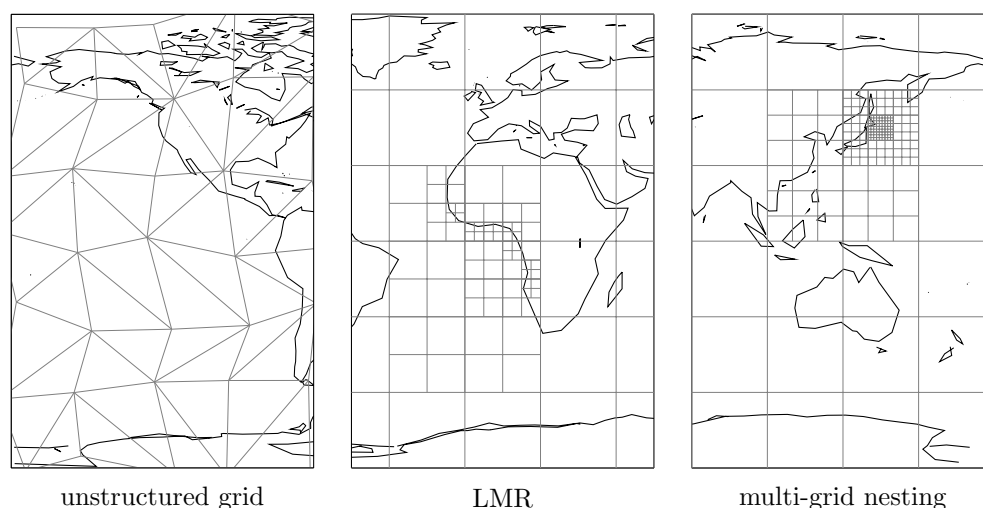


Figure 3.5: Different gridding approaches to deal with the change in spatial scales as a tsunami propagates towards the coastal zone

There are three main approaches to do this, as illustrated in Figure 3.5. One approach is to use unstructured grids (e.g. Zhang and Baptista, 2008). Unstructured grids do not have to conform to a regular grid pattern and thus can be fitted to follow the coastline and bathymetric effects accurately. Furthermore, they may be easily fitted to a range of grid sizes. A second example is local mesh refinement (LMR) where the mesh may be refined to a smaller size (e.g. $1/2$) anywhere on the the larger grid. This refined mesh can be further refined itself and so on. Local mesh refinement is often extended to adaptive mesh refinement (AMR) (e.g. LeVeque et al., 2011; Liang and Borthwick, 2009) where the local refinement is not necessarily set *a priori*. Instead the local refinement depends on the location of the tsunami and other local flow conditions in addition to

the regions of interest. The third and traditionally most common approach is multi-grid nesting (e.g. Liu et al., 1998; Titov and González, 1997; Goto et al., 1997). In some ways it is similar to LMR, however the best way to visualize multi-grid nesting is that multiple grids with gradually smaller sizes and finer scales are layered on top of each other zooming into the region of interest. The simulation can almost proceed independently in each layer however information between grids are exchanged at the boundaries. The information may be only in one-direction (from coarse grid to fine grid) or in both directions (two-way nesting). Additionally, the approaches described may be combined. For example, multi-grid nesting for unstructured grids. This may be adopted because it is more practical to consider a minimum grid size so that the grids are efficiently arranged.

In this thesis a FDM model on structured grids is used so only LMR, AMR and multi-grid nesting methods are available to us. Although LMR and AMR are attractive options if one is interested mainly in near-field simulations and there is an obvious region of interest they will not likely have much advantages over traditional multi-grid nesting (e.g. in terms of computational load, and *a posteriori* determination of refined regions). In general, the simplest method available is the multi-grid nesting one and it will be adopted in this thesis since the main application in Chapter 4 is for a near-field tsunami towards a specified region of interest. The method and procedure for multi-grid nesting is described in this section. It can be split into two parts: how to nest the regions in terms of the spatial setup, and how to nest the regions considering the temporal setup. These are described in §3.3.1 and §3.3.2 respectively. In addition, the form of multi-grid nesting is two-way in this thesis therefore the descriptions for exchange in both directions are described. Two-way nesting allows the finer details of the bathymetry to influence the wave field in the coarse grid which may be significant after reflections at the coast and with coastal structures take place.

3.3.1 Spatial Nesting

Multi-grid nesting couples together grids of different resolutions, and exchanges information at the interface where the grids. The simplest way to visualise the setup is the existence of multiple independent grids that have different sizes and resolutions. The grids are stacked on top of each other in an organised manner like layers. Hereafter, the different grids are referred to as layers to maintain the concept. Imagine now just two layers, a coarse grid which is referred to as, $L1$, and a fine grid, $L2$. A visualization of this from above is provided in Figure 3.6 where $L2$ has been placed in the middle of $L1$ where the edges of $L2$ line up with the grid lines of $L1$. This is an assumption that must be met for the numerical code to work correctly. Once this has been satisfied the first job of the program is find the cell numbers of $L1$ that correspond to the edges of $L2$. For example, the first (bottom-left) cell of $L1$ that is covered by $L2$ has the coordinates, $(is2^{L1}, js2^{L1})$. These cell numbers are used to map between the layers so that the correct location of the information is found.

Note that in Figure 3.6 the resolution of $L2$ is $(1/3) \times (1/3)$ that of $L1$ however this is arbitrary and just an illustration of a common setup. In fact, by the method of interpolation and averaging introduced there is no requirement on the ratio of the grid sizes between layers including non-integer ratios. The interpolating and averaging is required to transfer information from coarse grids to fine grids and from fine grids to coarse grids respectively. A description of the interpolating and averaging that takes place, in addition to what information and where it is exchanged is included in this section.

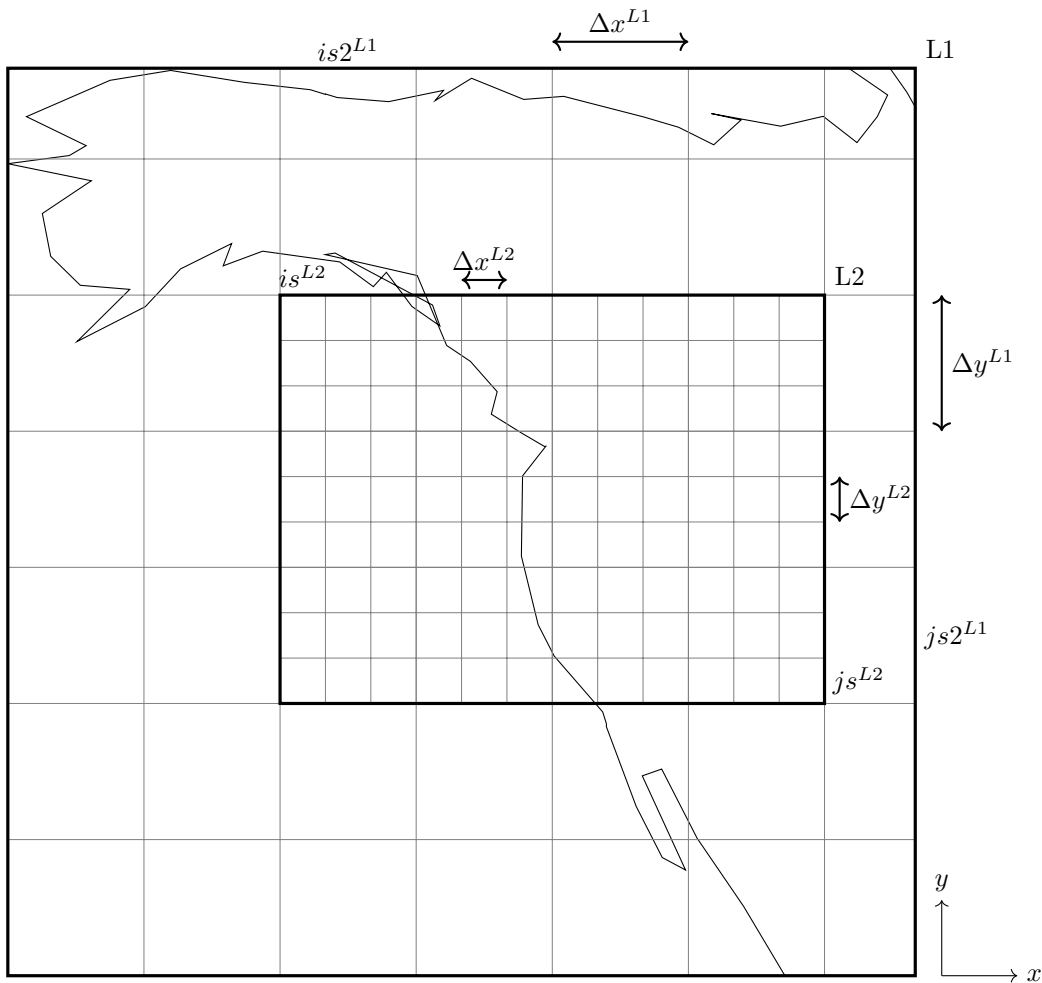


Figure 3.6: Example schematic of multi-grid nesting where a fine grid (layer), $L2$ has been placed in the centre of a coarse grid (layer), $L1$

Coarse Grid to Fine Grid Exchange

Information in multi-grid nesting must be passed from the coarse grid ($L1$) to the fine grid ($L2$) when either one-way and two-way nesting takes place. The information passed through in this

case is just the volume flux, Q . This should include both the normal flux at the actual boundary to $L2$ and the tangential flux adjacent to calculation domain in a ghost cell. Essentially the situation is the same as providing lateral boundary conditions (c.f. §3.2.4). To get the fluxes as boundary conditions for $L2$, interpolation of the fluxes from $L1$ is necessary as illustrated in Figure 3.7. Interpolation is achieved by linear means given the low-order of the numerical scheme.

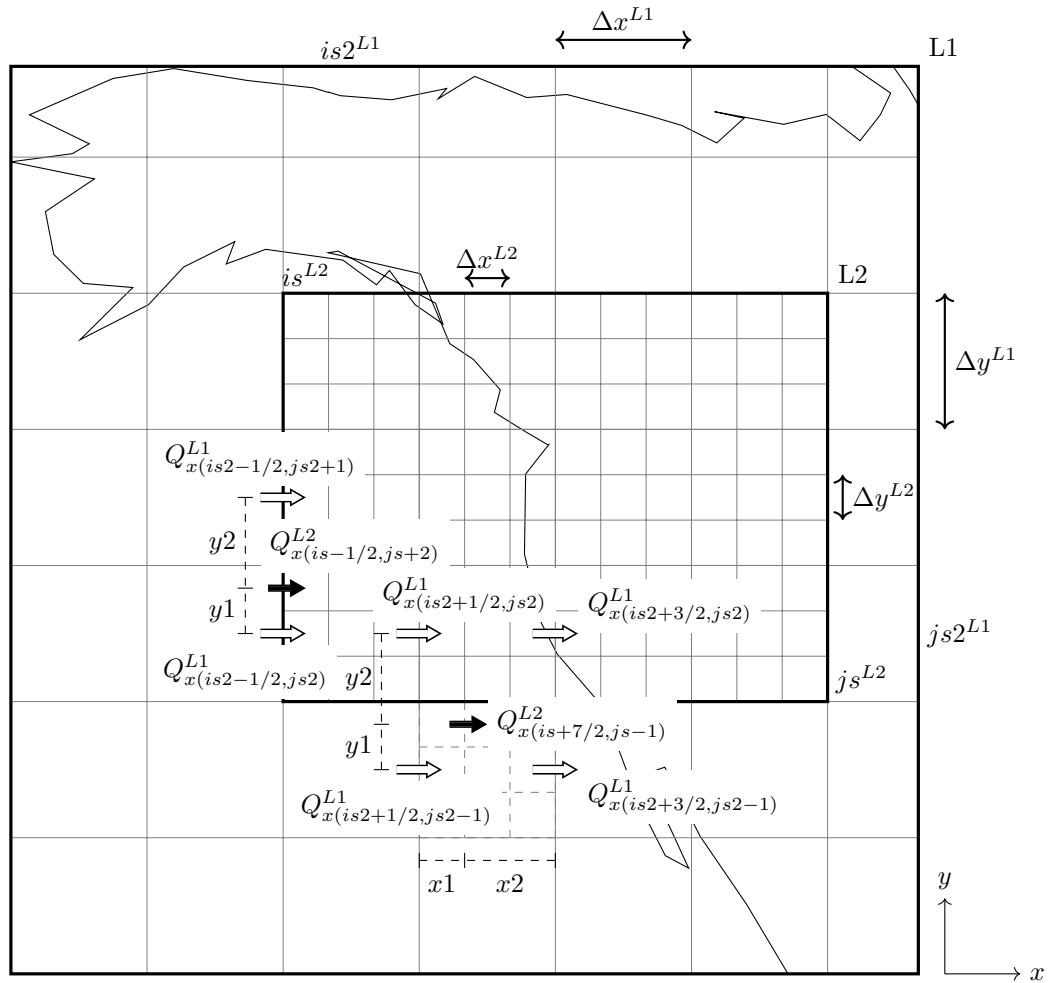


Figure 3.7: Illustration of the exchange of volume fluxes from the coarse grid, $L1$, to the fine grid, $L2$

To obtain the normal fluxes at the boundary only requires interpolation in the tangential direction since the boundary of $L2$ matches with the $L1$ grid. For example, the calculation of one of the normal fluxes on the west boundary, $Q_{x(is-1/2, js+2)}^{L2}$ (c.f. Figure 3.7) is achieved by the following:

$$Q_{x(is-1/2, js+2)}^{L2} = \frac{1}{\Delta y^{L1}} \left(Q_{x(is2-1/2, js2)}^{L1} (\Delta y^{L1} - y1) + Q_{x(is2-1/2, js2+1)}^{L1} y1 \right) \quad (3.37)$$

where $y1$ is the distance along the y axis from $js2^{L1}$ to $js^{L2} + 2$. Note that $y2$ in Figure 3.7 has

been replaced with $\Delta y^{L1} - y1$, which is a general statement. In the case that the distance $y1$ is between $Q_{x(is-1/2,js+2)}^{L2}$ and $Q_{x(is2-1/2,js2)}^{L1}$ as shown, $y1 = \Delta y^{L2}$. However, this is not true for any arbitrary position (e.g. distance between $Q_{x(is-1/2,js+3)}^{L2}$ and $Q_{x(is2-1/2,js2)}^{L1}$ is $y1 = 2\Delta y^{L2}$), thus an algorithm is used to find this exact distance. Normal fluxes on the north-south boundaries, Q_y^{L1} are also interpolated in a similar fashion.

On the other hand, to obtain the tangential fluxes in a ghost cell for $L2$ requires interpolation in both the normal and tangential directions as depicted in Figure 3.7. For example, the calculation of one of the tangential fluxes adjacent to the south boundary, $Q_{x(is+7/2,js-1)}^{L2}$ (c.f. Figure 3.7):

$$Q_{x(is+7/2,js-1)}^{L2} = \frac{1}{\Delta y^{L1} \Delta x^{L1}} \left[Q_{x(is2+1/2,js2-1)}^{L1} (\Delta y^{L1} - y1) (\Delta x^{L1} - x1) + Q_{x(is2+3/2,js2)}^{L1} y1 x1 \right. \\ \left. + Q_{x(is2+3/2,js2-1)}^{L1} (\Delta y^{L1} - y1) x1 + Q_{x(is2+1/2,js2)}^{L1} y1 (\Delta x^{L1} - x1) \right] \quad (3.38)$$

where $x1$ is the distance along x axis from $is2^{L1} + 1/2$ to $is^{L2} + 7/2$. Note that $x2$ in Figure 3.7 has been replaced with $\Delta x^{L1} - x1$, which is a general statement.

Fine Grid to Coarse Grid Exchange

If two-way nesting is invoked, information must also be passed through from the fine grid ($L2$) to the coarse grid ($L1$) in addition to the other direction. Essentially what this information must contain are values that affect the calculation of the fluxes in $L1$ that are interpolated and passed through to $L2$ as discussed in the previous section. Since we are dealing with shallow water flow and the pressure gradient dominates, the most important piece of information to pass through to $L1$ is the free surface. In order to influence the calculation of the normal or tangential fluxes then the free surfaces from $L2$ are averaged onto the $L1$ grid and passed through *everywhere* within the $L2$ boundary. Of course values of the free surface well within the $L2$ domain will not affect the calculation of the fluxes from $L1$ on the boundary, however for visualization purposes it is useful to gather the data from the region with the highest resolution everywhere and transform it onto the coarse grid.

As an example calculation, in order to get $\eta_{(is2,js2)}^{L1}$ from $L2$, the following operation is performed:

$$\eta_{(is2,js2)}^{L1} = \frac{\sum_j \sum_i \eta_{(i,j)}^{L2}}{\sum_j \sum_i 1} \quad \text{with} \quad \begin{cases} x(i) \in (x(is2) - \Delta x^{L1}/2, x(is2) + \Delta x^{L1}/2) \\ y(j) \in (y(js2) - \Delta y^{L1}/2, y(js2) + \Delta y^{L1}/2) \end{cases} \quad (3.39)$$

This equation may be visualised in Figure 3.8. The first step is to draw a bounding box (indicated by the dashed rectangle) just smaller than the size of a $L1$ grid around the centre point of the required quantity. All the quantities in $L2$ that fall within this bounding box are summed and divided by their number. Note that sometimes a few cells in $L2$ that are contained within the bounding box may have zero water depths often due to a sudden change in the bathymetry whereas the rest of the cells in the bounding box are wet cells. Including the free surface in these

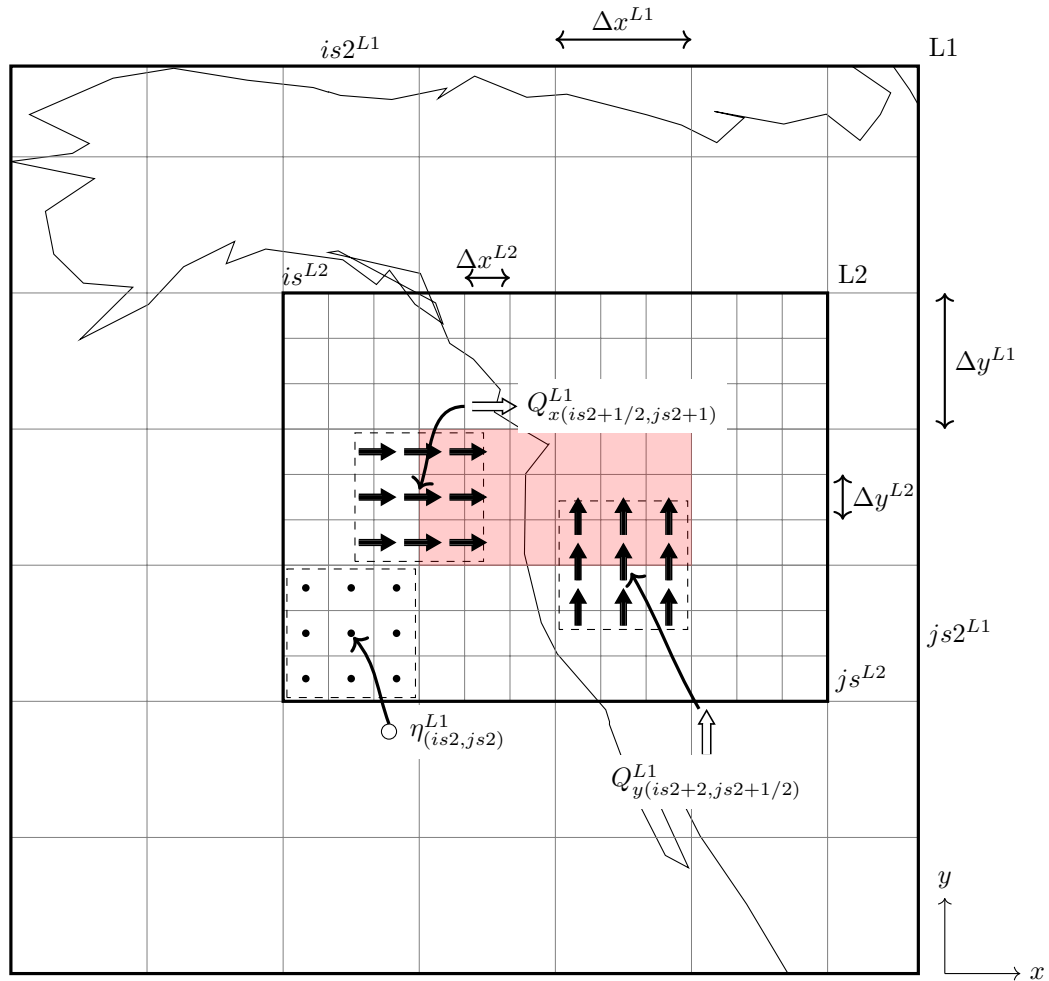


Figure 3.8: Illustration of the exchange of the free surface volume fluxes from the fine grid, $L2$ to the coarse grid, $L1$

cells (corresponding to the level of the seabed) can often upset the average for $L1$ which only knows of the average seabed elevation in that bounding box. Thus, when cells of zero water depth are detected they are excluded from the averaging calculation.

The other quantity to pass through to $L1$ are the volume fluxes which are required in the nonlinear advection difference when calculating the volume fluxes in $L1$ on the boundary to $L2$ (note that the free surfaces passed through are used to get the water depth also required in the nonlinear advection difference). Firstly, recall that the volume fluxes in $L1$ along the first row and columns within the $L2$ boundary (c.f. Figure 3.7) are required for interpolation to determine the tangential fluxes as a boundary condition for $L2$. Thus, we require boundary conditions for these fluxes rather than passing them through from $L2$. It has been found that this technicality is important to obtain smooth nesting in the tangential direction. Instead these fluxes on the outer ring of cells within $L2$ are calculated normally in the $L1$ momentum equation with boundary

conditions provided from $L2$. Thus, the fluxes that must be passed from $L2$ to $L1$ fall within or on the boundaries of the red shaded box in Figure 3.8. They are found from averages in the same way as Eqn. (3.39). Note of course that in the usual case the size of the domain of $L2$ and hence the red shaded box is much larger and many fluxes and free surfaces are required to be passed from $L2$ to $L1$ as either boundary conditions and/or visualization purposes. On that note, to save computational time, during calculation of the momentum equation for $L1$, the loop is cycled inside or on the boundary of the red shaded box.

3.3.2 Temporal Nesting

The nesting of grids of different spatial scales has been described in §3.3.1. Since the numerical method is based on an explicit method, its Courant number must be bounded. By a stability analysis the Courant number is limited to $\sqrt{2}/2$ in the 2DH case (and to 1 in the 1DH case). The Courant number for the grid is defined as, $Cr = \sqrt{gh_{max}}\Delta t/\Delta x$, where h_{max} is the largest depth in the grid. This implies that if $\Delta x^{L1}/\Delta x^{L2} = 3$ as in our example figures (Figure 3.6 - Figure 3.8), to have equal Cr with equal h_{max} , $\Delta t^{L1}/\Delta t^{L2}$ must also equal three. In practice though h_{max} is often smaller in fine grids since they are placed closer to the coastal zone. This reduces the dependence of Δx on Δt and if only two layers with $\Delta x^{L1}/\Delta x^{L2} = 3$ is used then the same Δt in both layers may be reasonable. However, if many layers are used and Δt is required to be the same in all layers then this could become quite restrictive on the time step in the coarse grids. Often the outer layers contain many grids for computation over a large area so a small Δt , hence Cr , may make the computational load unnecessarily large. In order to increase the efficiency of the scheme one can compute each layer with Cr that approaches the stability limit and interpolate in the temporal direction. This process is termed “temporal nesting” in this thesis.

Table 3.1: Example setup with three nested layers and their attributes

Layer No.	Δx (m)	h_{max} (m)	Δt (s)	Cr
1	1350	9900	3.03	0.70
2	450	3050	1.52	0.58
3	150	570	0.76	0.38

Practically in the numerical code this is achieved by looping over the calculation of each time step in $L2$, Δt_{ratio} number of times for each time step of $L1$, where Δt_{ratio} is equal to the ratio of Δt between $L2$ and $L1$. In order to achieve this in the numerical code, a data structure for each layer was created so that all the data at the current time for a certain layer is input into a subroutine that performs the calculation for the arbitrary layer before outputting the updated values of that layer. As a new example to explain the calculation process, lets assume that there are three layers, $L1$, $L2$ and $L3$. The values of $\Delta x = \Delta y$, h_{max} , Δt and Cr are presented in Table 3.1 for each layer. Note, that Δt and Cr are determined by a certain calculation process given Δx , and h_{max} for each layer, and the condition that Δt_{ratio} must be an integer one (since

performing a loop, say 5.33 times makes no sense). The algorithm starts by setting Δt in each layer so that Cr becomes close to the theoretical limit, e.g. 0.7, or any smaller desired value, Cr_{set} by the following operation:

$$\Delta t = \frac{Cr_{set}\Delta x}{\sqrt{gh_{max}}} \quad (3.40)$$

The second process is to adjust Δt so that the ratio between each adjacent layer is an integer ratio and Cr does not exceed Cr_{set} . Assuming that Δt^{L1} remains unchanged, the following loop is performed to update Δt in the remaining layers:

$$\begin{aligned} &\text{for } k = 2, LN \\ &\quad \Delta t_{ratio} = \text{ceiling}\left(\Delta t^{L(k-1)}/\Delta t^{L(k)}\right) \\ &\quad \Delta t^{L(k)} = \Delta t^{L(k-1)}/\Delta t_{ratio} \\ &\text{end} \end{aligned} \quad (3.41)$$

where LN is the total number of layers. The ‘‘ceiling’’ operation ensures that Δt_{ratio} is both an integer ratio and rounds up towards infinity so that Cr will always be less than Cr_{set} . Due to this process Cr may become significantly smaller than the theoretical limit for the fine grid layers as highlighted in Table 3.1. However this can be beneficial since these layers are where nonlinear effects and inundation occur where smaller Cr values are generally desirable. On the other hand in the coarse grids, such effects are less important and the numerical scheme can safely run very close to the theoretical limit.

Table 3.1 demonstrates that $\Delta t_{ratio} = 2$ between each adjacent layer. This means that for one loop of $L1$ to go from $t \rightarrow t + \Delta t^{L1}$ requires two time steps of $L2$ and four time steps of $L3$. Additionally, information is passed between the layers in both directions as discussed in §3.3.1. The information must be passed through in a certain order so that the situation where not yet known data is required for a layer does not arise. Specifically, exchanging flux data from the coarse grid to the fine grid requires that the momentum equation of the coarse grid is calculated first. This ensures for example, that the flux between t and $t + \Delta t^{L1}$ may be interpolated to get $Q^{n+1/2}$ which corresponds to the momentum flux at the boundary of $L2$ after one time step (which is half of one time step in $L1$). Additionally, volume fluxes and free surfaces must be passed back from the fine grid to the coarse grid when the absolute times in the layers align. An example flowchart for the three layers with $\Delta t_{ratio} = 2$ between each layer is shown in Figure 3.9. It is firstly assumed that flux data in each layer is known at time $t = n$, and free surface data is known at time, $t = n - \Delta t^{Lk}/(2\Delta t^{L1})$ for layer k .

The procedure starts by calculating continuity in each layer once starting from the finest grid, in this case, $L3$ moving through to $L1$. This reason for this order of calculation is due to the existence of the arrows between each calculation step of continuity: the free surface from the fine grid layer is exchanged to the coarse grid layer at the boundaries (c.f. (3.8)). The caveat

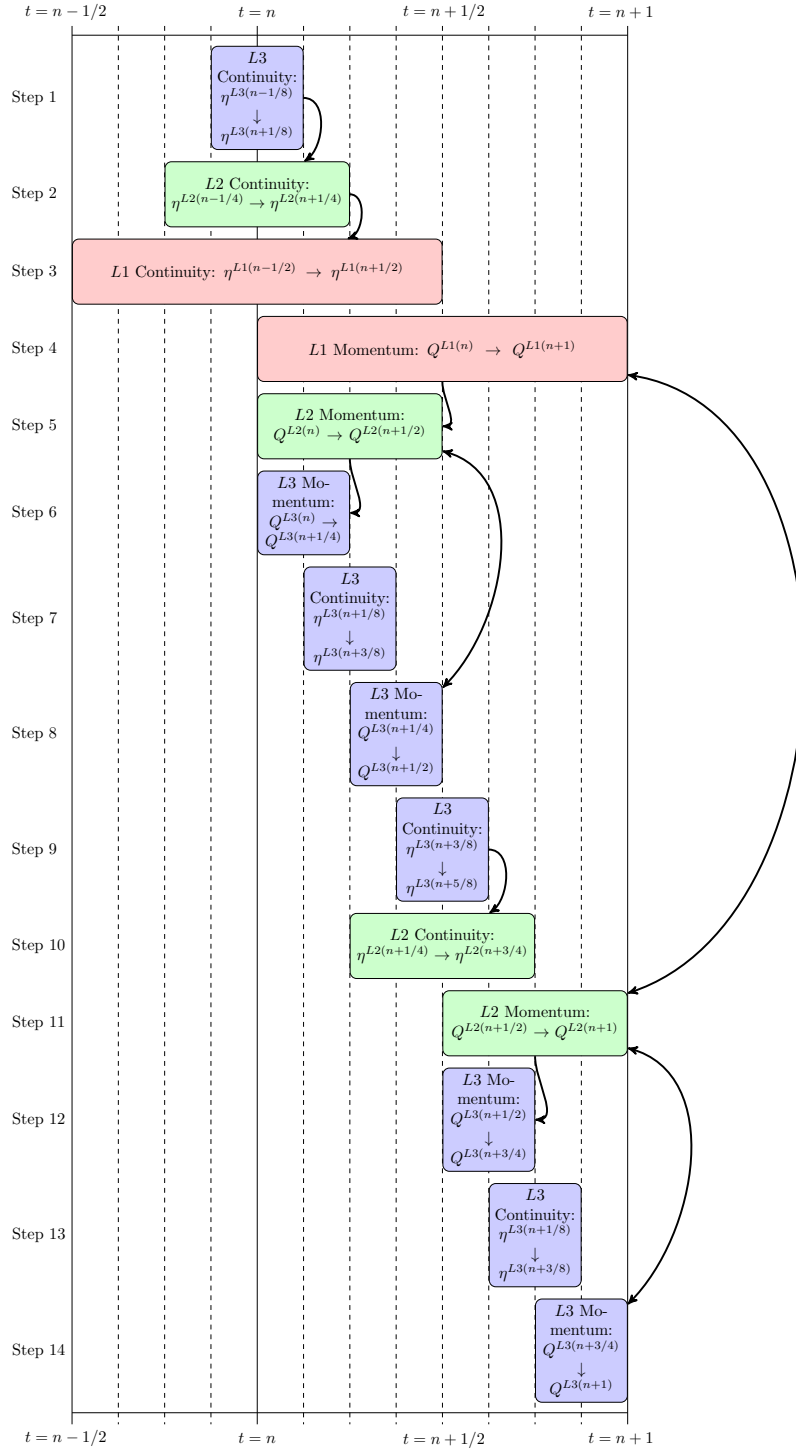


Figure 3.9: Example flowchart of the calculation order for temporal nesting of three layers where $\Delta t_{ratio} = 2$ between two adjacent layers. The arrows show the exchange of information where the horizontal position of the ends of the arrows indicate the time step of the exchanged data

is that for example when exchanging the free surface from $L3$ to $L2$ after step 1, only the free surface at $t = n + 1/8$ is known in $L3$ and can be passed to $L2$ as indicated by the arrow. However, after continuity in $L2$, the free surface at $t = n + 1/4$ is required. This means that for the free surfaces exchanged from the fine grid model to the coarse grid, a fractional time step of continuity is required:

$$\eta_{(i,j)}^{n+1/2} = \eta_{(i,j)}^{n+1/(2\Delta t_{ratio})} - \frac{1}{2} \left(1 - \frac{1}{\Delta t_{ratio}} \right) \left[r_x \left(Q_{x(i+1/2,j)}^n - Q_{x(i-1/2,j)}^n \right) + r_y \left(Q_{y(i,j+1/2)}^n - Q_{y(i,j-1/2)}^n \right) \right] \quad (3.42)$$

this is a general equation for any Δt_{ratio} between any two adjacent layers. The fine grid can only provide information to the coarse grid at $t = n + 1/(2\Delta t_{ratio})$ and so continuity using a multiple of $1/2(1 - 1/\Delta t_{ratio})$ (goes to zero if $\Delta t_{ratio} = 1$) is conducted to ensure that the free surface boundary condition is at the correct time for the coarse grid. Note that the fluxes at $t = n$ have already been exchanged from the fine grid to the coarse grid so that this step of continuity may be achieved. For example, in Figure 3.9 at $t = n + 1$, fluxes are exchanged in both directions between all the layers indicated by the double-headed arrows. The extra fractional step of continuity contains a small amount of numerical error associated with the indirect transfer of the free surface through the flux gradient. However, this error is non-accumulative since it is corrected by the direct transfer of the free surface beforehand, and it is not found to have a noticeable effect on the nesting performance.

After the calculation of continuity in each layer, the momentum equation in all layers may proceed one time step. The loop starts from the coarsest grid, $L1$ moving through to the finest grid, $L3$. This is because the fluxes are exchanged from the coarse grid to the fine grids (opposite to the free surface exchange explained above). In this case the information of the flux in the coarse grid is known in advance of the time step of the fine grid so interpolation is required e.g. $Q^{L1(n)}$ and $Q^{L1(n+1)}$ is linearly interpolated to get $Q^{L1(n+1/2)}$ and is passed to $L2$ after step 4. Hereafter, continuity and momentum is conducted once each in $L3$ at steps 7 and 8 to update $L3$ by one time step. Flux from $L2$ is exchanged (without need for interpolation) at $t = n + 1/2$ in both directions. Finally, Steps 9 to 14 are actually the same as Steps 1 to 8 sans the calculation of $L1$. It is this fact that allows a pattern of the calculation order to be recognised. In the numerical code a recursive subroutine has been written to achieve the calculation procedure illustrated in Figure 3.9. The recursive subroutine is able to calculate any arbitrary number of layers with arbitrary Δt_{ratio} between any two adjacent layers. Due to its usefulness, the FORTRAN code is included in Appendix A. Note that as the subroutine is written, Steps 4 to 14 are calculated first, before calculating Steps 1 to 3 (e.g. $\eta^{L1(n+1/2)} \rightarrow \eta^{L1(n+3/2)}$), however the concept is the same.

3.4 Reynolds-Averaged Navier-Stokes Equations Model

The RANS model used in this thesis is based on the model created by Professor Yoneyama and first presented in Yoneyama and Moriya (1995). Its major focus was on the accurate modelling of the free surface. It has been used in tsunami studies to accurately compute the locally runup during 1993 Hokkaido Tsunami in Okushiri (Yoneyama et al., 2002), and even to predict the movement of driftage by tsunamis (Yoneyama et al., 2012). A number of developments have been made in this research but its strength still lies in the accurate free surface representation which itself has been vastly improved.

3.4.1 Governing Equations

The governing Reynolds-averaged Navier-Stokes (RANS) equations and its conceptual basis was introduced in §2.1.1. For the model, a couple of additional parameters are inserted into the equations to consider Fractional Area/Volume Obstacle Representation (FAVOR) (Hirt and Sicilian, 1985). They are the void ratio, γ^v and the aperture ratio, γ_i^a . The void ratio refers to the volume fraction of a computational cell that does not contain an object:

$$\gamma^v = 1 - \frac{V_{object}}{\Delta x \Delta y \Delta z} \quad (3.43)$$

where V_{object} is the volume of the object in the cell. The aperture ratio refers to the fraction of the surface area of a computational cell boundary perpendicular to the i axis that is void (does not contain an object):

$$\gamma_x^a = 1 - \frac{(SA_{object})_x}{\Delta y \Delta z} \quad (3.44)$$

where $(SA_{object})_x$ is the surface area of the cell boundary that is occupied by an object perpendicular to the x axis. Similar equations are available for γ_y^a and γ_z^a . The introduction of the FAVOR parameters allow us to consider cells that are partially occupied by an object in order to describe geometries more accurately without resorting to restrictively small grid sizes. The governing equations with their addition become:

$$\frac{\partial \gamma_i^a \bar{u}_i}{\partial x_i} = 0 \quad (3.45)$$

$$\frac{\partial \bar{u}_i}{\partial t} + \frac{1}{\gamma^v} \frac{\partial \gamma_j^a \bar{u}_j \bar{u}_i}{\partial x_j} = g_i - \frac{1}{\rho} \frac{\partial \bar{p}}{\partial x_i} + \frac{1}{\gamma^v} \frac{\partial}{\partial x_j} \left[\gamma_j^a \left(\nu \frac{\partial \bar{u}_i}{\partial x_j} - \overline{u'_i u'_j} \right) \right] \quad (3.46)$$

The Reynolds stresses, $-\overline{u'_i u'_j}$ must be modelled by a turbulent closure scheme. A common approach is the eddy viscosity concept. This approach assumes that the Reynolds stresses should be proportional to the local mean strain rate of the fluid, similar to molecular viscosity. The simplest approach, called the Boussinesq approximation gives the following representation for the Reynolds stress:

$$-\overline{u'_i u'_j} = \nu_t \left(\frac{\partial \bar{u}_i}{\partial x_j} + \frac{\partial \bar{u}_j}{\partial x_i} \right) - \frac{2}{3} k \delta_{ij} \quad (3.47)$$

where ν_t is the eddy viscosity. Note that ν_t is represented here is a scalar quantity, which implies isotropy of the turbulent flow. In reality this is generally not the case but it is typically assumed to be so in most models. ν_t however is a property of the flow rather than the fluid which indicates it will vary in time and space as the flow evolves. The other term introduced here is the turbulent kinetic energy, $k(\equiv \frac{1}{2}\overline{u'_i u'_i})$. Additionally, δ_{ij} is the Kronecker delta which just indicates that k is only present when $i = j$. If Eqn. (3.47) is substituted into Eqn. (3.46) and the bars are dropped on the averaged variables for convenience the momentum equation becomes:

$$\frac{\partial u_i}{\partial t} + \frac{1}{\gamma^v} \frac{\partial \gamma_j^a u_j u_i}{\partial x_j} = g_i - \frac{1}{\rho} \frac{\partial p}{\partial x_i} + \frac{1}{\gamma^v} \frac{\partial}{\partial x_j} \left[\gamma_j^a (\nu + \nu_t) \left(\frac{\partial u_i}{\partial x_j} + \frac{\partial u_j}{\partial x_i} \right) \right] \quad (3.48)$$

Note that the $k\delta_{ij}$ term has been absorbed into the pressure term, i.e:

$$\frac{\partial p}{\partial x_i} = \frac{\partial}{\partial x_i} \left(p + \frac{2}{3}k \right) \quad (3.49)$$

Eqn. (3.48) represents the correct momentum equation including the FAVOR parameters (γ_i^a and γ^v). It is written here for consistency since the continuity equation includes γ_i^a . Moreover, the Poisson Pressure equation, advection of the fluid volume fraction and the turbulent transport equations that are introduced in §3.4.2, §3.4.4 and §3.4.5 respectively also include the fractional area parameters. However, it is considerably more difficult to include these parameters in the momentum equation robustly because of the staggering of u_i and the scalar quantities. Moreover, for the application of the model in thesis it is expected that the effect of these parameters at the seabed is small (in the momentum equation). Hence, the actual momentum equation solved in this thesis is the following (sans FAVOR parameters):

$$\frac{\partial u_i}{\partial t} + u_j \frac{\partial u_i}{\partial x_j} = g_i - \frac{1}{\rho} \frac{\partial p}{\partial x_i} + \frac{\partial}{\partial x_j} \left((\nu + \nu_t) \frac{\partial u_i}{\partial x_j} \right) \quad (3.50)$$

The $\frac{\partial u_j}{\partial x_i}$ term in Eqn. (3.48) has disappeared upon application of continuity. In both Eqns. (3.48) and (3.50), $-\overline{u'_i u'_j}$ has been replaced by ν_t , thus the problem now becomes one of modelling ν_t instead. Fortunately, there are a number of methods for doing so. One of those - the standard $k - \epsilon$ model - is adopted in this thesis and described in §3.4.5.

3.4.2 Numerical Procedure

In order to solve Eqns. (3.45) and (3.50) a pressure-velocity coupling technique is required. The main issue with the solution of RANS or N-S equations in general is the decoupled form of the momentum equations and the divergence free condition of continuity. The momentum equations may be solved to give a velocity field without a pressure gradient but in order to get the correct pressure field, the divergence free condition must be satisfied. However, since p is not explicitly included in the continuity equations the divergence-free condition must be somehow enforced onto the momentum equations in order to solve for p . This process is called

pressure-velocity coupling. There are a number of techniques available to this end, including PISO (Pressure-Implicit Separation of Operators) (Issa, 1986), SIMPLE (Semi-Implicit Method for Pressure-Linked Equations) (Patankar and Spalding, 1972) and its variants, SMAC (Simplified Marker and Cell) (Amsden and Harlow, 1970), and projection methods (Chorin, 1968) among others. SIMPLE methods have been found to be effective for steady/quasi-steady problems, or unsteady ones with coarse step sizes because of the iterative requirement to satisfy both momentum and mass after each time step. However, in a highly unsteady problem that usually requires small time steps the SMAC method is more appropriate because of its non-iterative nature. Under such situations the SMAC method has been shown to efficiently yield accurate results in comparison with other more computationally intensive methods such as SIMPLE and PISO (Saito et al., 2012; Kim and Benson, 1992). Given that wave computations and interactions with structures are highly unsteady by nature the SMAC method is adopted in this thesis.

The SMAC method along with projection methods, PISO and SIMPLE revolve around solving the solution to a Poisson Pressure equation to obtain the pressure-velocity coupling. For the SMAC method the solution procedure is as follows:

1. Solve Eqn. (3.50) using a forward Euler time integration to obtain an intermediate velocity field, u_i^* in the following form (where a pseudo-pressure, \tilde{p} should satisfy the normal stress condition (c.f. §3.4.7) on the free surface):

$$u_i^* = u_i^n - \Delta t \left[g_i + \frac{1}{\rho} \frac{\partial \tilde{p}}{\partial x_i} + \Theta_i^n \right] \quad (3.51)$$

where Θ_i^n is a representation of the advection and viscous stress terms using u_i^n . \tilde{p} is arbitrary and may be set to zero everywhere (except at the free surface), or the previous value of the pressure, p^n may be used. u_i^* satisfies the vorticity field but it does not yet satisfy the divergence free condition.

2. If u_i^{n+1} is the updated Solenoidal velocity field that we want to obtain then a similar equation is available using the updated corrected pressure field, p^{n+1} :

$$u_i^{n+1} = u_i^n - \Delta t \left[g_i + \frac{1}{\rho} \frac{\partial p^{n+1}}{\partial x_i} + \Theta_i^n \right] \quad (3.52)$$

3. Subtracting Eqn. (3.51) from Eqn. (3.52) gives:

$$u_i^{n+1} - u_i^* = -\frac{\Delta t}{\rho} \frac{\partial p^{n+1} - \tilde{p}}{\partial x_i} \quad (3.53)$$

4. If the divergence of Eqn. (3.53) is taken and the divergence free condition of u_i^{n+1} is enforced the following Poisson Pressure equation results (with the addition of γ_i^a for the FAVOR method):

$$\frac{\partial \gamma_i^a u_i^*}{\partial x_i} = \Delta t \frac{\partial}{\partial x_i} \left(\frac{\gamma_i^a}{\rho} \frac{\partial \Delta P}{\partial x_i} \right) \quad (3.54)$$

where $\Delta P = p^{n+1} - p^n$

5. Solve the Poisson Pressure equation using an appropriate matrix solver to get ΔP . Pre-conditioned conjugate gradient methods are usually adopted.
6. The corrected pressure becomes:

$$p^{n+1} = p^n + \Delta P \quad (3.55)$$

Furthermore, Eqn. (3.53) may be rearranged to get the Solenoidal velocity field, u_i^{n+1} :

$$u_i^{n+1} = u_i^* - \frac{\Delta t}{\rho} \frac{\partial \Delta P}{\partial x_i} \quad (3.56)$$

The SMAC solution method ensures that the conservation of mass is strongly satisfied but the conservation of momentum may only be weakly satisfied (Kim and Benson, 1992). However, if the time step is sufficiently small then accurate solutions can be obtained (Saito et al., 2012). SMAC is similar to projection methods introduced by Chorin (1968) around the same time which ignores the pressure gradient in the momentum equations before projecting the divergence free condition onto the velocity field.

3.4.3 Discretization Scheme

Eqns. (3.51) and (3.54) are discretized in a finite-difference manner onto a staggered Arakawa C-grid as illustrated in Figure 3.10. The velocities u_i are placed on the cell boundaries perpendicular to the i axis and all the other variables (the scalar ones) such as p and k are placed on cell centres. This helps to easily create second-order central finite-differences about u_i in the momentum equation and Δp in the Poisson Pressure equation. Doing so prevents issues like “checkerboarding” where a central difference approximation of both u_i^* and Δp in Eqn. (3.54) at the same location may permit independent sets of solutions at alternating cells.

The discretized form of the equations are shown below for the solution to u_c as shown in Figure 3.10. Firstly, Eqn. (3.51) is discretized as follows:

$$u_c^* = u_c^n - \Delta t \left[g_x + \frac{p_e^n - p_c^n}{\rho \Delta x_c} + \Theta_c^n \right] \quad (3.57)$$

where Θ_c^n is given as:

$$\begin{aligned} \Theta_c^n = & - \left(u \frac{\partial u}{\partial x} \right)_c^n - \left(v \frac{\partial u}{\partial y} \right)_c^n - \left(w \frac{\partial u}{\partial z} \right)_c^n \\ & + \left(v + \frac{v_{te}^n + v_{tc}^n}{2} \right) \left[\left(\frac{\partial^2 u}{\partial x^2} \right)_c^n + \left(\frac{\partial^2 u}{\partial y^2} \right)_c^n + \left(\frac{\partial^2 u}{\partial z^2} \right)_c^n \right] \end{aligned} \quad (3.58)$$

The nonlinear advection terms are usually solved using the third-order upwind method (QUICK) and the viscous terms have been solved through the central order difference method. The actual finite difference formulae can be found in Appendix B.

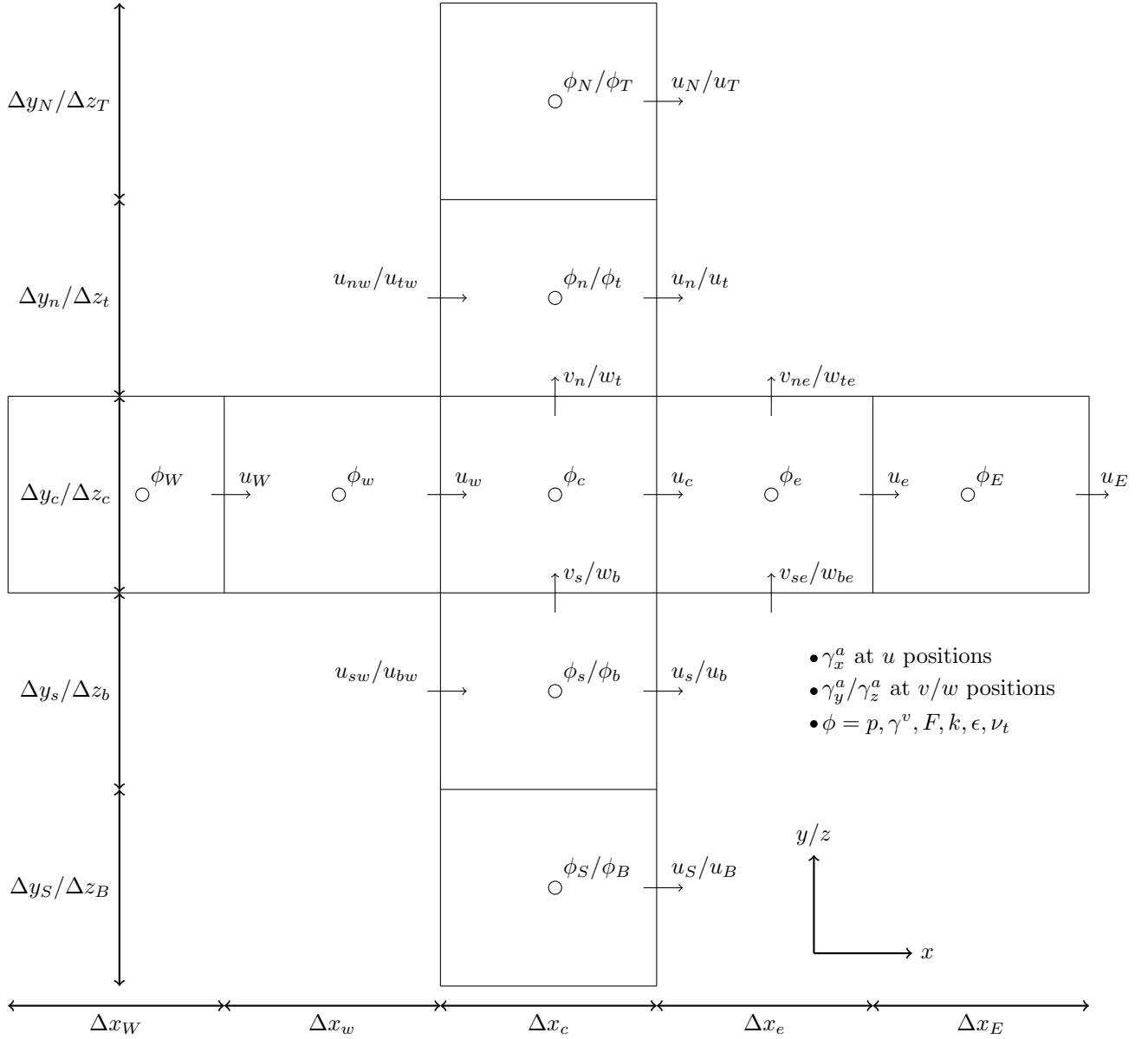


Figure 3.10: Finite-difference stencil of the RANS method in the $x - y/z$ plane, shown specifically for the calculation of u_c with positive velocity. Analogous stencils exist for finding v_c and w_c

Once u_i^* is found, $\frac{\gamma_i^a \partial u_i^*}{\partial x_i}$ is checked to give an “error of continuity”, ϵ_D by the following discretization:

$$\frac{\gamma_{xc}^a u_c^* - \gamma_{xw}^a u_w^*}{\Delta x_c} + \frac{\gamma_{yn}^a v_n^* - \gamma_{ys}^a v_s^*}{\Delta y_c} + \frac{\gamma_{zt}^a w_t^* - \gamma_{zb}^a w_b^*}{\Delta z_c} = \epsilon_{Dc} \quad (3.59)$$

If the maximum absolute value of the error of continuity, $|\epsilon_D|$ within the entire computational region is smaller than some prescribed value (usually set to 1×10^{-5} in the current model), then u_i^* , is already said to be divergence-free and becomes u_i^{n+1} indicating the end of the time step.

Otherwise, the Poisson Pressure equation is solved. It is discretized as:

$$A_e \Delta p_e + A_w \Delta p_w + A_n \Delta p_n + A_s \Delta p_s + A_t \Delta p_t + A_b \Delta p_b + A_c \Delta p_c = \frac{\epsilon_{Dc}}{\Delta t} \quad (3.60)$$

with,

$$\begin{aligned} A_e &= \frac{2\gamma_{xc}^a}{\Delta x_c(\Delta x_c + \Delta x_e)} & A_w &= \frac{2\gamma_{xw}^a}{\Delta x_c(\Delta x_c + \Delta x_w)} \\ A_n &= \frac{2\gamma_{yn}^a}{\Delta y_c(\Delta y_c + \Delta y_n)} & A_s &= \frac{2\gamma_{ys}^a}{\Delta y_c(\Delta y_c + \Delta y_s)} \\ A_t &= \frac{2\gamma_{zt}^a}{\Delta z_c(\Delta z_c + \Delta z_t)} & A_b &= \frac{2\gamma_{zb}^a}{\Delta z_c(\Delta z_c + \Delta z_b)} \\ A_c &= -(A_e + A_w + A_n + A_s + A_t + A_b) \end{aligned} \quad (3.61)$$

Eqn. (3.60) is solved using the BiCGSTAB matrix solving algorithm in this study. Δp is then used to update the velocities and pressure as follows:

$$u_c^{n+1} = u_c^* - \frac{\Delta t}{\rho} \frac{\Delta p_e - \Delta p_c}{(\Delta x_c + \Delta x_e)/2} \quad (3.62)$$

$$v_n^{n+1} = v_n^* - \frac{\Delta t}{\rho} \frac{\Delta p_n - \Delta p_s}{(\Delta y_c + \Delta y_n)/2} \quad (3.63)$$

$$w_t^{n+1} = w_t^* - \frac{\Delta t}{\rho} \frac{\Delta p_t - \Delta p_b}{(\Delta z_c + \Delta z_t)/2} \quad (3.64)$$

$$p_c^{n+1} = p_c^n + \Delta p_c \quad (3.65)$$

3.4.4 Free Surface Model

When free surfaces are present in the RANS model a method is required to consider the evolution of the free surface. One simple option is to assume a single free surface and integrate continuity over the depth while applying the boundary conditions on the free surface to get the 2DH continuity Eqn. (2.24). While this “height function” approach is a simple and accurate solution, it limits the model to only quasi-three dimensional behaviour. For example, wave overturning, and any other situations where multiple free surfaces in a vertical column may arise cannot be simulated. In fact, since our aim in this thesis is to only make use of the RANS model in regions where the physics is complicated i.e. where typical long wave models are insufficient, it is not a desirable solution. However, other methods must model the free surface indirectly which can be complicated and less accurate under simple conditions.

Indeed, the original focus of our pressure-velocity coupling solution method, SMAC (original is Marker and Cell (MAC) (Harlow and Welch, 1965)) was its novel approach to modelling the free surface. It uses markers placed on the free surface and in the fluid, then follows their Lagrangian motion with the velocities calculated on the Eulerian grid. Since the method simply moves markers arbitrarily anywhere it places no limit on the number of free surfaces in a vertical column like the height function approach. Drawbacks of this method include a large

computational memory required to store all the markers (requires many more markers than cells to work well), a long computational time to compute their movements, and can perform poorly in regions of converging/diverging flows. It was about 15 years later that another method known as the Volume-of-Fluid (VOF) method (Hirt and Nichols, 1981) came into existence for modelling the free surface on Eulerian grids. As its name suggests it tracks the movement of fluid volumes or rather volume fractions that can be used to describe the free surface. Since it only tracks a single volume fraction in each cell it has much lower memory requirements and computational costs than the MAC approach. Furthermore, the volume fraction is a continuous function while markers are discrete and therefore only have finite accuracy based on the density of the markers. Given these benefits of the VOF method, it is now ubiquitous in free surface modelling on Eulerian grids except where the height function is physically acceptable.

The VOF method fits with our requirements to model wave overturning and other three-dimensional effects on the free surface and it is adopted in this study. As mentioned, it tracks volume fractions in the computational cells to describe the free surface. The volume fraction, F is defined as:

$$F = \frac{V_{fluid}}{\Delta x \Delta y \Delta z} \tag{3.66}$$

where V_{fluid} is the volume of fluid in a computational cell. A straightforward visualization of how the distribution of F can be used to describe the free surface is illustrated in Figure 3.11.

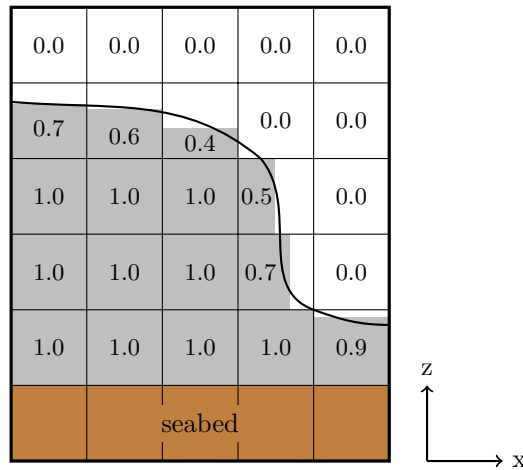


Figure 3.11: Illustration of fluid volume fractions (shown by the numbers) used to describe the free surface (drawn by the black line) which is of bore-like behaviour in this figure

Constructing Free Surface and Cell Flagging

As shown in Figure 3.11 the distribution of F may be used to construct the free surface, however it is not entirely obvious initially how it should actually appear. For example, in both the second cell from the top on the left and the second cell from the right and third up from the bottom, $F = 0.7$.

However, the orientations of F differ. The numerical code therefore requires some algorithm to determine which cells are indeed free surfaces and what is their orientation. The cells are appropriately flagged to indicate their status. Additionally the flagging of full fluid cells ($F = 1$), air cells ($F = 0$), and boundary cells is conducted. The flagged integers in the numerical code are as follows:

$$\begin{aligned}
 NF = -1 & \quad \text{boundary cell} \\
 NF = 0 & \quad \text{air cell} \\
 NF = 1 & \quad \text{fluid cell} \\
 NF = 2 & \quad \text{surface cell} \\
 \Rightarrow NFB = i & \quad \text{orientation of surface cell}
 \end{aligned} \tag{3.67}$$

where i is an integer corresponding to the direction of the inward normal vector to the surface. For example, the top left fluid cell in Figure 3.11 would have $NFB = -3$ since the inward normal vector points downwards in the z direction.

The algorithm that is used to determine the status of each computational cell and the allocation of the flags, NF and NFB is as follows:

1. Boundary cells never change and may be flagged at the start of the program to be $NF = -1$
2. For the computational cells, the status may change at each time step. The algorithm begins by dividing between air cells, $F \leq 1 \times 10^{-10}$ and fluid cells, $F > 1 \times 10^{-10}$, allocating $NF = 0$ and $NF = 1$ respectively
3. For those cells where $NF = 1$, if there is an adjacent cell where $NF = 0$, then they may be flagged as surface cells, $NF = 2$
4. For cells where $NF = 2$, if they do not have an adjacent cell where $NF = 1$ or $NF = -1$, they are reclassified as air cells, i.e. $NF = 0$, since the model cannot perform calculations for detached fluid of only a single cell size
5. For cells where $NF = 2$, if they are not sandwiched between both a $NF = 1$ or $NF = -1$, and a $NF = 0$ cell they are reclassified as air cells, i.e. $NF = 0$
6. Repeat Steps 3 to 5 until no reclassification of $NF = 2$ cells to $NF = 0$ cells occur
7. The orientation for the surface cells may now be determined by the direction in which it is sandwiched between a fluid cell and an air cell, or alternatively by a boundary cell and an air cell. For example, the top left surface cell in Figure 3.11 has $NFB = -3$ since there is a fluid cell below it and an air cell above it (in the z direction). For those cells at the bore face, there is a fluid cell to the left and an air cell to the right indicating $NFB = -1$. Additionally, for the bottom right surface cell, it is flanked by a boundary cell below and an air cell above therefore $NFB = -3$

8. In the case where the sandwiching occurs in more than one direction then priority is given to the direction that contains more fluid in behind it

The original example in Figure 3.11 would end up with the following flags as illustrated in Figure 3.12.

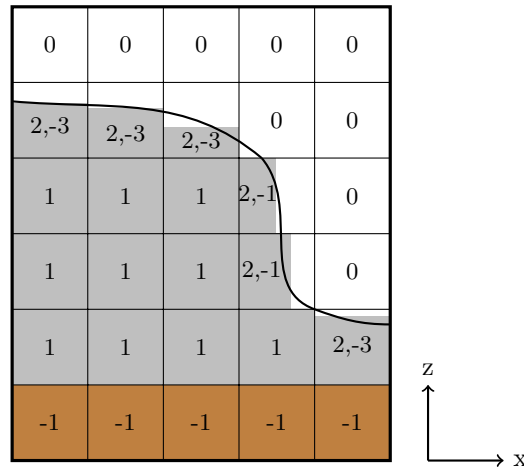


Figure 3.12: Illustration of the cell flags NF used to indicate their status and construct the free surface correctly. The surface orientation, NFB is also included for free surface cells (where $NF = 2$)

Free Surface Normal

Although the free surface may be constructed by the method outlined in the previous section, it is a crude discrete description, where the normal vector to the free surface is assumed to be entirely parallel to its axis of orientation. The construction can be improved by assuming a planar free surface so that the free surface normal vector can point in any direction. This improvement can help to track the fluid volume fraction more accurately as described in the following section. Note that the discrete flagged orientation NFB integers are still useful when constructing our boundary conditions (c.f. §3.4.7) on the free surface so the improvement described here does not replace NFB and the algorithm used to determine it - in fact, it makes use of it. The free surface unit normal vector, \vec{n} can be determined by the following:

$$\vec{n} = -\frac{\nabla F}{\|\nabla F\|} \quad (3.68)$$

Discretization of Eqn. (3.68) requires averaging of the F value at the corners of the cells. Another approach though is to find \vec{n} by geometric means which could be considered to give a result closer to the exact solution and thus it is adopted in this model. Since NFB can be obtained from the algorithm described in the previous section then the main orientation of \vec{n} is already

known *a posteriori*. For example, imagine a free surface cell where $NFB = -3$. It is thus already known that above it is an air cell where $F = 0$ and below is a fluid cell where $F = 1$. Therefore, the gradient of F that is important is only in the x and y directions. Suppose that the location of the centre of gravity of the free surfaces, η^{cg} in each cell is known (calculated from the value of F and the previous estimate of the normal vector as described in following section) and we want to find \vec{n} at cell, c as illustrated in Figure 3.13.

It can be assumed that the free surface in the adjacent cells is nearby cell c so the cells directly across (e and w) are searched to find η^{cg} . In the case that there is no free surface (e.g. cell e in Figure 3.13) then one cell above and below e and w are also searched. The same process is performed in the $y-z$ plane for cells n and s . The vectors pointing from η_c^{cg} to neighbouring η^{cg} points are calculated by (c.f. Figure 3.13):

$$\vec{CE} = \eta_{be}^{cg} - \eta_c^{cg} \quad (3.69)$$

$$\vec{CW} = \eta_w^{cg} - \eta_c^{cg} \quad (3.70)$$

$$\vec{CN} = \eta_n^{cg} - \eta_c^{cg} \quad (3.71)$$

$$\vec{CS} = \eta_s^{cg} - \eta_c^{cg} \quad (3.72)$$

To get the outward pointing free surface normal vector, \vec{n}_{temp} cross-products of the vectors is performed clockwise about cell c in both x and y directions as shown in Figure 3.13. This can be expressed as:

$$\vec{n}_{temp} = (\vec{CE} \times \vec{CN} + \vec{CN} \times \vec{CW} + \vec{CW} \times \vec{CS} + \vec{CS} \times \vec{CE})/4 \quad (3.73)$$

Finally, \vec{n}_c the unit free surface normal at cell c is equal to:

$$\vec{n}_c = \frac{\vec{n}_{temp}}{\|\vec{n}_{temp}\|} \quad (3.74)$$

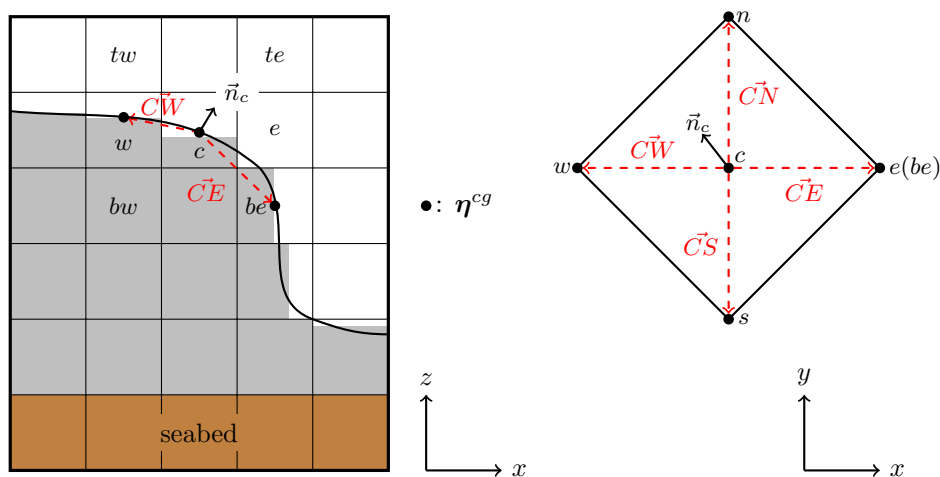


Figure 3.13: Illustration of the centre of gravity of the free surfaces and the vectors between the adjacent cells used to find the free surface normal vector at cell c , \vec{n}_c

Note that when the free surface normal at cell, be is calculated, since $NFB = -1$, the x direction of F is unimportant and the vectors between the centre of gravity of the free surfaces in the y and z directions are found instead. The improved reconstruction of the free surface in our example with free surface normal vectors that may point in any direction ends up like that illustrated in Figure 3.14.

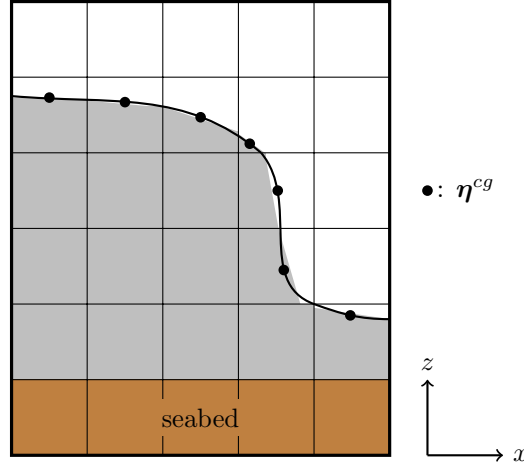


Figure 3.14: Illustration of the reconstructed free surface using an arbitrary free surface normal

Notice that the cell second from the top right now has fluid volume inside and it is completely triangular shaped (rather than a trapezium like the other cells) connecting the upwards orientated free surface and the rightwards orientated free surface cells. However, it is actually classified as an air cell since it is not flanked by both a full fluid cell, $NF = 1$ and a $NF = 0$ cell in any single direction. Thus, a special countermeasure is required in the model to get the free surface normal of air cells where F is larger than some trivially small value (e.g. when $F > 0.02$) such as this case. This helps to improve the tracking of the fluid volume fraction and the construction of free surface as shown in Figure 3.14. Additionally, the same countermeasure can be used to get the free surface normal of fluid cells, $NF = 1$ where F is non-trivially smaller than 1 (e.g. $F < 0.98$). Since $NF \neq 2$, NFB is not available. Thus, after \vec{n} is found in all $NF = 2$ cells, \vec{n} can be found by averaging the surface normal of the surrounding cells where $NF = 2$. For example, in this case referring to Figure 3.13:

$$\vec{n}_e = \frac{(\vec{n}_c + \vec{n}_{be} + \vec{n}_n + \vec{n}_s)/4}{\|(\vec{n}_c + \vec{n}_{be} + \vec{n}_n + \vec{n}_s)/4\|} \quad (3.75)$$

If no surrounding cells have $NF = 2$ then the cell must be a lone air cell or fluid cell and calculation of the surface normal is unnecessary.

Evaluating the Plane Equation of the Free Surface

Using the calculated value of \vec{n} , the plane equation of the free surface can be solved so that the volume fluid in the cell defined by the plane gives the correct value of F . Additionally for added

complexity, in this model the FAVOR method is used to describe the fractional volume of an object within a computational cell. It is possible that the free surface plane cuts through the object represented as a fraction of the cell, as illustrated in Figure 3.15. The current model can properly account for this occurrence to get the plane equation considering the presence of the object and hence we consider this to be an “improved” FAVOR method.

The solution to the plane equation considering the presence of an object can be found by a trial and error method where the volume of fluid is checked at each iteration to see whether it matches the required value F . The volume may be checked by geometrical methods however this thesis will not go into those details. Rather the iteration method co-introduced by the author (along with Nozomu Yoneyama and Yutaka Tanaka) will be described. The plane equation is given by:

$$\vec{n} \cdot \mathbf{p} = d \quad (3.76)$$

where \mathbf{p} is an arbitrary point on the plane, and d is the free parameter to be solved. The first initial guesses for d are found by substituting in the known vertices of the cell and object, which are plotted as points \mathbf{p}_1 to \mathbf{p}_4 in Figure 3.16. In this example the plane through \mathbf{p}_4 does not give a solution in the computational cell and is disregarded. While \mathbf{p}_2 gives a solution in the computational cell but with zero fluid volume since it only crosses through the object. \mathbf{p}_1 and \mathbf{p}_3 however do give solutions of some finite fluid volume indicated by the dashed lines through those points (with some slope given by \vec{n} of the free surface. The volume fraction is calculated from those initial guesses, F_{guess} and compared to the actual value of F , i.e.:

$$\epsilon^F = F_{guess} - F \quad (3.77)$$

ϵ^F is the error of the guess compared with the real F value. Clearly \mathbf{p}_1 gives the smallest value of positive ϵ^F and it is assigned as the initial “positive” solution, d_{pos} . The solution of \mathbf{p}_2 is assigned as the initial “negative” solution, d_{neg} that gives $\epsilon^F = -F$ since $F_{guess} = 0$. From here the double-false position algorithm may be used to iteratively approach the true solution. In this algorithm a new guess, d_{sec} calculated using the secant method is found at each iteration using

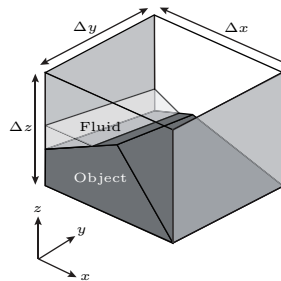


Figure 3.15: Illustration of both an object and fluid within a computational cell which may be accounted for by the improved FAVOR method used in this study

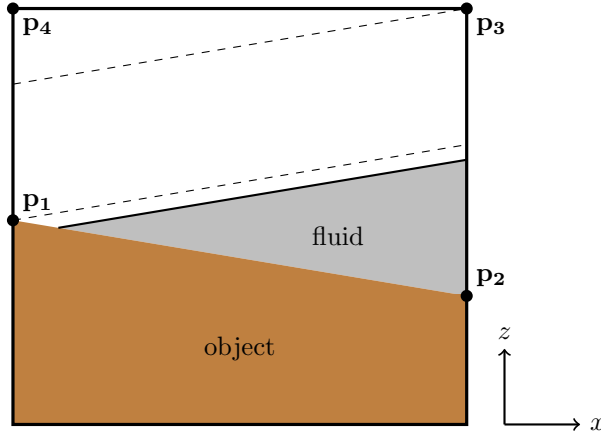


Figure 3.16: Illustration of the fluid surface cutting through the object. The bold line indicates the actual free surface plane to be solved and the dashed lines indicates the initial guesses

the equation:

$$d_{sec} = d_{pos} - \epsilon_{pos}^F \frac{d_{pos} - d_{neg}}{\epsilon_{pos}^F - \epsilon_{neg}^F} \quad (3.78)$$

d_{sec} is used to get a new estimated of ϵ^F . In the case that the new ϵ^F is negative, d_{sec} becomes the new d_{neg} . Similarly, if ϵ^F is positive d_{sec} becomes the new d_{pos} . The iterations for a new d_{sec} in Eqn. (3.78) and hence new d_{neg} or d_{pos} is repeated until ϵ^F becomes small enough within desired accuracy that is currently set to 1×10^{-9} in this model. A caveat of the double-false position method is that it is possible that at consecutive iterations only one side (positive or negative solution) is updated implying only linear (slow) convergence of the width of the solution bracket. Ideally at consecutive iterations one of each of the positive and negative solutions should be updated for faster convergence. To force this to happen, when the same side is updated consecutively the new value of ϵ_{pos}^F or ϵ_{neg}^F is multiplied by 0.5. This is known as the Illinois algorithm (Dowell and Jarratt, 1971) which guarantees faster convergence than the unmodified double-false position method.

Once d in the plane equation has been found it can be used to determine the vertices of the free surface that intersect with the cell and object boundaries. The centre of gravity (centroid) of the free surface, $\boldsymbol{\eta}^{cg}$ is thus given by:

$$\boldsymbol{\eta}^{cg} = \frac{\sum_{k=1}^{n-2} (\mathbf{p}_1 + \mathbf{p}_{k+1} + \mathbf{p}_{k+2}) \|\mathbf{p}_{k+1} - \mathbf{p}_1\| \times \|\mathbf{p}_{k+2} - \mathbf{p}_1\|}{3 \sum_{k=1}^{n-2} \|\mathbf{p}_{k+1} - \mathbf{p}_1\| \times \|\mathbf{p}_{k+2} - \mathbf{p}_1\|} \quad (3.79)$$

where \mathbf{p}_k is the k^{th} vertex of the fluid volume in the cell with total number of vertices n .

Tracking the Fluid Volume Fraction

Tracking the evolution of the fluid volume fraction is achieved through discretization of the following equation:

$$\frac{\partial \gamma^v F}{\partial t} + \frac{\partial \gamma_i^a F u_i}{\partial x_i} = 0 \quad (3.80)$$

It is equivalent to stating that the material derivative of F is equal to zero which is true for any quantity on the free surface. Eqn. (3.80) is simple, but a straightforward finite-difference form would lead to the smearing of the F function (Hirt and Nichols, 1981) despite the fact that F should give a sharp interface and is bounded between 0 and 1. In the case that free surface normals may only be parallel to the axes a common method is the donor-acceptor one to discretize Eqn. (3.80). It introduces flux limiters to ensure the the correct advection of F across cells to preserve the sharp interface. In this model, the arbitrary free surface normal is available which can be used to advect the F fraction in a precise manner. This method is known as Piecewise Linear Interface Calculation (PLIC) (Youngs, 1982). For example, imagine that we know all values of F and \vec{n} at time n . We now want to find the new F value in cell c , F_c^{n+1} (c.f. Figure 3.17) after getting the Solenoidal velocities, u_i^{n+1} as described in §3.4.3.

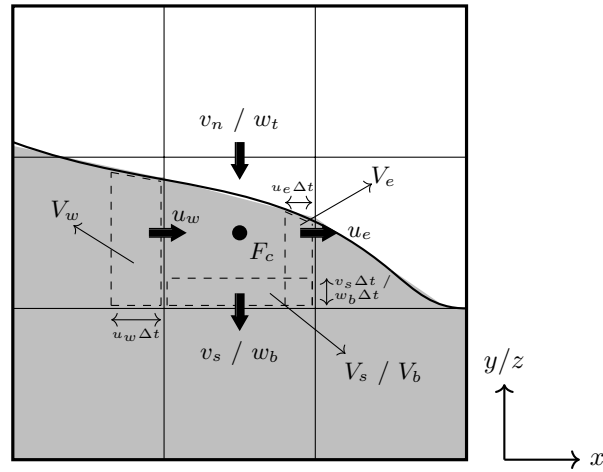


Figure 3.17: Illustration of the fluxes on the boundary to cell c that are calculated using the PLIC method when updating F_c

If the fluxes at every cell boundary are correctly calculated, Eqn. (3.80) can be discretized as follows:

$$F_c^{n+1} = F_c^n - \frac{\Delta t}{\gamma_c^v} \left(\frac{\gamma_{xe}^a (UF)_e - \gamma_{xw}^a (UF)_w}{\Delta x_c} + \frac{\gamma_{yn}^a (VF)_n - \gamma_{ys}^a (VF)_s}{\Delta y_c} + \frac{\gamma_{zt}^a (WF)_t - \gamma_{zb}^a (WF)_b}{\Delta z_c} \right) \quad (3.81)$$

where (UF) , (VF) and (WF) are the fluxes at the cell boundaries that are determined by the PLIC method from the new velocities, u_i^{n+1} and previous values of the volume fraction, F^n and surface normal, \vec{n}^n (to get the plane equation of the free surface). The calculation of the fluxes

is illustrated in Figure 3.17. Firstly, similar to the donor-acceptor method, the upwind value of F is used. Secondly, the volume of fluid in the upwind cell, V that has width in the direction of the velocity normal to the boundary equal to $u_i \Delta t$ is determined by geometric methods given the known plane equation of the surface. Clearly if the slope of the free surface is considerable this volume will be different to V calculated by the traditional donor-acceptor method. Lastly, the flux (e.g. $(UF)_w$) is found by:

$$(UF)_w = \text{sign}(u_w) \frac{V_w}{\gamma_{xw}^a \Delta y_c \Delta z_c \Delta t} \quad (3.82)$$

3.4.5 Turbulence Model

The eddy viscosity approach has been assumed in the current RANS model. As mentioned in §3.4.1 the challenge now becomes one to model the eddy viscosity. Recall that the turbulent kinetic energy, $k (\equiv \frac{1}{2} \overline{u'_i u'_i})$ was introduced in §3.4.1. Therefore, the transport of this energy must also be important to determine the eddy viscosity. The transport equation for k can be found by subtracting the RANS equations from the N-S equations to obtain an equation for u'_i . Multiplying this by u'_i , averaging and simplifying gives:

$$\frac{\partial k}{\partial t} + u_j \frac{\partial k}{\partial x_j} = \frac{\partial}{\partial x_j} \left[\left(\nu + \frac{\nu_t}{\sigma_k} \right) \frac{\partial k}{\partial x_j} \right] - \overline{u'_i u'_j} \frac{\partial u_i}{\partial x_j} - \epsilon \quad (3.83)$$

where σ_k is the turbulent Prandtl number which correlates the turbulent momentum diffusivity to heat diffusivity. Note, that the gradient of k is assumed to approximate the turbulent diffusion. The turbulent kinetic energy dissipation rate, ϵ has also been introduced defined by:

$$\epsilon \equiv \nu \overline{\frac{\partial u'_i}{\partial x_j} \frac{\partial u'_i}{\partial x_j}} \quad (3.84)$$

Since ϵ is also a scalar that varies with time and space like k , an extra consideration or equation is required to close the system. Firstly, consider the relative length scales of the turbulence, l : $\nu_t \propto k^{1/2} l$ and $\epsilon \propto k^{3/2} / l$. If l is known *a priori* then the system can be closed by setting, $\nu_t = C_\mu^{1/4} k^{1/2} l$ and, $\epsilon = C_\mu^{3/4} k^{3/2} / l$ (Cox et al., 1994) in Eqn. (3.83), where C_μ is some empirical constant. However, it is usually non-trivial to evaluate l in real applications so another approach is typically required. The above expressions can also be arranged to eliminate the dependence on l , which give, $\nu_t \propto k^2 / \epsilon$. The combination of these two parameters is reasonable since it can be expected that the turbulent energy and its dissipation rate is related. The relationship may be more formally defined as:

$$\nu_t = C_\mu k^2 / \epsilon \quad (3.85)$$

If an extra transport equation is introduced for ϵ then the system will close since ν_t can be found from just k and ϵ in Eqn. (3.85), the only two turbulent scaling parameters. This approach is known as a two-equation model. Specifically it is the standard $k - \epsilon$ model first introduced by Launder and Spalding (1974). Where standard refers to its application to high Reynolds numbers

and the linear constant relationship between ν_t , k and ϵ . The transport equation for ϵ can be written as:

$$\frac{\partial \epsilon}{\partial t} + u_j \frac{\partial \epsilon}{\partial x_j} = \frac{\partial}{\partial x_j} \left[\left(\nu + \frac{\nu_t}{\sigma_\epsilon} \right) \frac{\partial \epsilon}{\partial x_j} \right] - C_{\epsilon 1} \frac{\epsilon}{k} \overline{u'_i u'_j} \frac{\partial u_i}{\partial x_j} - C_{\epsilon 2} \frac{\epsilon^2}{k} \quad (3.86)$$

where σ_ϵ , $C_{\epsilon 1}$ and $C_{\epsilon 2}$ are extra constants to be determined empirically. A total of five constants appear in the standard $k - \epsilon$ model (Eqns. (3.83), (3.85) and (3.86)). After a number of extensive investigations based on plane jets and mixing layers Launder and Spalding (1974) has suggested that those constants should be equal to:

$$C_\mu = 0.09 \quad C_{\epsilon 1} = 1.44 \quad C_{\epsilon 2} = 1.92 \quad \sigma_k = 1.0 \quad \sigma_\epsilon = 1.3 \quad (3.87)$$

Note that σ_k , the turbulent Prandtl number, can be approximated as 1 through Reynolds analogy. The values of these constants are however based on steady flow. For example, Cox et al. (1994) has shown that C_μ should vary for spilling waves in the cross-shore and vertical directions. C_μ was found to be generally less than 0.09 over the entire domain, with $C_\mu \approx 0.03$ in the transition zone and $C_\mu \approx 0.05$ in the inner surf zone. Hence, care must be taken when applying such theoretical turbulent models. This thesis does however, due to limited alternative knowledge apply the constants of Launder and Spalding (1974) shown here.

Governing Equations

The governing equations of the $k - \epsilon$ model with the addition of the fractional volume parameters and the introduction of a turbulent production term, $P_k \left(\equiv -\overline{u'_i u'_j} \frac{\partial u_i}{\partial x_j} \right)$, the equations become:

$$\frac{\partial k}{\partial t} + \frac{1}{\gamma^v} \frac{\partial(\gamma_j^\alpha u_j k)}{\partial x_j} = \frac{1}{\gamma^v} \frac{\partial}{\partial x_j} \left[\gamma_j^\alpha \left(\nu + \frac{\nu_t}{\sigma_k} \right) \frac{\partial k}{\partial x_j} \right] + P_k - \epsilon \quad (3.88)$$

$$\frac{\partial \epsilon}{\partial t} + \frac{1}{\gamma^v} \frac{\partial(\gamma_j^\alpha u_j \epsilon)}{\partial x_j} = \frac{1}{\gamma^v} \frac{\partial}{\partial x_j} \left[\gamma_j^\alpha \left(\nu + \frac{\nu_t}{\sigma_\epsilon} \right) \frac{\partial \epsilon}{\partial x_j} \right] + C_{\epsilon 1} \frac{\epsilon}{k} P_k - C_{\epsilon 2} \frac{\epsilon^2}{k} \quad (3.89)$$

where P_k is equal to:

$$P_k = 2\nu_t S^2 \quad (3.90)$$

where $S^2 \equiv S_{ij} S_{ij}$ and S_{ij} is the mean strain rate tensor:

$$S_{ij} = \frac{1}{2} \left(\frac{\partial u_i}{\partial x_j} + \frac{\partial u_j}{\partial x_i} \right) \quad (3.91)$$

The relationship, $\nu_t = C_\mu k^2 / \epsilon$ and the constants introduced in the previous section remain the same.

Discretization and Solution Scheme

The $k - \epsilon$ model is discretized onto the same staggered grid used for continuity and momentum, which is illustrated in Figure 3.10. The scalars k , ν_t and ϵ are defined on cell centres. Once the

new Solenoidal velocities, u_i^{n+1} are found by the SMAC solution scheme new values of k , ϵ and hence v_t are updated from the old ones using a first-order explicit Euler forward-difference. This firstly requires an estimate of the turbulent production term, P_k using v_t^n and u_i^{n+1} :

$$P_{kc} = v_{tc}^n \left[\left(\frac{\partial u}{\partial z} + \frac{\partial w}{\partial x} \right)^2 + \left(\frac{\partial u}{\partial y} + \frac{\partial v}{\partial x} \right)^2 + \left(\frac{\partial v}{\partial z} + \frac{\partial w}{\partial y} \right)^2 + 2 \left(\frac{\partial u^2}{\partial x} + \frac{\partial v^2}{\partial y} + \frac{\partial w^2}{\partial z} \right) \right]_c^{n+1} \quad (3.92)$$

where the derivatives can be easily found from central differences about the cell centre, c , which are explicitly shown in Appendix B.

After finding P_k , the transport equations for k and ϵ are solved. Eqn. (3.88) for k and Eqn. (3.89) for ϵ are solved through the following operations:

$$k_c^{n+1} = k_c^n - \frac{\Delta t}{\gamma_c^v} [(ADV_k)_c - (DIFF_k)_c] + \Delta t (P_{ck} - \epsilon_c^n) \quad (3.93)$$

$$\epsilon_c^{n+1} = \epsilon_c^n - \frac{\Delta t}{\gamma_c^v} [(ADV_\epsilon)_c - (DIFF_\epsilon)_c] + \Delta t \left(C_{\epsilon 1} \frac{\epsilon_c^n}{k_c^n} P_{ck} - C_{\epsilon 2} \frac{(\epsilon_c^n)^2}{k_c^n} \right) \quad (3.94)$$

where ADV_ϕ is the advection and $DIFF_\phi$ is the diffusion of some scalar ϕ (either k or ϵ). In Eqns. (3.88) and (3.89), ADV_ϕ corresponds to the last term on the right of the LHS, and $DIFF_\phi$ the first term on the left of the RHS. ADV_ϕ is discretized using a second-order Total Variation Diminishing (TVD) upwind difference (c.f. Versteeg and Malalasekera, 2007):

$$(ADV_\phi)_c = \frac{\gamma_{xc}^a u_c^{n+1} \Phi_c - \gamma_{xw}^a u_w^{n+1} \Phi_w}{\Delta x_c} + \frac{\gamma_{yn}^a v_n^{n+1} \Phi_n - \gamma_{ys}^a v_s^{n+1} \Phi_s}{\Delta y_c} + \frac{\gamma_{zt}^a w_t^{n+1} \Phi_t - \gamma_{zb}^a w_b^{n+1} \Phi_b}{\Delta z_c} \quad (3.95)$$

in which Φ_c is the value of ϕ interpolated onto the east cell boundary (where u_c^{n+1} is defined - see Figure 3.10) in an upwind TVD sense. Φ_w is the value of ϕ interpolated onto the west cell boundary, and so on. For example, Φ_c is found by:

$$\begin{cases} \Phi_c = \phi_c + \frac{\Delta x_c}{\Delta x_e + \Delta x_c} L(r+) (\phi_e - \phi_c) & \text{if } u_c^{n+1} \geq 0 \\ \Phi_c = \phi_e + \frac{\Delta x_c}{\Delta x_e + \Delta x_c} L(r-) (\phi_c - \phi_e) & \text{if } u_c^{n+1} < 0 \end{cases} \quad (3.96)$$

$L(r)$ is an appropriate TVD limiter function with

$$r+ = \frac{\phi_c - \phi_w}{\phi_e - \phi_c} \frac{\Delta x_c + \Delta x_e}{\Delta x_c + \Delta x_w} \quad (3.97)$$

$$r- = \frac{\phi_E - \phi_e}{\phi_e - \phi_c} \frac{\Delta x_e + \Delta x_c}{\Delta x_E + \Delta x_e} \quad (3.98)$$

In the current model the Van Leer limiter function (van Leer, 1974) is adopted:

$$L(r) = \frac{r + |r|}{1 + r} \quad (3.99)$$

The other values of Φ on the remaining cell boundaries may be found in a similar manner. Finally, $DIFF_\phi$ is discretized using a straightforward second-order central difference (which is explicitly written in Appendix B):

$$(DIFF_\phi)_c = \left(\frac{\partial}{\partial x} \left[\gamma_x^\alpha \left(v + \frac{v_t}{\sigma_\phi} \right) \frac{\partial \phi}{\partial x} \right] \right)_c + \left(\frac{\partial}{\partial y} \left[\gamma_y^\alpha \left(v + \frac{v_t}{\sigma_\phi} \right) \frac{\partial \phi}{\partial y} \right] \right)_c + \left(\frac{\partial}{\partial z} \left[\gamma_z^\alpha \left(v + \frac{v_t}{\sigma_\phi} \right) \frac{\partial \phi}{\partial z} \right] \right)_c \quad (3.100)$$

Note that σ_ϕ here refers to either constants, σ_k or σ_ϵ . Once k^{n+1} and ϵ^{n+1} have been found, v_t^{n+1} is evaluated through the following operation:

$$v_t^{n+1} = C_\mu \frac{(k^{n+1})^2}{\epsilon^{n+1}} \quad (3.101)$$

3.4.6 Temporal Stability

The current model is based upon explicit differencing in the momentum equation, turbulent transport equations and the advection of F . Because of this the stability is mainly controlled by the Courant-Friedrichs-Lewy (CFL) condition which states that the fluid cannot travel more than one fluid cell in a time step, i.e.:

$$Cr_f = \max \left(\frac{u_i \Delta t}{\Delta x_i} \right) < 1 \quad (3.102)$$

the “max” condition indicates the maximum value in the computational domain over all the dimensions ($i = 1, 2, 3$). Cr_f is the Courant number based on the fluid velocity. Furthermore, a Courant number should also be defined based on the wave speed so that the wave will not travel more than one fluid cell in a time step:

$$Cr_w = \max \left(\frac{\sqrt{gh} \Delta t}{\Delta x_i} \right) < 1 \quad (3.103)$$

here the dimensions are limited to the horizontal ones ($i = 1, 2$). It has been found that the CFL condition based on the wave speed does not need to be as restrictive as that based on the fluid velocity. So within the numerical code a multiple $\alpha_c > 1$ is introduced so that an overall Courant number, Cr can be defined by:

$$Cr = \max [\alpha_c Cr_f, Cr_w] < 1 \quad (3.104)$$

$\alpha_c > 3.33$ has been set in the computational code at present following Bakhtyar et al. (2009). The value of this constant should depend on the temporal integration and the advection discretization scheme so it may be defined larger or smaller than this (a detailed investigation of an optimum value for the current model has not been conducted). Usually Cr is restricted to less than 0.33 for extra stability. This implies that Cr_f is in fact restricted to less than 0.10. Such a condition has been found to be necessary for stability upon violent processes such as wave breaking. Fortunately, Cr_f is generally small for a wave offshore where Cr_w dominates. Hence, during wave propagation and shoaling larger time steps are used in the model which gradually transition to the smaller time steps required during wave breaking where the flow becomes momentum-driven.

Although the flows here are generally advection dominated (rather than diffusion dominated) for completeness the Von Neumann stability condition for diffusion is included:

$$Cr_d = \max \left(\frac{2(v + v_t) \Delta x_i \Delta x_i \Delta x_i \Delta x_i \Delta t}{(\Delta x_1)^2 (\Delta x_2)^2 (\Delta x_3)^2} \right) < 1 \quad (3.105)$$

where Cr_d is the dimensionless stability number for diffusion and must be less than unity. Note that if v_t is large due to a very turbulent flow, Cr_d may also become non-trivial. On that note,

a final stability condition for the turbulent quantities, k and ϵ are required. The ratio k/ϵ is equivalent to a turbulent time scale, which represents the time scale that the eddies decay (the eddy turnover time). The time step should be smaller than this time scale for stability of the $k - \epsilon$ model. Also, in the ϵ equation the term $C_{\epsilon 2}\epsilon^2/k$ represents the destruction of ϵ based on the turbulent time scale. Hence if $C_{\epsilon 2} > 1$, ϵ will actually be destroyed faster than k and this constant should also be included in the stability condition:

$$Cr_t = \max\left(\frac{\max[C_{\epsilon 2}, 1.0]\epsilon\Delta t}{k}\right) < 1 \quad (3.106)$$

where Cr_t is the dimensionless stability number for the turbulence quantities and must be less than unity.

An overall stability condition a hence the determination of a suitable Δt is possible by finding the maximum value of Cr , Cr_d , and Cr_t . Usually the limit of this value is set to 0.33 as discussed for Cr above. Δt is allowed to vary with each time step in order to satisfy the stability criterion and to maximise computational efficiency.

3.4.7 Boundary Conditions

In all the previous discussion on the SMAC solution scheme, VOF free surface modelling, and $k - \epsilon$ turbulence modelling, the boundary conditions that need to be applied for each method have been ignored. This is partly because boundary conditions for one method are often slightly connected with other methods so it makes the discussion easier to include everything already introduced into a single section. This section is split into free surface boundary conditions, and boundary conditions with object cells ($NF = -1$). Boundary conditions are required for the Poisson Pressure equation, velocities, pressure and the turbulent quantities. It is worth mentioning that the lateral boundary conditions in this study are provided by the two-way multiscale coupling procedure described in §3.5.

Free Surface Boundary Conditions

(i) Poisson Pressure Equation

Continuity can only be applied through the Poisson Pressure equation onto full fluid cells ($NF = 1$). But, the pressure on free surface cell centres is found by linear interpolation/extrapolation between the pressure on the adjacent fluid cell centre (in the direction of NFB) and the pressure on the surface as illustrated in Figure 3.18 for the case where $NFB = -3$.

The interpolation/extrapolation can be achieved in the Poisson Pressure equation in order to get the change in pressure at a free surface cell, Δp_c based on the change in the fluid cell, Δp_b through the following:

$$A_c\Delta p_c + \Delta p_b = 0 \quad (3.107)$$

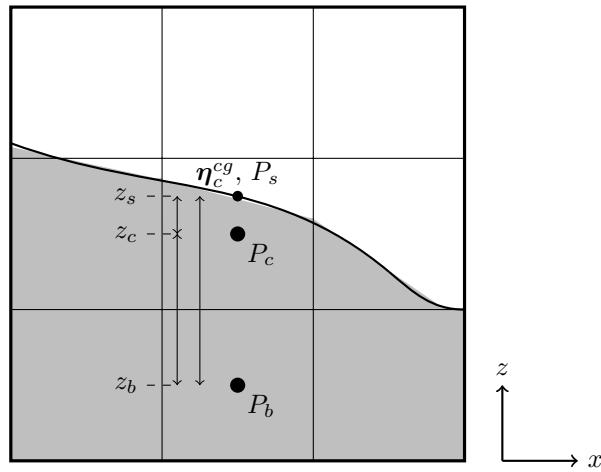


Figure 3.18: Linear interpolation/extrapolation of the pressure from the fluid cell to the centre of the surface cell. The case where $NFB = -3$ is drawn.

with,

$$A_c = -\frac{z_s - z_b}{z_s - z_c} \quad (3.108)$$

and z_s is the z coordinate of the centre of gravity of the free surface, η_c^{cg} . A_c can be constructed in a similar way by linear interpolation/extrapolation for different orientations of the free surface.

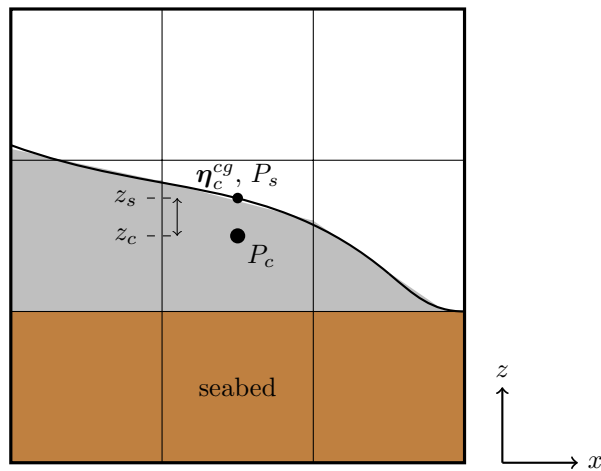


Figure 3.19: Pressure in a surface cell centre with $|NFB| = 3$ when it is directly above an object cell

(ii) Pressure

The pressure boundary condition at the free surface cell centre is not only required within the Poisson Pressure equation to get Δp . Additionally, the pressure at the free surface cell

centre should be interpolated/extrapolated directly before calculating u_i^* in the momentum equation, i.e (c.f. Figure 3.18):

$$P_c = P_b \frac{z_s - z_c}{z_s - z_b} + P_s \frac{z_c - z_b}{z_s - z_b} \quad (3.109)$$

where P_s is the pressure on the free surface. Including the viscous stresses on the free surface P_s is equal to:

$$P_s = 2\rho(\nu + \nu_t)(n_c)_i \frac{\partial u_i}{\partial x_i} \quad (3.110)$$

where $(n_c)_i$ is the i^{th} component of \vec{n}_c . Moreover, in the case of a free surface above an object cell, pressure is assumed hydrostatic as illustrated in Figure 3.19 (this is only available for $|NFB| = 3$ since it is orientated in the direction of gravity assumed to be the z axis):

$$P_c = P_s + g\rho(z_s - z_c) \quad (3.111)$$

(iii) Velocities

Velocities need to be evaluated at cell boundaries which separate a surface cell and an air cell for the finite-difference approximations. In order to get this velocity the tangential stress boundary condition is used. It states that the tangential stresses vanish at the free surface implying:

$$\frac{\partial u_i}{\partial n_j} (1 - \delta_{ij}) = 0 \quad (3.112)$$

where n_j is the major direction of the free surface normal. Within the model we make use of the value of NFB of the free surface cell to determine its orientation in order to apply zero gradient of the velocity in the tangential direction as required. Once the tangential velocities have been found, the remaining normal velocities can be evaluated from continuity. A problem example is illustrated in Figure 3.20.

For the free surfaces in Figure 3.20 lets say they all have $NFB = -3$. In this case the no gradient condition for the velocities tangential to the z direction is applied ($\frac{\partial u}{\partial z}, \frac{\partial v}{\partial z} = 0$), e.g.:

$$u_{wt} = u_w \quad u_e = u_{eb} \quad v_{st} = v_s \quad v_n = v_{nb} \quad (3.113)$$

Once the tangential stress condition has been applied, the remaining velocities normal to the z direction can be found from continuity, e.g:

$$w_t = w_b - \Delta z_c \left(\frac{u_e - u_w}{\Delta x_c} + \frac{v_n - v_s}{\Delta y_c} \right) \quad (3.114)$$

(iv) Turbulent Quantities

Values inside air cells adjacent to free surface cells are required for the finite-volume approximations of the transport equations for k and ϵ . In this study the no gradient condition is applied for ϵ while k is 80% of the value of the free surface, i.e.:

$$k_a = 0.8k_s \quad \epsilon_a = \epsilon_s \quad (3.115)$$

where a indicates the value of the turbulent quantity defined in the air cell and s is that in the free surface cell.

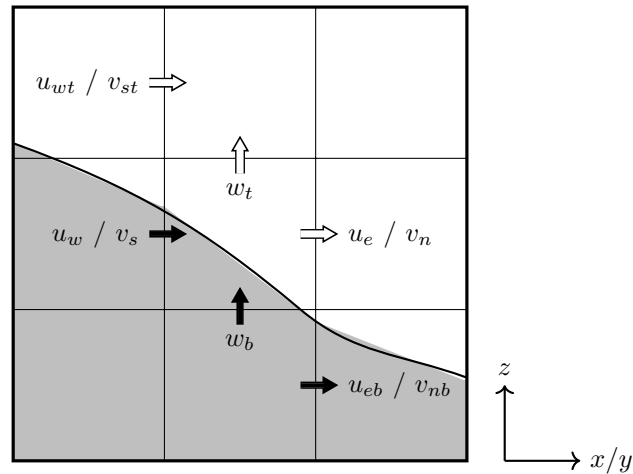


Figure 3.20: Velocities that need to be determined at the interface between fluid cells and air cells (shown by the white arrows) via the tangential stress boundary condition and continuity. Black arrows indicate velocities that are calculated normally through momentum and the Poisson Pressure equation

Boundary Conditions with Object Cells

(i) Poisson Pressure Equation

If an object cell, b is adjacent to the centre cell c where Δp_c is to be evaluated, then the coefficient, A_b is simply set to zero. This is equivalent to a no gradient condition of Δp across the cells.

(ii) Velocities

The normal velocities at the interface between a boundary cell and non-boundary cell are always zero since flow cannot pass through the boundary. Note, that since this is the case a condition for pressure on the boundary is not required because the pressure gradient term no longer appears in any of the equations here.

The boundary conditions for the tangential velocities may however be somewhat more complicated depending on the choice. The tangential velocity boundary conditions are important to correctly evaluate the viscous stresses arising from the influence of the boundary. We know that physically the no-slip boundary condition should be applied. Unfortunately however, in the sort of modelling performed in this thesis the cell size will be too coarse to capture the boundary layer. This means that the simple application of the no-slip boundary condition will instead introduce unphysical numerical viscosity onto the system. This is also a result of the staggering of the velocities which means that the velocity tangential to the boundary can never be defined explicitly on the boundary. Instead we should provide a velocity inside the boundary as a ghost cell for the finite-difference

as shown in Figure 3.21. The simplest method to avoid the problems associated with evaluating the shears stresses is to avoid calculating them, i.e. to just apply the inviscid slip boundary condition:

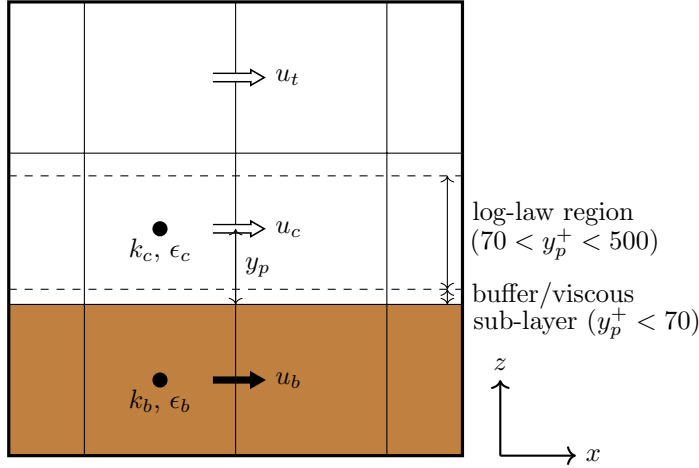


Figure 3.21: Velocity u_b tangential to and within the boundary, and the turbulent quantities, k_b and ϵ_b that may be applied as ghost cell values when evaluating the finite-difference approximation of the bed shear stress. However, if the wall function approximation is adopted, the shear stress on the boundary is directly calculated based on the value of u_c to get u_τ . Similarly, k_c and ϵ_c are directly inserted based on this calculation. The wall function approach assumes that u_c , k_c and ϵ_c fall within the log-law region

$$u_b = F_c u_c \quad (3.116)$$

where $F_c = 1$. As has been introduced in §2.1.2, an inviscid solution is often a fairly good approximation of surface waves in general so for the most part the slip condition is a reasonable one. However, in the surf zone, for breaking waves, runup and the like, the viscous effects on the seabed are likely to become more important. Note that setting, $F_c = -1$ in Eqn. (3.116) corresponds to the no-slip boundary condition since the interpolation of u_c and u_b will give zero tangential velocity on the boundary in this case. In fact, any value of, $-1 < F_c < 1$ can be applied to simulate some viscous boundary condition that may be calibrated with data for the specific problem at hand if it is available.

However, data is not often available, it is difficult to calibrate since it can depend on the cell resolution, and scientifically it is a lousy solution. To estimate the viscous stresses on the bed another approach is more attractive. Firstly, we rewrite the momentum equations in the following form:

$$\frac{\partial u_i}{\partial t} + u_j \frac{\partial u_i}{\partial x_j} = g_i - \frac{1}{\rho} \left(\frac{\partial p}{\partial x_i} + \frac{\partial \tau_{ij}}{\partial x_j} \right) \quad (3.117)$$

where the viscous stresses, τ_{ij} are equal to:

$$\tau_{ij} = \rho(\nu + \nu_t) \frac{\partial u_i}{\partial x_j} \quad (3.118)$$

To evaluate the viscous stress at the boundary, $\tau_{ij} \Big|_b \equiv \tau_{bi}$ the following equation may be used:

$$\tau_{bi} = \rho u_{\tau i}^2 \quad (3.119)$$

where $u_{\tau i}$ is the shear velocity (in the i direction which can only be perpendicular to the boundary). If the assumption is made that the velocity in the last cell at a distance, y_p from the boundary, u_c (see Figure 3.21) falls within the so called log-law region ($70 < y_p^+ = y_p/\delta_v < 500$ (Versteeg and Malalasekera, 2007; Schlichting and Gersten, 2000)), then it is possible to evaluate u_{τ} from u_c which can then be used to evaluate the bed shear stress on the boundary to insert into Eqn. (3.117). Note that the log-law is defined as:

$$u_c = \frac{u_{\tau}}{\kappa_v} \ln \frac{y_p}{y_k} \quad (3.120)$$

where $\kappa_v (= 0.41)$ is the von Kármán constant, and y_k is the roughness length that depends on the equivalent sand roughness of the bed, k_s . From Schlichting and Gersten (2000), y_k is equal to:

$$y_k = \begin{cases} \delta_v \exp(-5.0\kappa_v) & \text{if } 0 \geq k_s^+ \leq 5 \\ \delta_v \exp(-C^+(k_s^+)\kappa_v) & \text{if } 5 < k_s^+ < 70 \\ k_s \exp(-8.0\kappa_v) & \text{if } 70 \leq k_s^+ \end{cases} \quad (3.121)$$

where $y_p^+ = y_p/\delta_v$, $k_s^+ = k_s/\delta_v$, and $\delta_v = \nu/u_{\tau}$ is the wall layer thickness. The three sets of cases in Eqn. (3.121) are known as the hydraulically smooth, transition, and fully rough regions, top to bottom respectively. In the case of the transition region, the solution for some ‘‘constant’’ of integration, $C^+(k_s^+)$ which is a function of k_s^+ is however, not constant. Referring to Figure 17.8 in Schlichting and Gersten (2000), $C^+(k_s^+)$ is assumed to follow a linear relationship between $5 < k_s^+ < 70$ from 5.0 to -2.5 for use in this study. The log-law relationship is used to find $u_{\tau i}$, perhaps by iterative means in the case of the hydraulically smooth or transition region, which is then used to evaluate τ_{bi} and is directly inserted into the momentum equation at the seabed (or any other solid boundary).

(iii) Turbulent Quantities

Just like the velocities, in reality the turbulent quantities vary rapidly near the wall. However, in general our grids are too coarse to capture this variation hence a method is required to deal with this. Just like the case of the velocities, the simplest solution is to assume an inviscid slip condition at the bed. In this case a no gradient or a percentage gradient condition for the values of the turbulent quantities between computational cells and object cells is applied. For the most part it is not particularly important since within

the finite-volume discretization presented in Eqn. (3.93) and (3.94) γ_i^a will always be zero on the boundary between object cells and computational cells. It is possible however that the the second-order TVD limiter function will use the value specified in the ghost cell (object cell) so it is included for completeness, i.e. (c.f. Figure 3.21):

$$k_b = 0.8k_c \quad \epsilon_b = \epsilon_c \quad (3.122)$$

Similar to the free surface, k_b on the boundary is set to 80% of k_c .

Additionally, in the event a viscous solution is defined at the bed another approach is required. This is a wall function approach based on the same assumption in the momentum equations to get the bed stress. Strictly speaking the wall function approach requires that the near-bed tangential velocity is within the log-law region ($70 < y^+ < 500$), since it is based on measurements which show that the production and dissipation rate of the turbulent kinetic energy are approximately equal (Versteeg and Malalasekera, 2007; Schlichting and Gersten, 2000; Sondak, 1992) in this region:

$$P_k = \epsilon \quad (3.123)$$

Since the turbulent bed shear stress multiplied by the tangential velocity gradient is equal to P_k one can equate the values of k and ϵ at the near-bed cell centre to the turbulent bed shear stress. Furthermore, taking the log-law assumption (Eqn. (3.120)) it is possible to derive the equations for k_c and ϵ_c as (Sondak, 1992):

$$k_c = \frac{u_\tau^2}{\sqrt{C_\mu}} \quad (3.124)$$

$$\epsilon_c = \frac{u_\tau^3}{\kappa_\nu y_p} \quad (3.125)$$

where u_τ is found from u_c which in this case should be the vector sum of the tangential velocities.

3.4.8 Initial Conditions

Initial conditions include those for pressure, velocity and the turbulent quantities. In the majority of cases a still water solution is taken as an initial condition. Here the pressure is set to hydrostatic and the velocities are set to zero. In the case of a real tsunami simulation like that presented in Chapter 5, the free surface may be arbitrarily defined as an initial condition according to the instantaneous movement of the seabed. However, the pressure is still assumed hydrostatic and velocities are set to zero. Additionally, for the turbulent quantities it is necessary to “seed” the domain with initial non-zero values of k , ϵ , and v_t , as will be explained below.

Seeding of Turbulent Quantities

The seeding of the turbulent quantities, k , ϵ and ν_t is required since if there is no initial value of ν_t , turbulence can never be produced. Furthermore, the determination of ν_t relies on the division of k^2 by ϵ , hence if k or ϵ is equal to zero problems arise. The study of Lin and Liu (1998) is one of the seminal studies of breaking waves using the VOF method for free surface modelling and the $k - \epsilon$ turbulence closure scheme. They suggest that the initial value of k to be seeded should be equal to:

$$k = \frac{1}{2} u_t^2 \quad (3.126)$$

where $u_t = c\delta_0$ is some representative of the size of the fluctuations of the velocity about the mean. c is the wave speed which for long waves (tsunamis) can be estimated as \sqrt{gh} . The choice of δ_0 is arbitrary where Lin and Liu (1998) found that it is relatively unimportant in the surf zone but if the initial seeding of the turbulence quantities is too low the initiation of wave breaking may be delayed. Lin and Liu (1998) suggests $\delta_0 = 2.5 \times 10^{-3}$ is a good choice. Moreover the initial value of ν_t may be set equal to:

$$\nu_t = \zeta_0 \nu \quad (3.127)$$

where ζ_0 is a constant that is also arbitrary and relatively unimportant in the surf zone. A value of $\zeta_0 = 0.1$ has been suggested as a suitable solution (Lin and Liu, 1998). Finally ϵ can be determined by:

$$\epsilon = C_\mu \frac{k^2}{\nu_t} \quad (3.128)$$

3.4.9 Variable Grid Construction

In the RANS model, in order to reduce computational time a variable grid is often employed. For example, Δx may be made gradually smaller from the surf zone to the swash zone, and similarly Δz gradually smaller from the seabed to the free surface region. This can avoid unnecessarily fine grids in regions where the flow is fairly simple while employing fine grids in complicated regions of the flow. Still, Δz must be the same value near the free surface in both the surf zone and the swash zone, i.e. Δz cannot be a function of horizontal distance (nor can Δx be a function of vertical distance). This is one of the major drawbacks of the RANS model that can be avoided by using the coupled model presented in §3.5. In any case, when varying say Δx from the surf zone to the swash zone, it is desirable that two adjacent values of Δx be some multiple close to 1, α of each other to avoid errors in the finite-difference formulae associated with large changes between adjacent cell sizes. Thus, one can assume a power law relationship of the form:

$$\Delta x_0 \alpha^n = \Delta x_n \quad (3.129)$$

where Δx_0 is the initial cell size in the surf zone at x_0 . Δx_n is the n^{th} cell from x_0 at x_n as shown in Figure 3.22. Thus, the following geometric series follows:

$$\sum_{i=0}^{n-1} \Delta x_0 \alpha^i \equiv \Delta x_0 \frac{1 - \alpha^n}{1 - \alpha} = x_n - x_0 \quad (3.130)$$

Note that, $\alpha < 1$ in the case sketched in Figure 3.22 but we may also adopt the reverse of this case so that $\alpha > 1$.

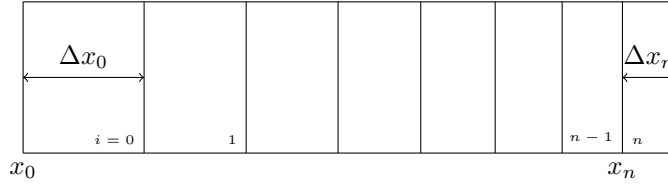


Figure 3.22: Sketch of the power law variation in cell size between two prescribed locations

Solving Eqns. (3.129) and (3.130) simultaneously gives the following equations for α and n respectively:

$$\alpha = 1 + \frac{\Delta x_n - \Delta x_0}{x_n - x_0} \quad (3.131)$$

$$n = \frac{\log \Delta x_n - \log \Delta x_0}{\log \alpha} \quad (3.132)$$

The number of cells, n must be an integer and if this requirement is met the problem is solved. However Eqn. (3.132) does not guarantee that n is an integer. In such a case we take, $n = \text{floor}(n)$ and re-calculate α to satisfy Eqn. (3.130) using the floored integer, n . To perform this operation Newton-Raphson iterations are adopted:

$$\alpha_{i+1} = \alpha_i - \frac{\Delta x_0(1 - \alpha_i^n) + (1 - \alpha_i)(x_0 - x_n)}{x_n - x_0 - \Delta x_0 n \alpha_i^{n-1}} \quad (3.133)$$

The corrected solution of α to within some desired accuracy is found in just a few iterations because the initial guess of α from Eqn. (3.131) is already close to the final solution. Furthermore, the algorithm guarantees that $\Delta x_{i+1} < \Delta x_i$ (or $\Delta x_{i+1} > \Delta x_i$ for $\alpha > 1$) is always satisfied thus it is judged to be effective. This method allows for the automated calculation of variable grid sizes by specifying only the beginning and end coordinates and the grid cells at those coordinates. One should take care that α after calculation is in fact close to 1. The author recommends that $0.95 < \alpha < 1.05$.

3.5 Two-way Multiscale Coupling

Multiscale coupling consists of combining two or more models together that assume different governing equations for the wave motion due to scaling disparities. The two-way aspect refers to the transfer of information in both directions between two models that are coupled at some spatial location. In this thesis the use of just two models overall is adopted for simplicity. However, for possibly even better performance it may be useful to consider coupling multiple models in the future. Those two models, a 2DH NSWE one and a 3D RANS one, have been described in detail in §3.2 and §3.4 respectively. The NSWE model has been shown to be especially adept at modelling long waves like tsunamis over large areas with accuracy and computational efficiency. A method for two-way nesting has been described in §3.3 that allows the NSWE model to simulate the tsunami from the source down to fairly fine grids in a region of interest. The idea when combining this with the RANS model is that one extra, further refined and smaller layer is simply added to the multi-grid nested NSWE setup except that the governing equations in this layer becomes the RANS equations. This implies that the same spatial nesting and temporal nesting scheme used in the multi-grid nesting is valid for the two-way multiscale coupling scheme when different horizontal grid sizes and time steps are used.

Thus, almost half of the two-way multiscale coupling technique has already been introduced in §3.3 that described the two-way multi-grid nesting scheme. The trick simply becomes one where the depth-averaged information in the NSWE model must be transferred somehow to include a vertical profile, described in §3.5.1. For the transfer of information back in the other direction, the velocities are integrated to get the volume flux and a single free surface must be assumed near the boundary to be able to pass that information back to the depth-averaged model. This is explained in §3.5.2. Note, that since the explanation of interpolation, summation and averaging on different horizontal spatial scales has already discussed in §3.3.1, this section will avoid much description about those horizontal effects. Instead, the focus will be on the vertical effects. In reality the two-way multiscale coupling adopts the multi-grid nesting techniques. With regards to coupling in the temporal direction, a few differences exist compared with the NSWE-NSWE multi-grid nesting procedure. These are highlighted in §3.5.3 along with a detailed description of the overall procedure.

Figure 3.23 illustrates the basic setup of the two-way coupling of the models which the reader can refer to when reading through the equations presented. Lastly, the two-way coupled model used in this thesis has been given a name. It is “2CLOWNS-3D” (**2**-way **C**oupled **L**ong **W**ave to Reynolds-Averaged Navier-**S**tokes **3D**). In the 1DH to 2DV dimensional case (c.f. Chapter 4) the “-3D” part is omitted. The 2CLOWNS(-3D) abbreviation will be used in this thesis hereafter.

3.5.1 Shallow Water to RANS Exchange

The boundary condition for the RANS domain most importantly requires knowledge of the vertical distribution of the horizontal velocities, $u_{c,k}$ and $v_{c,k}$, and the vertical velocity, $w_{c,k}$ at the domain interface, where the k refers to a cell number in the vertical direction. This profile must be obtained from the volume fluxes, Q in the NSW model. Furthermore, values of the fluid volume fraction, $F_{c,k}$ as well as the turbulent quantities $k_{c,k}$ and $\epsilon_{c,k}$ are also required. A description of these boundary conditions and how to obtain them is described in this section.

Horizontal Velocities

In the 3D case, two horizontal velocity distributions are required. One is the normal velocity and the other is the tangential velocity to the boundary. Similar to multi-grid nesting, the normal velocity (e.g. $u_{c,k}$ in Figure 3.23) must be defined directly on the interface so no interpolation of the volume flux in the normal direction is required. Interpolation may be required in the tangential direction, as detailed in §3.3.1. This normal velocity is a driving boundary condition to the RANS model since it is responsible for the correction of the pressure through continuity on the water column adjacent to the boundary. Thus, it is inserted as $u_{c,k}^{n+1}$ and $u_{c,k}^*$, i.e. it is the correct Solenoidal velocity after the time step *and* it is used as the “guessed” velocity in the Poisson Pressure equation. The previous value may be used to evaluate the momentum equation as normal. Contrastingly, the tangential velocity, denoted $v_{c,k}$, exists inside the boundary and thus plays no role in the Poisson Pressure calculation. It is used only to update the momentum equation. Interpolation of the flux in the normal and tangential directions may be required which is again detailed in §3.3.1.

Lets assume that the flux Q_{xc} refers to the interpolated normal flux, and h_{xc} is the interpolated initial water depth, both in the position of $u_{c,k}$. η_c and η_e are the water levels that align in the tangential direction with $u_{c,k}$. The depth-averaged normal velocity, U_c can thus be found by:

$$U_c = \frac{Q_{xc}}{(\eta_c + \eta_e)/2 + h_{xc}} \quad (3.134)$$

The problem now becomes how to transform U_c onto some vertical profile for $u_{c,k}$ to use as a boundary condition for the RANS model. The simplest choice is the shallow water assumption that the horizontal velocities are uniform over the depth:

$$u_{c,k} = U_c \quad (3.135)$$

In order for this assumption to be valid the flow in the RANS model should obey the true long wave assumptions so that the vertical profile of the horizontal velocities become close to uniform at the boundary. This may require the domain of the RANS model to be very large so that reflections with rotations and non-hydrostatic effects inside the RANS domain do not return to the boundary to complicate things. Sometimes this may be quite a restriction. One method to

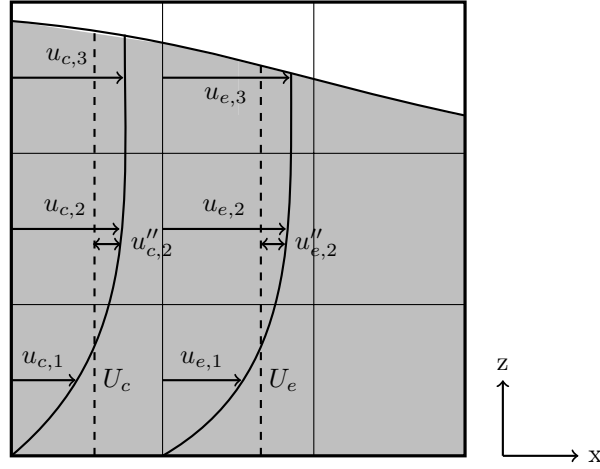


Figure 3.24: Illustration of the arbitrary velocity profile based on no-gradient of the fluctuation, u'' from the depth-averaged component, U

alleviate this strictness at the boundary is to introduce an arbitrary velocity distribution so that vortices rotating in the vertical plane may freely cross the boundary in the form:

$$u_{c,k} = U_c + u''_{c,k} \quad (3.136)$$

where $u''_{c,k}$ is the fluctuation from the depth-averaged velocity as illustrated in Figure 3.24.

Following Fujima et al. (2002), a suitable boundary condition is obtained by setting the difference in u'' across the boundary to zero. When referring to Figure 3.23, this means equating $u''_{c,k}$ to $u''_{e,k}$. Finally, the equation for $u_{c,k}$ can be written as:

$$u_{c,k} = U_c + \frac{\gamma_{xe,k}^a (F_{eL,k} + F_{eR,k})}{\gamma_{xc,k}^a (F_{c,k} + F_{eL,k})} (u_{e,k} - U_e) \quad (3.137)$$

The ratio of the F volume fractions and aperture ratios, γ_x^a exists to ensure that the volume flux, Q_c is conserved. This equation is correct for any cell sizes as long as U_c and U_e have been correctly determined from interpolation. It is easy to extend this idea to the tangential fluxes, $v_{c,k}$ as well but generally more interpolation is required to get the depth-averaged velocities in the correct locations.

Vertical Velocities

The shallow water profile for the vertical velocities, $w(z)$, is found by integrating the continuity equation assuming uniform horizontal velocity profiles, and applying the kinematic boundary conditions at the sea bed and free surface. This results in a linear profile ($i = 1, 2$):

$$w(z) = -\frac{\partial U_i}{\partial x_i} (z + h) \quad (3.138)$$

where z is the elevation from the initial undisturbed free surface. Note that even assuming a Boussinesq type profile of the horizontal velocities (quadratic) would result in a linear profile for the vertical velocities after ignoring terms of $O(\mu^4)$ (Sitanggang and Lynett, 2010). Eqn. (3.138) implies that the vertical velocities depend on the gradient of the depth-averaged velocities which are found from the volume fluxes and the water depths. In our example (Figure 3.23), a combination of U_w , U_c , and U_E must be considered in order to compute $\frac{\partial U_c}{\partial x_c}$. Similarly, a combination of V_c , and V_n , must be considered in order to compute $\frac{\partial V_c}{\partial y_c}$. After those depth-averaged velocities have been found via the appropriate interpolation, $w_{c,k}$ can be determined by:

$$w_{c,k} = -(z_k + h_c) \left[\frac{1}{(\Delta x_{NSWE})^2} (\Delta x_{RANS} U_c + (\Delta x_{NSWE} - \Delta x_{RANS}) U_E / 2 - (\Delta x_{NSWE} + \Delta x_{RANS}) U_w / 2) + \frac{V_n - V_c}{\Delta y_{RANS}} \right] \quad (3.139)$$

where z_k is the elevation from the initial free surface at the vertical cell integer k , and h_c is the initial water depth of the water column where $w_{c,k}$ is defined (cell centre in terms of the horizontal plane). However, it may be that if an arbitrary profile of the horizontal velocities is specified (Eq. (3.137)) to account for the reflected waves with some rotation, the simple linear profile of the vertical velocities could become a poor approximation to the RANS profile near the boundary. In this case, simply a no gradient boundary condition for $w_{c,k}$ may be more appropriate:

$$w_{c,k} = w_{e,k} \quad (3.140)$$

Scalars

The free surface level is defined inside the boundary in terms of the cell volume fraction, $F_{c,k}$. This ensures that the correct volume flux is transported into the domain via the VOF method (Eqn. (3.81)). $F_{c,k}$ is determined from the interpolation of η_c and η_e in the NSWE model:

$$F_{c,k} = \begin{cases} 0, & \text{if } z_k \geq \eta_c^*, \\ 1, & \text{if } z_{k+1} \leq \eta_c^*, \\ (\eta_c^* - z_k) / \Delta z, & \text{otherwise} \end{cases} \quad (3.141)$$

$$\eta_c^* = \left(\frac{\Delta x_{NSWE} + \Delta x_{RANS}}{2\Delta x_{NSWE}} \right) \eta_c + \left(\frac{\Delta x_{NSWE} - \Delta x_{RANS}}{2\Delta x_{NSWE}} \right) \eta_e$$

Finally, the remaining scalars that must be defined inside the boundary are the turbulent ones, k_c and ϵ_c . Unfortunately the NSWE model provides no information on these parameters. Furthermore, the NSWE model has been derived from inviscid and irrotational assumptions which implies no turbulent energy. For lack of a better method, no gradient conditions are set for k and ϵ across the boundary:

$$k_{c,k} = k_{e,k} \quad \epsilon_{c,k} = \epsilon_{e,k} \quad (3.142)$$

Our real hope is that the turbulent energy remains small at the boundary in the RANS model so that the turbulent boundary conditions are unimportant on the flow. This in turn would validate the main assumption implied when coupling the two models together: that the physics of the flow must be a good approximation of the weakest link (the model with the most assumptions) in the coupling region.

3.5.2 RANS to Shallow Water Exchange

The boundary conditions for NSWE model in the two-way coupling procedure are identical to those for the multi-grid nesting: the free surface and the volume flux. They are summed and averaged in the case of different spatial resolutions between the NSWE and RANS layers as described in §3.3.1. Thus, a large proportion of the RANS to shallow water exchange algorithm has already been introduced implicitly by the explanation of multi-grid nesting technique. The major difference is that a couple of basic calculations are required to convert the three-dimensional values within the RANS layer into these 2DH type quantities. This conversion takes place throughout the entire RANS domain since it is convenient to use the 2DH type data for visualization purposes and analysis.

Firstly, in order to get the free surface from the RANS model a simple procedure is followed. A loop is conducted over all the vertical cell numbers, k from the top down. When a cell is found to be a free surface one ($NF = 2$), the vertical component of the centre of gravity of the free surface, $(\eta^{cg})_z$ is taken to be the free surface elevation in that vertical column and the loop is exited. For example, $(\eta_{eL}^{cg})_z$ and $(\eta_{eR}^{cg})_z$ (c.f. Figure 3.23 ($x - z$ plane)) represent the free surfaces η_{eL} and η_{eR} respectively. Once the free surfaces in the RANS domain are found they are summed and averaged onto the NSWE grid. To get η_t from the RANS in the example illustrated in Figure 3.23 ($x - y$ plane) requires the following calculation:

$$\eta_t = (\eta_{tLD} + \eta_{tRD} + \eta_{tLU} + \eta_{tRU})/4 \quad (3.143)$$

Note that this procedure assumes that only one free surface exists in a vertical column. This is reasonable because if more than one free surface has arisen in the RANS model at the boundary, then it is unlikely to be a good position to couple the models since one of the main assumptions of the NSWE model has been violated.

The volume fluxes are found by integration of the velocity multiplied by the fluid height at each cell boundary over the water depth. For example, to get Q_{xE} (c.f. Figure 3.23 ($x - z$ plane)) the following operation is conducted:

$$Q_{xE} = \Delta z \sum_{k=1}^{ke} \left[\gamma_{xE,k}^\alpha u_{E,k} (F_{eR,k} + F_{eL,k})/2 \right] \quad (3.144)$$

in which $k \in [1, ke]$ is the vertical cell number and ke is the total number of vertical cells. Note that the two values of F are used to get the average of F across the cell boundary.

3.5.3 Temporal Coupling

Just like temporal nesting described in §3.3.2, when the time step is different between the last NSWE layer and the RANS domain, interpolation of the values in time is required. Moreover, a specific order of calculation of the models is necessary so that all known values are used at the correct time when passing information from one model to another. This is termed “temporal coupling” in this thesis. Different time steps arise firstly, because the solution algorithms and governing equations are different in the models. While the NSWE layer can run at Courant numbers close to $\sqrt{2}/2$, due to the explicit SMAC algorithm of the RANS model, generally smaller Courant numbers are required. It has been found by the author that Courant numbers for the wave speed around 0.3 is usually suitable, but smaller values < 0.1 , based on the flow velocity may be required during highly unsteady and turbulent flows like wave breaking. Additionally, the horizontal spatial grids scales are typically finer in the RANS model, further increasing the ratio of Δt between the coupled models, Δt_{ratio} .

The major difference between temporal coupling (between a RANS layer and a NSWE layer), and temporal nesting between two NSWE layers is that there is no staggering of the variables in time in the RANS model. In other words, the scalar variables defined at the cell centres are defined at the same time as the velocity vectors on the cell boundary. One time step in the RANS model updates everything from time, $t = n$, to $t = n + 1$. In contrast one time step in the NSWE model updates the volumes fluxes from $t = n$, to $t = n + 1$, but the free surfaces from $t = n - 1/2$, to $t = n + 1/2$. Hence, the temporal nesting algorithm splits up the calculation of momentum and continuity into two separate steps, while for the RANS model no splitting of calculation steps is required (or possible).

The temporal coupling procedure begins just like temporal nesting where the Δt in each layer is determined from the desired Courant number and the requirement of an integer value of Δt_{ratio} between two adjacent layers (Eqns. (3.40) and (3.41)). Lets consider an example similar to the one described in §3.3.2 where there are three layers, $L1$, $L2$, and $L3$. The difference in this section is that the last layer is a RANS model one (while the first two layers are NSWE ones). Due to the considerations of the spatial grid resolutions and different Courant numbers between models, imagine that $\Delta t_{ratio} = 2$ between any two adjacent layers.

The three layers can be summarised as: $L1$ (NSWE coarse grid), $L2$ (NSWE fine grid) and $L3$ (RANS). A flowchart of the calculation procedure is illustrated in Figure 3.25 which the reader can refer to. The following explanation will focus on the $L2$ to $L3$ exchange. Firstly, the continuity equation in $L2$ is performed: $\eta^{n-1/4} \rightarrow \eta^{n+1/4}$. At this point the free surface from the RANS layer is exchanged to $L2$. However, the RANS model has no knowledge of $\eta^{n+1/4}$ because it is not staggered in time. In fact it only knows η^n independent of the time step in the RANS model. This is different to temporal nesting for the NSWE model which encounters a similar problem for different time steps between layers but due to the time staggering a value at a time closer to $n + 1/4$ is available after one calculation of continuity. In fact, if $\Delta_{ratio} = 1$ between NSWE

layers an extra loop of continuity is unnecessary. However, for any Δ_{ratio} between the coupled the NSWE and RANS layers (including $\Delta_{ratio} = 1$), a half time step of continuity is required to account for the unmatched values in time:

$$\eta_{(i,j)}^{n+1/4} = \eta_{(i,j)}^n - \frac{\Delta t^{L2}}{2} \left[r_x \left(Q_{x(i+1/2,j)}^n - Q_{x(i-1/2,j)}^n \right) + r_y \left(Q_{y(i,j+1/2)}^n - Q_{y(i,j-1/2)}^n \right) \right] \quad (3.145)$$

Although this may introduce a small error through the indirect determination of the free surface by the continuity equation, since the free surface itself is directly passed through at $t = n$, the error cannot accumulate. Thus, the overall effect on the calculation can be considered small.

The next step is to update the volume flux in $L2$ through the momentum equation: $Q^n \rightarrow Q^{n+1/2}$. The value of the flux at the two time steps is interpolated to get $Q^{n+1/4}$ as required for the RANS model. $Q^{n+1/4}$ is converted to the horizontal and vertical velocities as explained in §3.5.1. The normal velocities at $t = n + 1/4$ are used in the Poisson Pressure equations to get the Solenoidal velocity field in the next time step of the RANS model. All the velocities (normal, tangential and vertical ones) from the previous time step ($t = n$) are used in the forward Euler step of the momentum equation.

Moreover, to get the depth-averaged velocities (requires division of the volume flux by the water depth) and the values of F on the boundary (based on free surface level), values of the free surface are required from the NSWE model at $t = n + 1/4$. In this case, $\eta^{n+1/4}$ is actually already available and can be directly used. If $\Delta t_{ratio} > 2$ then interpolation of $\eta^{n-1/4}$ and $\eta^{n+1/4}$ would be required at this step. Since all the boundary conditions may now be applied for the RANS model, one time step is performed updating all the values from $t = n \rightarrow n + 1/4$. Furthermore, because $Q^{n+1/2}$ is available in $L2$, one extra time step of the RANS model may now be instantly performed. However, the free surfaces in $L2$ are only available at $t = n + 1/4$, but those at $t = n + 1/2$ are required to get the depth-averaged velocities. Although, it is possible to update the continuity equation locally on the boundary to the RANS layer and outside of it, it cannot be updated inside the RANS layer since $Q^{n+1/2}$ is not yet known here. Note that the average of the values of $\eta^{n+1/2}$ inside and outside of the RANS layer is required to get the depth on the boundary for division. Thus, extrapolation is our only option and the values of $\eta^{n+1/2}$ are obtained by:

$$\eta^{n+1/2} = 2\eta^{n+1/4} - \eta^{n-1/4} \quad (3.146)$$

Fortunately since the values of η are only used to get the water depth and η is generally small in comparison to h , the error associated with the extrapolation step is expected to be small. The next time step of the RANS model can be now be performed, updating all values from $t = n + 1/4 \rightarrow n + 1/2$. At this stage the fluxes at $t = n + 1/2$ may be passed from the RANS layer to $L2$. Hereafter, Steps 8 to 11 (c.f. Figure 3.25) are actually the same as Steps 1 to 7 sans the calculation for $L1$, so their explanation will not be repeated. Finally, when everything is updated to $t = n + 1$ after Step 11, flux data can be exchanged between all layers ($L1$, $L2$, $L3$) in both directions (although the volume flux has already been passed from $L2$ to $L3$ before Step 11). This marks the end of a time step.

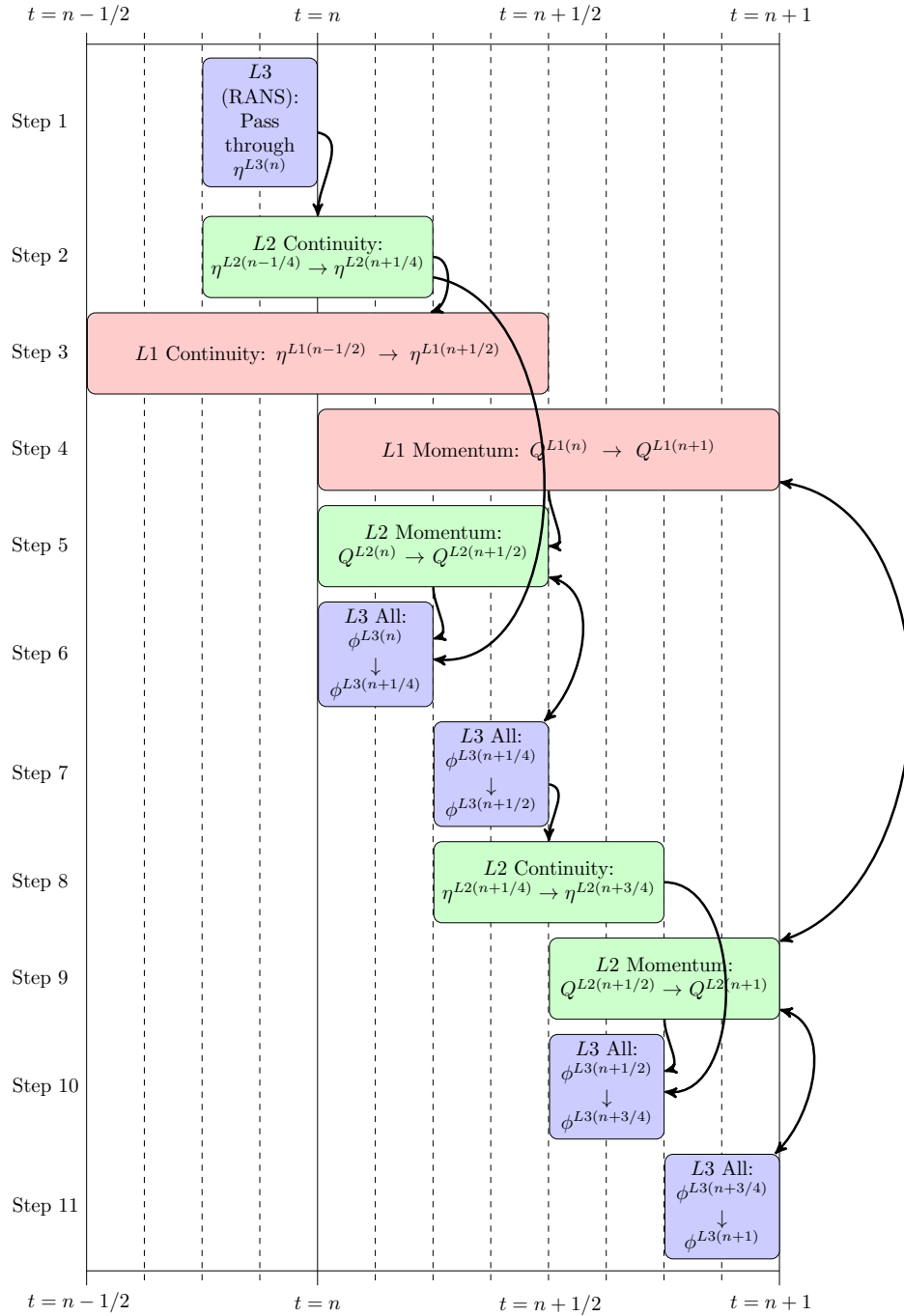


Figure 3.25: Example flowchart of the calculation order for temporal coupling with three layers (L3 is a RANS model layer) where $\Delta t_{ratio} = 2$ between two adjacent layers. The arrows show the exchange of information where the horizontal position of the ends of the arrows indicate the time step of the exchanged data. ϕ in the L3 block is a dummy variable to indicate all scalar and vector quantities in the RANS model

Similar to temporal nesting, to achieve the coupling calculation procedure illustrated in Figure 3.25 a recursive subroutine is adopted. It is able to calculate any arbitrary number of layers with arbitrary Δt_{ratio} between any two adjacent layers. It is almost identical to Appendix A except that it calls the RANS model solver in place of the NSWE momentum equations for calculation in the RANS layer. No continuity equation is calculated in this layer.

SOLITARY WAVE TRANSFORMATION AND BREAKING ON A PLANE BEACH

In order to verify and identify a suitable range of application of the 2CLOWNS (1DH-2DV dimensions) model that was described in detail in Chapter 3, a study on the shoaling and breaking of solitary waves on a plane beach was conducted. The study investigated a range of offshore wave heights of solitary waves on three different slopes ranging from fairly steep to mild as described in §4.2. By comparing the shoaling capabilities of the individual NSWE (nonlinear shallow water equations), FNBM (fully nonlinear Boussineaq model) and RANS (Reynolds-averaged Navier-Stokes) models in §4.3.1 plus the coupled 2CLOWNS model in §4.4.1 two outcomes were achieved: Firstly, the effects of beach slope, offshore wave height, and boundary conditions related to the two-way coupling were highlighted. As a result, a suitable range of allowable solitary waves and slopes according to some dimensionless parameter was identified. Secondly, local depths on the slope where two-way coupling takes place that maximises performance and minimises computational load was expressed as a function of a related dimensionless parameter as demonstrated in §4.3.2. Interestingly this location appeared to correspond to the transition from the zone of gradual shoaling to the zone of rapid shoaling. Following this, the performance in terms of the physics of shoaling and prediction of the breaking point was compared with experiments and other numerical analyses as found in §4.4. As a result new empirical expressions were proposed for the breaking index and the depth at breaking to complement existing ones as shown in §4.4.3. A qualitative evaluation of the capabilities of the model to predict post-breaking behaviour such as touchdown of the plunging jet was conducted and is presented in §4.4.4. Lastly, a comparison of the velocity profiles at different stages of transformation between the three models NSWE, FNBM and RANS is shown in §4.4.5 to highlight their disparities.

4.1 Introduction

In long wave modelling it is important to obtain good estimations of wave shoaling and breaking in the nearshore area. These phenomena can affect sediment transport, hydrodynamic forces on coastal structures and transport of driftage significant during tsunami and storm disasters. As a representation of tsunamis and other long waves a significant amount of attention has been paid to the evolution of solitary waves. Synolakis (1987) derived an analytical solution to the nonlinear shallow water equations valid for non-breaking solitary waves. These solutions has since been often used in tsunami benchmarking (Synolakis et al., 2009). Additionally, Synolakis and Skjelbreia (1993) provided a semi-quantitative description of the evolution of breaking waves where dispersion and nonlinearity become important so that the Synolakis (1987) solutions breakdown. Four distinct regions of solitary wave transformation were identified where the rate of shoaling could be approximated according to a power law equivalent to Green's law and Boussinesq's law in the two shoaling stages respectively, followed by two zones of decay after wave breaking. Both Hsiao et al. (2008) and Hwang et al. (2007) presented experimental studies investigating breaking solitary waves on a 1/60 (mild) slope. Hsiao et al. (2008) confirmed the analysis of Synolakis and Skjelbreia (1993) and further identified a fifth region, that of post-breaking bore propagation. Grilli et al. (1994, 1997) developed a fully nonlinear potential flow (FNPF) model that was applied to the transformation of solitary waves on plane slopes and was shown to be in excellent agreement with experiments performed on a 1/35 slope. They proposed empirical formulae for breaking characteristics based on a nondimensional slope parameter. Hsiao et al. (2008) also shows that the formulae were in excellent agreement on the mild slope. However, Grilli et al. (1994, 1997) note that on the steeper slopes ($> 1/35$) Green's law and Boussinesq's law are not very good descriptors of solitary wave evolution and in fact on very steep slopes the solitary wave height essentially does not change in height at all.

To model the propagation of solitary waves and other long waves from far offshore towards the coastal zone depth-integrated two dimensional wave equations (2DH) have been typically utilized, in particular the shallow water equations (NSWE) for tsunami modelling. Simple finite-difference approximations of the NSWE have been widely used in models such as TUNAMI (Imamura et al., 2006) and COMCOT (Liu et al., 1998) with reasonable success. Moreover, such models are well adapted to computing over large scales with various spatial resolutions (grid nesting). When linear dispersive effects are important for long distance propagation, numerical dispersion inherent in the model can be utilized in TUNAMI and COMCOT to match those of the linear Boussinesq equations (Cho et al., 2007). However, for more local dispersive effects Boussinesq models are better suited. Both weakly nonlinear (Wei and Kirby, 1995; Nwogu, 1993; Madsen and Sorensen, 1992) and fully nonlinear Boussinesq models (FNBM) exist. COULWAVE (Kim et al., 2009) and FUNWAVE (Shi et al., 2012a) are examples of the latter which has been shown to demonstrate excellent performance for shoaling on slopes over a wide range of nonlinearity ratios (Wei et al., 1995). COULWAVE is also formally 'weakly-rotational', a rare divergence from

the typical irrotational assumption of most long wave models that otherwise have ad hoc or no consideration of mixing effects aside from numerical manifestations.

Depth-integrated models are not exact forms of the governing equations of fluid motion and contain theoretically a truncation error of some order (Wei et al., 1995). They also lose the ability to model wave-overturning and other three-dimensional effects. However, some models have been developed to solve the original fully nonlinear potential flow (FNPF) equations, in particular a boundary element method (BEM) (Grilli et al., 1994, 1997). Such inviscid models however break down on the touchdown of the overturning jet before turbulent effects become significant. To simulate the physics hereafter and provide detailed information on turbulence and bottom stresses as well as interaction with irregularly shaped structures Navier-Stokes (N-S) based solvers are required. Such solvers however suffer from very high computational costs, require a fine resolution in space and time to model the physics of the problem to greater accuracy than its depth-integrated counterpart, and are often susceptible to numerical dissipation over long distances due to the indirect modelling of the free surface and thus are not suitable for calculation over wide areas.

Typically the advantages of N-S models may only encompass a relatively small area around a structure or region of interest particularly around the time when wave breaking would occur. This realization has encouraged modellers to investigate coupling of depth-integrated and N-S models in space to obtain the advantages and reduce the disadvantages of both models. Fujima et al. (2002) and Fujima (2006) first demonstrated this type of hybrid model using the shallow water equations combined with a N-S model where the free surface was approximated by the height function approach. Sitanggang and Lynett (2010) presented and validated a scheme that coupled a FNBM (COULWAVE) model and a vertical two-dimensional (2DV) Reynolds-averaged Navier-Stokes (RANS) model using the Volume-of-fluid (VOF) method for free surface modelling. Further, Pringle and Yoneyama (2013) applied a coupled model combining the 2DH shallow water equations with a fully three-dimensional RANS model to the 2011 Tohoku Tsunami in Kamaishi Bay, Iwate Prefecture with reasonable success. However, little comprehensive research on the validation of the coupling of depth-integrated wave equations and N-S equations has been conducted. Moreover, it is required to evaluate errors when matching the solutions of the two models at the interface and optimise locations of that interface.

In this study a two-way coupled NSWE (in 1DH mode) to RANS (in 2DV mode) model, called 2CLOWNS that has been described in detail in Chapter 3 is applied. To evaluate the capabilities of 2CLOWNS and its constituent models, solitary wave shoaling and breaking characteristics on a plane beach are analysed in detail for a range of slopes and offshore wave heights. Water depths on the beach slope where the NSWE model cannot reproduce the required shoaling characteristics in comparison with a FNBM (COULWAVE) are identified to determine optimal coupling positions to the RANS model in 2CLOWNS. Furthermore, the effect of beach slope, offshore wave height and boundary conditions related to the two-way coupling are investigated. Prediction of the

wave breaking characteristics such as the water depth at breaking and the breaker index by 2CLOWNS are compared with experiments and the FNPF model. A new empirical equation is proposed to complement existing ones for the prediction of these characteristics. Furthermore, the post-breaking wave behaviour and wave shape in 2CLOWNS is compared qualitatively with expected behaviours to demonstrate its ability to model the entire wave transformation and breaking process. Finally, velocity profiles of 2CLOWNS and depth-integrated models are shown for comparison, and their disparities are discussed.

4.2 Problem Setup and Model Conditions

This section begins by outlining the definition of the canonical problem for solitary wave propagation, transformation and breaking on a plane beach in §4.2.1. The models used for analysis, boundary/initial conditions, permanent wave forms, grid sizes, and assumptions for wave breaking are introduced in §4.2.2. Finally, the combination of slopes and offshore wave heights investigated in this study are outlined in §4.2.4.

4.2.1 Canonical Problem Definition and Dimensionless Variables

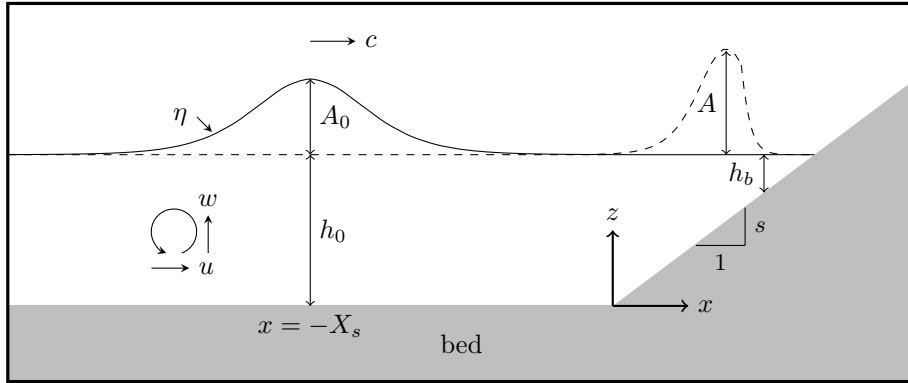


Figure 4.1: Sketch of the canonical problem definition for solitary wave propagation, transformation and breaking on a plane beach

The canonical problem definition is sketched in Figure 4.1. There exists a plane beach with slope s , where the origin of the x coordinate begins at the toe of the slope with x positive onshore of it. The offshore initial undisturbed water depth, h_0 is constant in the negative x direction of the toe of the slope. Thus, the initial undisturbed water depth, h is described by the following function:

$$\begin{cases} h = h_0 & \text{if } x \leq 0 \\ h = h_0(1 - xs) & \text{if } x > 0 \end{cases} \quad (4.1)$$

Centred at a distance X_s from the toe of the slope there exists a permanent form solitary wave at $t = 0$ with offshore wave height, A_0 . The free surface of the solitary wave is described by η , it is moving with wave speed, c and has horizontal and vertical orbital velocities, u and w respectively. Additionally, as the wave transforms over the slope the local wave height, A is constantly increasing until it breaks with a wave breaking height, A_b in an initial undisturbed

water depth, h_b . It is customary to introduce dimensionless variables based on h_0 and g :

$$\begin{aligned} x' &= \frac{x}{h_0} & h' &= \frac{h}{h_0} & A'_0 &= \frac{A_0}{h_0} & A' &= \frac{A}{h_0} & \eta' &= \frac{\eta}{h_0} \\ u' &= \frac{u}{\sqrt{gh_0}} & w' &= \frac{w}{\sqrt{gh_0}} & t' &= \frac{t}{\sqrt{h_0/g}} \end{aligned} \quad (4.2)$$

where ' indicates a dimensionless variable. The dimensionless variables will be used hereafter in the analysis. Using Boussinesq's first approximation for a solitary wave gives the following offshore free surface profile and wave speed respectively:

$$\eta' = A'_0 \operatorname{sech}^2 \left(\sqrt{\frac{3A'_0}{4}} x' \right) \quad (4.3)$$

$$c = \sqrt{gh_0(1 + A'_0)} \quad (4.4)$$

For consistency between numerical experiments we can define the distance X'_s to be equal to half a measure of the wavelength, L_0 of a solitary wave which is defined as containing 97.5% of the fluid volume according to Boussinesq's approximation (this is within 0.3% agreement to the length defined in Synolakis (1987)):

$$L_0 = \frac{4h_0}{\sqrt{3A'_0}} \operatorname{arctanh}(0.975) \quad (4.5)$$

$$X'_s = \frac{L_0}{2h_0} = \frac{2}{\sqrt{3A'_0}} \operatorname{arctanh}(0.975) \quad (4.6)$$

This ensures that waves go through the same distance before transformation up the slope. Additionally, in this study we wish to investigate a number of slopes and offshore wave heights in order to identify a range of application of the 2CLOWNS model. A surf-similarity parameter is commonly used to collapse the beach slope and offshore wavelength (uniquely tied to a wave height for solitary waves) variables into one for analysis. In this study the slope parameter introduced by Grilli et al. (1997) is adopted. It is defined as:

$$S_0 = \frac{s}{\mu_s} \quad (4.7)$$

where $\mu_s (= h_0/L_s)$ is the inverse of the characteristic dimensionless length of the wave offshore for use in the slope parameter based on L_s instead of L_0 defined in Eqn. (4.5). Grilli et al. (1997) suggests that it is more appropriate to use the following definition for solitary waves for use in the slope parameter:

$$L_s = \frac{4h_0}{\sqrt{3A'_0}} \operatorname{arctanh} \left(\frac{\sqrt{3}}{3} \right) \quad (4.8)$$

which is equivalent to the length between the locations of maximum slope on the solitary wave. Thus, S_0 can be reduced to following expression for solitary waves:

$$S_0 = 1.5207 \frac{s}{\sqrt{A'_0}} \quad (4.9)$$

Furthermore, the non-dimensional initial water depth at breaking, h'_b and wave breaking index, A_b/h_b are important parameters to compare with experiments and theory to verify the 2CLOWNS model for wave breaking prediction. This study will derive expressions for these in terms of S_0 to compare with existing ones.

4.2.2 Model Conditions

In this study a total of four models are employed: the NSWE model, the RANS model, 2CLOWNS (combination of the previous two), and a FNBM (COULWAVE). Firstly, comparison of the individual constituent models of 2CLOWNS with each other is important to show where the strengths and weaknesses of each model lie. Secondly, their comparison with 2CLOWNS is important to see whether 2CLOWNS can do a good job of combining the best attributes of the NSWE model and the RANS model together. Thirdly, FNBMs have been shown to give good approximations of solitary wave shoaling in comparison with a FNPF model (Wei et al., 1995) and are very reliable for solitary wave propagation offshore. For shoaling before breaking starts to take place these models can be expected to give accurate solutions that may be taken to be the correct ones and plays the role of a “control model”. Moreover, since the full RANS model takes a long time to compute, and is not so accurate for stable waveform propagation from far offshore, it is useful to compare the NSWE and 2CLOWNS solutions with the FNBM instead for the majority of the analysis. This section will describe the relevant model conditions, boundary/initial conditions, and grid sizes used for each model in this study.

NSWE Model

For this study the NSWE model is run in 1DH mode. Since solitary wave propagation is conducted and a range of offshore wave heights will be used where $\mu_0 = h_0/L_0$ often exceeds 0.05, the implicit dispersion correction procedure is required to ensure that the wave speed is correctly calculated and that the wave keeps its shape offshore. This procedure invokes the nonlinear advection truncation error correction so that the amplitude dispersion terms are correctly balanced with the frequency dispersion ones. Additionally, since only wave transformation (and breaking) is analysed in this study the bottom friction terms are set to zero as it can be expected that they will not play an important role. With regards to wave breaking, the (depth-averaged) NSWE model cannot approximate it in any rigorous manner, and a simple ad-hoc method is adopted. This approach relies on the deactivation of dispersion terms when wave breaking is detected to prevent the anomaly of balancing amplitude dispersion with frequency dispersion in flux-dominated regions of flow (Roeber and Cheung, 2012). In this case, an empirical criterion to determine deactivation is required. For example, Tonelli and Petti (2009) suggests wave breaking can be

detected where $\eta/h > 0.80$. This is suitable for breaking waves on a flat bed or very mild slope although this can be far exceeded on steep slopes (Grilli et al., 1994). For this study a better approximation would incorporate the local surface gradient, s . Camfield and Street (1969) devised such an empirical formula for solitary waves on plane slopes to give the following criterion: $\eta/h > \max[0.75 + 25s - 112s^2 + 3780s^3, 0.8]$. If the criterion is not used the wave will continue shoaling unbounded until it reaches the shoreline where the dispersion terms are ignored by default in the model. It is implemented in the NSW model by switching off the dispersive terms in cells where η/h exceeds the criterion.

For solitary wave propagation an initial condition is set following the Schemmer (1982) method that is described in §3.2.5. The offshore lateral boundary is set to an open condition to allow some remnants of the wave to flow out. The grid size is set equal to $\Delta x'/\mu = 1/200$ for this study, where $\mu_0 = h_0/L_0$ is a measure of the offshore dispersion parameter with L_0 defined in Eqn. (4.5). Negligible difference has been found for smaller mesh sizes. The Courant number is set to $Cr = 0.35$ for stability.

FNBM (COULWAVE)

The FNBM - COULWAVE - is run in 1DH mode. It uses a high-order finite-volume scheme to fourth-order in space and time. More details of the computational scheme can be found in Kim et al. (2009). For discretization of the numerical fluxes no limiter is used. Similar to the NSW model, bottom friction terms are ignored in this analysis. Wave breaking in the FNBM is achieved including some dissipative effect into the governing equations. An eddy viscosity model (Kennedy et al., 2000) is adopted that is activated when the the gradient of the flux exceeds some threshold value. The FNBM is formally *weakly* rotational, dispersive and turbulent (although the rotational and turbulent parts are not activated when friction terms are zero) and represents the state-of-the-art for Boussinesq modelling.

For solitary wave propagation an initial condition is set using the weakly nonlinear dispersive solution for Nwogu (1993) type Boussinesq models (Wei and Kirby, 1995). A sponge layer may be set at the offshore lateral boundary to remove small perturbations from the domain. The grid sizes are usually specified in terms of some ratio of the wave length automatically in COULWAVE, i.e. $\Delta x'/\mu_0$. $\Delta x'/\mu_0$ was set equal to 1/250 in this study to get converged shoaling performance. A Courant number of $Cr = 0.20$ was found to give a stable calculation.

RANS

For this study the RANS model is run in 2DV mode. Since mainly wave transformation and breaking will be analysed by the RANS model, the slip condition is employed at the bottom boundary. However, we would like to demonstrate some of the capabilities of the RANS model so the $k - \epsilon$ model is indeed utilised where it should influence the mixing in the wave during post-breaking. Furthermore, the RANS model is able to simulate the overturning of the wave

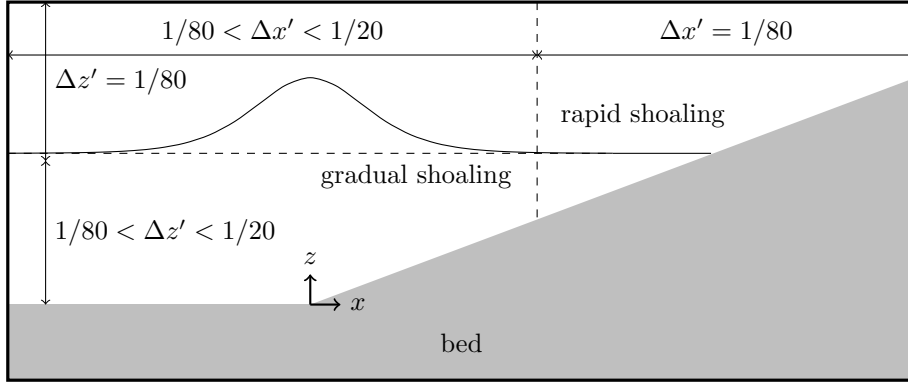


Figure 4.2: Illustration of suitable grid setup for the RANS model. The gradual shoaling and rapid shoaling interface may be estimated from Eqn.(4.12). The variation in grid sizes can be achieved using the power law technique described in §3.4.9

through the VOF method hence wave breaking is naturally modelled without any ad-hoc additions that are required for the 1DH models (NSWE and FNBM) in this study.

The computation takes a long time in the RANS model, and throughout most of this study the solitary wave into the domain will be specified via the boundary condition with the NSWE model in 2CLOWNS. For these reasons, a lateral boundary condition type input of the solitary wave is used to send a solitary wave into the domain where the boundary is set at $x' = -X'_s$ for the preliminary analysis here. The wave theory employed is McCowan's (McCowan, 1891) high-order approximation that has been detailed in Munk (1949). This theory is able to give an accurate specification of the orbital velocities important as a boundary condition in the RANS model. For the grid sizes a choice of $\Delta x'$ and $\Delta z'$ is required. The RANS model may be quite sensitive to this choice. It was found though that for most of the transformation (gradual shoaling), $\Delta x'$ and $\Delta z'$ is not particularly important. Here, $\Delta x' \mu_0 < 1/200$ is suitable ($\Delta x'$ may be allowed to vary). But when the shoaling becomes more rapid (an equation to estimate this location is presented in §4.3.2), $\Delta x' \mu_0 < 1/800$ and $\Delta z' = \Delta x'$ is more appropriate ($\Delta x'$ should be kept constant). The fact that $\Delta z' = \Delta x'$ from above the initial free surface is found to be important. Below the initial free surface, $\Delta z'$ may be gradually increased as desired and this was not found to have any effect. Additionally, it was found that to correctly model wave breaking effects such as the overturning wave shape, irrespective of the offshore wave height, $\Delta x' = 1/80$ was more suitable than scaling by μ_0 which is really only valid offshore before breaking. Because of this we instead adopt $\Delta x' = 1/20$ offshore and $\Delta x' = \Delta z' = 1/80$ in the rapid shoaling region for all wave heights. Figure 4.2 gives an illustration of the grid setup, and a demonstration of the grid size convergence and accuracy is presented in Appendix C. A Courant number for the SMAC scheme is set equal to, $Cr = 0.33$ (based on the wave speed; this is further multiplied by 0.3 to get the corresponding Cr based on the fluid velocity; $Cr < 0.1$).

4.2.3 Permanent Form Solutions

Initial conditions using the weakly nonlinear dispersive solitary wave solutions for the FNBM and NSW models have been used. However, there is a sudden initial decrease in the peak height before stabilizing off as the wave propagates up the slope. If the waves are initialised further offshore and allowed to propagate for a long enough simulation time a permanent waveform results with little or no further decrease in the local wave height with propagation distance. This is the actual initial condition that should be used at $x' = -X'_s$ for the remainder of the study. Here, back substitution of the truncation terms in the upwind scheme of the NSW model is important to mitigate dissipation errors. Due to the initial decrease of wave profile in both models, the initial wave height was tuned to give the desired permanent wave height. By running numerous simulations in each model and assessing the wave height after travelling 250 water depths, a quadratic function was found to transform the desired stable wave height, A'_0 into a suitable wave height on input, A'_i :

$$A'_i = a(A'_0)^2 + b(A'_0) + c \quad (4.10)$$

where the coefficients, a , b , c for each model are presented in Table 4.1, valid at least on the interval, $A'_i \in [0.02, 0.34]$ and when no bottom friction is included. The resulting permanent waveforms of the FNBM and NSW models for the range of A'_0 are plotted in Figure 4.3 for comparison. Although little difference is noticeable for small values of A'_0 , the wave profile is considerably narrower in the FNBM model as A'_0 increases. Since FNBM models have been shown to accurately reproduce waveforms (c.f Wei and Kirby, 1995) it must be concluded that the NSW model loses accuracy in terms of reproducing the solitary waveform for larger values of A'_0 . The potential wave energy from the plots in Figure 4.3 were calculated and it was found that the relative excessive error of potential wave energy in the NSW model compared with FNBM, E_{re} could be approximated by:

$$E_{re} = 0.342A'_0 - 0.007 \quad (4.11)$$

This means that for $A'_0 = 0.05$ the error is close to 1.0% but for $A'_0 = 0.30$ the error becomes 9.6%. Hence it can be already recommended here that large values of A'_0 should be avoided when using the current 2CLOWNS model.

Concerning the RANS model, a permanent form solution is not pursued since it requires huge computational effort to simulate the wave offshore with sufficient resolution. In fact of

Table 4.1: Coefficients to transfer desired solitary wave height into required input wave height and the average number of wavelengths of propagation to obtain the permanent waveform

Model	Coefficients		
	a	b	c
NSWE	0.2821	1.0147	-0.0003
FNBM	0.0564	1.0102	-0.0002

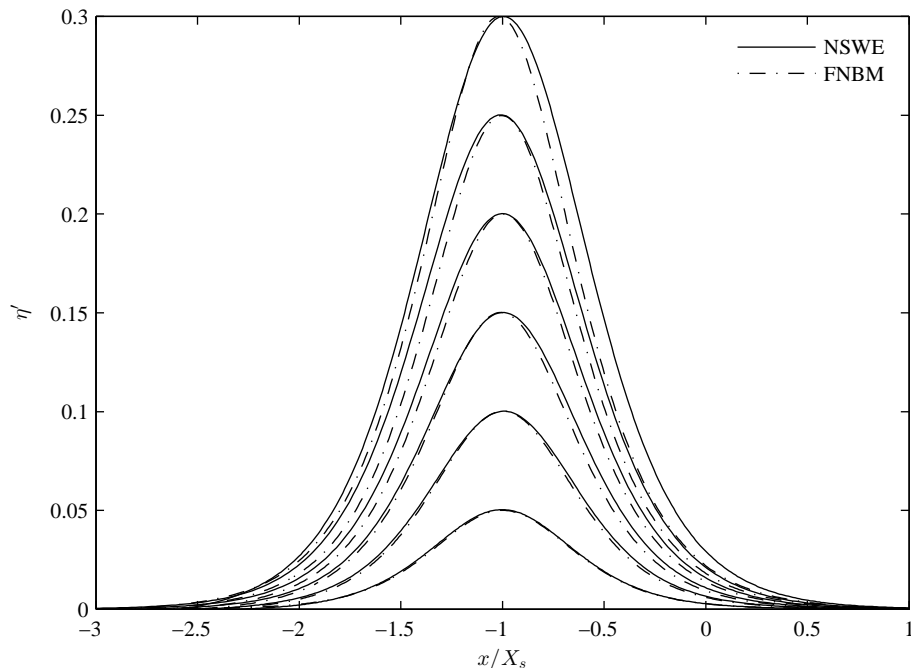


Figure 4.3: Comparison of the offshore permanent waveform centred at $x' = -X'_s$ between the NSWE and FNBM models for the full range of offshore wave heights ($0.05 \leq A'_0 \leq 0.30$) investigated in this study

course, this is one of the main drivers behind using the coupled 2CLOWNS model where it is computationally far more efficient and often more accurate to use the NSWE model offshore. Instead, the target wave height at the lateral boundary condition is adjusted so that the wave height at $x' = -X'_s$ is equal to the desired one. This adjustment depends on how far the lateral boundary is from $x' = -X'_s$ so the coefficients to transform the input wave height to the desired one is not included here as they are far from universal.

4.2.4 Range of Variables Investigated

As mentioned in §4.1, the shoaling of solitary waves on plane beaches has been extensively studied and is particularly useful for tsunami research and as a representation of short waves near breaking. Using 2CLOWNS, Pringle and Yoneyama (2014) showed a preliminary study for non-breaking solitary waves on a 1/20 slope. The model appeared to perform very well in terms of both the coupling and the prediction of free surface profiles, depth-averaged velocities and maximum runup for both the individual NSWE model and the coupled 2CLOWNS model simulating runup in the 2DV RANS domain. Furthermore, it was found that the results were not sensitive to the coupling position since the long wave assumptions are reasonable anywhere in the non-breaking tests. In this study we would like to investigate breaking solitary waves

Table 4.2: Matrix of slopes and offshore wave heights investigated in this study. The values in the cells indicate the value of S_0 and hence breaker types as written underneath

Slope (s)	Offshore wave height (A'_0)					
	0.05	0.10	0.15	0.20	0.25	0.30
1/20	N/A	0.24	0.20	0.17	0.15	0.14
1/35	0.19	0.14	0.11	0.097	0.087	0.079
1/60	0.11	0.08	0.065	0.057	0.051	0.046
1/100	0.068	0.048	0.039	0.034	0.030	0.028

Note: $s = 1/20, A'_0 = 0.05$ case rejected

Breakers types (Grilli et al., 1997):

$0.30 < S_0 < 0.37$: Surging breaker

$0.025 < S_0 < 0.30$: Plunging breaker

$S_0 < 0.025$: Spilling breaker

to determine the limit of applicability and to see if the coupled model can correctly reproduce breaking wave phenomena that is otherwise difficult or impossible for NSW model to reproduce.

Table 4.2 presents the matrix of offshore wave heights and slopes with their corresponding value of S_0 , and hence breaking type according to Grilli et al. (1997). The waves are all plunging breakers which are the most interesting type to test complex breaking behaviour in the RANS model such as wave overturning, touchdown of the plunging jet, and splashup. The slopes from fairly steep to mild have been chosen because experimental and FNPF results are available for a comparison. For example, Hsiao et al. (2008) and Hwang et al. (2007) conducted experiments on the fairly mild 1/60 slope, Grilli et al. (1994, 1997) presents the most detailed data from the FNPF model on the intermediate 1/35 slope (since experiments were also conducted on this slope), and the Synolakis (1986) experiments were conducted on the fairly steep 1/20 slope. The mild 1/100 slope is also chosen because such slopes are common in tsunami cases although limited comparative data is available aside from experimental (Camfield and Street, 1969) and FNPF results for $A'_0 = 0.20$.

4.3 Comparisons of Solitary Wave Shoaling on a Plane Beach for Individual Models

Comparisons between NSWE, full RANS, and FNBM (COULWAVE (Kim et al., 2009)) are investigated in this section to determine the applicable range of each model. The results of the comparison will be a guide to the limitations of each individual model and to determine the optimisation of coupling positions.

4.3.1 Basic Model Comparisons

This section compares solitary wave shoaling up to just beyond the point of decay (usually around the breaking point that can be defined as the point where the vertical tangent develops at the wave front) between the NSWE, FNBM and RANS models for five selected cases to show their individual strengths and weaknesses. The computation for the RANS model begins at the lateral boundary from $x' = -X'_s$ (see Figure 4.1). In terms of computational time, for example on the fairly mild slope, $s = 1/60$ that should take quite long to compute in comparison to the steeper slopes, with $A'_0 = 0.10$ the calculation took 423 minutes on an Intel®Xeon®3.33GHz dual processor with six parallel threads (OpenMP) for 25 s simulation time. It should be kept in mind that the NSWE or even FNBM model can compute such calculations within a minute even from very far offshore (to allow for the permanent form solution to be obtained, c.f. §4.2.3). Additionally, significant numerical dissipation in the RANS model may occur just after the lateral boundary and when propagating from offshore for larger wave heights. These two points are the main disadvantages of the RANS model for wave application that the 2CLOWNS model can ease. Moreover, such factors will of course be much greater in real tsunami applications which are calculated in 2DH/3D, and over much larger scales.

Figure 4.4 plots the local wave height, A' versus the inverse of the dimensionless water depth, h_0/h for the five selected cases which are: (a) $A'_0 = 0.05$ on $s = 1/100$ (b) $A'_0 = 0.10$ on $s = 1/60$, (c) $A'_0 = 0.15$ on $s = 1/35$, (d) $A'_0 = 0.20$ on $s = 1/35$, and (e) $A'_0 = 0.30$ on $s = 1/20$. For the mild slope cases shown in (a) and (b), all models demonstrate identical shoaling rates early on in the region known as the zone of gradual shoaling (Synolakis and Skjelbreia, 1993) that correspond well with Green's law ($\sim h^{-1/4}$). The FNBM and RANS model results start to diverge from those of the NSWE model where the deviation from Green's law is accentuated and the regime enters the zone of rapid shoaling (Synolakis and Skjelbreia, 1993), which is beyond $h_0/h \approx 3.5$ in (a) and $h_0/h \approx 2.3$ in (b). The behaviour of the NSWE model diverging as the regime in the FNBM model changes to rapid shoaling is noted for all the cases. It is in fact clear the the RANS model accurately calculates this rapid shoaling rate as well which is in good agreement with the FNBM until these two models themselves diverge further along the slope. The divergence between the FNBM and RANS models are quite different depending on the slope. For the mild slopes $s = 1/100$ and $s = 1/60$, the RANS model will shoal far more rapidly in the final moments before breaking

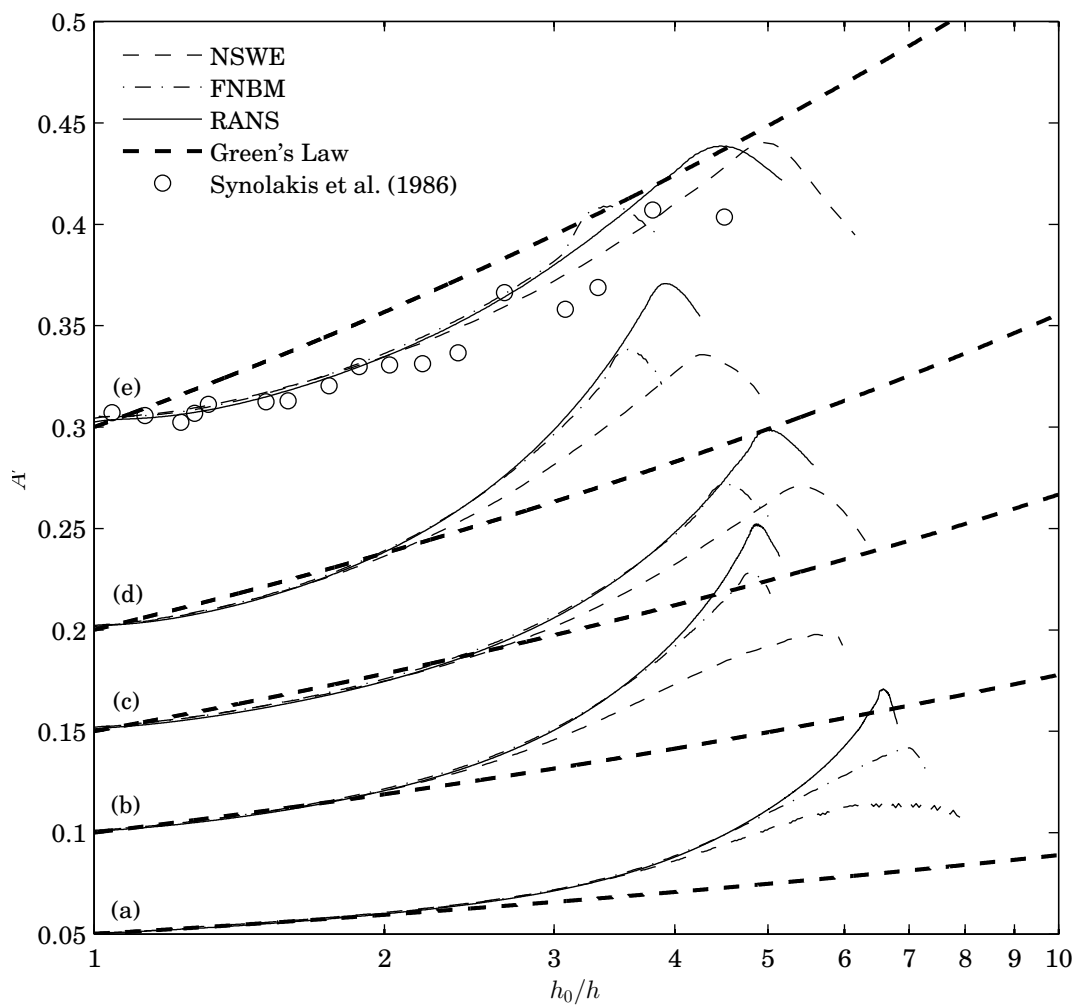


Figure 4.4: Selected solitary wave transformation of the local wave height, A' versus h_0/h comparing: NSWE, FNBM, RANS models, Green's law and Synolakis (1986) experiments in (e). (a) $A'_0 = 0.05$, $s = 1/100$, (b) $A'_0 = 0.10$, $s = 1/60$, (c) $A'_0 = 0.15$, $s = 1/35$, (d) $A'_0 = 0.20$, $s = 1/35$, (e) $A'_0 = 0.30$, $s = 1/20$

than the FNBM and break in similar water depths but with very different breaking wave heights. In contrast, as s is steepened, the FNBM model will start to shoal at similar rates on $s = 1/35$ and even more steeply on $s = 1/20$ just before breaking. In these cases, FNBM will predict breaking in much larger water depths than the RANS model in addition to smaller wave heights at breaking. Additionally, it is noted that as s is steepened, the rate of shoaling predicted by all three models is less steep than Green's law in the gradual shoaling region, which agrees well with the Synolakis (1986) experiments as can be seen on the steep slope (e), and as noted by Grilli et al. (1994).

Overall, the initial shoaling characteristics of FNBM and the RANS model are shown to be comparable at least before the final transformation before wave breaking and decay of the waves deep inside the zone of rapid shoaling. Conversely, after the transition from the zone of gradual shoaling to the zone of rapid shoaling, the NSW model cannot reproduce the required shoaling steepness that is shown by the FNBM and RANS models. It can be hypothesised that this is because of the low-order consideration of the nonlinear terms both analytically and numerically in the NSW model. It would make physical sense that shoaling suddenly becomes rapid as nonlinear effects exceed some critical amount as the wave becomes gradually narrower. Beyond this critical location the nonlinear effects reinforce each other making the wave rapidly steeper and narrower until it destabilises and breaks.

4.3.2 Optimisation of the Coupling Position

This section investigates the shoaling disparities between the NSW model and FNBM for the various wave heights and slopes to find a relationship between calculation conditions and an optimal coupling position. As demonstrated in §4.3.1, FNBM showed similar pre-breaking shoaling characteristics to the RANS model. In addition, Wei et al. (1995) also presents excellent agreement of a FNBM with a FNPF model. Thus, FNBM is taken as a proxy for the correct pre-breaking shoaling characteristics to determine suitable coupling positions between the RANS and NSW models since computations are much faster and generally more reliable (until close to the breaking point) in the FNBM compared to the full RANS simulation. The idea is to identify the position on the slope where the solutions diverge indicating optimal positions for coupling in the 2CLOWNS model.

Plots of A' versus h_0/h are found in Figure 4.5 for the entire range of variables shown in Table 4.2. In all cases it is observable that at some point along the slope the two numerical solutions diverge. This location is at larger values of h_0/h for lower values of A'_0 and larger s . To obtain an empirical equation that describes the location where the two solutions diverge and hence a suitable coupling position, the absolute relative errors in A' between the two models were analysed versus h' . Since the solutions diverge in larger water depths for larger A'_0 and milder slopes, the slope parameter, S_0 combining the two parameters is suitable that will convert the data into a function only of this variable. Through some combination of S_0 and A'_0 ($S_0 A'^{-0.5}$), a logarithmic function was found to approximate the local water depth where the solutions diverge,

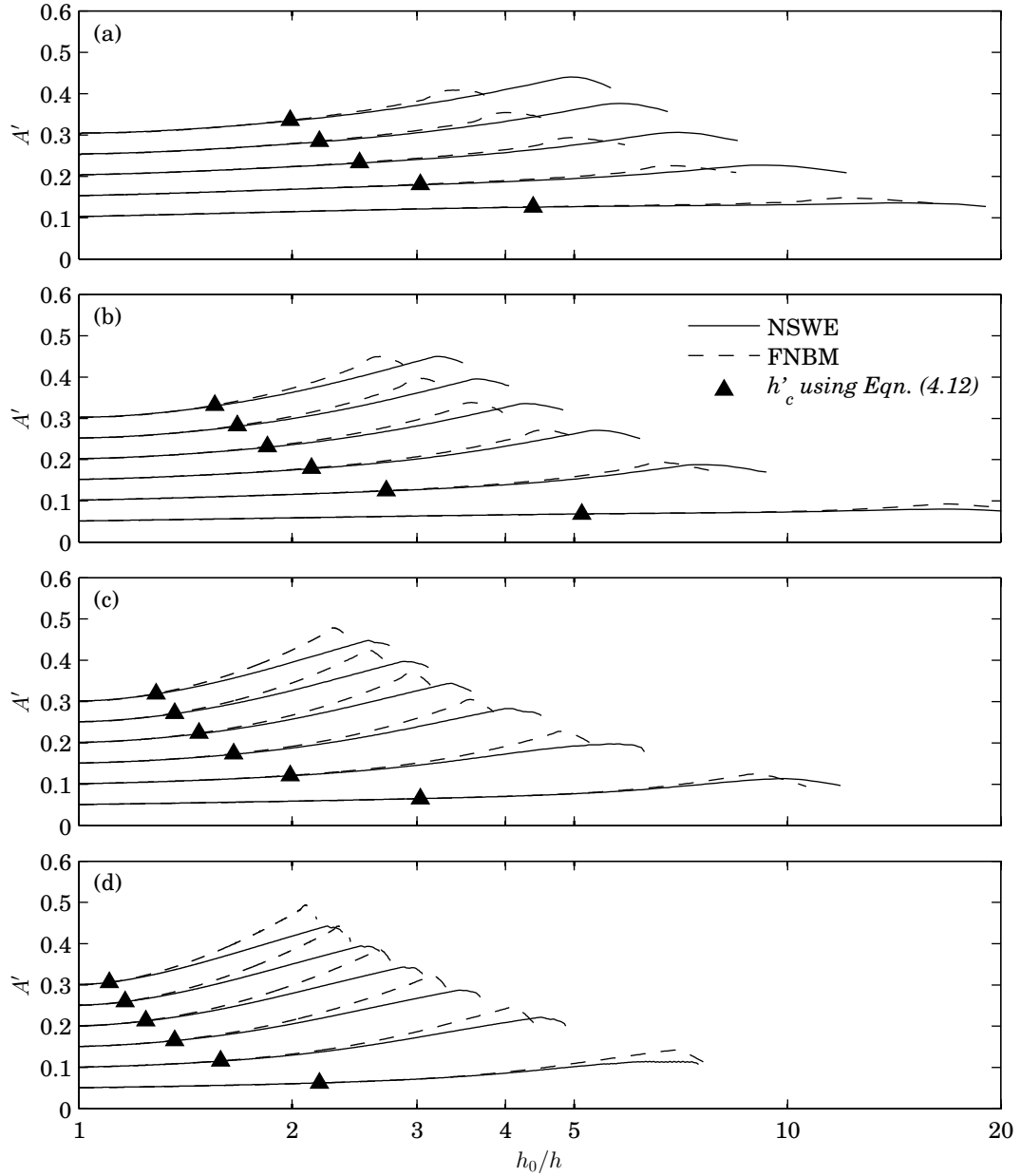


Figure 4.5: Solitary wave transformation of the local wave height, A' versus h_0/h until breaking on various slopes for $A'_0 = 0.05, 0.10, 0.15, 0.20, 0.25$ and 0.30 using NSWE and FNBM models. (a) $s = 1/20$, (b) $s = 1/35$, (c) $s = 1/60$, (d) $s = 1/100$. Filled triangles indicate the water depth, h'_c where divergence of the NSWE and FNBM models is estimated through Eqn. (4.12)

h'_c . To get the exact equation an arbitrary cutoff of the relative error in local wave height between the models, $(A'_{FNBM} - A'_{NSWE})/A'_0$, was varied up to 7.5% to find best fits (least squares error). In general, the greater the cutoff of the error the better the fit which approached $R^2 = 0.995$. Cutoff errors smaller than 1% did not provide reliable equations. However, it is optimal to obtain an equation based on the position where the cutoff error approaches zero. To achieve this the coefficients in each reliable best fit equation ($R^2 > 0.98$) were extrapolated towards a cutoff error of zero. As a result the following equation was approximated:

$$h'_c = 0.16 - 0.25 \ln(S_0 A_0'^{-0.5}) \quad (4.12)$$

The resulting estimates of h'_c in Eqn. (4.12) are included in Figure 4.5 to indicate its effectiveness at estimating the divergence depth for each case. Taking the limits of h'_c to be 1 and 0, it is possible to determine lower and upper bounds of $S_0 A_0'^{-0.5}$ to be 0.035 and 1.9 respectively. For large incident wave heights and/or mild slopes with $S_0 A_0'^{-0.5} < 0.035$ coupling anywhere on the slope is unlikely to be accurate. While $S_0 A_0'^{-0.5} > 1.9$ means that coupling at any position on the slope is possible. In general, $S_0 A_0'^{-0.5} > 1.9$ corresponds to non-breaking or surging breakers so such a conclusion would appear valid. An additional note about Eqn. (4.12) is that the deviation of the NSW and FNBM models has been demonstrated to correspond to the transition from the zone of gradual shoaling to the zone of the rapid shoaling (e.g. Figure 4.4(a),(b) deviation of FNBM from Green's law and NSW both occur at similar locations). Thus, it may be possible to use Eqn. (4.12) to estimate the location of the edge of the gradual shoaling zone as it transitions to the rapid shoaling region. However, further research into the validity of this claim is required.

4.4 Solitary Wave Shoaling and Breaking on a Plane Beach using 2CLOWNS

§4.3.2 demonstrated that the NSWE model was reasonable up to a certain point along the slope before it diverged from the fully nonlinear Boussinesq model, FNBM. Eqn. (4.12) was derived to give a suitable water depth for coupling in 2CLOWNS based on a surf-similarity parameter so that shoaling errors are minimised while keeping the RANS domain as small as possible. This setup is illustrated in Figure 4.6 with appropriate grid sizes also indicated. In this section, initially the basic performance of the 2CLOWNS coupling for selected wave cases is shown in detail in §4.4.1. Here the sensitivity to: two-way coupling versus one-way coupling, the velocity boundary condition for the RANS model, coupling depth, slope and offshore wave height on the performance of coupling is investigated. Following this 2CLOWNS was used to model all the solitary wave cases shown in Table 4.2 and the overall performance for pre-breaking shoaling is summarised.

Furthermore, one of the major advantages of using the RANS model contained within 2CLOWNS compared with a depth-integrated model is that it can simulate wave breaking without ad-hoc dissipaters as well as the overturning wave shape. Moreover, it has advantages over FNFP flow models since it includes viscosity which may be significant for smaller scale waves, and it can model the post-breaking turbulent flow induced during the touchdown of the plunging jet, wave splash-up, bore propagation and resulting runup. With this in mind, this section demonstrates the ability of the 2CLOWNS model not only to reproduce rapid shoaling, but to also predict the wave breaking characteristics and the overturning wave shape. Comparisons are made against FNBM and FNFP flow models plus experimental observations where possible. In addition, vertical profiles of the velocities at selected locations are compared between NSWE and FNBM models to help explain the differences between the models. Analysis of the post-breaking turbulent flow and runup will be left to future studies.

4.4.1 Basic Evaluation of 2CLOWNS Coupled Model

This section summarises the basic performance of the coupling between the NSWE and RANS models. Three different aspects are investigated: a test of the two-way coupling and velocity boundary conditions, how the position (water depth) of coupling will affect the solution, and how the slope and offshore wave height can impact on the performance at the coupling interface.

Examples of the difference in calculation time between the singular RANS and 2CLOWNS simulations are summarised in Table 4.3. The major contributor to the difference in the computational times is the reduction in the number of cells by coupling far up the slope reducing both horizontal and vertical cell numbers. Calculation times are shown for the time it takes for the wave to travel from $x' = -X'_s$ to far up the slope in small water depths ($h' = 0.10$). Hence this is a conservative comparison of the difference in calculation times expected during realistic scenarios

4.4. SOLITARY WAVE SHOALING AND BREAKING ON A PLANE BEACH USING 2CLOWNS

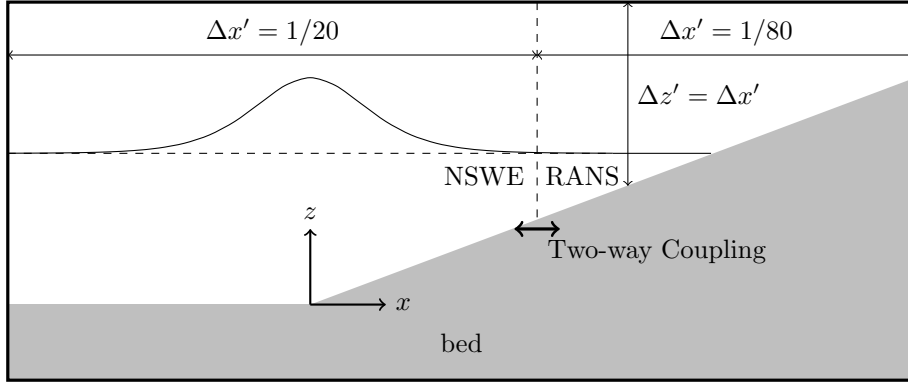


Figure 4.6: Illustration of the usual setup of the 2CLOWNS model with appropriate grid sizes indicated. The suitable location for coupling (approximation of interface between gradual and rapid shoaling) may be estimated from Eqn.(4.12)

Table 4.3: Computational time taken for wave to travel from $x' = -X'_s$ to $h' = 0.10$ depending on RANS or 2CLOWNS simulations each conducted using six OpenMP threads

Conditions		Simulation time (min)		Comparison (%)
s	A'_0	RANS	2CLOWNS	2CLOWNS/RANS
1/100	0.05	931	58	6.2
1/60	0.10	423	44	10
1/35	0.15	64	12	19
1/35	0.20	92	20	22
1/20	0.30	44	5	11

when a wave may be propagated from far offshore. In such a case an even larger proportion of the calculation time will be reduced because during the initial propagation from offshore towards the slope only the NSWE model would be utilised until the wave reaches the RANS domain and the RANS model is switched on. For real tsunami simulations conducted in 2DH the potential for time reduction will be much greater given the size of the overall calculation domain beginning from possibly the tsunami source.

In addition, the ratio of spatial and temporal resolution between the NSWE and RANS models was, $\Delta x'_{NSWE}/\Delta x'_{RANS} = 4$ and $1 < \Delta t_{NSWE}/\Delta t_{RANS} < 21$ respectively for all simulations. $\Delta t_{NSWE}/\Delta t_{RANS}$ may be initially equal to 1 because of the smaller depth in the RANS domain compared with the NSWE one balancing the difference in cell resolution. However, $\Delta t_{NSWE}/\Delta t_{RANS}$, became as large as 21 during violent wave breaking. It did not appear that the difference in model resolutions, particularly the temporal ones, had any negative effect on the coupling performance. Additional simulations however did hint that overly large ratios of $\Delta x'_{NSWE}/\Delta x'_{RANS}$ would lead to poor performance at the coupling interface identified through

Table 4.4: Test combinations used to investigate two-way coupling and the effects of the RANS velocity boundary condition

Case Name	1-way	2-way	uniform u	no gradient on u''	linear w	no gradient on w
1CLOWN UL	○		○		○	
1CLOWN UN	○		○			○
2CLOWNS UL		○	○		○	
2CLOWNS UN		○	○			○
2CLOWNS NN		○		○		○

animations of the waveform. Hence it is recommended here that $\Delta x'_{NSWE}/\Delta x'_{RANS}$ is limited to no more than 4 or 5.

Two-way Coupling and Boundary Condition Test

A test of the two-way coupling scheme and the differences due to the boundary condition for the RANS model i.e. the assumption on the velocity profile specified is investigated in this section. The different combinations of one-way or two-way coupling and the type of velocity profiles tested are defined in Table 4.4. Here, 1-way and 2-way refer to one-way and two-way coupling. Uniform u and no gradient on u'' refer to the vertical distribution of the horizontal velocity as a boundary condition to the RANS model. Uniform means that the shallow water assumption is applied and u is constant over the depth (Eqn. (3.135)). No gradient on u'' is the condition where the difference from the depth-averaged velocity is set to zero across the interface, i.e. the velocity profile of the RANS model itself in the cell column adjacent to the coupling interface is used to form the vertical distribution (Eqn. (3.136)). Linear w and no gradient on w refer to the vertical distribution on the vertical velocity as a boundary condition to the RANS model. Linear is the shallow water assumption that the vertical velocities follow a linear distribution from zero at the seabed to a maximum at the free surface (Eqn. (3.138)). No gradient uses the velocity profile of the RANS model in the cell column adjacent to the coupling interface to set a no gradient condition on w (Eqn. (3.140)).

Firstly, primarily the efficacy of the two-way coupling scheme is investigated. For this test incident solitary waves of $A'_0 = 0.05$ and $A'_0 = 0.15$ are reflected off a vertical wall using both the singular RANS and two-way coupled 2CLOWNS models. The coupling in the 2CLOWNS model takes place a distance $x' = 5$ from the vertical wall. Two versions of 2CLOWNS are run (2CLOWNS NN and 2CLOWNS UL) to compare results based on the velocity boundary condition. Snapshots of both the incident wave profiles and reflected wave profiles are plotted in Figure 4.7. In both tests it is demonstrated that the incident waves travel through from the NSWE domain into the RANS domain and that the reflected waves also freely travel back from the RANS domain into the NSWE domain. In the case of $A'_0 = 0.05$, no particular disparities are apparent between both 2CLOWNS simulations and the RANS one. However, as A'_0 is increased to $A'_0 = 0.15$ the

4.4. SOLITARY WAVE SHOALING AND BREAKING ON A PLANE BEACH USING 2CLOWNS

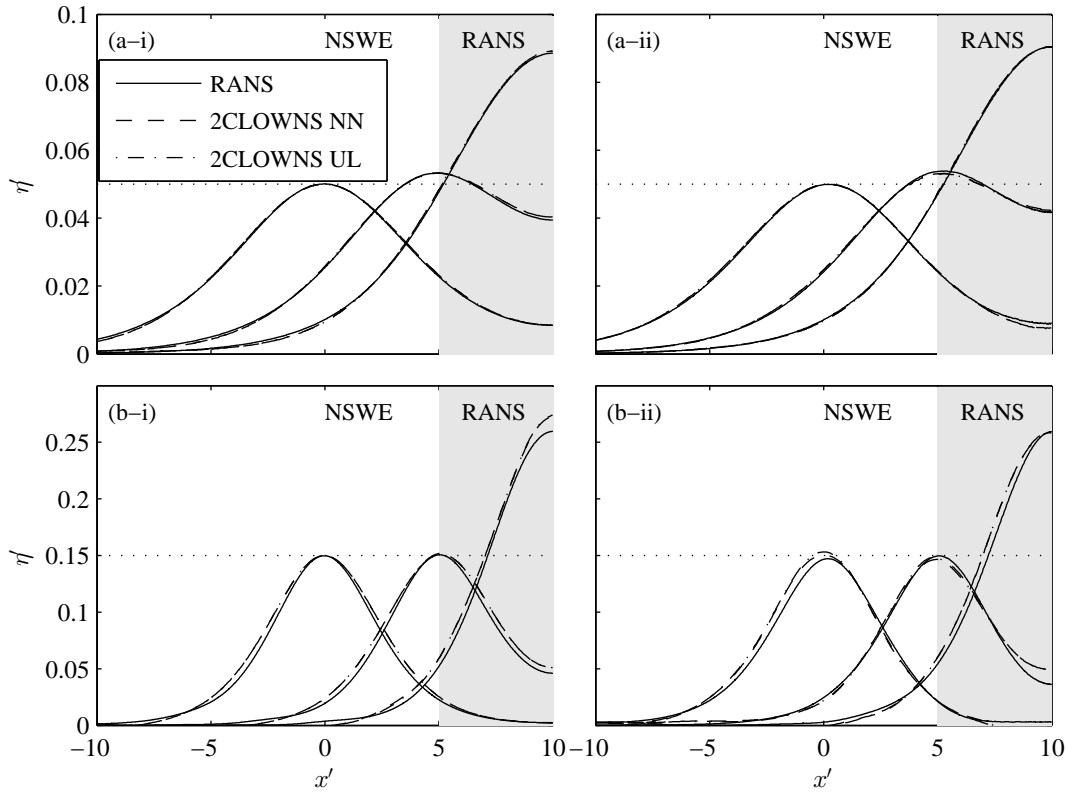


Figure 4.7: Snapshots of the wave profile of incident waves and waves reflected off the vertical wall on the right, comparing the singular RANS simulation with 2CLOWNS ones (coupling takes place at $x' = 5$) where two types of coupling boundary conditions for the velocity profiles are used. (a) $A'_0 = 0.05$, (b) $A'_0 = 0.15$, (i) incident waves, (ii) reflected waves.

profile of the incident wave in the NSWE model is slightly wider than the RANS one. This fact has already been discussed in §4.2.3 comparing the NSWE and FNBM solutions, where it was shown that the potential energy of the wave is greater in the NSWE model. Apparently, due to this extra energy the incident wave travelling from the NSWE domain into the RANS domain becomes larger close to the vertical wall than recorded in the RANS simulation. Finally, after the wave is reflected back out from the RANS domain into the NSWE one the wave height has indeed become slightly larger even in the NSWE domain. In both tests the results were not demonstrably sensitive to the velocity profile boundary condition to the RANS model. One noticeable difference appears for the reflected wave in the NSWE domain in the $A'_0 = 0.15$ case where the 2CLOWNS NN simulation gives a smaller wave height that is closer to the RANS result.

Secondly, the effect of one-way or two-way coupling and the different combinations of the velocity profiles are investigated. In the first test coupling takes place on a flat bed and little difference arises between the 2CLOWNS NN and 2CLOWNS UL simulations. However, if coupling takes place on a steep slope differences arising from the assumption of the velocity

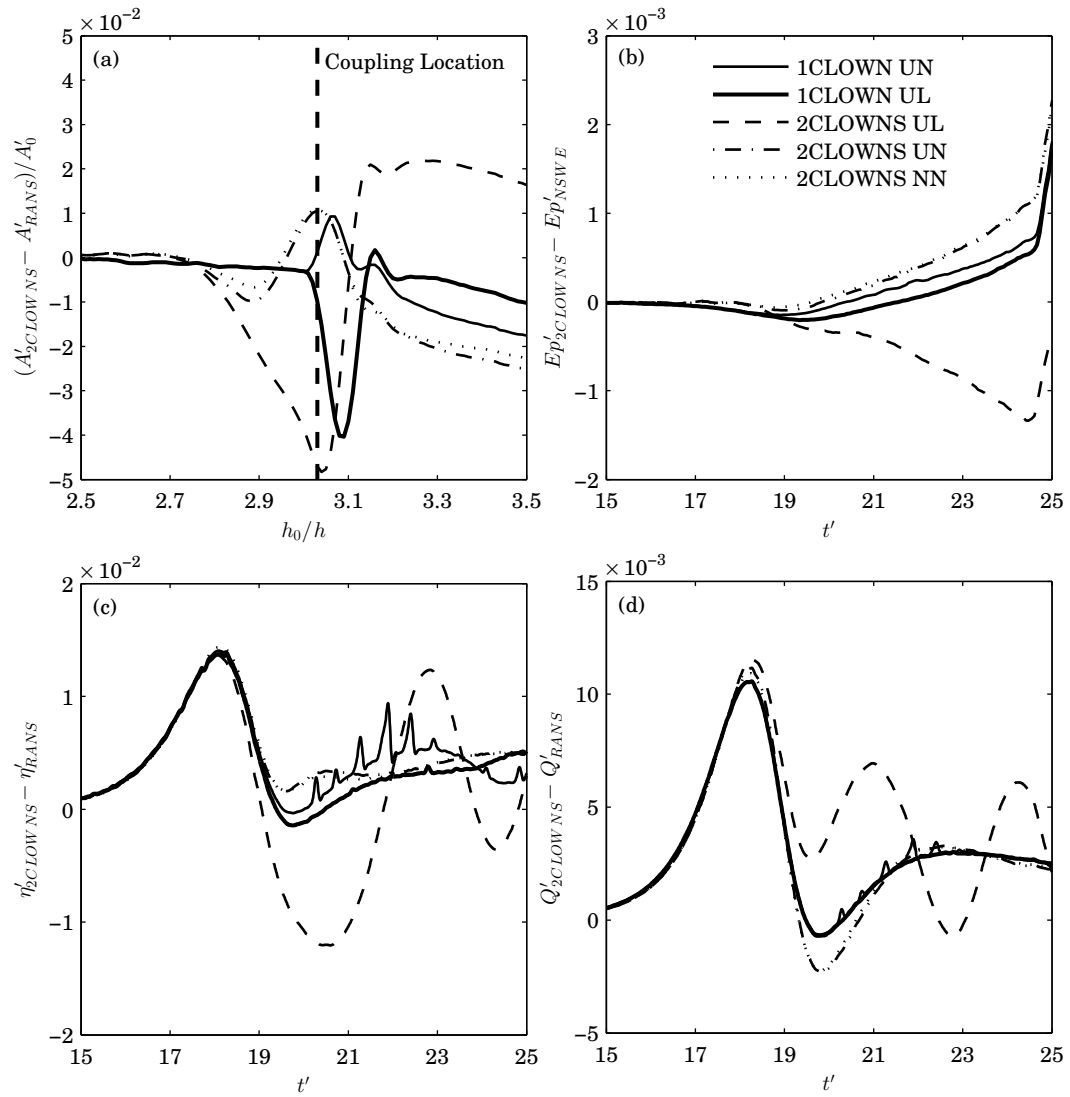


Figure 4.8: Testing of one-way and two-way coupling (at $h_0/h_c = 3.03$), and the velocity boundary condition type for $A'_0 = 0.15$ on $s = 1/20$ as summarised in Table 4.4. Plots show differences between 2CLOWNS simulations and the singular RANS one; (a) difference in the local wave height, A' normalised by A'_0 versus h_0/h , (b) difference in the potential energy of the entire computational domain, Ep' versus t' , (c) difference in the the free surface level, η' at the coupling interface ($h_0/h_c = 3.03$) versus t' , (d) difference in the the volume fluxes, Q' at the coupling interface ($h_0/h_c = 3.03$) versus t'

4.4. SOLITARY WAVE SHOALING AND BREAKING ON A PLANE BEACH USING 2CLOWNS

profile is likely to become more apparent. In this step the slope is chosen to be $s = 1/20$ and the offshore wave height $A'_0 = 0.15$ is selected. A singular RANS simulation and all five combinations of 2CLOWNS simulations as specified in Table 4.4 is conducted for comparison. Eqn. (4.12) is used to determine the coupling location, $h'_c = 0.33$ ($h_0/h_c = 3.03$).

Figure 4.8(a) plots the difference in the local wave height around the coupling location between the 2CLOWNS and singular RANS simulations normalised by A'_0 , i.e. $(A'_{2CLOWNS} - A'_{RANS})/A'_0$. The target wave height of the RANS solution was adjusted so that there is almost zero difference offshore. At the interface where coupling occurs, $(A'_{2CLOWNS} - A'_{RANS})/A'_0$ rises and falls to different degrees depending on the boundary condition. For both 1CLOWN cases the effects are only noticeable after the coupling interface in the RANS domain. A large drop in the wave height takes place just inside the RANS domain equivalent to a maximum of 4.0% before recovering some small distance further onshore for 1CLOWN UL. In comparison, a rise smaller in magnitude (0.9%) occurs for 1CLOWNS UN. When two-way coupling is used the transfer of the information from the RANS domains affects the local wave height inside the NSWE domain as well. For the 2CLOWNS UL simulation the drop in the wave height around the coupling interface becomes even greater than 1CLOWN UL (maximum of 4.8%). Thereafter, the wave height actually becomes larger than the RANS simulation up to a maximum of 2.2%. The 2CLOWNS UN simulation results in a slight rise in the wave height around the coupling interface equal to a maximum of 1.1%.

Figure 4.8(b) plots the difference in the potential energy of the wave over the entire computational domain, Ep' between the 2CLOWNS and NSWE simulations, i.e. $Ep'_{2CLOWNS} - Ep'_{NSWE}$ versus t' . Ep' is defined here as:

$$Ep' = \int_{x'_0}^{s^{-1}} \left[(\eta' + h') \frac{\eta' + h'}{2} - h' \frac{h'}{2} \right] dx' \quad (4.13)$$

where x'_0 indicates the ordinate of the offshore lateral boundary and s^{-1} indicates the position of the shoreline which does not change in the time interval shown. Figure 4.8(b) indicates whether the potential energy is conserved during coupling (the peak of the wave passes the coupling position at $t' \approx 19.5$). For $t' < 19.5$, in both 1CLOWN simulations $Ep'_{2CLOWNS}$ drops slightly in comparison to Ep'_{NSWE} while the potential energy of the 2CLOWNS simulations remain roughly the same. This indicates that two-way coupling allows the potential energy to be correctly conserved across the boundary while one-way coupling cannot achieve this balancing effect. For $t' > 19.5$ after the peak of the wave has passed the coupling position, $Ep'_{2CLOWNS}$ starts to increase relative to Ep'_{NSWE} for all cases except 2CLOWNS UL. The increase of $A'_{2CLOWNS}$ for 2CLOWNS UL as plotted in Figure 4.8(a) appears to correspond to a smaller value of the potential energy where it is converted into kinetic energy more quickly.

Figure 4.8(c) and Figure 4.8(d) plot the difference in the free surface level, η' and the volumes fluxes, Q' at the coupling interface ($h_0/h_c = 3.03$) respectively between the 2CLOWNS simulations and the singular RANS one, i.e. $\eta'_{2CLOWNS} - \eta'_{RANS}$ and $Q'_{2CLOWNS} - Q'_{RANS}$. Initially, for $t' < 19.5$

both $\eta'_{2CLOWNS}$ and $Q'_{2CLOWNS}$ are larger than those in the RANS model because of the increase in the width of the wave as plotted in Figure 4.7(b-i). But at the time of the wave peak at $t' \approx 19.5$ the differences between the simulations become relatively small except for the 2CLOWNS UL case which is vastly different to the other cases and can be ignored. For $t' > 19.5$ the differences in η' and Q' increase again but to a smaller extent than $t' < 19.5$. Comparing the 2CLOWNS UN and NN simulations with the 1CLOWN simulations shows how the interaction between the RANS and NSWE models affect the input into the RANS domain itself. Q' into the RANS domain was reduced in the 2CLOWNS UN and NN simulations between $19 < t' < 21$ presumably because of the higher free surface level inside the RANS domain in comparison to the NSWE one in this time frame. The effect of this was to keep $\eta'_{2CLOWNS}$ slightly above and steady against η'_{RANS} . In comparison the 1CLOWN simulations show a dip and rise of $\eta'_{2CLOWNS}$ in this time frame. The 1CLOWN UN result for $\eta'_{2CLOWNS}$ shows numerous spikes against η'_{RANS} for $t' > 20$. This is likely related to the reflections resulting from the differences between the RANS and NSWE models that are otherwise allowed to escape back into the NSWE model when two-way coupling is invoked. On inspection of the model, small humps in the free surface near the boundary could be clearly seen in both 1CLOWN simulations. For what appears simply by chance these did not affect the free surface right at the coupling interface in the 1CLOWN UL simulation. The existence of small humps in the free surface were not present in the two-way simulations.

Overall, the best condition in Figure 4.8 is found to be 2CLOWNS NN which best conserves the potential energy across the boundary and produces a relatively small change in the local wave height. Furthermore, the difference in η' is relatively small and steady after the wave peak passes through the coupling interface. This was achieved by adjustment in Q' through the boundary to account for reflections from the RANS domain. It also noted that the 2CLOWNS NN and 2CLOWNS UN results are almost identical indicating that the change in wave height is primarily sensitive to the distribution of the vertical velocity rather than the horizontal velocity. On inspection of the horizontal velocity profiles, u' shown in Figure 4.9, clear disparity between the 2CLOWNS UN and 2CLOWNS NN simulations are shown. At $t' = 17.6$ profiles of u' in both simulations are quite different from those of the RANS simulation because of the greater volume flux entering the domain at this point in time (see Figure 4.8(d)). At $t' = 19.6$ where the volume fluxes are in good agreement with the RANS simulation, there is a large curvature in u' that the 2CLOWNS NN simulation can partially replicate. The velocity near the bed and the free surfaces in 2CLOWNS NN are in particularly good agreement with the RANS simulation but some disparity is demonstrated at mid-depths. By $t' = 21.6$ the non-uniformity of u' is small in the RANS simulation except near the sea bed which the 2CLOWNS NN model also predicts. However, in other areas the 2CLOWNS NN velocity profile is quite different from the singular RANS one where 2CLOWNS UN gives a better estimate. This may be especially evident in this simulation in relatively small depths on the steep slope where coupling is not easily achieved. On milder slopes and in greater coupling depths better agreement should be more likely.

4.4. SOLITARY WAVE SHOALING AND BREAKING ON A PLANE BEACH USING 2CLOWNS

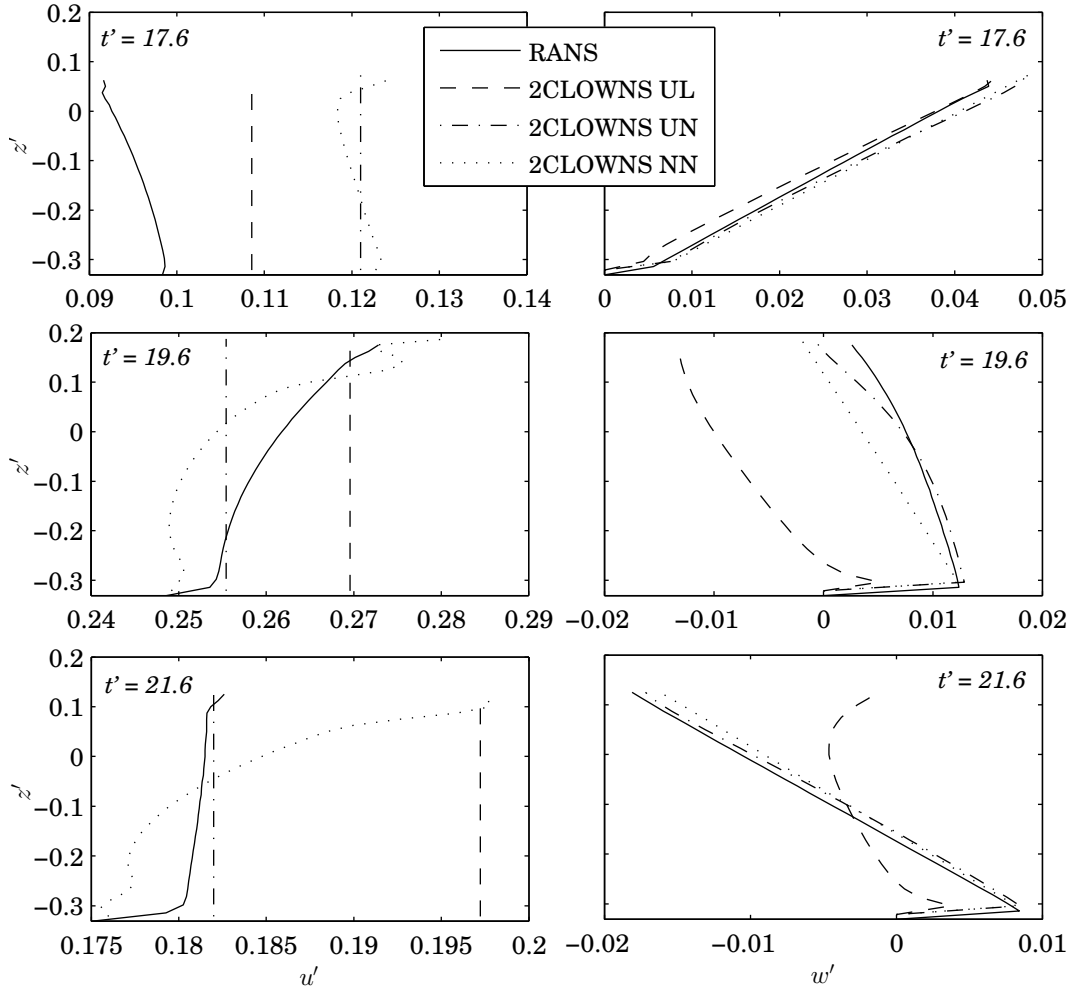


Figure 4.9: Velocity profiles (u' on the left and w' on the right) measured at the coupling interface ($h_0/h_c = 3.03$) at three snapshots in time for the $A'_0 = 0.15$ on $s = 1/20$ case comparing the singular RANS simulation result with 2CLOWNS simulations

Whether conducting either one-way or two-way coupling the no gradient condition on w' generally gives better results than the linear distribution on w' . For example, Figure 4.9 illustrates that early on the linear profile of w' derived from the NSW equations gives a suitable boundary condition at $t' = 17.6$. However, at later times the boundary condition cannot be an accurate one since the profile of w' in the first column of the RANS domain (as plotted) becomes curved and very different from the no gradient conditions which largely agree with those in the singular RANS simulation.

Sensitivity to Coupling Depth

In this section the effect of coupling at different positions or local water depths, h'_c is assessed. The offshore wave height, $A'_0 = 0.15$ is chosen and simulated on three of the slopes, $s = 1/20$, $1/35$, and $1/60$. Comparisons are made between coupling in 2CLOWNS NN at three different values of h'_c . Eqn. (4.12) is used to get the “optimal” h'_c for each slope. Two other test depths are used; 1) in between the toe of the slope and the optimal h'_c , and 2) in between the estimate of the breaking point and the optimal h'_c . Figure 4.10 plots the difference in the local wave height normalised by A'_0 between the 2CLOWNS and singular RANS simulations during shoaling, i.e. $(A'_{2CLOWNS} - A'_{RANS})/A'_0$.

The idea of Figure 4.10 is to show that if coupling takes place in small depths further from the optimal h'_c then $A'_{2CLOWNS}$ will diverge far from A'_{RANS} . On the other hand, coupling in depths larger than the optimal h'_c may produce similarly accurate results but the size of the RANS domain and hence calculation time will be unnecessarily extended. Indeed if coupling takes place in small depths on each slope, initially the NSWE solution diverges from the RANS one even before coupling as expected. At the coupling interface a hump-like increase and decrease in $A'_{2CLOWNS}$ occurs before extremely rapid shoaling takes place where, for example, the wave height almost returns to the RANS one on $s = 1/60$ in Figure 4.10(c). The magnitude of the increase and decrease of $A'_{2CLOWNS}$ around the coupling location is larger for smaller coupling depths. Comparing coupling in larger depths than coupling at the optimal h'_c , the general trend is that $A'_{2CLOWNS}$ will end up being greater in the former situation. The accuracy of either solution in comparison to A'_{RANS} is dependent on the slope. On $s = 1/20$ the best result in terms of the final $A'_{2CLOWNS}$ near breaking point is the case where coupling takes place in large depths ($h'_c = 0.50$) rather than the optimal ($h'_c = 0.33$). On the other hand, the best results for $s = 1/35$ and $s = 1/60$ occur when coupling takes place at the optimal depth.

Hence, Eqn. (4.12) may not be particularly accurate on $s = 1/20$ where it would be better to couple in even larger depths. However, the fact that coupling in larger depths on $s = 1/35$ and $s = 1/60$ induces over-shoaling means that the wave in the 2CLOWNS model with offshore wave height, $A'_0 = 0.15$ has the propensity to shoal at greater rates than the singular RANS model. This presumably is due to greater volume flux entering the domain from the NSWE model into the RANS model as plotted in Figure 4.8(d). This is related to the extra potential energy of the waveform in the NSWE model which can be estimated as being $\approx 4.4\%$ larger offshore according to Eqn. (4.11). In other words, the issue is related to the NSWE solution rather than the coupling scheme itself. To confirm this Figure 4.10(d) plots examples of similar set-ups to (a)-(c) for $A'_0 = 0.05$ ($\approx 1.0\%$ error of potential energy) on $s = 1/100$. Here, when coupling at large depths or the optimal one ($h'_c = 0.63$ or $h'_c = 0.46$ respectively) the final wave height at breaking is essentially identical. A slight decrease in A' occurs after coupling at the optimal location while this is not evident when coupling in the deeper location on the slope. This small decrease is offset by a faster computational time and the ability to estimate breaking at the same location in the

4.4. SOLITARY WAVE SHOALING AND BREAKING ON A PLANE BEACH USING 2CLOWNS

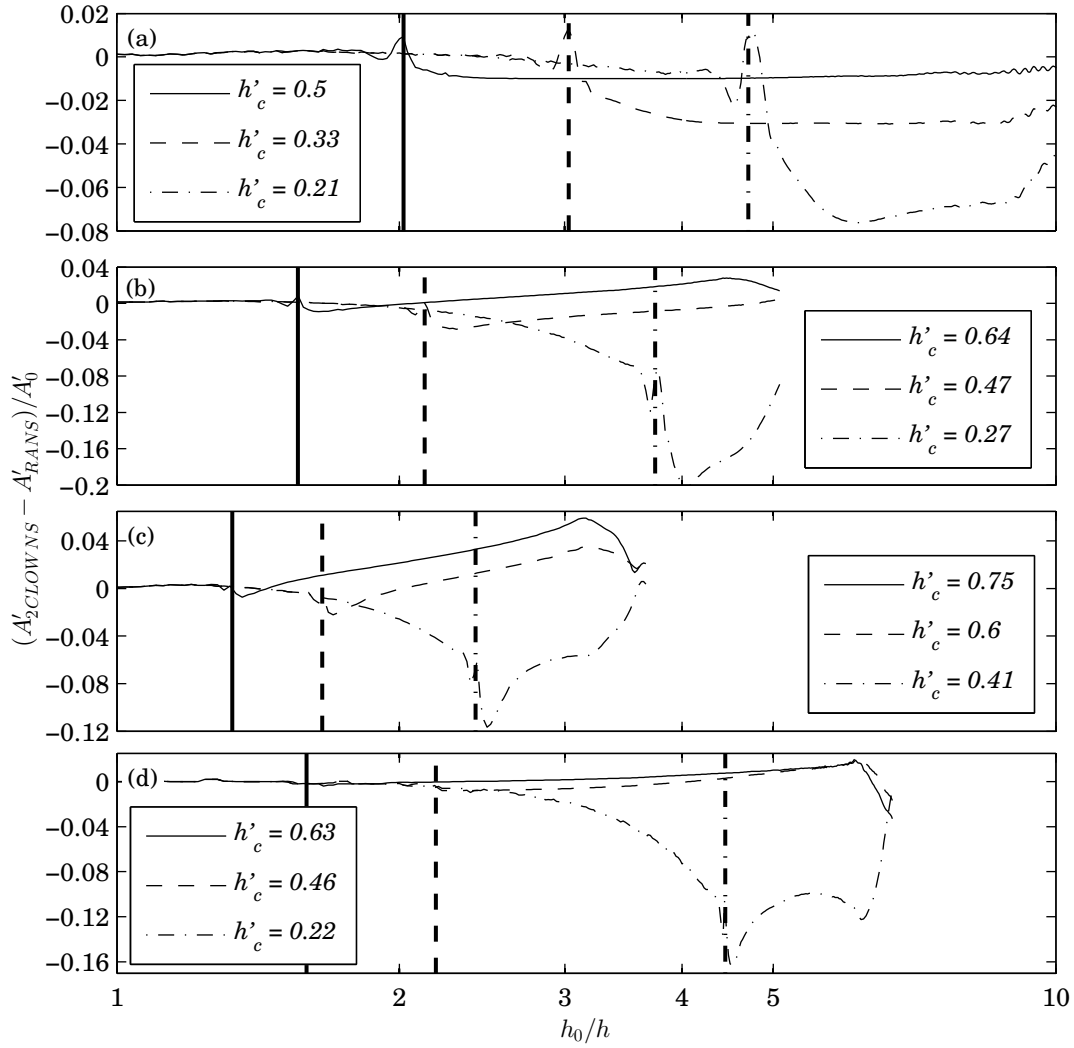


Figure 4.10: Difference in the local wave height, A' normalised by A'_0 between 2CLOWNS NN and singular RANS simulations until wave breaking. Coupling at three different depths for each slope (positions indicated by the vertical lines) are conducted where the middle depth is derived from Eqn. (4.12) and the other two coupling depths are in between this location and; the toe of the slope and breaking point respectively. (a) $A'_0 = 0.15$ on $s = 1/20$, (b) $A'_0 = 0.15$ on $s = 1/35$, (c) $A'_0 = 0.15$ on $s = 1/60$, (d) (c) $A'_0 = 0.05$ on $s = 1/100$

end. However, when coupling takes place in very shallow depths ($h'_c = 0.22$) the solution diverges far from the RANS one similar to in Figure 4.10(a)-(c).

The optimal location is hence shown to be fairly effective in order to mimic rapid shoaling and breaking wave heights computed in a singular RANS simulation. In one case, ($A'_0 = 0.15$ on $s = 1/20$) the optimal location produced noticeably worse results than coupling in greater depths. Hence, Eqn. (4.12) perhaps should be re-evaluated separately on steep slopes. However, for tsunami-like problems with mild slopes and small wave heights coupling at the depths predicted by Eqn. (4.12) appears reasonable.

Sensitivity to Slope and Offshore Wave Height

To get a brief idea of the performance of 2CLOWNS with different slopes and offshore wave heights, snapshots of the waveform where the peak is centred on the coupling position (calculated using Eqn. (4.12)) are shown in Figure 4.11 and Figure 4.12 comparing NSWE, RANS and 2CLOWNS NN simulations.

Figure 4.11 plots $A'_0 = 0.05, 0.15,$ and 0.30 on $s = 1/35$. The waveforms of all the models conform best for $A'_0 = 0.05$ which has been shown to be true even offshore in Figure 4.3 where the NSWE permanent waveform is wider than that in the FNBM and RANS models. For $A'_0 = 0.15$ and 0.30 it is even noticeable that the 2CLOWNS waveform slightly deviates from the NSWE one due to the influence of the RANS calculation. Inside the RANS domain the 2CLOWNS NN waveform tends to be closer to that of the NSWE model so that the wave front is further onshore than the RANS one. This is because the NSWE model is used to generate the wave inside the RANS domain. For $A'_0 = 0.30$ in particular the wave front is even further onshore than the NSWE waveform and a small hump in the waveform at the coupling interface is noticeable.

Figure 4.12 plots $A'_0 = 0.15$ and $s = 1/20, 1/60,$ and $1/100$. The major differences between the waveforms are that the 2CLOWNS results diverges further from the NSWE one on the steeper slopes. The waveform is also more asymmetric and a greater hump exists at the coupling interface for the 2CLOWNS simulation on the steeper slope where coupling occurs in smaller depths than on mild slopes. Figure 4.10 also demonstrates how the steeper slope can increase the hump in A' at the coupling interface. Furthermore, it was shown that coupling in greater depths on $s = 1/20$ would give a better result. An improved version of Eqn. (4.12) could take into account the difficulty of coupling at small depths on steep slopes even though divergence of A' between NSWE and FNBM (or RANS) is still small.

All the experimental cases were simulated using 2CLOWNS NN. The results of wave transformation until breaking is plotted in Figure 4.13. It is shown that in all cases there is a small decrease in $A'_{2CLOWNS}$ near the coupling interface inside the NSWE domain and a larger increase in $A'_{2CLOWNS}$ just inside the RANS domain. To better quantify this effect when adopting the optimised coupling location (Eqn. (4.12)) for different slopes and offshore wave heights, the relative error of the local wave height in 2CLOWNS NN simulations against FNBM ones in

4.4. SOLITARY WAVE SHOALING AND BREAKING ON A PLANE BEACH USING 2CLOWNS

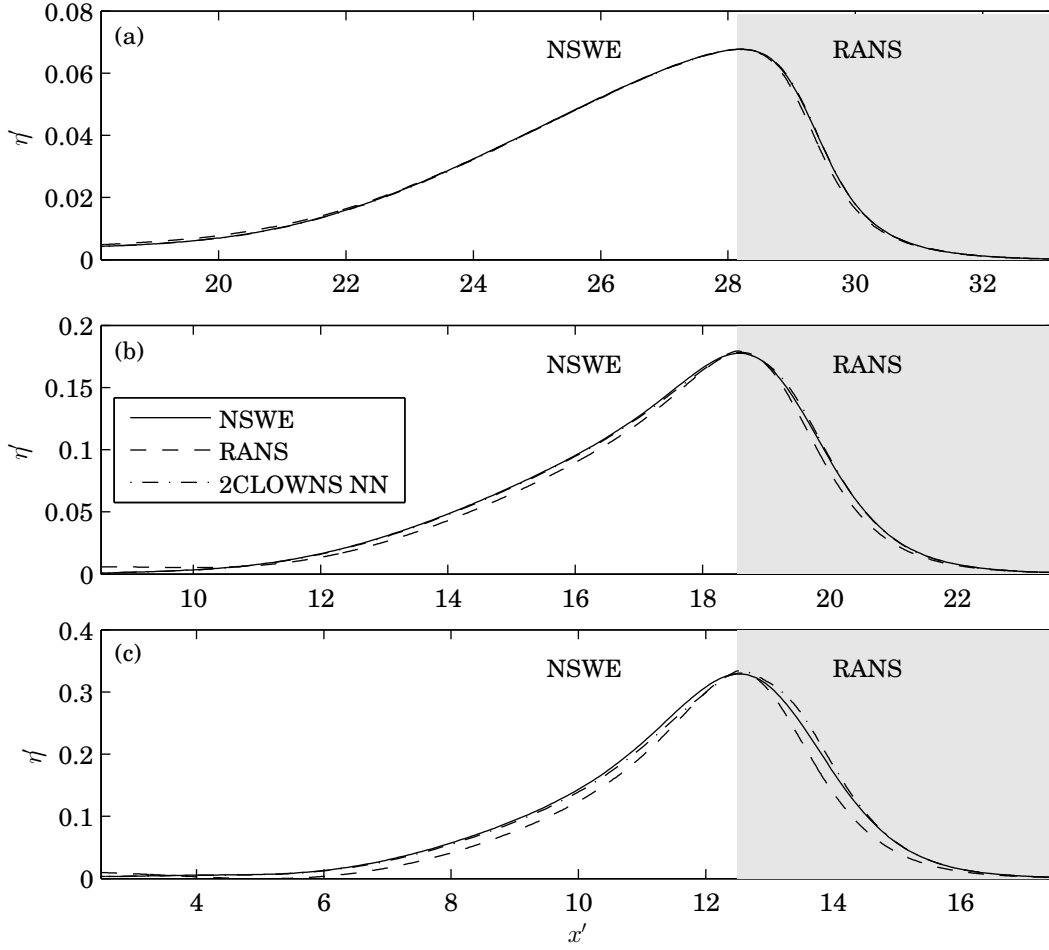


Figure 4.11: Snapshots of selected solitary waves on $s = 1/35$ centred on the 2CLOWNS coupling position calculated using Eqn. (4.12). Shaded area indicates RANS domain in 2CLOWNS simulation. (a) $A'_0 = 0.05$, (b) $A'_0 = 0.15$, (c) $A'_0 = 0.30$

the vicinity of the coupling interface, i.e. $(A'_{2CLOWNS} - A'_{FNBM})/A'_{FNBM}$, was calculated for all experimental combinations. The difference between these two local maximum and minimums of $(A'_{2CLOWNS} - A'_{FNBM})/A'_{FNBM}$, denoted A_{RE} was calculated and the following empirical equation ($R^2 = 0.994$) was derived based on some combination of S_0 and s ($S_0 s^{-1.095}$):

$$A_{RE} = 0.132 \exp(-0.410 S_0 s^{-1.095}) \quad (4.14)$$

The data points along with the best fit line (Eqn. (4.14)) is plotted in Figure 4.14 for reference. The negative exponential function of the parameter $S_0 s^{-1.095}$ in Eqn. (4.14) implies that errors at the coupling interface increase with both s and A'_0 . The effect of A'_0 on A_{RE} is significantly stronger than the effect of the slope ($A_{RE} \sim A_0^{-0.5}, s^{-0.095}$). It is probable that the dependency of Eqn. (4.14) on s could in fact be removed by improving Eqn. (4.12) to take into account the

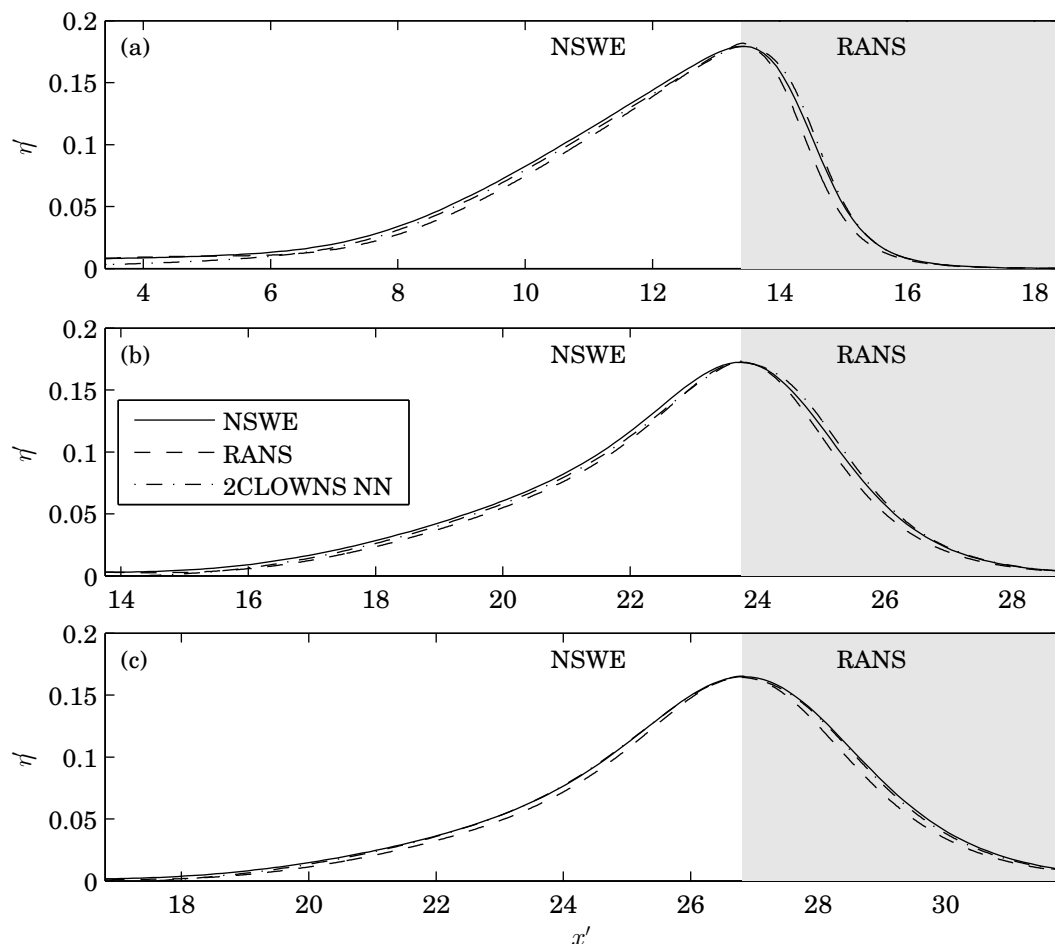


Figure 4.12: Snapshots of solitary waves with $A'_0 = 0.15$ on various slopes centred on the 2CLOWNS coupling position calculated using Eqn. (4.12). Shaded area indicates RANS domain in 2CLOWNS simulation. (a) $s = 1/20$, (b) $s = 1/60$, (c) $s = 1/100$

increased difficulty of coupling in the shallower depths that Eqn. (4.12) prescribes on steeper slopes. Thus, the major errors associated with coupling are mostly due to the difference in the permanent waveforms between the governing equations. If high-order models such as the FNBM one is used instead of the NSWE model to couple with the RANS model (c.f. Sitanggang and Lynett, 2010) the coupling will most likely improve. However, it is stressed that for large values $S_0 s^{-1.095}$ the use of the NSWE model is highly recommended given its efficiency in computation over wide areas and simplicity in grid nesting. This condition is also likely to be satisfied in most cases of tsunami and other long wave problems. For example, the minimum value of $A_{RE} = 0.0018$ occurs at the maximum value of $S_0 s^{-1.095} = 10.5$ ($A'_0 = 0.05$ and $s = 1/100$). Setting an arbitrary allowable limit on A_{RE} to 1% for example would require $S_0 s^{-1.095} > 6.3$. This limits the offshore wave height to, $A'_0 \leq 0.103$ on the steepest slope ($s = 1/20$) and to, $A'_0 \leq 0.140$ on the mildest slope ($s = 1/100$) investigated in this study.

4.4. SOLITARY WAVE SHOALING AND BREAKING ON A PLANE BEACH USING 2CLOWNS

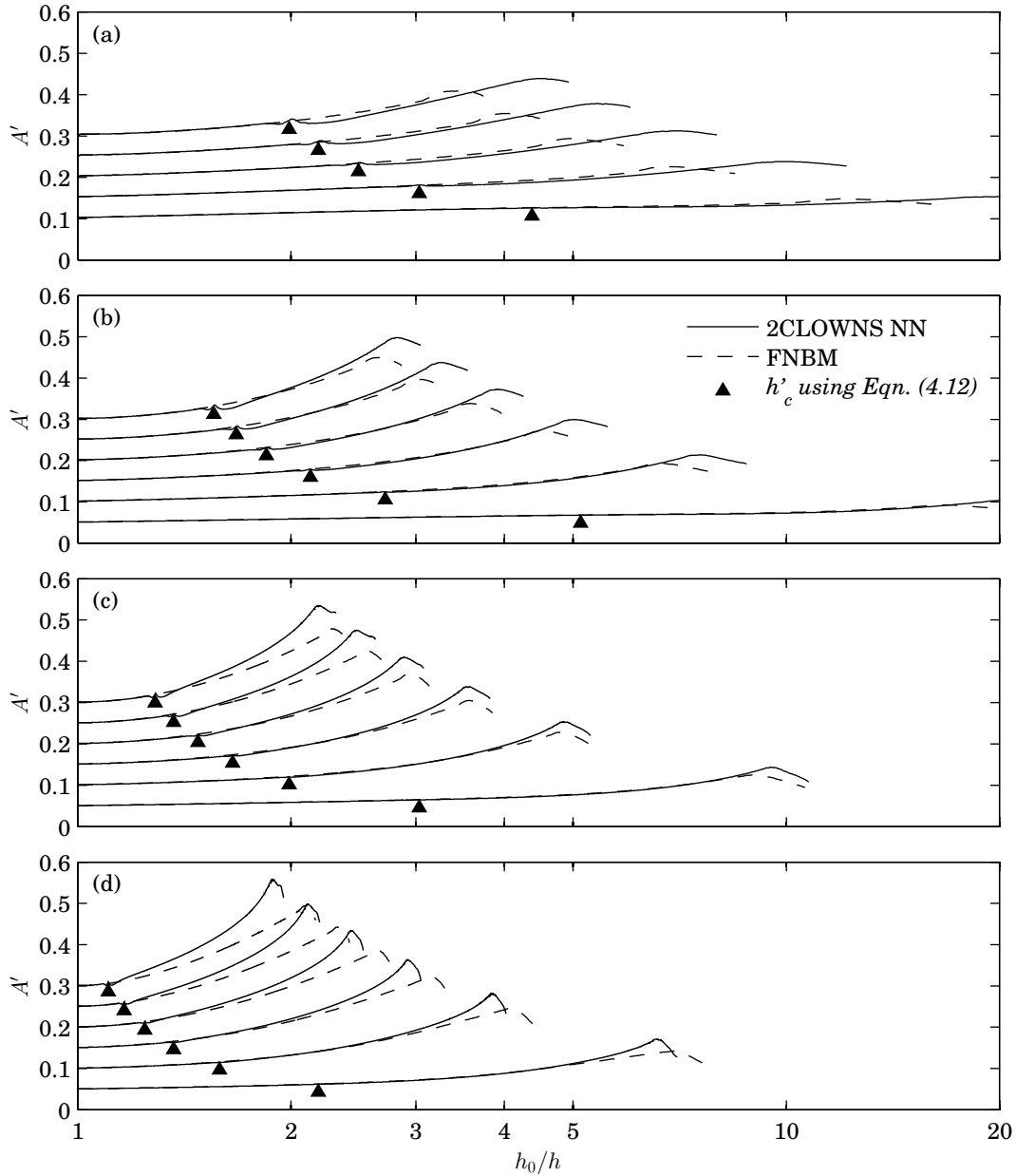


Figure 4.13: Solitary wave transformation of the local wave height, A' versus h_0/h until breaking on various slopes for $A'_0 = 0.05, 0.10, 0.15, 0.20, 0.25$ and 0.30 comparing 2CLOWNS NN with FNBM simulations. (a) $s = 1/20$, (b) $s = 1/35$, (c) $s = 1/60$, (d) $s = 1/100$. Filled triangles indicate the water depth, h'_c where coupling in 2CLOWNS occurs calculated using Eqn. (4.12)

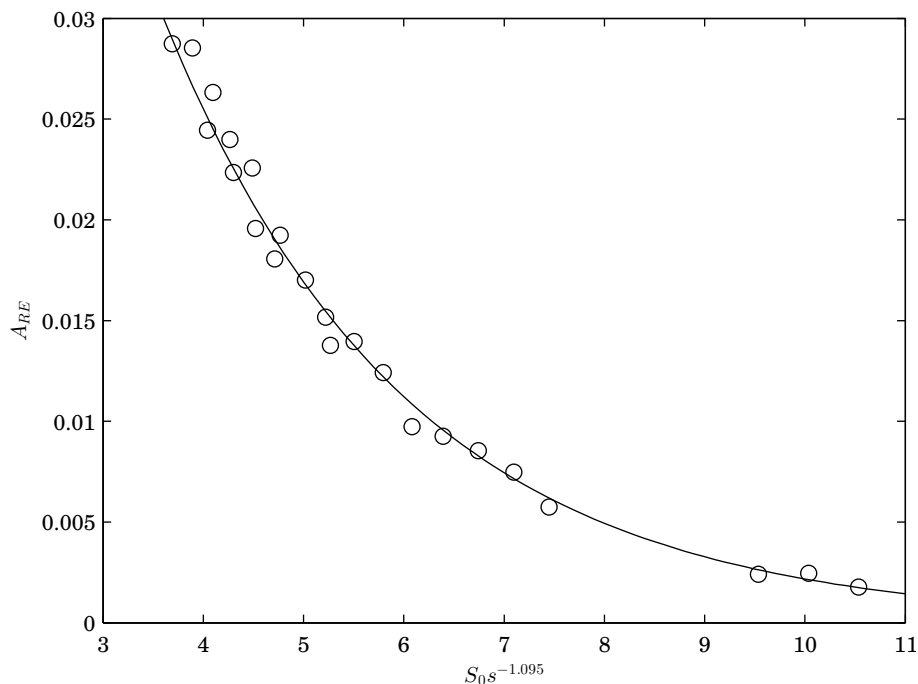


Figure 4.14: The total error of $(A'_{2CLOWNS} - A'_{FNBM})/A'_{FNBM}$ denoted, A_{RE} around the coupling interface for all 2CLOWNS NN simulations with best fit line (Eqn. (4.14)) included

4.4.2 Pre-breaking shoaling performance

In this section the accuracy of the wave transformation prior to breaking is discussed. As an initial example the entire shoaling transformation plus post-breaking decay (covered in §4.4.4) of the 2CLOWNS NN simulation compared with the NSWE and FNBM models for the case with $A'_0 = 0.05$ and $s = 1/60$ is plotted in Figure 4.15. The axes have been nondimensionalised by the water depth at breaking, h_b recorded in the 2CLOWNS model and a discussion of its estimation will take place in §4.4.3. Normalisation with h_b is to allow for easy comparison with the plot presented in Hsiao et al. (2008) for $A'_0 \approx 0.05$ on the same slope. Expected shoaling rates from Synolakis and Skjelbreia (1993) are also plotted for reference (note that these are *not* best fit lines). In the zone of gradual shoaling the 2CLOWNS model utilizes the efficient NSWE model and no major differences between any of the models is evident. Thereafter, in the transition region coupling takes place ($h'_c = 0.33 \rightarrow h/h_b = 3.22$) and the zone of rapid shoaling is modelled through the RANS calculation. The shoaling rate described by 2CLOWNS NN in this zone is shown to follow approximately that of FNBM both agreeing with Boussinesq's theoretical shoaling law ($\sim h^{-1.0}$). Agreement between the models continues up until $h/h_b \approx 1.1$ where wave breaking occurs in the FNBM prematurely according to the 2CLOWNS NN simulation. The rate of rapid shoaling in the NSWE model is slow in comparison to Boussinesq's law ($\sim h^{-0.7}$ instead).

Figure 4.13 plots the transformation of A' for all the experimental conditions. It is demon-

4.4. SOLITARY WAVE SHOALING AND BREAKING ON A PLANE BEACH USING 2CLOWNS

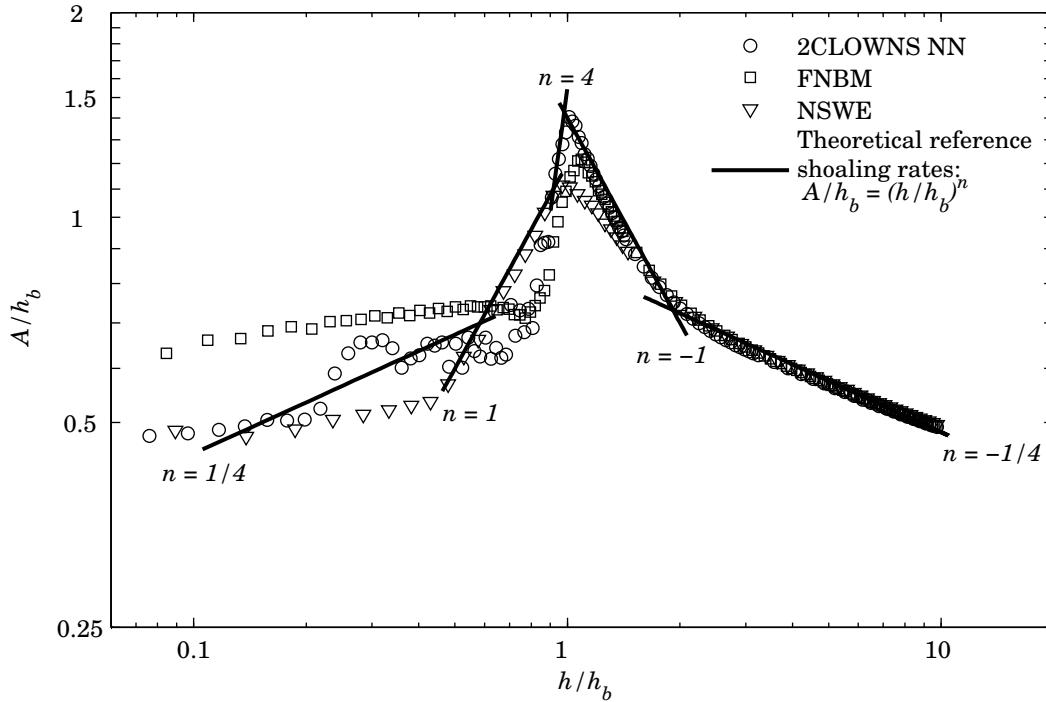


Figure 4.15: Evolution of the local wave height of a solitary wave ($A'_0 = 0.05$) on a $1/60$ slope comparing 2CLOWNS NN, FNBM, NSWE models with theoretical reference shoaling rates (Synolakis and Skjelbreia, 1993) included

strated how the shoaling rate in 2CLOWNS NN generally increases against the FNBM result as the slope becomes milder and also as A'_0 increases. In particular, as s is steepened a larger dip in A' occurs that does not easily recover versus FNBM in comparison to mild slopes. This may simply be because of inherent disparities in shoaling rates between the RANS and FNBM models themselves rather than a coupling issue as Eqn. (4.14), a function only weakly dependent on s , suggests. To demonstrate the effect of the two-way coupling process on the shoaling rate rather than the effect of the difference simply between the RANS and FNBM models, Figure 4.16 plots a comparison of the wave transformation for 2CLOWNS NN, singular RANS and FNBM model simulations for those same cases in Figure 4.4. Particularly in plots (c) - (e) a dip in $A'_{2CLOWNS}$ around the coupling interface is noticeable. Despite this the solution is able to recover and excellent agreement between the singular RANS and 2CLOWNS NN simulations is shown close to the breaking point in all cases implying that the effect of coupling on the final solution (at breaking/post breaking which in this study only the RANS/2CLOWNS NN model can rigorously simulate) is minimal. Hence it is conjectured that most of the differences shown between FNBM and 2CLOWNS in Figure 4.13 is simply due to actual difference between the RANS and FNBM models rather than the coupling process. Of course the 2CLOWNS solution does diverge from the correct one around the coupling interface to various degrees which itself may be undesirable.

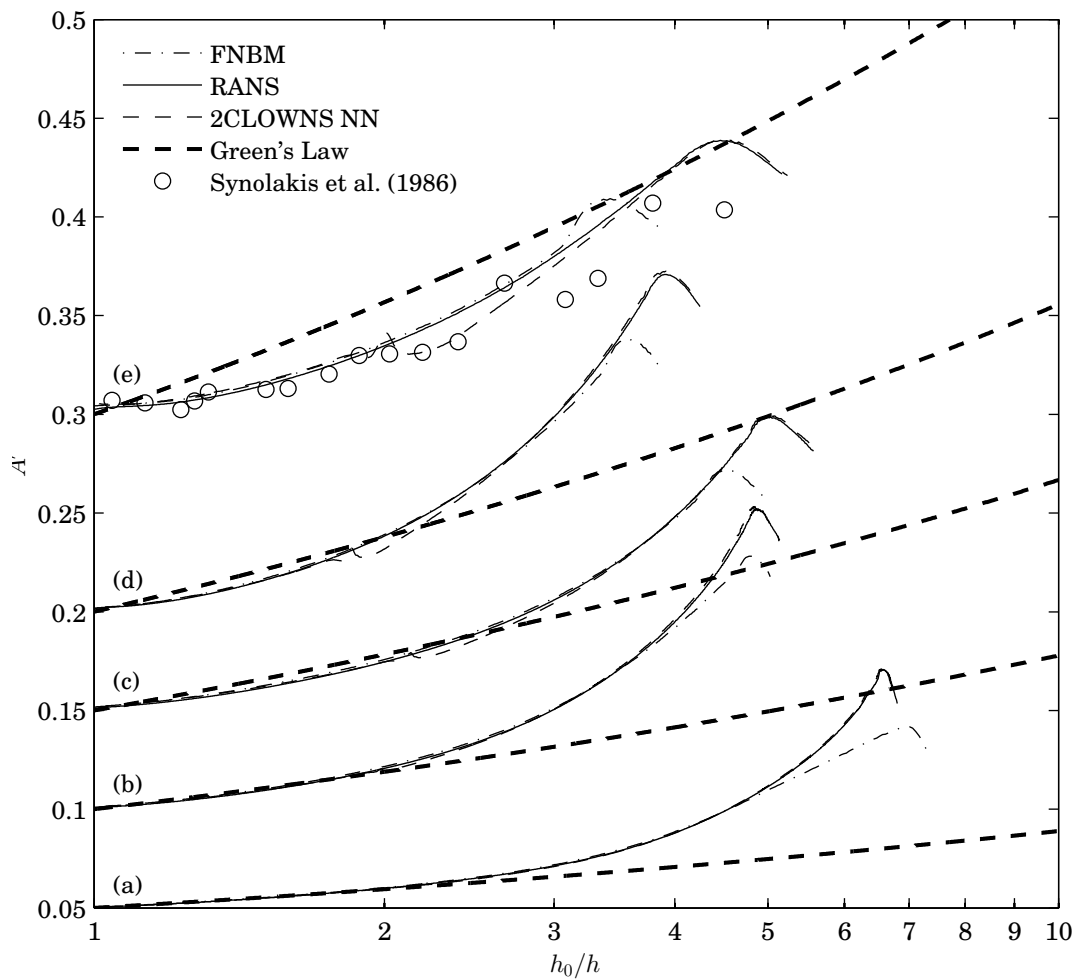


Figure 4.16: Selected solitary wave transformation of the local wave height, A' versus h_0/h comparing: RANS and 2CLOWNS models, Green's law and Synolakis (1986) experiments in (e). (a) $A'_0 = 0.05$, $s = 1/100$, (b) $A'_0 = 0.10$, $s = 1/60$, (c) $A'_0 = 0.15$, $s = 1/35$, (d) $A'_0 = 0.20$, $s = 1/35$, (e) $A'_0 = 0.30$, $s = 1/20$

However, given sufficient room to recover, the final solution is considerably accurate.

4.4.3 Wave Breaking Characteristics

Prediction of the wave breaking characteristics is important to show the improved performance of the 2CLOWNS NN model over long wave models including higher-order ones such as FNBM. The breaking point is usually defined as the location where the wave front has a vertical tangent (Grilli et al., 1997). This can be accurately determined in the 2CLOWNS (RANS) model since the free surface normal in each computational grid is explicitly determined. Wave breaking is said to have occurred in the 2CLOWNS simulations once the x component of the free surface normal vector in any cell around the wave face is larger than 0.999. The resulting values of the water depth at breaking, h'_b and the wave height at breaking, A'_b is then determined from the free surface profile at that exact snapshot in time.

Firstly, the example shown in Figure 4.15 for $A'_0 = 0.05$ and $s = 1/60$ is analysed in detail. The value of h'_b in the 2CLOWNS NN simulation was found to be equal to $h'_b = 0.103$. To make a comparison the empirical formula for plunging breakers presented in Grilli et al. (1997) based on their FNFP flow simulations is introduced:

$$h'_b = \frac{0.149}{(S_0/A'_0)^{0.523}}, \quad S_0 < 0.3 \quad (4.15)$$

Eqn. (4.15) gives $h'_b = 0.097$ for $A'_0 = 0.05$ and $s = 1/60$. The experiments of Hsiao et al. (2008) on $s = 1/60$ were also found to be within good agreement to this equation particularly for $S_0/A'_0 > 2$ which is the case here (Eqn. (4.15) slightly underestimates h'_b otherwise). 2CLOWNS gives a prediction of h'_b in this example to within 6.2% of Eqn. (4.15). In comparison h'_b in FNBM can be estimated as $h'_b = 0.111$ based on the location of the maximum value of A' which is an overestimation of approximately 14%.

The other wave breaking characteristic of concern is the wave breaking index, A_b/h_b . In the 2CLOWNS NN simulation for $A'_0 = 0.05$ and $s = 1/60$ the local wave height at breaking is, $A'_b = 0.141$ (in comparison $A'_b = 0.126$ in FNBM). This is equivalent to a breaking index of $A_b/h_b = 1.37$. Again for a comparison, the Grilli et al. (1997) empirical formula for the breaking index is as follows:

$$\frac{A_b}{h_b} = 0.841 \exp(6.421S_0) \quad (4.16)$$

Eqn. (4.16) gives $A_b/h_b = 1.74$ for $A'_0 = 0.05$ and $s = 1/60$. However, Hsiao et al. (2008) note that for $S_0 > 0.10$ Eqn. (4.16) may tend to overestimate A_b/h_b , and they found little deviation from $A_b/h_b = 1.1$ in all of their experimental cases. This is because h'_b is very small here and a slight variation will affect the A_b/h_b ratio significantly. Taking into account both Eqn. (4.16) and the experimental results of Hsiao et al. (2008) the “middle ground” estimation of $A_b/h_b = 1.37$ can be considered a reasonable result.

Based on all the experimental cases simulated by the 2CLOWNS model in this study, empirical equations are derived for the prediction of h'_b ($R^2 = 0.944$) and A_b/h_b ($R^2 = 0.964$) in a similar

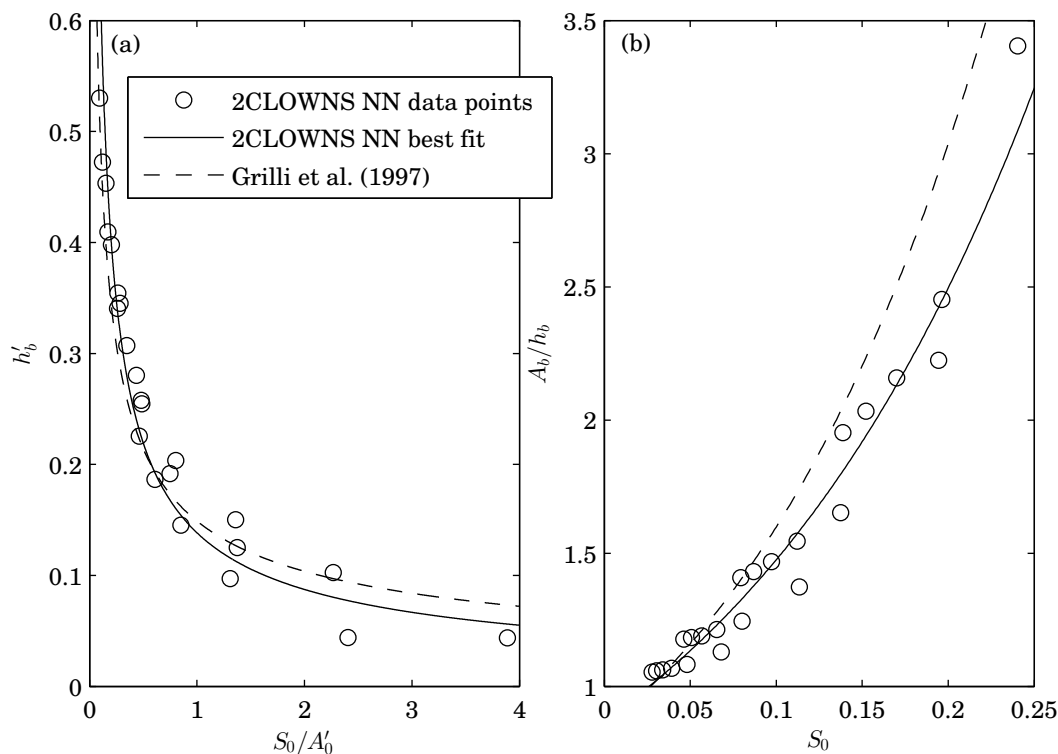


Figure 4.17: Breaking criteria calculated in 2CLOWNS NN for all wave cases in this study with best fit curves compared to those calculated in Grilli et al. (1997): (a) water depth at breaking, h'_b versus S_0/A'_0 with Eqn. (4.17) - this study and Eqn. (4.15) - (Grilli et al., 1997); (b) wave breaking index, A_b/h_b versus S_0 with Eqn. (4.18) - this study and Eqn. (4.16) - (Grilli et al., 1997)

form to Eqns. (4.15) and (4.16):

$$h'_b = \frac{0.138}{(S_0/A'_0)^{0.664}}, \quad S_0/A'_0 < 4 \quad (4.17)$$

$$\frac{A_b}{h_b} = 0.872 \exp(5.258S_0), \quad S_0 < 0.25 \quad (4.18)$$

where the upper limits of the data included in derivation of Eqns. (4.17) and (4.18) are shown. The data points are plotted in Figure 4.17 along with the best fit (least-squares) curves corresponding to Eqns. (4.17) and (4.18). The curves corresponding to Eqns. (4.15) and (4.16) found in Grilli et al. (1997) are also drawn for comparison.

Concerning the calculation of h'_b in Figure 4.17(a), Eqn. (4.17) is shown to match Eqn. (4.15) fairly well overall particularly for $S_0/A'_0 < 1$. It is worth mentioning that Eqn. (4.15) from Grilli et al. (1997) was derived with only one data point for $S_0/A'_0 > 1$. In this study six cases of $S_0/A'_0 > 1$ (which corresponds to combinations of smaller wave heights and steeper slopes) is included which mostly likely accounts for the differences between Eqns. (4.17) and (4.15). It is noted that the values for larger $S_0/A'_0 > 1$ are more scattered than those in the $S_0/A'_0 < 1$ bracket. For example,

Eqn. (4.17) is largely affected by the results of the two cases $A'_0 = 0.05$ on $s = 1/35$ ($S_0/A'_0 = 3.89$) and $A'_0 = 0.10$ on $s = 1/20$ ($S_0/A'_0 = 2.40$).

The breaking index A_b/h_b is plotted in Figure 4.17(b). Eqn. (4.18) derived in this study is in good agreement with Eqn. (4.16) from Grilli et al. (1997) for small values of $S_0 < 0.1$. For $S_0 > 0.1$, A_b/h_b in this study is somewhat smaller than that described by Eqn. (4.16). This may be because $S_0 > 0.3$ in Grilli et al. (1997) corresponds to surging breakers which could have affected the slope of Eqn. (4.16) over the interval $0.10 < S_0 < 0.25$ for plunging breakers where comparatively little data was available. In contrast all the wave types were plunging breakers in this study. As mentioned earlier, Hsiao et al. (2008) indeed noted that Eqn. (4.16) had a tendency to overestimate values of S_0 within this range because the ratio A_b/h_b is extremely sensitive to h'_b here since wave breaking occurs near the initial shoreline.

4.4.4 Post-breaking Behaviour and Wave Shape

As described in Synolakis and Skjelbreia (1993), after wave breaking the local wave height undergoes transformation according to a zone of rapid decay on the order of $\sim h^4$, followed by a zone of gradual decay $\sim h$. Hsiao et al. (2008) also postulated that on their mild slope, $s = 1/60$ a fifth region corresponding to bore front propagation exists, where decay follows $\sim h^{1/4}$. Figure 4.15 for $A'_0 = 0.05$ and $s = 1/60$ plots the 2CLOWNS NN data alongside expected shoaling rates. The rate of rapid decay is demonstrably in close agreement to the theoretical $\sim h^4$ rate. The rate of gradual decay appears slightly steeper than theoretically suggested but the data is quite scattered due to the overturning wave shape. The final bore front propagation region on average appears to follow the rate ($\sim h^{1/4}$) suggested by Hsiao et al. (2008).

To give the readers an idea of the performance of the RANS model in terms of its ability to model the overturning wave shape, touchdown of the plunging jet and wave splashup, Figure 4.18 shows snapshots of the breaking wave with $A'_0 = 0.20$ on $s = 1/35$. This case was chosen because illustrations are also found in Grilli et al. (1997) for the exact same case that readers may refer to. Figure 4.18 (a) - (e) plots snapshots of the wave shape at five different stages in the breaking phase along with velocity vectors and greyscale intensities of the normalised velocity magnitude, u' . The five different stages in order are; (a) wave shape prior to breaking, (b) at the onset of breaking, (c) the formation of the plunging jet, (d) touchdown of the plunging jet and, (e) wave splashup. Figure 4.18 demonstrates that the RANS model in 2CLOWNS has the ability to at least qualitatively model the full process of wave breaking. The accuracy of the jet profile is strongly linked to the cell resolution and it is very difficult for the VOF model to get a beautifully smooth jet profile similar to those generated by the FNPF model as shown in Grilli et al. (1997) without resorting to very fine grid sizes. Nevertheless, the RANS model appears to give a fair representation of the jet shape and it has the distinct advantage of modelling the touchdown of the plunging jet and wave splashup as shown in Figure 4.18 (d), (e).

The normalised turbulent kinetic energy, k' is also shown for the same snapshots in Fig-

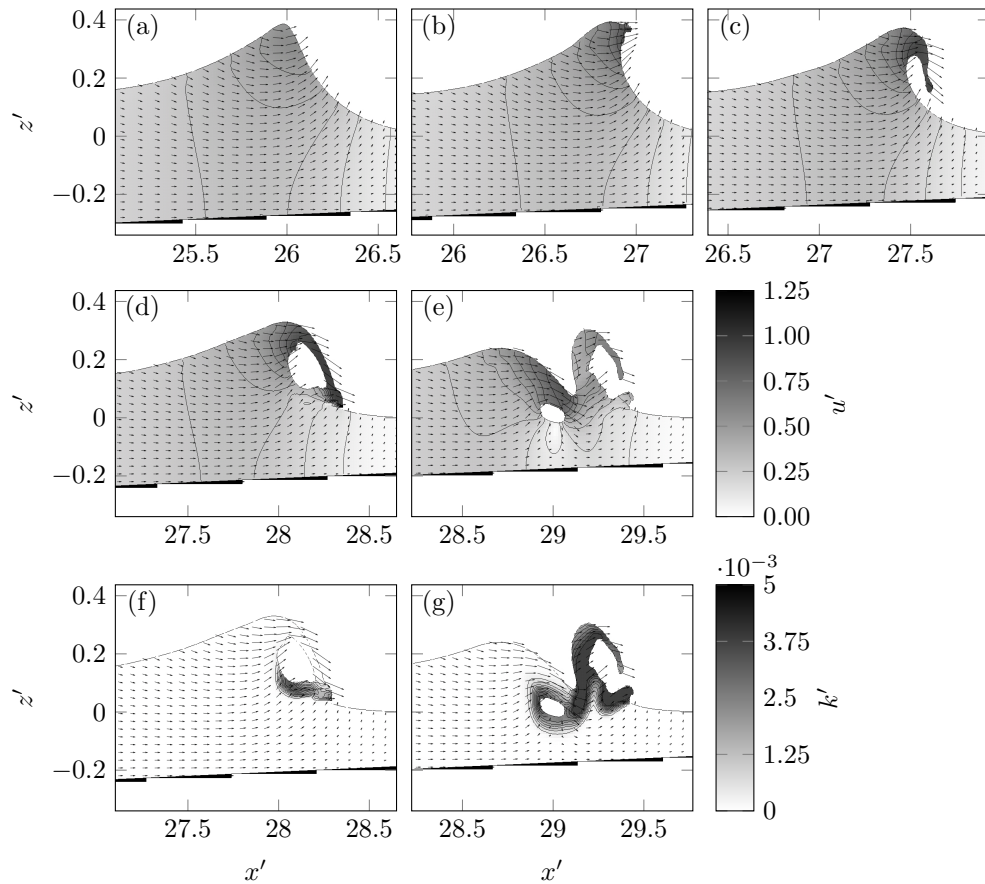


Figure 4.18: Breaking wave shape and kinematic quantities (velocity magnitude, u' and turbulent kinetic energy, k') for $A'_0 = 0.20$ on $s = 1/35$: (a) prior to breaking (u'), (b) at the onset of wave breaking (u'), (c) formation of the plunging jet (u'), (d) touchdown of the plunging jet (u'), (e) wave splashup (u'), (f) touchdown of the plunging jet (k'), (g) wave splashup (k')

Figure 4.18(f), (g) demonstrating the onset of the turbulent flow that a FNPf model and in general depth-integrated models cannot simulate. The wave splashup in Figure 4.18(e), (g) is shown to contain three distinct regions of air (although the air flow itself is not computed) and counterrotating vortices as illustrated through sketches and high quality photographs in Li and Raichlen (2003). Hence the model is shown to possess qualitative predictive ability to describe the full wave breaking process. Full quantitative analysis of the breaking process plus that of bore front propagation and wave runup will be undertaken in future studies.

4.4.5 Velocity profiles

In order to provide some explanation for the disparate wave transformation and breaking behaviour of 2CLOWNS, FNBM, and NSWf models, velocity profiles for both u' and w' are plotted at four separate locations for $A_0 = 0.05$ on $s = 1/60$, in Figure 4.19. The locations

4.4. SOLITARY WAVE SHOALING AND BREAKING ON A PLANE BEACH USING 2CLOWNS

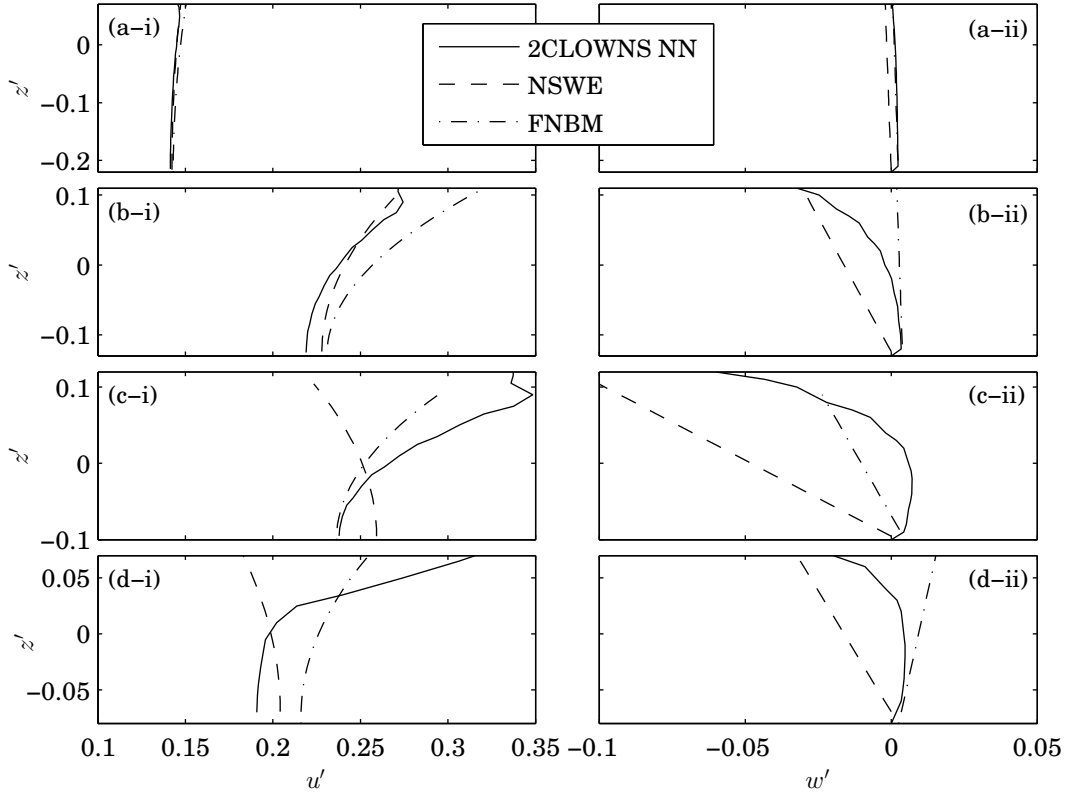


Figure 4.19: Velocity profiles ((i) u' on left, (ii) w' on right) under the wave crest of a solitary wave ($A_0 = 0.05$) on a $1/60$ slope at four separate locations comparing 2CLOWNS NN, NSWE, and FNBM simulations; (a) $h/h_b = 2.1$, (b) $h/h_b = 1.2$, (c) $h/h_b = 0.93$, (d) $h/h_b = 0.68$

correspond to the four zones of shoaling and decay introduced in Synolakis and Skjelbreia (1993). The vertical velocity profiles for u' and w' in NSWE are found from the following equations based on the weakly nonlinear Boussinesq assumption using the depth-averaged velocity:

$$u(z) = U + \left(\frac{1}{6}h^2 - 0.5(z+h)^2 \right) \frac{\partial^2 U}{\partial x^2} \quad (4.19)$$

$$w(z) = -\frac{\partial U}{\partial x} (z+h) \quad (4.20)$$

Velocity profiles for FNBM are found from the equations based on a fully nonlinear Boussinesq assumption using the velocity at an arbitrary depth, z_α (Sitanggang and Lynett, 2010):

$$u(z) = u_\alpha + \frac{1}{2} (z_\alpha^2 - z^2) \frac{\partial^2 u_\alpha}{\partial x^2} + (z_\alpha - z) \frac{\partial^2 (hu_\alpha)}{\partial x^2} \quad (4.21)$$

$$w(z) = -\frac{\partial u_\alpha}{\partial x} z - \frac{\partial (hu_\alpha)}{\partial x} \quad (4.22)$$

The 2CLOWNS velocity profiles are taken directly from the RANS model.

Firstly, at $h/h_b = 2.1$, Figure 4.19 (a) confirms that all three models have good agreement for both u' and w' even at the edge of the zone of gradual shoaling where $h/h_b = 2.1 \rightarrow h' = 0.22$ is located. The magnitude of w' is small and the profile of u' has small curvature where u' at the free surface is only slightly larger than at the bed. It is these reasons that help explain why the NSWE model is just as accurate at predicting shoaling as the FNBM and RANS model in this zone, since the assumptions of the NSWE model are still valid.

However, in the zone of rapid shoaling at $h/h_b = 1.2$ (Figure 4.19 (b)), significant discrepancies of both u' and w' are shown between all three models. The curvature of the u' profile between FNBM and 2CLOWNS are similar but the magnitude is larger in FNBM. This could explain why wave breaking occurs earlier in FNBM as the speed of the fluid near the wave crest approaches that of the wave celerity quickly. Although the magnitude of u' is more agreeable between 2CLOWNS and NSWE, the curvature is underestimated implying smaller steepness of the wave shape. The profile of w' in NSWE is negative over the entire depth in contrast to FNBM which is small and positive everywhere indicating little asymmetry of the wave shape. However the 2CLOWNS velocity profile is also negative near the free surface but positive in the lower half of the depth. A nonlinear profile of w' such as that present in the 2CLOWNS simulations cannot be replicated by NSWE and FNBM models.

Similarly, in the zone of rapid decay at $h/h_b = 0.93$ (Figure 4.19 (c)), the profiles of u' and w' in 2CLOWNS are highly nonlinear. Although the prediction of u' and w' in FNBM at the seabed is in good agreement with 2CLOWNS, both u' and w' at the free surface are underestimated. The NSWE u' and w' profiles are very different from either of the FNBM or 2CLOWNS ones. These observations may be expected since at this point rapid decay ($\sim h^4$) occurs in 2CLOWNS but the same degree of decay does not occur for either of the NSWE or FNBM models as plotted in Figure 4.15. In fact, NSWE does not have a region where rapid decay is evident and appears to only mimic gradual decay. Hence, it is unsurprising that the velocity profiles are not in agreement.

Finally, the velocity profiles in the zone of gradual decay at $h/h_b = 0.68$ where bore propagation has begun to form are plotted in Figure 4.19 (d). Notably the magnitude of u' near the free surface is much larger than that u' in the lower half depth in 2CLOWNS which may be expected in bore formation. FNBM appears to do a good job in approximating the average magnitude of u' and w' but the velocities particularly at the free surface are significantly different. It is this irregularity of the velocity profiles and the addition of turbulence that makes modelling through traditional wave equations very challenging after wave breaking, even for fairly small wave heights as shown in this example. This is one of the main advantages of using the RANS model in these regions over depth-integrated ones. In addition, although here only solitary wave transformation is analysed, major differences of the vertical velocity profile between RANS, NSWE and FNBM will induce significant differences in the undertow flow for ordinary periodic waves.

4.5 Conclusions

This study applied the two-way coupled long wave to Reynolds-averaged Navier-stokes (2CLOWNS) model to shoaling and breaking of solitary waves on a plane beach. Validation of the two-way coupling scheme and its sensitivity to the vertical distribution of the velocities as an input to the RANS model, the coupling depth, and the slope and wave height was shown. Optimal coupling depths depending on the offshore wave height and slope were determined, and a demonstration of the ability of 2CLOWNS to model the entire wave transformation and breaking process was carried out.

Shoaling characteristics of the individual NSWE and RANS models were analysed in comparison with theoretical reference shoaling rates and a FNBM. It was found that the RANS model and FNBM models could predict shoaling rates similarly until close to the breaking point. However, RANS models are computationally expensive, may suffer from significant numerical dissipation when propagating from offshore and are highly sensitive to the grid resolution. Conversely, the NSWE model was reliable and efficient in calculating wave propagation from far offshore however it could not match the required shoaling rate of the FNBM and RANS models in the zone of rapid shoaling. By measuring the location (depth) where the NSWE model diverges from FNBM, Eqn. (4.12) was derived based on a nondimensional slope parameter. Eqn. (4.12) was used to compute the “optimal” coupling depth for the 2CLOWNS model in order to maximise accuracy and efficiency.

A basic evaluation of the 2CLOWNS model was performed to investigate the the two-way coupling algorithm and sensitivity to the; 1) assumption of the velocity profile used as a boundary condition to the RANS model during coupling, 2) coupling depth, 3) beach slope and offshore wave height. Incident and reflected waves off a vertical wall could seamlessly pass through the NSWE and RANS domains in both directions using the two-way coupling algorithm. Two-way coupling was found to affect the computation of the volume fluxes entering the RANS domain that occurs in order to balance the wave energy during solitary wave shoaling on a steep slope. This balancing effect is not possible in one-way coupling simulations. Regarding the velocity boundary conditions, the sensitivity to the assumption of the vertical velocity profile was large in comparison to the horizontal velocities. A no gradient condition on both the vertical velocity and the difference in the depth-averaged horizontal velocities was found to give the best results. If coupling occurs in depths much smaller than that prescribed by Eqn. (4.12) the NSWE model has diverged too far from the RANS model and accurate wave transformation could not be achieved. The differences between coupling at the optimal depth and a larger one was relatively small but better performance was generally achieved when coupling in larger depths. However, computational time rapidly increases as the coupling depth increases which must be offset against small changes in accuracy. As the slope and offshore wave height increased the relative errors in the form of a deviation in the local wave height at the coupling interface compared with the FNBM model approached approximately 3% at the maximum values of slope and wave height. An equation

was derived to describe the deviation in the local wave height as a function of $S_0 s^{-1.095}$. This indicates that the coupling performance is far more sensitive to the offshore wave height in comparison to the slope. Deviations at the coupling interface are smaller than 1% for any offshore wave height, $A'_0 \leq 0.10$. For example, on the slope, $s = 1/60$ with $A'_0 = 0.05$, the 2CLOWNS model could model the entire wave shoaling and breaking process remarkably well in accordance with theoretical expectations and experimental observations. Moreover, the computational time of 2CLOWNS simulations was between 6.2% and 22% that of the computational time using the singular RANS model under the same conditions. In real 2DH/3D large-scale simulations the effect on computational time will be even more dramatic and important.

The ability of 2CLOWNS to predict wave breaking characteristics was analysed and found to give reasonable approximations overall when compared with experimental observations and empirical equations based on results from a FNPF model (Grilli et al., 1997). Eqns. (4.17) and (4.18) were derived to determine the water depth at breaking and wave breaking index based on the results of the the 2CLOWNS simulations. The new equations may be a useful complement to the existing ones presented in Grilli et al. (1997) particularly for $0.10 < S_0 < 0.25$, $S_0/A'_0 > 1$. Moreover, the post-breaking behaviour and overturning wave shape was presented. The three zones of decay in the local wave height were approximated well overall following estimated rates of decay. Furthermore, the wave shape upon breaking, the formation of the plunging jet, the touchdown of the plunging jet, and wave splashup were all captured in the wave breaking process. Based on plots from FNPF simulations (Grilli et al., 1997) and experimental photographs (Li and Raichlen, 2003) qualitative agreement was found.

Finally, velocity profiles under the wave crest at different locations were compared between NSWE, FNBM and 2CLOWNS simulations for the case $A'_0 = 0.05$ on $s = 1/60$. Good agreement was shown between all three models for both horizontal and vertical velocities near the edge of the zone of gradual shoaling. However, in the zone of rapid shoaling, nonlinear profiles of both u' and w' develop in 2CLOWNS that could not be predicted by NSWE. After breaking, in the zone of gradual decay highly irregular profiles of u' in particular are found in 2CLOWNS which were not possible for NSWE and FNBM to replicate.

Overall it can be concluded that the 2CLOWNS model may prove to be a powerful tool in long wave modelling. This is particularly true for relatively large values of $S_0 s^{-1.095}$ ($A'_0 \leq 0.10$ on mild slopes) as suggested, corresponding to the majority of tsunami situations. For wider applicability to wave problems with larger nonlinearities the use of a higher-order long wave model such as a FNBM instead of a NSWE model to couple to the RANS one should be adopted. Future studies should focus on extending the model and relations presented in this paper in order to apply them robustly to real situations such as computation around offshore and onshore structures of engineering interest. In addition, detailed analysis of the post-breaking physics such as wave splash-up, bore propagation and wave runup will be undertaken in subsequent studies.

FLOW HYDRODYNAMICS NEAR THE KAMAISHI BAY OFFSHORE TSUNAMI BREAKWATER DURING THE 2011 TOHOKU-OKI EARTHQUAKE TSUNAMI

The extension of 2CLOWNS analysed in Chapter 4 for solitary waves to 2DH-3D (2CLOWNS-3D) is required in order to verify the model's ability to simulate real-world scenarios and thus demonstrate its usefulness. A study was conducted that analysed the effects and forces on an offshore tsunami breakwater in Kamaishi Bay on the 2011 Tohoku-oki Earthquake Tsunami (see §5.2 for the setup and model conditions). The results of this study are presented in this chapter. Firstly, the model setup and accuracy of the source conditions are verified via the maximum inundation heights recorded around Kamaishi Bay during the 2011 Tohoku-oki Earthquake Tsunami in §5.3. Following this, two main themes were investigated. Firstly, the offshore breakwater creates a very large jet-like structure and vortex onshore of it as the tsunami flows through the submerged section constructed for traversing vessels. §5.4 analyses the major flow hydrodynamics of this jet-like structure onshore of the breakwater and comparisons of the 2CLOWNS-3D results are made with those of the 2DH NSW model. The second major focus of the study was to quantify the hydrodynamic forces and stresses on the breakwater, particularly through the opening which is presented in §5.5. The simulated values are compared with the critical ones for sliding of the caissons as punching failure of the rubble mound foundation.

5.1 Introduction

The March 2011 Tohoku-oki Earthquake Tsunami event in northeastern Japan caused catastrophic widespread damage resulting in 15,892 fatalities with an additional 2,574 missing. In total, 124,663 buildings fully collapsed, 274 638 buildings partially collapsed and 116 bridges were damaged as of July 10, 2015 (National Police Agency of Japan, 2015). The direct economic damage has been estimated at US\$183bn while costs for recovery might reach US\$122bn (Norio et al., 2011).

Due to its long history of tsunami disasters, Japan may have been one of the most prepared nations with regard to its construction of coastal protection structures e.g. seawalls, gates, offshore tsunami breakwaters and planted trees to act as natural tsunami barriers. Suppasri et al. (2013) demonstrates examples where each of such coastal protection structures were significantly damaged during the 2011 tsunami event. For example, the construction of a pair of offshore tsunami breakwaters with lengths of 990 m and 670 m connected by a 300 m long submerged section in a water depth of 63 m in Kamaishi Bay, Iwate Prefecture located on the Sanriku ria coast was completed in 2008 making it the deepest caisson breakwater in the world (Tanimoto and Takahashi, 1994). Nevertheless, even this breakwater succumbed to the force of the tsunami where many caissons either completely slid out or leaned out of position (Arikawa et al., 2012).

Previous studies have investigated the influence of the Kamaishi Bay offshore tsunami breakwater on inundation heights along the Kamaishi Bay coast (Mori et al., 2015; Pringle and Yoneyama, 2013; Port and Airport Research Institute of Japan, 2011b) using various numerical techniques including both three-dimensional (3D) and horizontal two-dimensional (2DH) shallow water equation (NSWE) based models, and a two-way coupled 2DH NSWE to 3D Reynolds-averaged Navier-Stokes (3D RANS) model. The differences in tsunami heights into the bay with and without the breakwater have been shown to be approximately 25 - 40% different (Mori et al., 2015). Comparisons with survey measurements (Mori et al., 2011, 2012) have verified that the two simulation cases provide upper and lower bounds for the actual event which is a combination of the two (the breakwater was partially damaged). For investigating possible failure modes of the breakwater, Arikawa et al. (2012) conducted hydraulic model tests while Bricker (2013) utilized a vertical two-dimensional (2DV) RANS model of the overtopping flow. Their conclusions attribute water level difference, scour and punching failure of the rubble mound foundation to be major causes of breakwater failure. However, an estimation on the hydrodynamic forces that the breakwater was subjected to in different regions, particularly through the middle submerged section has not been investigated in any detail.

In addition to the large scale impacts of coastal structures on inundation heights, it is also intriguing to analyse the effect on tsunami currents and their distribution into the bay. Maritime damage due to tsunami currents and drag forces such as destroying boats and docks, ripping vessels from moorings and impacts from floating debris may be significant even in otherwise largely unaffected regions (Lynett et al., 2014). Furthermore, tsunamis can induce

severe topographical changes and sediment depositions that may provide geological evidence from past tsunami events as well as erosion around coastal structures that can negatively affect their performance (Kihara et al., 2012). In addition, excess deposition of sediment can also affect the movement of vessels in and out of harbours and other harbour operations. This may result in dredging costs, or in some cases erosion may even save dredging costs, e.g. the February 27, 2010 Chile tsunami saved US\$100,000 in such costs for Ventura Harbor, California (Wilson et al., 2012).

In order to detail the tsunami currents as well as the hydrodynamic effects on the breakwater a suitable numerical technique is required that can generate and propagate a realistic tsunami forcing as well as compute both horizontal and vertical distributions of current velocities and small scale hydrodynamics. Boussinesq type models (e.g. Roeber and Cheung, 2012; Shi et al., 2012a; Kim et al., 2009) and other depth-integrated non-hydrostatic models (e.g. Yamazaki et al., 2011a) may approximate horizontal and less so vertical distributions satisfactorily in many areas although they are bounded by underlying assumptions. While models such as SELFE (Zhang and Baptista, 2008), a 3D NSWE based one solved on unstructured grids provide an elegant and seamless solution to consider both inundation and 3D distributions of the flow, thus are well suited to complex bathymetry. However, in order to simulate full non-hydrostatic behaviour, small scale turbulence, and hydrodynamic effects on structures, RANS or other similar Navier-Stokes based models may be preferred. Recently, a number of RANS models have become popular as numerical wave tanks (e.g Kim et al., 2010; del Jesus et al., 2012; Higuera et al., 2014), but these are unreasonable for simulation over entire bays, let alone further offshore. In Kim et al. (2010) two-way coupling of the RANS model with a fully nonlinear potential theory boundary element method (BEM) model takes place that can help to reduce some of the computational cost. Even so, this is generally still limited to application in numerical wave tanks. In order to enable application of RANS models to real large scale scenarios, coupling with computationally efficient 2DH models (Pringle and Yoneyama, 2015, 2013; Sitanggang and Lynett, 2010; Fujima et al., 2002) is required. The 2DH model provides realistic wave forcings that have propagated from far field towards the small region of interest where the RANS model takes over.

This study details and applies the two-way coupled 2DH NSWE to 3D RANS model referred to as 2CLOWNS-3D that has been described in detail in Chapter 3. The aim is to use the model to 1) analyse the velocities of the tsunami flow and their three-dimensional distribution onshore of the Kamaishi Bay offshore tsunami breakwater, and 2) quantify the hydrodynamic forces on the submerged section of the breakwater during the 2011 Tohoku-oki Earthquake Tsunami. Calculation in the 3D RANS model is set around the breakwater opening while the 2DH NSWE model is adopted elsewhere from the tsunami source in the open ocean to the coast also modelling inundation. For verification of the real scale application to Kamaishi Bay, comparisons with offshore wave buoy data and 2011 Tohoku Earthquake Tsunami Joint Survey Group (TTJS) (Mori et al., 2012) survey measurements of the maximum inundation heights are shown. When

analysing the hydrodynamics of the flow, comparisons are commonly made with simulation results that utilise only the 2DH NSW model in order to highlight areas where 2CLOWNS-3D can be advantageous for use.

5.2 Model Conditions and Setup for Application

§4 shows that within a suitable range of offshore wave parameters and beach slopes, 2CLOWNS can reproduce shoaling and breaking characteristics of solitary waves. It is expected that the long length scales of tsunamis in comparison to solitary waves will make 2CLOWNS-3D at least as effective in a real-scale scenario. However, different problems arise due to the interaction with coastal structures that cause the wave to develop turbulent eddies and strongly non-hydrostatic conditions that may propagate to the multiscale coupling interface.

5.2.1 Kamaishi Bay and Offshore Tsunami Breakwater

Kamaishi Bay is located in Iwate Prefecture, on the Sanriku ria coastal area of Japan. Kamaishi Bay is separated from Ryoishi Bay in the north by a short peninsula and Toni Bay in the south by a longer peninsula. At the mouth of Kamaishi Bay existed the deepest offshore caisson breakwater in the world extending to a maximum depth of 63 m and spanning a total of almost 2 km in length (Arikawa et al., 2012). It was constructed for the purpose of protecting Kamaishi City from tsunami attacks. The breakwater's crest height sits at 6 m above average low tide level in the bay (L.W.L), and is formed from up to 36,000 ton trapezoidal and rectangular caissons sitting on a layer of armour rock and rubble mound with a 2:1 slope. The offshore tsunami breakwater has two main sections, north and south that span 990 m and 670 m respectively. They are connected by a submerged section where the crest height is -19.0 m L.W.L allowing vessels to traverse through.

During the 2011 Tohoku-oki Earthquake Tsunami the wave motion on and over the structure induced failure of the breakwater caissons, causing them to either slide out or lean out of position. A schematic of the breakwater is shown in Figure 5.1 where caissons are marked red indicating failure as shown in Arikawa et al. (2012). Despite its failure, survey results of water marks by TTJS (Mori et al., 2012) indicate that the inundation levels were considerably lower within Kamaishi Bay, compared to levels at adjacent Ryoishi Bay where an offshore tsunami breakwater was not present. Previous numerical studies have also indicated that the breakwater likely reduced the tsunami into the bay by 25-40% (Mori et al., 2015).

5.2.2 Bathymetry/Tsunami Source Data and Computational Grids

This section summarises the bathymetry data, tsunami source data and computational grids for both the 2DH NSWE and 3D RANS models.

2DH NSWE Data and Grid

In all the simulations, bathymetry and topography data from Kotani et al. (1998) with five levels of resolution; 1350 m, 450 m, 150 m, 50 m and 10 m (see Figure 5.2) are used. The data from the first four layers were created in the old Tokyo datum geodetic system with the origin

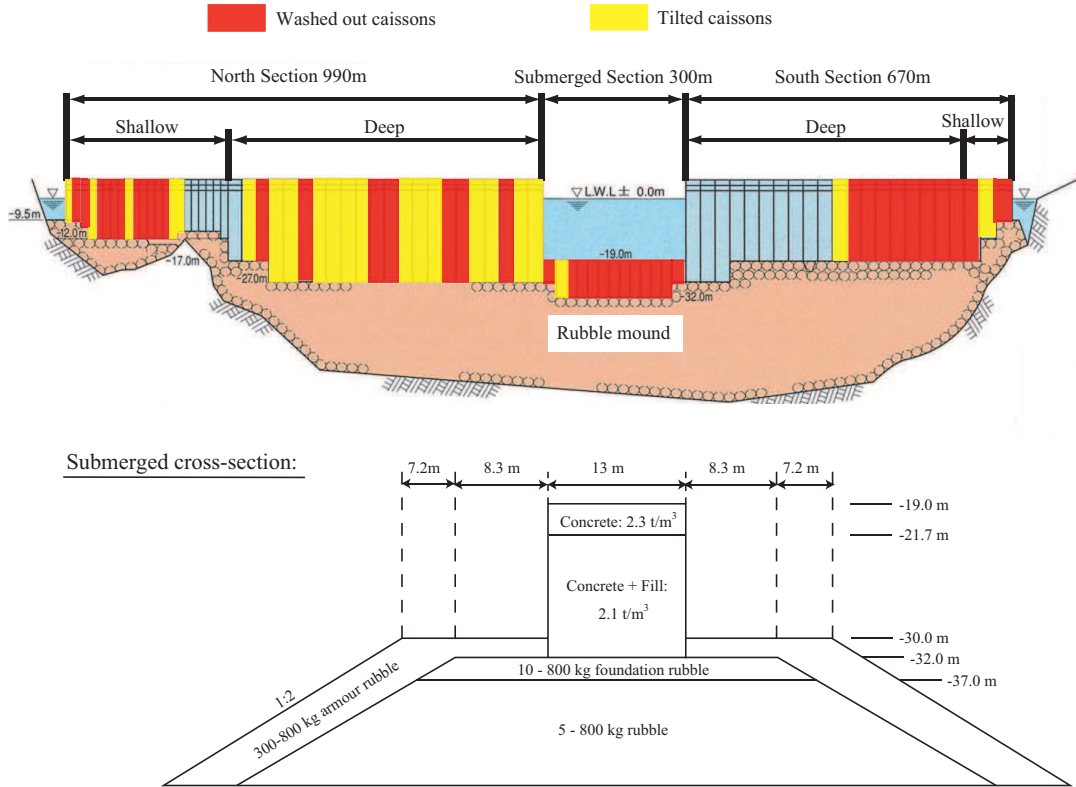


Figure 5.1: Sketch of Kamaishi Bay breakwater with the damaged caissons shaded red and yellow. Front on view and cross-section of the submerged section; adapted from: Arikawa et al. (2012); Port and Airport Research Institute of Japan (2011b)

point at UTM 143° longitude and 0° latitude. 500 km was added onto the easting coordinate to avoid negative numbers. To generate the 10 m mesh, bathymetry from the 50 m dataset was combined with 0.2 arcsecond (\approx 5 m) mesh Digital Elevation Measurement (DEM) topography data (Geospatial Information Authority of Japan, 2009). All ground levels are given in T.P (= L.W.L.+0.86 m), the mean sea level in Tokyo Bay. Initially, three simulations are conducted using only the 2DH NSW model to test the sensitivity to the offshore breakwater. The three different cases are: no offshore breakwater, post-tsunami partially damaged breakwater, and pre-tsunami undamaged breakwater. The latter condition is the one conducted using 2CLOWNS-3D. Colour plots of the 10 m mesh layer for the three offshore breakwater conditions are shown in Figure 5.3.

Furthermore, roughness data in the form of Manning's n friction coefficients are included in the dataset that vary throughout the domain depending on the land use. Manning's n is equal to 0.025 in offshore areas, 0.020 over plain fields, 0.030 over forestland and 0.040 in areas of population. Finally, seawall and harbour breakwater crest heights are also contained in the dataset and these are set on the cell boundaries using Eq. (3.20) to calculate the volume fluxes here.

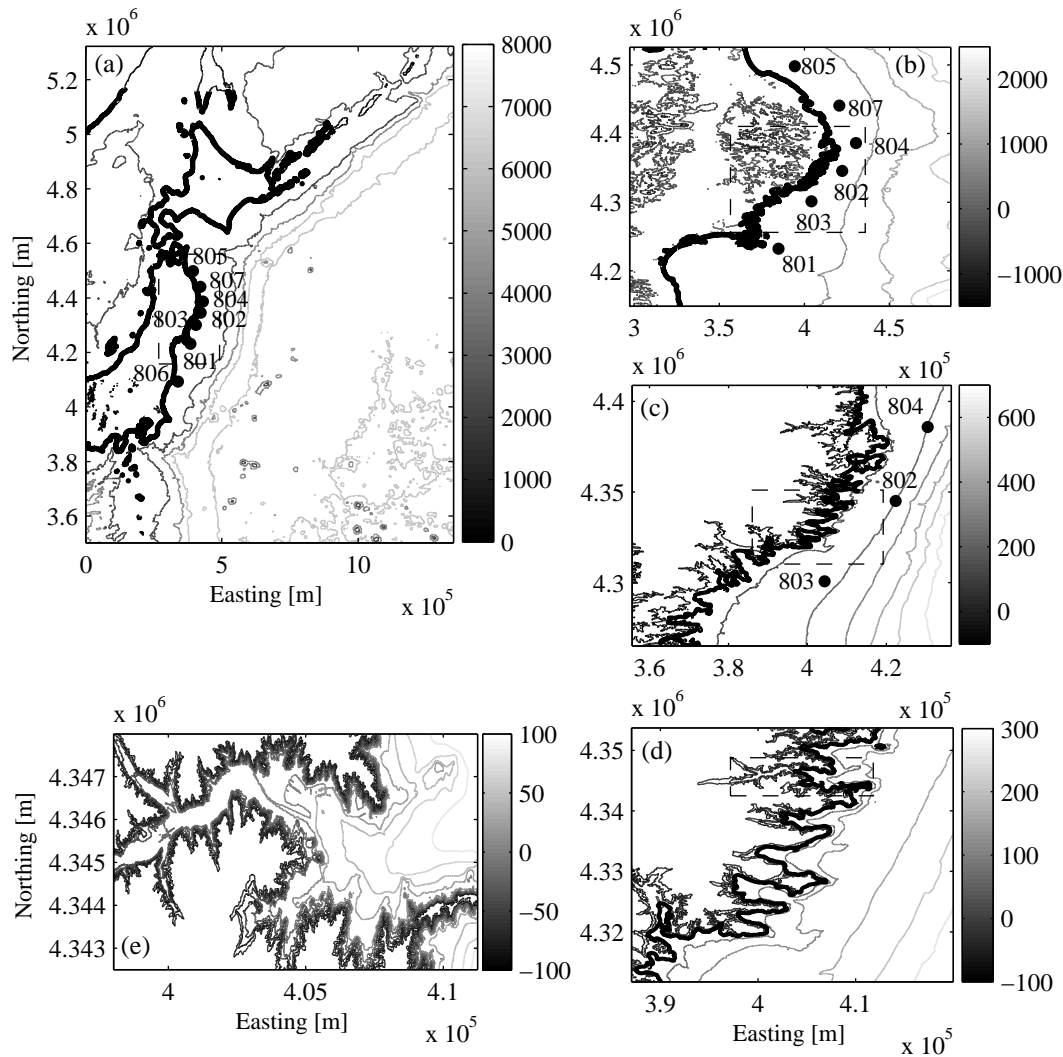


Figure 5.2: Contour plot of the bathymetry (water depth from T.P. (m)) data (Kotani et al., 1998) in five layers of resolution and the position of the Port and Airport Research Institute of Japan (2011a) GPS wave buoys (#801 - #807). Dashed rectangle indicates the location of the next layer. (a) 1350 m resolution, (b) 450 m resolution, (c) 150 m resolution with contours omitted below -100 m depth, (d) 50 m resolution with contours omitted below -100 m depth, (e) 10 m resolution (no offshore breakwater) with contours omitted below -100 m depth

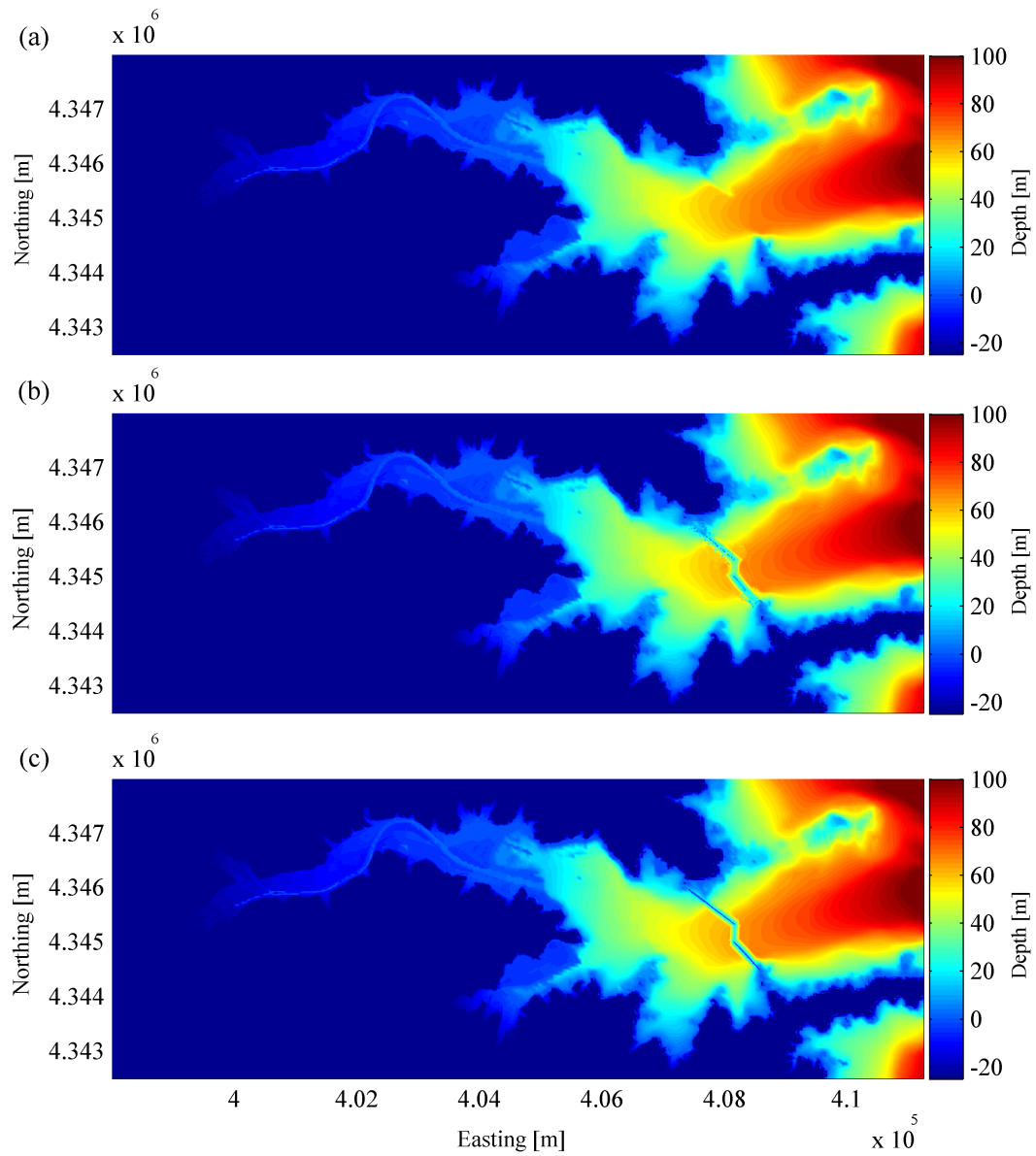


Figure 5.3: Colour plots of the 10 m mesh later for the three offshore breakwater conditions. (a) no offshore breakwater, (b) post-tsunami partially damaged breakwater, (c) pre-tsunami undamaged breakwater

The tsunami source model used in this study is based on the Tohoku University version1.2 (TUv1.2) (Imamura et al., 2012). The source is activated in the 2DH model by sudden deformation of the seabed and consequential deformation of the free-surface. TUv1.2 is created using the Okada (1985) method with 10 segments each of 100 km², with strike equal to 193°, dip equal to 14° and rake equal to 81° everywhere. Depth is either 1 km or 24.2 km and slip varies from 2 m to 35 m.

3D RANS Grid

The same bathymetry from the 2DH NSWE 10 m mesh (Figure 5.2(e)) is further refined onto the 3D RANS grid and combined with a polygon representation of the breakwater. The north-south grid size (Δy) and the east-west grid size (Δx) remain at 10 m near the lateral boundaries but are equal to 5 m around the submerged section of the breakwater. There is a small zone connecting the two grid sizes where there is a gradual increase or decrease in the grid size. The vertical grid size (Δz) also gradually reduces according to a power law from 2.5 m at the greatest depth to 1.25 m near the top of the rubble mound (-32.0 m T.P). It remains at 1.25 m hereafter until the arbitrary vertical extent of the mesh (+13.0 m T.P). A schematic of the mesh showing the landform and breakwater is found in Figure 5.4.

The position and length of the 3D RANS grid was chosen so that the boundaries are far enough from the breakwater so that the horizontal velocity distribution and pressure can be almost assumed uniform and hydrostatic respectively for the most part, as required by our assumptions for the 2CLOWNS-3D model. The simulations using just the 2DH NSWE model were used to get an estimate of the extent of possible complex flow. In particular, the length of the large jet-like structure towards the shoreline forces the calculation domain to become considerably long in the east-west direction extending the calculation time. Even so, there are still times when the velocity distribution becomes non-uniform at the boundary which motivated the arbitrary velocity distribution formulation in Eqn. (3.137). This aspect will be discussed further in §5.4.

To justify that coupling for this specific scenario is reasonable, appropriate dimensionless variables introduced in Chapter 4 can be calculated and compared with the suggested applicable range. Following Chan and Liu (2012), a crude estimate of the slope from wave buoy #802 (South Iwate) closest to Kamaishi Bay, into Kamaishi is given as $s = 1/70$, where the buoy is at an offshore depth of $h_0 = 204$ m. The peak wave amplitude was recorded to be $A_0 = 6.7$ m ($A'_0 = 0.033$) at this location, and Chan and Liu (2012) approximate the effective wave length to be $L_0 = 45$ km. This results in the the dimensionless slope parameter, $S_0 = sL_0/h_0 = 3.15$. Using Eqn. (4.12), a minimum water depth for reliable coupling can be determined from the value of $S_0A_0'^{-0.5}$ which in this case is $S_0A_0'^{-0.5} = 1.22$. $h'_c = 0.11$ hence a minimum water depth for coupling can be estimated to be 22 m. Since most of the coupling occurs in depths larger than 50 m for the current grid we can be confident that the NSWE model is correctly computing the wave at the

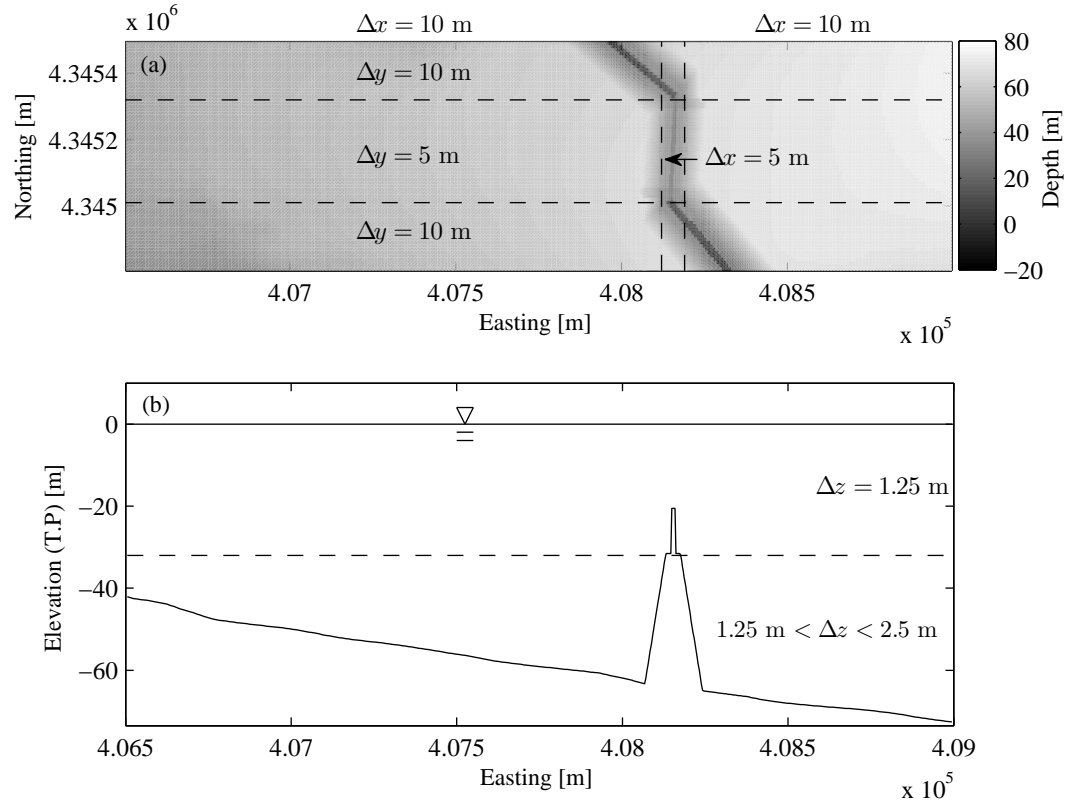


Figure 5.4: Schematic of the 3D RANS mesh with range of grid sizes indicated. (a) Plane view of the mesh where the shading indicates initial water depths (T.P.), (b) $x-z$ cross-section of the mesh along the $y = 4,345,150$ m northing

interface. Furthermore, coupling errors decrease with large values of S_0s^{-2} which is equal to $S_0s^{-2} = 15,435$ in this case, an extremely large value. Thus coupling errors at the interface are expected to be almost negligible for this scenario.

5.2.3 Model Conditions

The initial water level in all the simulations is set at +0.0 m T.P., and the tsunami is simulated for a total of 90 minutes from the earthquake rupture. Open boundary conditions are employed in the outermost 2DH NSWE layer to reduce reflections of the tsunami wave. The nesting algorithm of 2CLOWNS-3D is used to simulate the tsunami from the source towards to Kamaishi Bay with increasing resolution. Different time steps, Δt are utilized so that the C.F.L condition is satisfied ($Cr < \sqrt{2}/2$) in each nested layer. However, Δt between two connecting layers must be some integer multiple of each other, so the Courant number, Cr will be slightly lower or higher in some regions than in others. Δt ranges between 0.13 s in the innermost 10 m 2DH NSWE layer and 3.1 s in the outermost 1350 m 2DH NSWE layer so that the ratio of Δt is 2:1 between each

set of consecutive layers except for a 3:1 ratio between the 50 m and 10 m layers.

Additionally, an extra measure was introduced for the simulation using the pre-tsunami breakwater condition in the innermost 10 m 2DH NSWE layer. Usually small scale breakwaters and seawalls are represented at the cell boundary by the countermeasure introduced in §3.2.3. For the large-scale offshore tsunami breakwater the bathymetry itself must be used to describe the breakwater. However, the depth at the cell boundary is found by the average of the adjacent cell centre depths. When the change in bathymetry actually represents a vertical wall rather than a slope, averaging the cell depths will produce a water depth at the cell boundary greater than the actual depth. Therefore, in this scenario the water depth at the cell boundary is set equal to the minimum of the adjacent cell centre depths to correctly account for the presence of the vertical wall.

The time step in the 3D RANS layer ranges from $\Delta t = 0.014 - 0.043$ s depending on the instantaneous Cr which is kept at around 0.33 for stability of the SMAC algorithm (see §3.4.6). Hence the ratio of Δt becomes up to 9:1 between the 10m 2DH NSWE layer and the 3D RANS one. Interestingly this does not appear to result in any adverse effects on the simulation. Concerning friction effects, a wall function is used to approximate the bed shear stress with an appropriate roughness height specified (1 mm is used in this study).

5.3 Validation of Tsunami Height and Inundation Measurements

This section gives an overview of the simulation results that are measured in the 2DH NSWE layers. This is to verify that the incoming tsunami wave, and maximum inundation measurements are comparable to reality so that we have confidence in the wave forcings into the 3D RANS model as well as the coupling scheme between layers and both models in 2CLOWNS-3D.

5.3.1 Wave Buoy Measurements

Temporal variation in the water level is shown at positions corresponding to three of the GPS wave buoys closest to Kamaishi Bay in Fig. 5.5. In particular, the large tsunami peak equal to 6.7 m was almost reproduced at wave buoy #802 (South Iwate), the closest to Kamaishi Bay. The time series after the wave peaks at all the locations shown are also generally in good agreement and is within similar error to the preferred fault model in Yamazaki et al. (2011b). The main apparent weakness of the TUv1.2 source model is that it overestimates the initial wave trough at all locations and overestimates the wave peak for buoy #803 (North Miyagi).

5.3.2 Maximum Inundation Heights and Inundation Area

In this section the maximum recorded free surface level, η_{max} , and the inundation area is plotted and compared for the various cases. η_{max} is equivalent to the maximum inundation height on land and hence comparisons are made with TTJS survey measurements tide-corrected survey measurements (Mori et al., 2012). An estimation of the inundation area in the greater Kamaishi City region has also been made by Geospatial Information Authority of Japan (GSI) (2011) for comparison.

2DH NSWE Model Simulations

Simulations using the 2DH NSWE model were conducted for the three offshore tsunami breakwater conditions to quantify the effects of the breakwater. This is firstly quite useful to know from an engineering point of view, although a couple of previous studies have already looked into this effect (Mori et al., 2015; Port and Airport Research Institute of Japan, 2011b). Thus, this exercise simply serves the purpose of confirming those results in addition to an illustration of the sensitivity of the inundation results to the breakwater condition. For this reason it is difficult to accurately reproduce the actual survey measurements in this particular bay. Figure 5.6 firstly shows a colour plot of the maximum recorded free surfaces, η_{max} in the three simulations. The TTJS survey measurements are included as filled circles with their colour representing the maximum inundation height.

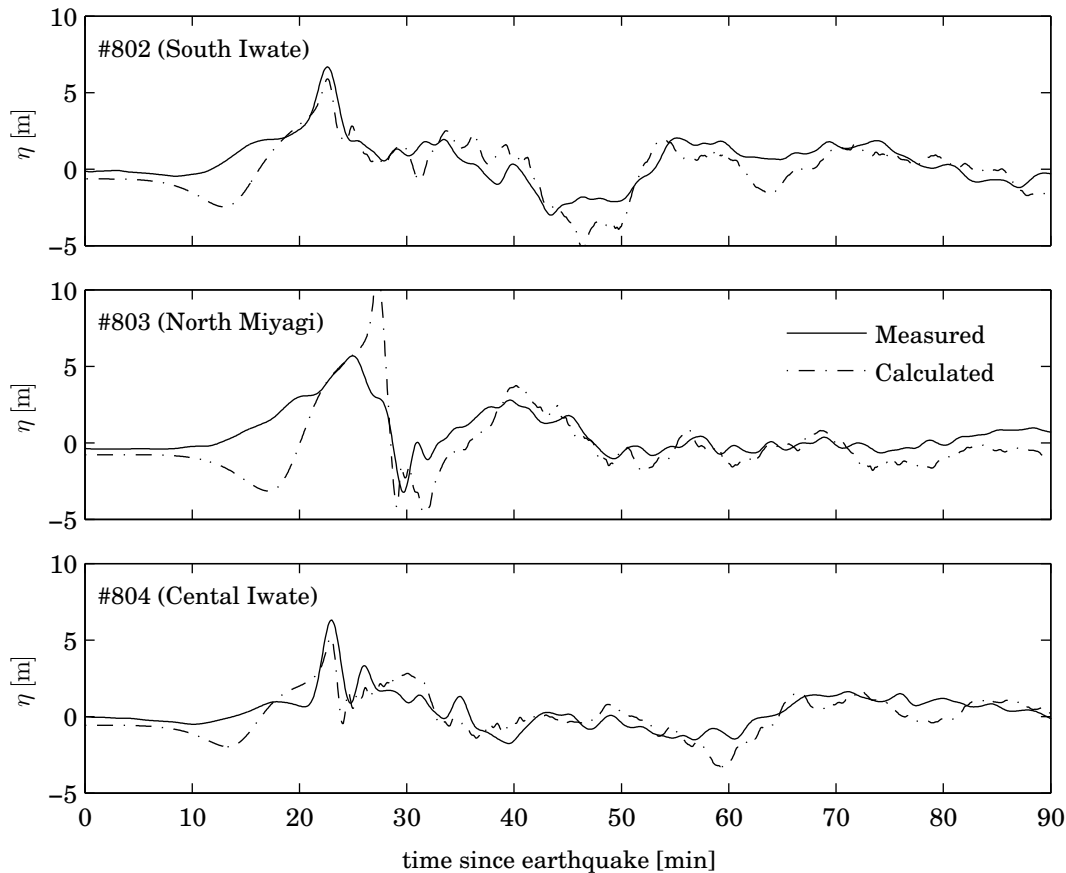


Figure 5.5: Water level time series at three Port and Airport Research Institute of Japan (2011a) GPS wave buoys closest to Kamaishi Bay, comparing simulation results in this study using the Tohoku University version1.2 source (Imamura et al., 2012) with the measured water levels

The tsunami height for the no breakwater case in Figure 5.6(a) ranges from 14 m at the bay mouth to 20 m at the back of the V-shaped bays. The inundation extends very far inland via the river. The inundation heights are much larger than any of the survey measurements (this is quantified in more detail below). When the post-tsunami damaged offshore breakwater condition is set (Figure 5.6(b)) the tsunami heights in the bay reduced by approximately 4 m so that at the back of the bays the heights is near 16 m while at the bay mouth the tsunami height is 10 m. Still in this case the survey inundation heights are significantly larger than those of the simulation. This can be attributed to the fact that the breakwater was destroyed at some point during the event, probably during the largest wave, but not immediately. Thus the breakwater could still offer more protection than its post-tsunami state. In comparison, the pre-tsunami undamaged breakwater condition reduces the tsunami height considerably inside of the Kamaishi bay. Offshore of the breakwater the tsunami height climbs to 12 m while just onshore of the breakwater the tsunami height is less than 6 m. At the back of the bays the

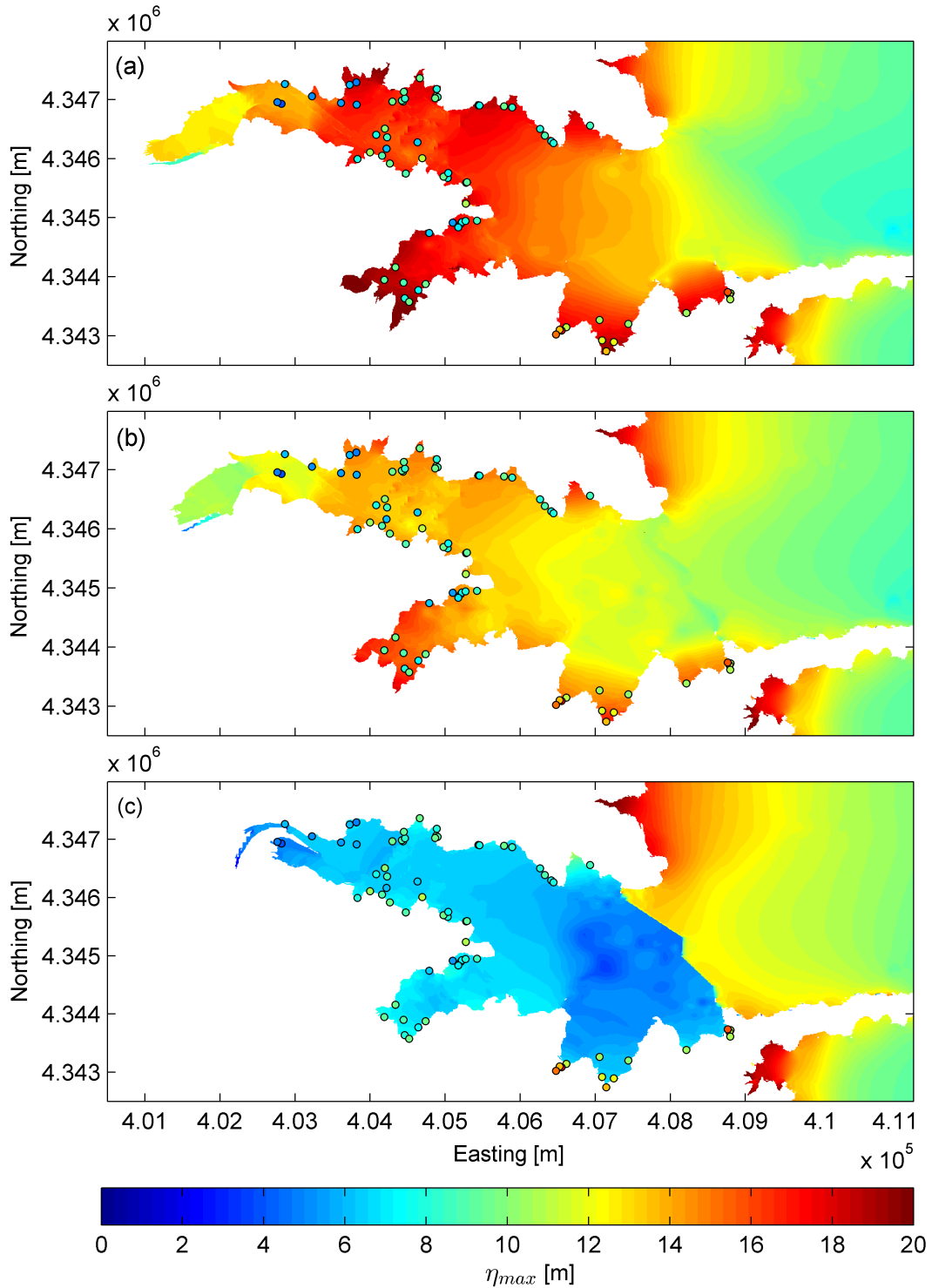


Figure 5.6: Colour plots of the maximum recorded free surfaces, η_{max} using the NSW model for three conditions of the offshore tsunami breakwater, with a comparison to TTJS survey measurements (Mori et al., 2012) (indicated by filled circles). (a) No offshore breakwater, (b) Post-tsunami damaged breakwater, (c) Pre-tsunami undamaged breakwater

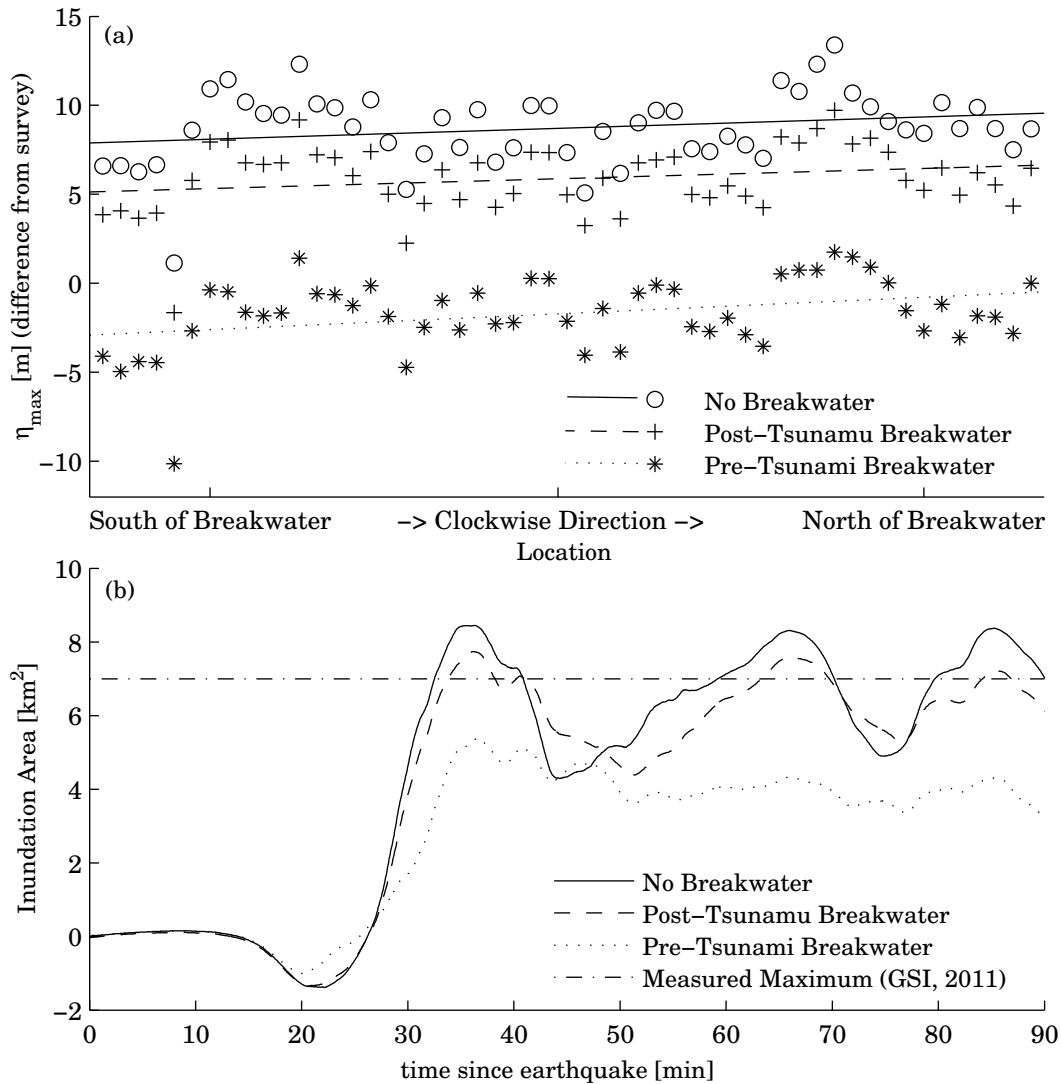


Figure 5.7: Effect of the offshore tsunami breakwater on inundation heights and area for 2 hours of simulation with the NSW model. (a) Difference in maximum inundation heights between TTJS survey measurements and simulated ones at locations ordered in a clockwise direction around the coast with least-squares lines of regression (lsline) also plotted, (b) Time series of the inundation area with estimate of actual maximum area (in the greater Kamaishi City region larger than our computational domain) shown for comparison

tsunami height reaches approximately 8 m. This is a substantial difference to the no breakwater case. In general this case indeed matches the survey measurements to the best accuracy overall although slight underestimation of the inundation heights is apparent.

In order to quantify the the comparison of the three cases and with survey measurements more precisely, Figure 5.7 plots the difference of η_{max} with the TTJS survey measurements

for inundation heights in (a) and the inundation area in (b). Least-squares lines in (a) are also included. A trend that is immediately apparent is that the inundation heights were predicted to be larger in the northern region than in the southern region. This could be attributed to the fact that the northern region mainly corresponds to the major Kamaishi City center thus in reality many buildings and infrastructure were present that could have reduced the inundation heights. The current simulation only approximates such effects through a larger Gauckler-Manning coefficient (that is also derived from coarse 50 m mesh data) which may be inadequate. In other areas along the coast the presence of buildings and infrastructure is scarce so the simulation results will be more reliable here. For all cases the slope of the trend lines are almost identical. This indicates that the breakwater has an influence over the entire bay as to be expected because it is placed at the bay mouth, which is one major advantage of the large-scale tsunami breakwater in comparison with smaller breakwaters or seawalls near the coastline that may only have very local effects. On average the pre-tsunami breakwater condition underestimates the inundations height by 1.7 m (2.1 m), whereas the post-tsunami breakwater overestimates the tsunami inundation heights by 5.9 m (1.9 m). Without a breakwater the inundation heights are on average 8.7 m (2.1 m) larger than the TTJS survey measurements. This is considerable, equivalent to on average a 51% reduction. Other studies has suggested the reduction is on the order of 20-40% (Mori et al., 2015) which according to this study may in fact be a lower bound estimate. It should be noted that the estimate in Mori et al. (2015) was only based on the reduction either side of the breakwater and not the actual reduction between a no breakwater case and the measured inundation heights. However, for the pre-tsunami undamaged tsunami breakwater case in this study the reduction can also be estimated to be at least 50% based on the tsunami height either side of the breakwater although this should indeed be an upper bound estimate given the damage to the breakwater.

Similarly, concerning the inundation area in (b), the three breakwater conditions result in different magnitudes of the inundation area. The maximum inundation area generally occurs due to the peak positive wave at approximately 35 minutes after the earthquake rupture. The difference between the no breakwater case and the pre-tsunami breakwater case is approximately 3 km² which is equivalent to a 36% reduction in the inundation area due to the presence of the breakwater. For validation, a comparison can be made with an approximation of the actual measured inundation area for the greater Kamaishi City region. It has been estimated to be 7 km² (Geospatial Information Authority of Japan (GSI), 2011), but this includes areas outside of the computational domain so the actual measured inundation area in the computational domain is likely to be closer to the maximum predicted by the pre-tsunami breakwater condition case.

In summary, the range of inundation heights and areas for the three breakwater conditions provide upper and lower bounds of the actual recorded ones. This gives us confidence that the NSWE numerical model and the tsunami source model is reasonable because the actual case can be assumed to be a combination of the pre-tsunami and post-tsunami breakwater conditions due to the damage of the breakwater during the event.

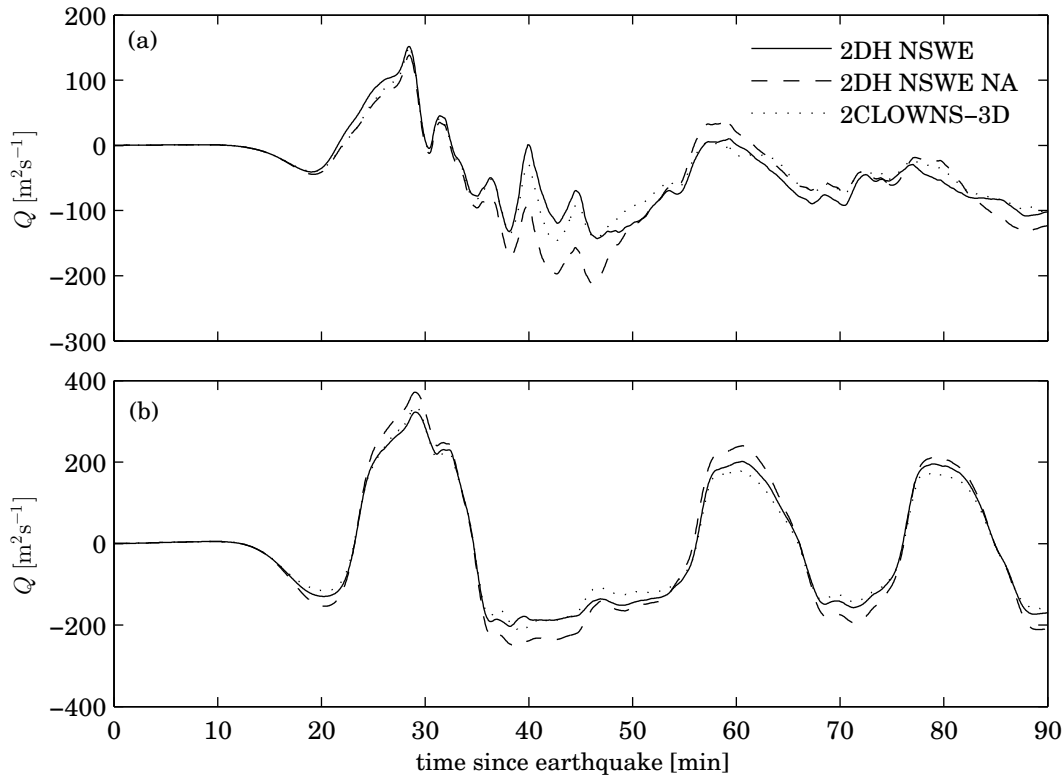


Figure 5.8: Time series of the measured volume flux per unit width, Q (averaged in the north-south direction) for 90 minutes of simulation comparing the 2DH NSWE and 2CLOWNS-3D simulations. Positive indicates flow in the onshore direction (east to west). (a) east boundary of the RANS domain, (b) submerged section of the breakwater

2CLOWNS-3D Simulation

One simulation using the 2CLOWNS-3D model was conducted for the pre-tsunami breakwater case. The 2CLOWNS-3D model allows for the full scale tsunami computed from the source to be conducted with a detailing of the 3D hydrodynamics on the offshore tsunami breakwater. This is usually unobtainable because of the computational load required for full 3D simulations over an entire domain. Furthermore, 3D simulations of this type where multiple free surfaces are possible (VOF method employed) and the $k-\epsilon$ turbulence model is used are generally numerically inaccurate over very large scales compared with long wave models.

Firstly, it is important to test whether the flow rates between the 2CLOWNS-3D model and the 2DH NSWE model are correctly comparable at certain cross-sections to show the boundary conditions into the RANS model from the NSWE model, and the RANS calculation itself are reasonable. Figure 5.8 plots the time series of the volume flux, Q (per unit width averaged in the north-south direction) at: (a) the east boundary of the RANS model where coupling takes place with the 2DH NSWE model, and (b) over the submerged breakwater section. Also included

for interest is Q from the 2DH NSWE simulation without the adjustment for depth at the cell boundaries to represent the vertical walls of the breakwater as described in §5.2.3, denoted “2DH NSWE NA”. Initially over the first 15 minutes all the models are the same predicting almost zero volume flux. Following this the initial drawback takes place where flow is sucked through the breakwater from the onshore side to offshore. Here, the 2DH NSWE and 2CLOWNS-3D models are in good agreement while the flow rate at the submerged breakwater in the 2DH NSWE NA case is greater. Similarly when the tsunami peak arrives after approximately 30 minutes the corrected 2DH NSWE and 2CLOWNS-3D models are in good agreement (the flow rate in 2CLOWNS-3D is 4.5% greater at the time of the peak flow rate at the submerged breakwater section) while the 2DH NSWE NA case overestimates the flow rate by 15%. This trend continues for most of calculation. As time proceeds the differences between the 2CLOWNS-3D and corrected 2DH NSWE model simulations slightly increase probably as the flow structure produced by the RANS model such as turbulent structures and vorticities become pronounced. Two conclusions can be drawn from this figure: First, the similarities of the flow rate between the 2DH NSWE and 2CLOWNS-3D simulations suggest that the two-way coupling scheme is robust in terms of the boundary conditions and the ability of the RANS model to correctly simulate the flow. Second, when using NSWE models in the vicinity of structures such as a breakwater with a vertical wall it is important to take care about how the depth is being approximated across the cell boundary so that the volume flux is correctly simulated (to avoid the demonstrated simulation result denoted by “2DH NSWE NA”).

The difference in maximum recorded free surfaces, η_{max} between the 2CLOWNS-3D and 2DH NSWE simulation - $(\eta_{max})_{2CLOWNS} - (\eta_{max})_{NSWE}$ - is plotted in Figure 5.9 on the 2DH NSWE 10 m mesh. Offshore of the breakwater almost no difference is generated between the simulations but over the breakwater and onshore of it differences become evident. Onshore of the breakwater, η_{max} is larger in the 2CLOWNS simulation by up to 2 m and is highly location dependent. For example, north in Kamaishi City Main, and in the two southernmost bays, η_{max} is approximately 0.5 - 1 m greater in the 2CLOWNS simulations. In contrast very little difference is found in Heita between the two simulations. The directional dependence on η_{max} could be due to the difference in the structure of the jet that forms through the submerged breakwater section as well as vorticity formation. Similarly, the general increase in magnitude of η_{max} in 2CLOWNS-3D is likely to do with the slight increase of Q through the submerged breakwater section (Figure 5.8) followed by the differing hydrodynamics of the flow over the caissons and the resulting jet. These hydrodynamic aspects will be addressed in more detail in the §5.4.

Another major difference of η_{max} between the models emerges just offshore and over the breakwater section. In 2CLOWNS-3D, over the breakwater section (on top of the caissons during overtopping flow) η_{max} is larger while η_{max} is smaller just offshore compared with the 2DH NSWE simulation. These differences arise because of the differing mechanism during overtopping flow and as the tsunami flows over the submerged caissons between the models. For example, the flow

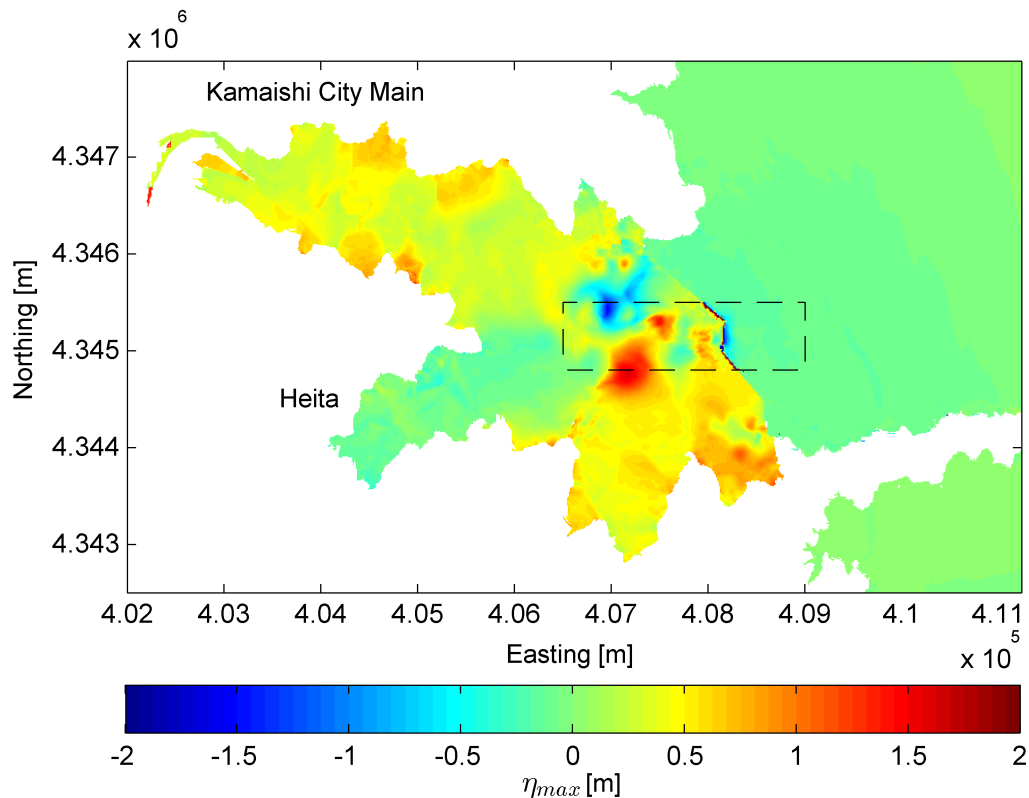


Figure 5.9: Difference in maximum recorded free surfaces, η_{max} between the 2CLOWNS-3D and 2DH NSW simulation - $(\eta_{max})_{2CLOWNS} - (\eta_{max})_{NSWE}$ - for 2 hours of simulation. Dashed black rectangle indicates the location of the 3D RANS domain

is allowed to become non-hydrostatic in the RANS model which as will be shown later can vastly change the structure of the flow over the submerged caissons compared with the hydrostatic NSW model. Secondly, for overtopping the NSW makes use of the overtopping weir formula introduced in §3.2.3, whereas the RANS model calculates the overtopping flow rate via the normal governing equations. It should be noted however that due to the coarseness in the horizontal resolution, accurate overtopping calculations should not be expected in either model. In this study, the overtopping is not the main target, so the accuracies and model differences in overtopping will not be pursued in detail here but are suggested for future studies.

Figure 5.10 provides a concrete comparison of the difference in inundation estimations between the 2DH NSW and 2CLOWNS-3D simulations. In general the inundation heights and area are slightly greater when using the 2CLOWNS-3D model perhaps due to the 4.5% increase in the peak flow rate through the breakwater section. As demonstrated in Figure 5.9 this is also location dependent. However, since there are some locations where the 2CLOWNS-3D simulation predicts a marginally smaller inundation height, e.g. in the Heita area which corresponds to the 10 locations to the right of the “South of Breakwater” tick in Figure 5.10. The

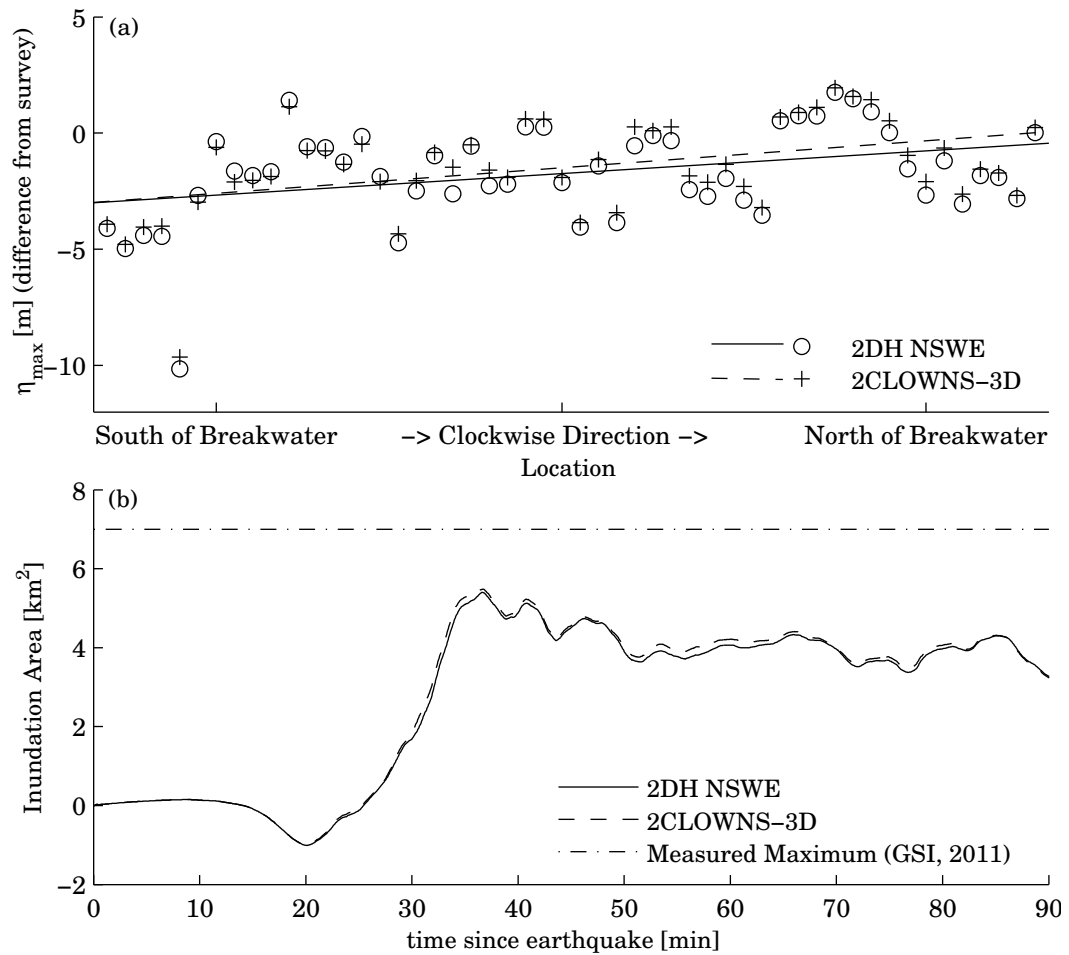


Figure 5.10: Difference in inundation between the 2CLOWNS-3D and 2DH NSWE model simulations. (a) Difference in maximum inundation heights between TTJS survey measurements and simulated ones at locations ordered in a clockwise direction around the coast with least-squares lines of regression (lsline) also plotted, (b) Time series of the inundation area with estimate of actual maximum area (in the greater Kamaishi City region larger than our computational domain) shown for comparison

RMSE (Root Mean Squared Error) between survey measurements was 2.7 m for the 2DH NSWE pre-tsunami breakwater simulation compared with 2.5 m for the 2CLOWNS-3D one. On average the 2CLOWNS-3D simulation underestimated by the survey measurements by 1.5 m (2.0 m). Recall that the 2DH NSWE underestimated measurements by 1.7 m (2.1 m). Furthermore, the maximum inundation area is 1.6% greater in the 2CLOWNS-3D simulation. Hence, using the 2CLOWNS-3D simulation results in inundation heights and areas slightly closer to the measured ones. However, it cannot be said that using the 2CLOWNS-3D model can give improved prediction of the inundation (the actual situation of the breakwater such as the evolution of the damage is unknown). The main conclusion to be drawn is that overall using a RANS model in the vicinity of the breakwater to potentially more correctly model the hydrodynamics of the flow does not result in vast differences in the final inundation heights. This is good news because; it demonstrates the robustness of the 2CLOWNS-3D model and, if inundation is the only concern in a study then 2DH NSWE is probably sufficient even though in some regions (e.g. over a submerged breakwater) the model cannot be expected to give an accurate description of the flow.

5.4 Flow Hydrodynamics Onshore of Breakwater

This section quantifies the hydrodynamics of the flow onshore of the submerged section of the offshore breakwater. Firstly, an overview of the depth-averaged velocity distribution is shown including a comparison of the 2CLOWNS-3D results with those of the 2DH NSWE simulation. Secondly, the horizontal and vertical distribution of the flow hydrodynamics in the 3D RANS domain is discussed. Finally, an estimation of the maximum shear stresses in the vicinity of the breakwater is shown.

5.4.1 Velocity Comparisons with 2DH NSWE Simulation

The maximum recorded magnitudes of the depth-averaged velocities, U_{max} on the 2DH NSWE 10 m grid are shown in Figure 5.11. Furthermore, a snapshot of the depth-averaged velocity field at $t = 1740$ s after the earthquake rupture (time of peak incoming tsunami wave) is illustrated in Figure 5.12. Both figures compare the 2CLOWNS-3D and 2DH NSWE simulation. In addition, snapshots of the depth-averaged velocity field with flow vectors at a number of selected instances for the 2CLOWNS-3D simulation are shown in Figure D.1 - D.3 located in Appendix D. These figures illustrate how rotational structures and jets can pass freely through the NSWE-RANS interface thanks to the robust two-way coupling algorithm in 2CLOWNS-3D.

Outside of the RANS domain no noticeable difference in the velocities arise from its insertion around the breakwater opening. Inside of the RANS domain two major differences are shown. The first difference is the magnitude of the velocity over the submerged caissons. U_{max} in the 2DH NSWE simulation is shown to reach 20 ms^{-1} which is considerably large. In comparison the 2CLOWNS-3D simulation shows that U_{max} is on the order of 13 ms^{-1} . U at $t = 1740$ s is approximately equal as to be expected since that is the time of the peak incoming tsunami wave. The second major difference is the horizontal structure and magnitude of the velocities in the jet emanating from the submerged breakwater section towards the coast. Here, U_{max} in the middle of jet in 2CLOWNS-3D is on the order of 14 ms^{-1} whereas they are on the order of 11 ms^{-1} in the 2DH NSWE simulation. Reasons for these effects will be illuminated in §5.4.5 after the vertical effects of the flow in the 3D RANS domain are highlighted. In addition, the jet in 2CLOWNS-3D becomes quite pronounced towards the north direction (in the direction of Kamaishi City Main). In 2DH NSWE the jet remains fairly straight and lacks north-south direction. This can help to explain the directional dependency on the maximum inundation heights in 2CLOWNS-3D compared with 2DH NSWE such as larger heights in Kamaishi City Main up to ~ 1 m and slightly smaller heights in Heita. The difference in the horizontal jet structure and direction can at least partially be attributed to the absence of horizontal mixing in the NSWE model. In the 3D RANS model the effect of turbulent mixing is accounted for in a complex fashion through the modelling of the eddy viscosity. It may be possible to improve the approximation of the jet structure in the NSWE model by including an approximation of the horizontal mixing. However, it will be shown

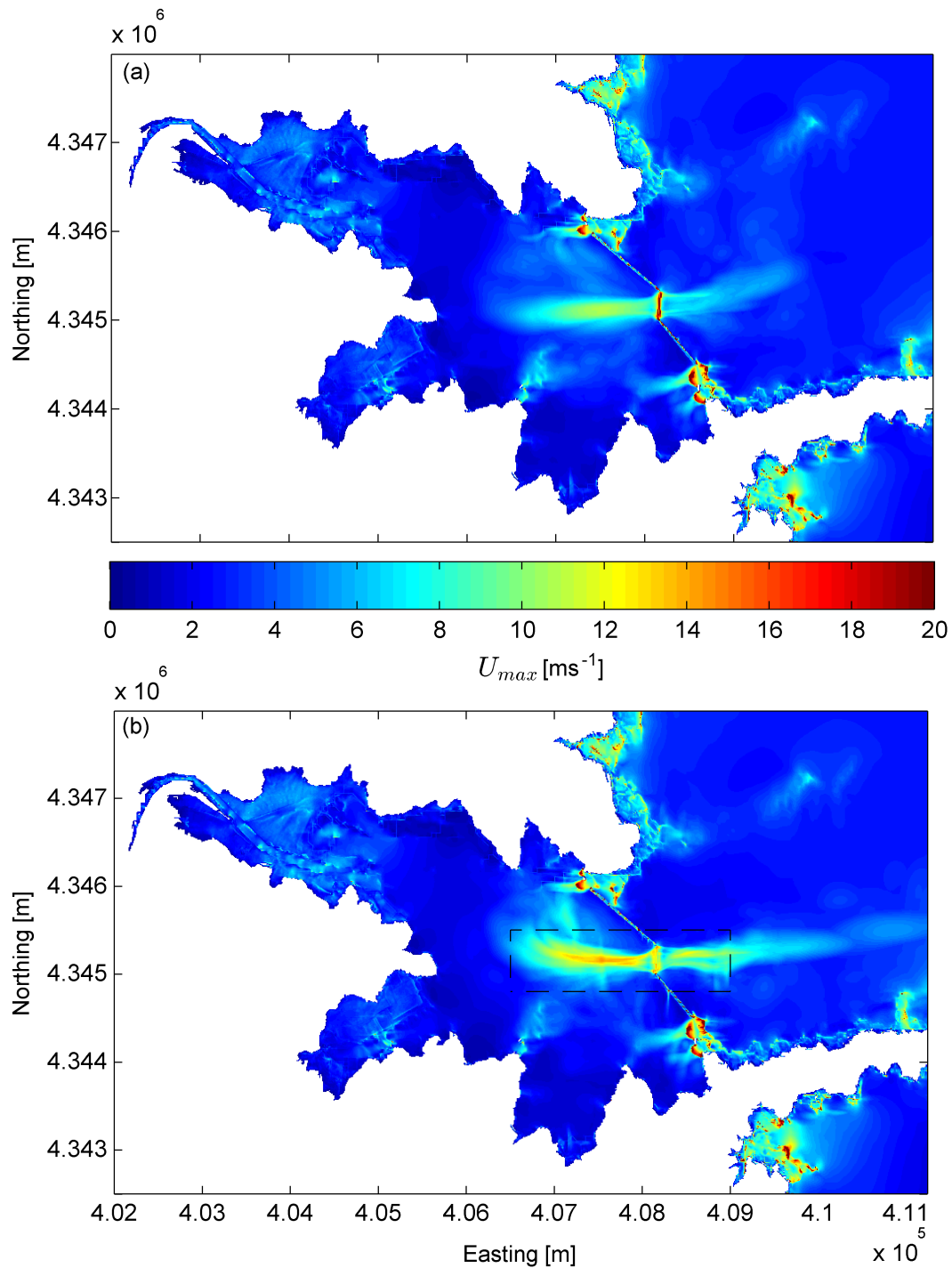


Figure 5.11: Map of the maximum recorded magnitudes of the depth-averaged velocities, U_{max} during the 2DH NSWE and 2CLOWNS-3D model simulations for 2 hours of simulation on the 10 m 2DH NSWE mesh. (a) 2DH NSWE simulation, (b) 2CLOWNS-3D simulation - dashed black rectangle indicates the location of the 3D RANS domain

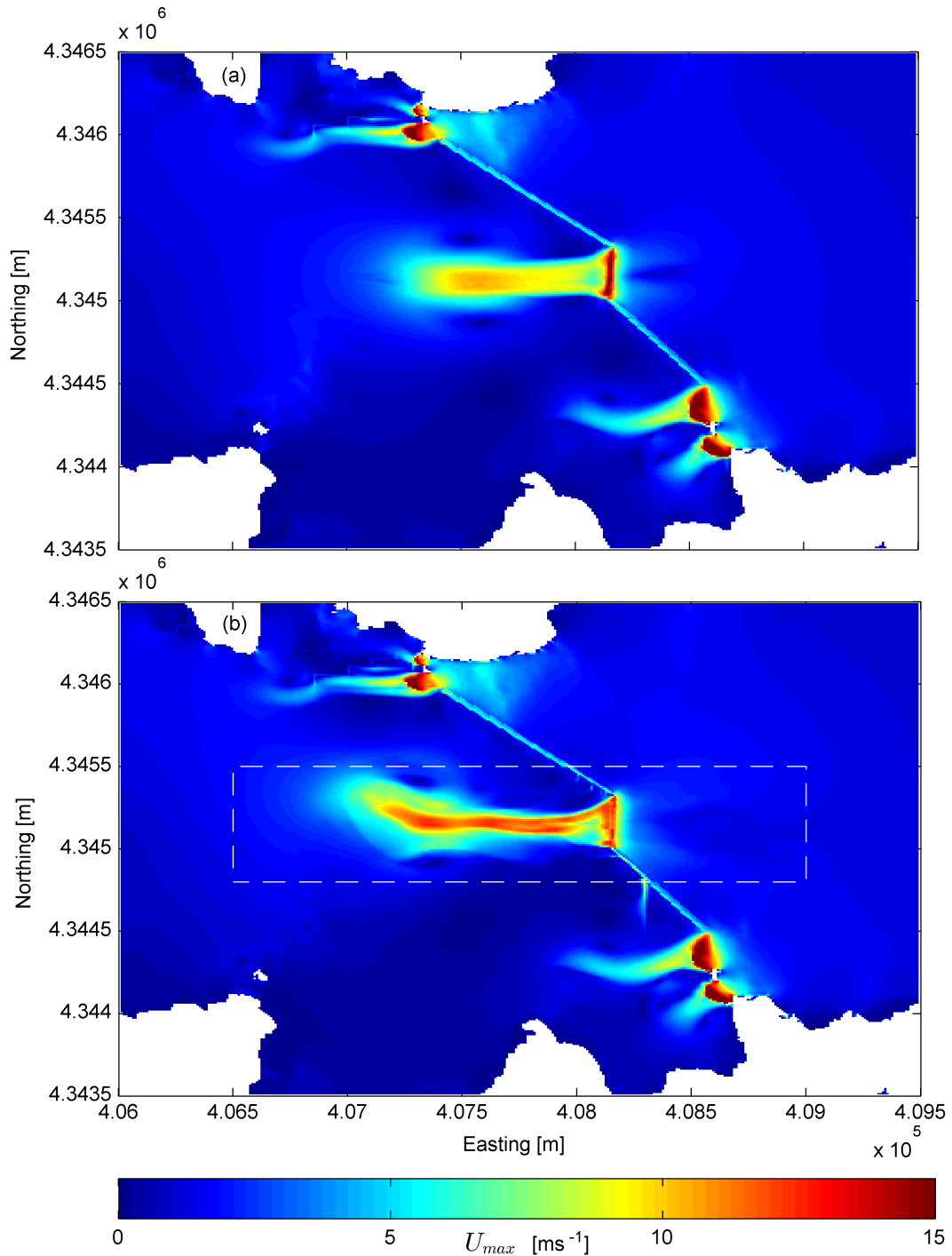


Figure 5.12: Colourplot of the magnitudes of the depth-averaged velocities, U during the 2DH NSWE and 2CLOWNS-3D model simulations on the 10 m 2DH NSWE mesh at $t = 1740$ s after the earthquake rupture. (a) 2DH NSWE simulation, (b) 2CLOWNS-3D simulation - dashed white rectangle indicates the location of the 3D RANS domain

that vertical effects are also non-trivial in §5.4.3.

One minor issue that was found with the two-way coupling in this study was on the north and south boundaries over the breakwater. For example, at the south boundary over the breakwater in Figure 5.12(b) there is a streak of fast flow that has arisen when water overtopping the breakwater in the 3D domain on the boundary induces overtopping into the 2DH NSWE domain perpendicular to the main flow direction. This occurs because the breakwater is at an angle to the Cartesian grids, calculation is conducted on a coarse grid relative to the breakwater width, and due to the slight difference in overtopping behaviours between the models. Furthermore, it has already been shown in Figure 5.9 that the maximum tsunami height becomes quite different over the overtopped partially submerged caissons. Since the current problem was found to have a trivial effect on most of the flow in general and the main objectives of this study does not concern overtopping, this issue was ignored in this study. However, it may be of interest to look at the overtopping problem in future work.

5.4.2 Horizontal Distribution of the Hydrodynamics

In this section the horizontal distribution of the velocities (with magnitude, $V = \sqrt{u^2 + v^2}$), horizontal vorticity, ω and the turbulent kinetic energy, k at snapshots in time are shown to get a better understanding of the flow. Figure 5.13 and Figure 5.14 plot, V , ω and k on the $z = -20.8$ m contour at $t = 1740$ s and 2340 s after the earthquake rupture respectively. These two times correspond to that of the peak positive incoming wave and peak drawback respectively (c.f. Figure 5.8). The $z = -20.8$ m contour is at the level just above the submerged caisson. Similar plots at different times (including ones for v_t) may be found in Figure D.4 - Figure D.7 located in Appendix D for further reference.

During the time of the onshore directed peak positive wave ($t = 1740$ s) plotted in Figure 5.13, the jet-like structure onshore extends for roughly 1 km onshore of the breakwater. V is as large as 15 ms^{-1} near the submerged caissons. Further onshore near the end of the jet, V in the centreline of the jet is approximately equal to 12 ms^{-1} . The major magnitude of vorticities generated are related to the eddies that spin off the edges of the north and south breakwater section. The size of these vorticities are shown to go beyond 0.30 s^{-1} in magnitude. To give an idea of the relative magnitude, the large vortex filmed in Oarai Port, Japan resulting from the 2011 Tohoku-oki Earthquake Tsunami has been simulated seemingly accurately in comparison with actual snapshots and predicted to have a maximum vorticity of approximately 0.15 s^{-1} in its center (Lynett et al., 2012) which is less than half the magnitude shown here. The vorticities spinning off the breakwater are however small in scale and quickly lose their magnitude. They generate into larger rotating currents centred at approximately the 4.074×10^5 m easting coordinate that are almost symmetrical in the north and south direction. Here, the vorticities are shown to be on the order of 0.1 s^{-1} rotating clockwise on the north side and anticlockwise on the south side. Figure D.1 illustrates that the velocity vectors are undisturbed across the boundaries even in

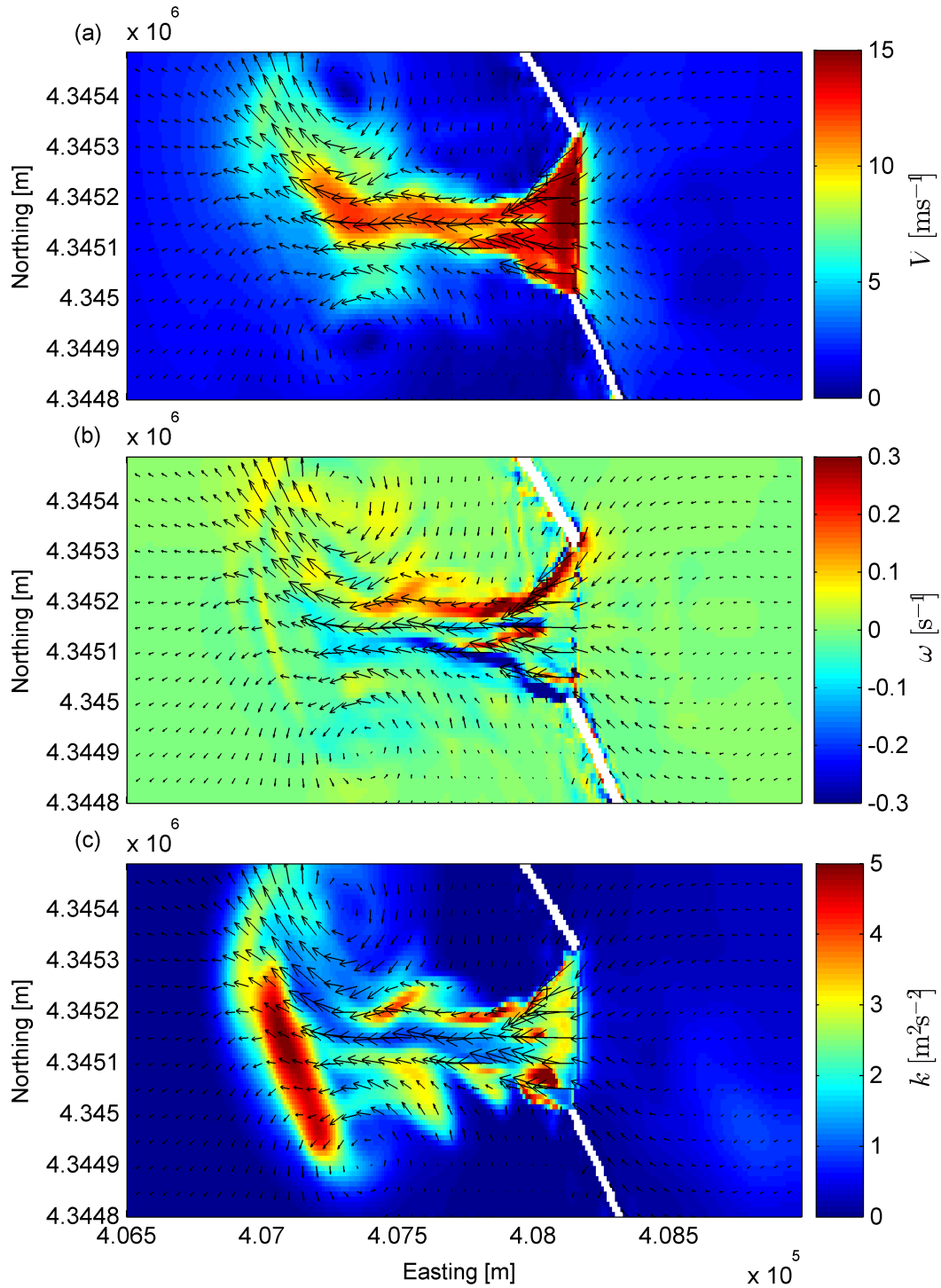


Figure 5.13: Horizontal distribution of the velocity and colour plots of various scalar indicators of the hydrodynamics on the $z = -20.8$ m contour within the 3D RANS domain for the 2CLOWNS-3D model simulation at $t = 1740$ s after the earthquake rupture: (a) horizontal velocity magnitude, V , (b) horizontal vorticities, ω , and (c) turbulent kinetic energy, k

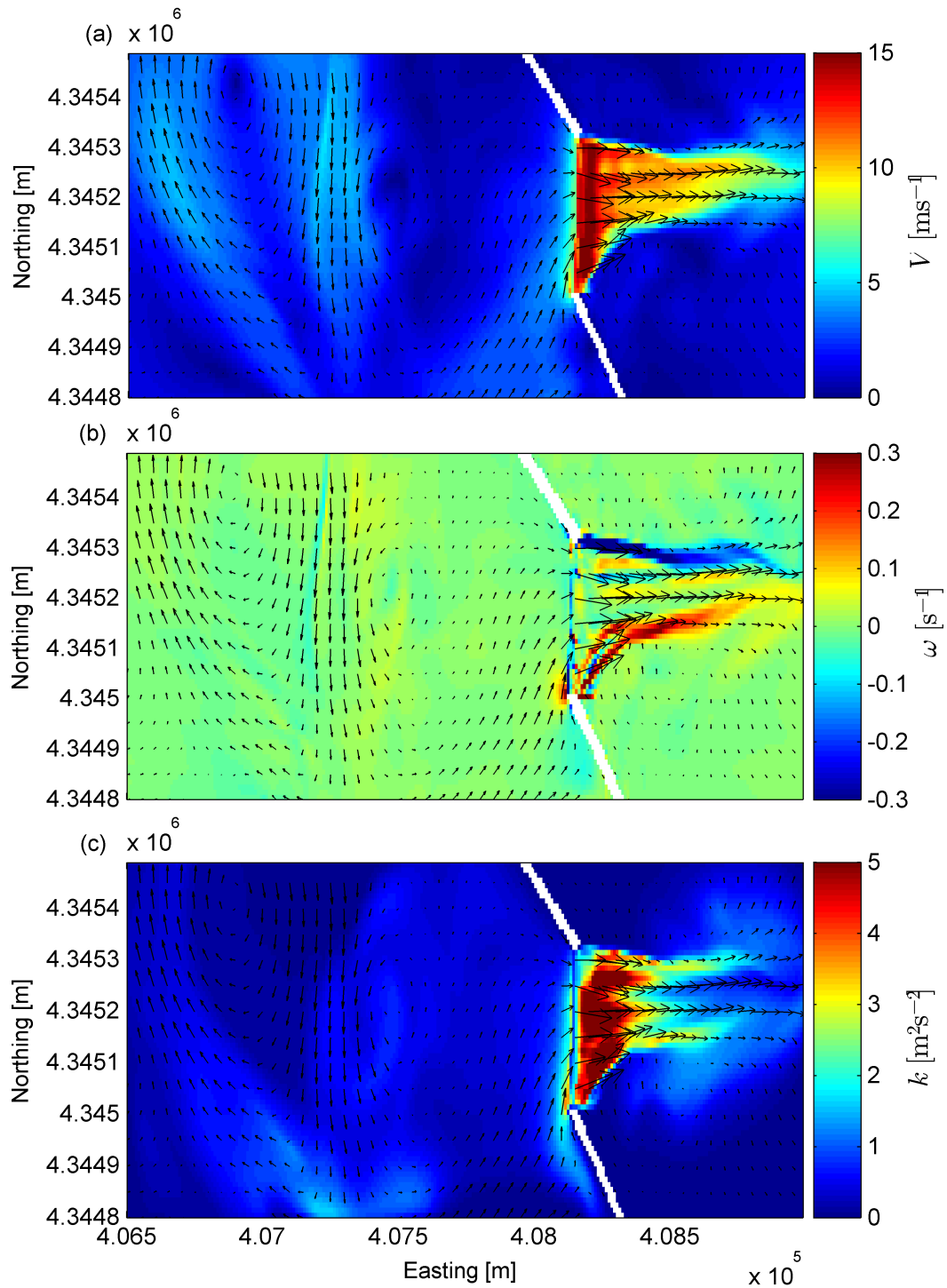


Figure 5.14: Horizontal distribution of the velocity and colour plots of various scalar indicators of the hydrodynamics on the $z = -20.8$ m contour within the 3D RANS domain for the 2CLOWNS-3D model simulation at $t = 2340$ s after the earthquake rupture: (a) horizontal velocity magnitude, V , (b) horizontal vorticities, ω , and (c) turbulent kinetic energy, k

the presence of the rotating flow. However, it is not clear that the vorticities themselves can be correctly passed through undisturbed since vorticities of opposite signs to the major rotation are generated near the boundaries. Almost all of the turbulent energy is located onshore of the breakwater due to the squeezing of the flow through the submerged section. k is shown to be largest at the edges of the jet structure and smallest in the centreline. At the edges production of k is large due to the shear with the slower moving flow outside of the jet. The magnitude of k is as large as $k = 5 \text{ m}^2\text{s}^{-2}$ in these regions. Figure D.7 also shows that the turbulent viscosity, ν_t is highly correlated with k except close to the submerged breakwater with magnitude as large as $\nu_t = 13 \text{ m}^2\text{s}^{-1}$. The turbulent energy is allowed to dissipate to almost zero at the west boundary indicating that the length of the boundary in this direction is adequate. Some of the turbulent energy ($k \approx 2 \text{ m}^2\text{s}^{-2}$) makes it way to the north boundary. In an ideal simulation the north boundary would be extended to avoid this situation, although numerical issues at this boundary were not encountered.

During the peak drawback phase ($t = 2340 \text{ s}$) shown in Figure 5.14, on the onshore side of the breakwater elongated rotating currents are present that are transported through the northwest boundary. Between the $4.07 \times 10^5 \text{ m}$ and $4.075 \times 10^5 \text{ m}$ easting coordinates the flow is almost completely north to south. Judging from the flow patterns between $t = 2004 \text{ s}$ and $t = 2412 \text{ s}$ in Figure D.2, the large rotating current is in the process of transforming from the predominantly east-west flow to a fully circular one. At $t = 2412 \text{ s}$ a large coherent vortex structure is formed similar to the one filmed in Oarai Port. The coherent vortex structure remains thereafter at least up to $t = 4500 \text{ s}$ and beyond (c.f. Figure D.3). In Figure 5.14, on the offshore side of the breakwater the jet structure extends to the eastern edge of the RANS domain. The magnitudes of the velocities reach up to 15 ms^{-1} near the submerged caissons at this time similar to the peak positive wave. Large vorticities spin off the ends of the partially submerged caissons. The turbulent energy is very large and concentrated close to the breakwater on the offshore side. This may be because existing energy has been transported from the onshore side to the offshore in addition to the production at the edges of the jet. Conversely ν_t is not large here (c.f. Figure D.7), presumably because large ϵ is also transported from the onshore region and cancels out the turbulent energy. In other words, the size of the eddies here are small and dissipative, thus the effect on the mean flow is also small. At this point in time k does not quite reach the edge of the domain in large quantities. However, it does in later times as the drawback flow becomes more developed (c.f. Figure D.6) and this has been found to lead to numerical instabilities in the simulation. It will be briefly mentioned here that the east boundary of the RANS domain is not as far offshore as would be optimal given the fact that the jet, vorticities and turbulent energy reach the edge of the domain (the same is true for the north boundary in particular as well as the south boundary at certain times, e.g Figure D.6 at $t = 2004 \text{ s}$). This is in contrast to the west boundary where no numerical issues (in addition to breaches of the physical assumptions) were encountered since it is located far onshore of the breakwater.

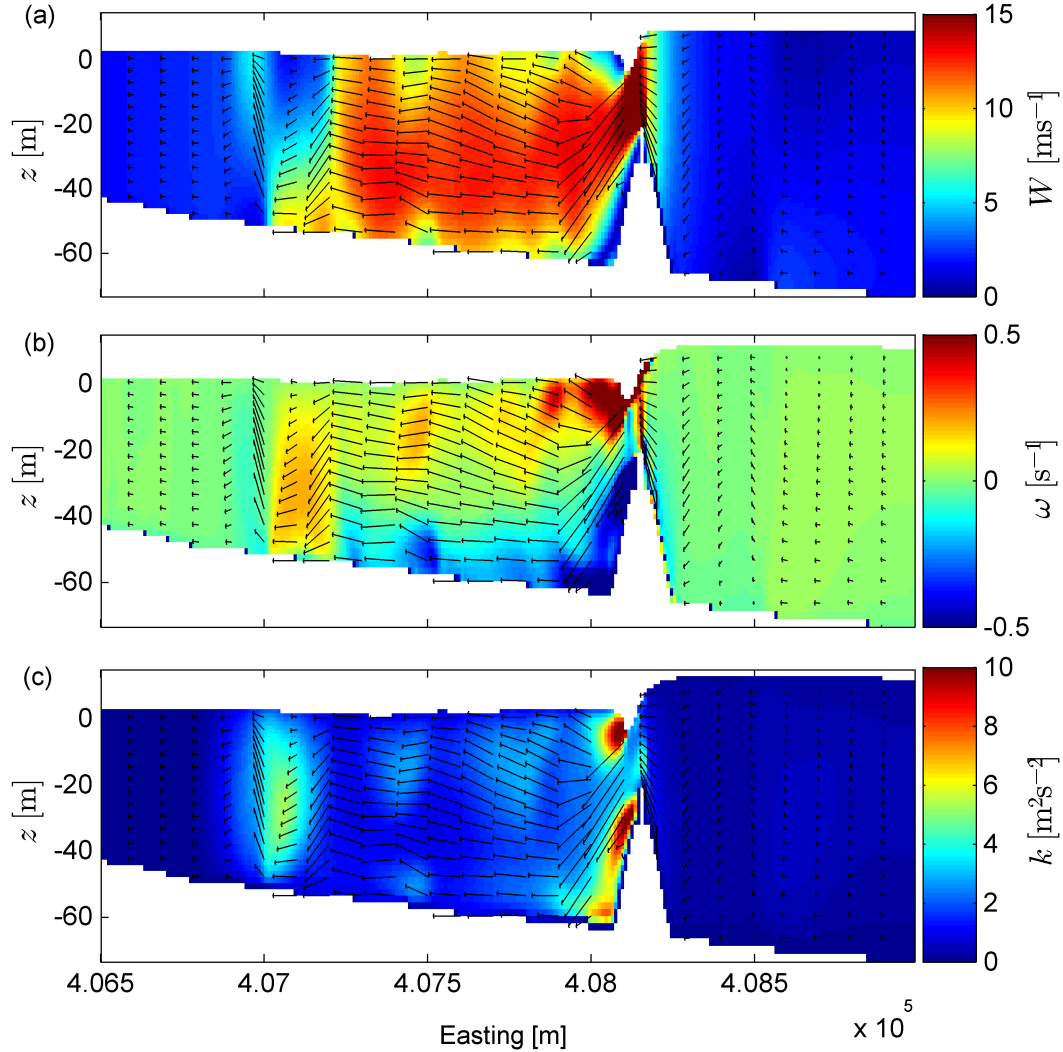


Figure 5.15: Vertical distribution of the velocity and colour plots of various scalar indicators of the hydrodynamics along the $y = 4,345,175$ m northing cross-section of the 3D RANS domain for the 2CLOWNS-3D model simulation at $t = 1740$ s after the earthquake rupture: (a) velocity magnitude in $x-z$ plane, W , (b) vertical vorticities, ω , and (c) turbulent kinetic energy, k

5.4.3 Vertical Distribution of the Hydrodynamics

This section investigates the vertical distribution of the velocities (with magnitude, $W = \sqrt{u^2 + w^2}$), vertical vorticity, ω , the turbulent kinetic energy, k (and ν_t) and the dynamic pressure at a nominal cross-section. The cross-section is taken to be in the east-west direction at the $y = 4,345,175$ m northing coordinate which is approximately along the centreline of the submerged breakwater section. The times chosen for presentation here are $t = 1740$ s and 2340 s after the earthquake rupture to be consistent with §5.4.2. Plots at other times may be found in Appendix D.

Colour plots of W , ω , and k are shown in Figure 5.15 and Figure 5.16 ($t = 1740$ s and

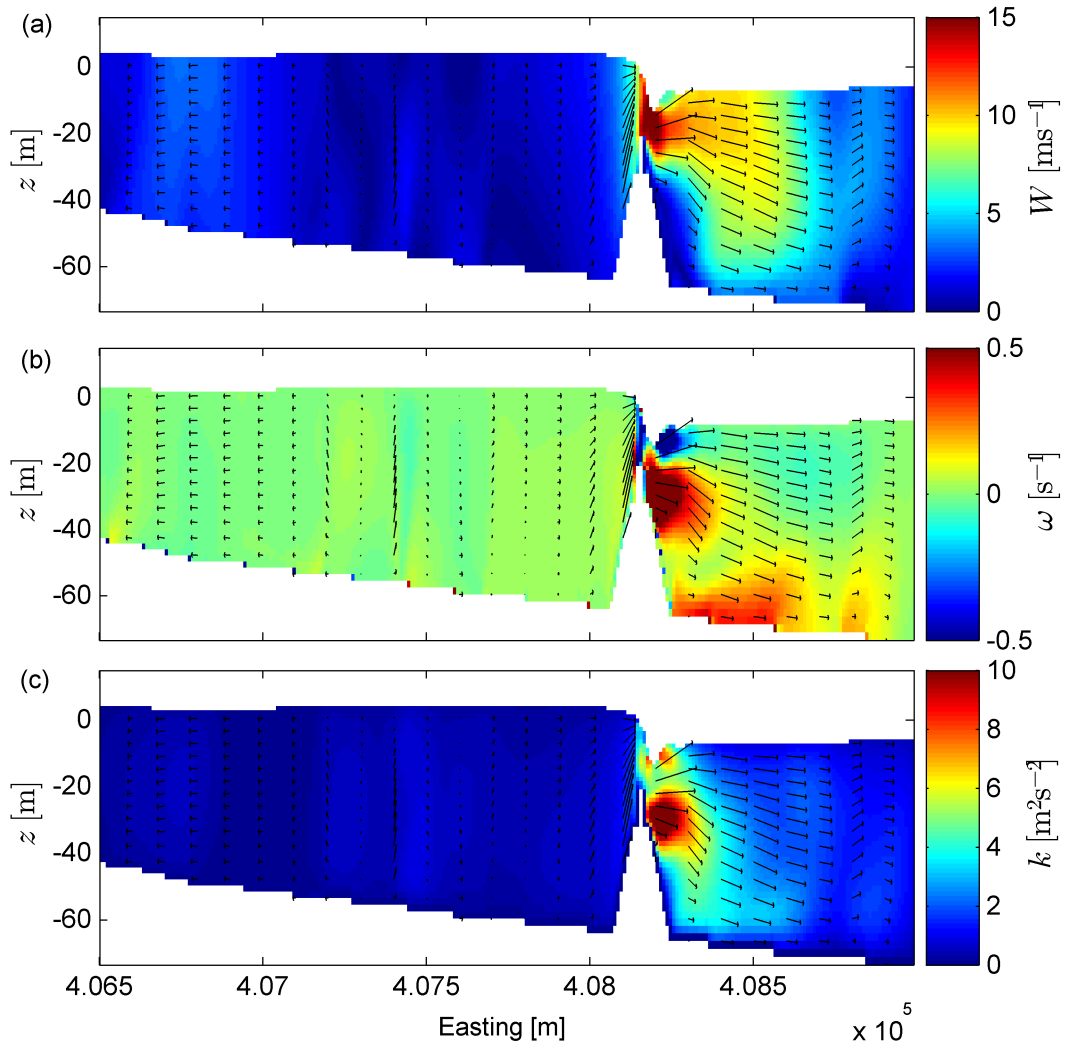


Figure 5.16: Vertical distribution of the velocity and colour plots of various scalar indicators of the hydrodynamics along the $y = 4,345,175$ m northing cross-section of the 3D RANS domain for the 2CLOWNS-3D model simulation at $t = 2340$ s after the earthquake rupture: (a) velocity magnitude in $x - z$ plane, W , (b) vertical vorticities, ω , and (c) turbulent kinetic energy, k

2340 s respectively). Velocity vectors are also included. Plots at other times may be found in Figure D.8 - Figure D.11 (including v_t). Furthermore, precise plots of the vertical distribution of the dynamic pressure, p_d (difference from the hydrostatic pressure) plus the horizontal, u and vertical velocities, w are shown in Figure 5.17 ($t = 1744$ s) and Figure 5.18 ($t = 2260$ s).

Firstly, during the peak positive wave ($t = 1740$ s), the vertical profiles at the east and west boundaries both exhibit similar characteristics. u has a fairly uniform value of approximately 2 ms^{-1} in the onshore direction while w , ω , k and p_d are very small. Near the submerged breakwater section the velocity vectors indicate how the flow dramatically changes in the vertical

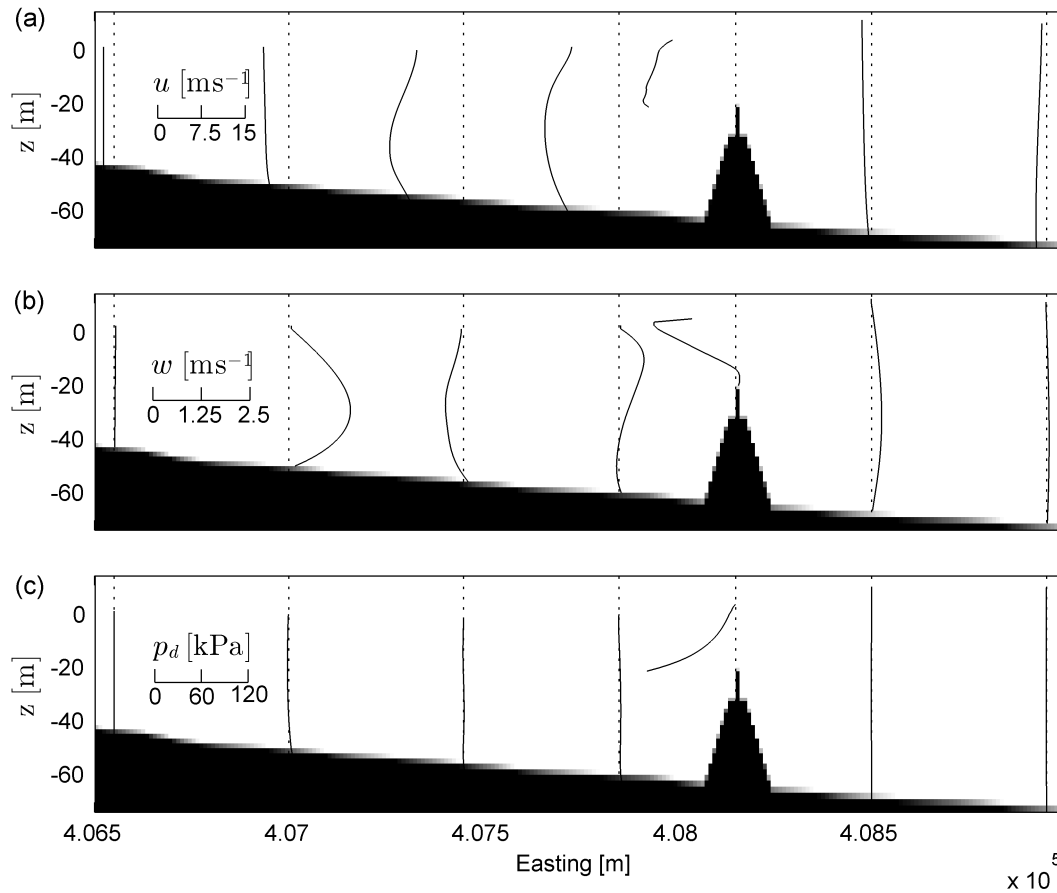


Figure 5.17: Vertical profiles of, (a) the horizontal velocity, u , (b) vertical velocity, w and, (c) the dynamic pressure (difference from hydrostatic), p_d along the $y = 4,345,175$ m northing coordinate within the 3D RANS domain for the 2CLOWNS-3D model simulation at $t = 1740$ s after the earthquake rupture. The direction of u is given by its position from the dotted line that indicates the location of the profile measurement. For w and p_d a positive value is right (east) of the dotted line

and horizontal directions. Just offshore of the breakwater the flow is accelerated upwards from below the submerged caissons. Flow near the free surface on the other hand is acting downwards following the drop in the free surface. Over the submerged caissons the magnitude of the velocity becomes very large, equal to approximately 15 ms^{-1} over most of the depth, although both u and w are smaller near the free surface. The vorticities are also very large ($> 0.5 \text{ s}^{-1}$) over the submerged section especially near the free surface. k also becomes large ($> 10 \text{ m}^2\text{s}^{-2}$) near the free surface due to the formation of the hydraulic jump. The dynamic pressure becomes negative close to the submerged caisson - as low as $p_d = -110 \text{ kPa}$. This is the main location where distribution of p_d deviates considerably from zero. The jet that is formed onshore of the breakwater due to the sudden contraction and reduction in depth is acting on an angle down towards the sea bed. The

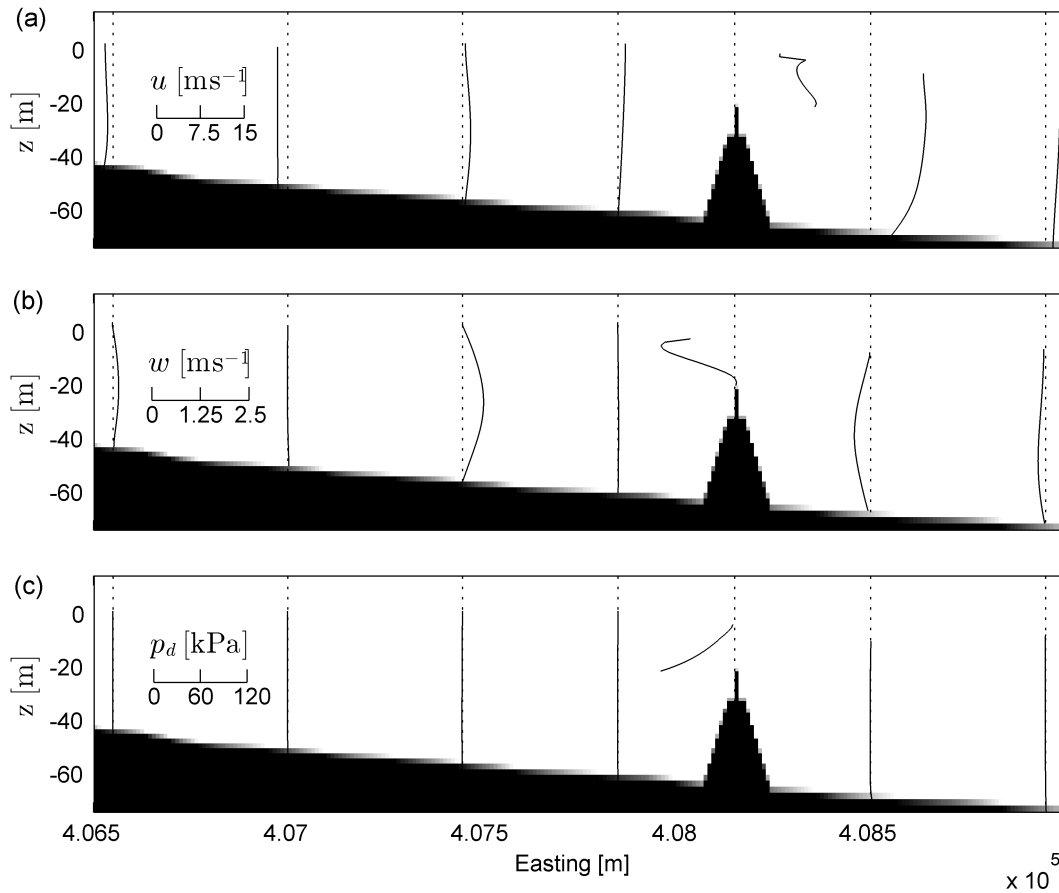


Figure 5.18: Vertical profiles of, (a) the horizontal velocity, u , (b) vertical velocity, w and, (c) the dynamic pressure (difference from hydrostatic), p_d along the $y = 4,345,175$ m northing coordinate within the 3D RANS domain for the 2CLOWNS-3D model simulation at $t = 2340$ s after the earthquake rupture. The direction of u is given by its position from the dotted line that indicates the location of the profile measurement. For w and p_d a positive value is right (east) of the dotted line

jet touches down at the sea bed at approximately $x = 4.08 \times 10^5$ m. In between the breakwater and the jet large negative vorticities and turbulent energy is produced due to the shear of the jet and the slow flow in this pocket. Onshore of the location of the touchdown of the jet with the sea bed the jet has fully spread out so that the velocities are largest around mid-depth and slightly smaller at both the free surface and sea bed. The jet extends one kilometre to $x = 4.07 \times 10^5$ m. At the edge of the jet the velocities are larger near the sea bed than at the free surface. Turbulent energy and positive vorticities are formed at the jet edge as the vertical velocities suddenly become very large in the positive direction ($\approx 2 \text{ ms}^{-1}$) around mid-depth.

In the peak drawback phase ($t = 2340$ s), u and w near the east boundary deviates slightly from a uniform distribution and small value respectively. This is because the distance from the

submerged breakwater to the east boundary is rather short and the flow does not quite have the chance to return to a normal uniform distribution. The non-uniformity of u that is generated here is an example of the benefit of introducing the arbitrary velocity distribution in this study (c.f. Eqn. (3.137)). This avoids introducing unwanted effects near the boundary in the 3D RANS model associated with forcing the flow to become uniform at the boundary. Note that introducing this velocity profile does not greatly affect the coupling performance since the 2DH NSWE model has no knowledge of this distribution. As long as the pressure is largely hydrostatic at the boundaries as is shown to be the case here, the two-way coupling process can in general succeed. The distribution of the u , w and p_d is very similar over the submerged breakwater during the drawback phase compared with the peak positive wave. However, the distribution of the vorticities and turbulent energy is quite different. In the case of the jet during drawback, the flow does not angle downwards and reach the sea bed with same velocity compared with the peak positive wave. Rather, the jet quickly becomes almost horizontal in direction followed by gradual spreading out over the depth. The velocities are generally faster near the free surface than in the lower depths. Hence, the shear of the jet structure and a region of slow ambient flow just offshore of the submerged caisson causes the small pocket of vorticity and turbulent energy to form here. k is quickly dissipated and is almost zero offshore of $x \approx 4.086 \times 10^5$ m. It is notable however, that the turbulent viscosity is not small in this region (c.f. Figure D.11). In fact ν_t is quite uniform over the entire offshore side of the breakwater. Furthermore, ν_t is very large just onshore of the submerged section.

5.4.4 Bed Shear Stresses

The fast flow onshore of the breakwater can cause large bed shear stresses leading to significant sediment transport in the harbour. This could induce unwanted erosion and deposition of sediment which if in the vicinity of coastal structures can lead to their instability.

The bed shear stress, τ_b has been automatically calculated by the RANS model through the wall function approach (c.f. §3.4.7). For a comparison the bed shear stress is also calculated from the depth-averaged velocity in the 2DH NSWE model simulation *and* the 2CLOWNS-3D simulation. τ_b is calculated from the depth-averaged velocity through the quadratic form using a drag coefficient (Eqn. (2.29)). For consistency with τ_b calculated by the wall function approach, the drag coefficient is estimated by the Darcy coefficient, f (Eqn. (2.30)) which makes use of the value of the equivalent sand roughness, k_s also used in wall function formula (Eqn. (3.120)). Fully rough turbulent flow is assumed where, f can be estimated through (Chanson, 1999):

$$\frac{1}{\sqrt{f}} = 2.0 \log_{10} \left(\frac{H}{k_s} \right) + 1.14 \quad (5.1)$$

k_s is taken to be equal to the median grain size, D_{50} which is assumed to be 1 mm here for simplicity. From the bed shear stress, τ_b , the dimensionless bed shear stress can be determined

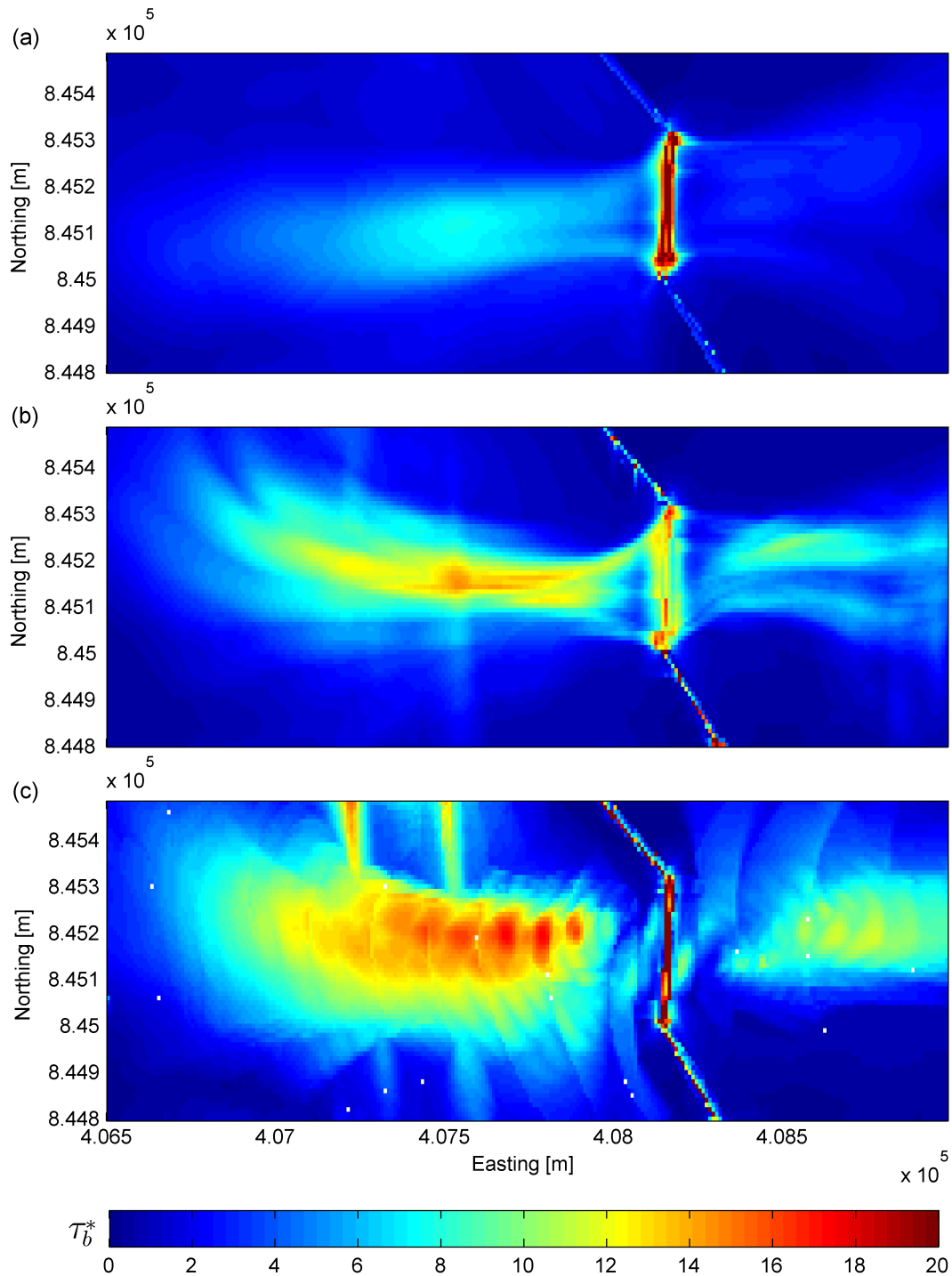


Figure 5.19: Colour plot of the maximum dimensionless bed shear stress, τ_b^* within the 3D RANS domain comparing the 2DH NSWE and 2CLOWNS-3D simulations. A uniform grain size, $D_{50} = 1$ mm is assumed. (a) 2DH NSWE simulation, shear stress calculated from depth-averaged velocity, (b) 2CLOWNS-3D simulation, shear stress calculated from depth-averaged velocity, (c) 2CLOWNS-3D simulation, shear stress calculated through wall function based on the velocity just above the sea bed

by the following:

$$\tau_b^* = \frac{\tau_b}{(\rho_s - \rho)gD_{50}} \quad (5.2)$$

where ρ_s is the density of the sediment and is taken to be 2650 kg/m^3 . The density of the sea water, ρ is assumed to be 1025 kg/m^3 . The dimensionless shear stress indicates how easy it will be to disturb particles that have resistance to movement at least equal to their weight.

Figure 5.19 shows the resulting plot of the maximum dimensionless shear stress. The spatial distribution and magnitude of the shear stress is vastly different between 2CLOWNS-3D and 2DH NSW simulation and the two calculation methods. Firstly, the shear stress based on the depth-averaged velocity in the 2DH NSW is mainly large over the submerged caissons because the depth-average velocity became very large here exceeding 20 ms^{-1} . In comparison the shear stress based on the depth-averaged velocity in the 2CLOWNS-3D simulation is smaller over the submerged caissons but much larger in the jet section onshore and offshore of the breakwater. The comparison of shear stress distribution based on the depth-averaged velocity will follow the distribution of the depth-averaged velocity itself which is shown in Figure 5.11. More interesting then is the comparison with the shear stress calculated from the bed velocity through the wall function approach. The magnitude and distribution of the shear stress resulting from the jets travelling in both the onshore and offshore directions is significantly larger than that estimated through the depth-averaged velocity. Significant shear stresses are present in a large area onshore of the breakwater roughly $1300 \text{ m} \times 400 \text{ m}$ in size. Here, τ_b^* becomes as large as $\tau_b^* = 17$ in a central band which is $\approx 20\%$ larger than that based on the depth-averaged velocity, and $\approx 110\%$ larger than the maximum in the 2DH NSW simulation (in the onshore section under the jet). This area thus would have been highly susceptible to erosion and a large volume of sediment may have transported towards the harbour and spread around the bay. Unless the sediment is dredged and replenished the topography is likely to remain this way after the tsunami if the everyday ocean wave influence is comparatively weak (Kihara et al., 2012).

Also interesting is that the shear stress on the submerged caisson becomes very large in exceedance of $\tau_b^* = 20$. Figure 5.17 does show that the velocity is significantly larger near the caisson than over the rest of the depth. However, the dimensionless shear stress loses its meaning over the rigid concrete structure since it is no longer a sediment transport issue. Lastly, there exists a couple of isolated streaks of large bed shear stresses near the north boundary in Figure 5.19(c) which in the opinion of the author are unlikely to be realistic. It is thought that during the calculation at some time the turbulence near the boundary became very large near the bed causing instability in the velocity which may itself induce more turbulence in a feedback loop process. Such numerical issues still require further inspection to rectify.

5.4.5 Summary

It is now possible to grasp the 3D distribution and dynamics of the flow calculated by the 2CLOWNS-3D model. As the flow approaches the breakwater it is accelerated up the slope of the rubble mound and finally up over the submerged caisson. Because of this a significant proportion of the accelerations are occurring in the vertical direction. Significant vertical acceleration implies that the pressure distribution will become considerably different from the hydrostatic one. Indeed, Figure 5.17 clearly demonstrates how the dynamic pressure, p_d becomes large (in the negative direction) over the submerged caisson up to $p_d = -110$ kPa very close to the caisson. Further, consider a control volume encompassing a region just offshore of the submerged caisson and over the submerged caissons. The flow over the caisson becomes much faster at the edge of the control volume over the submerged caissons than that just offshore due to the conservation of mass as the depth rapidly decreases. While the free surface may also decrease at the same time the momentum flux which is proportional to the square of the velocity will rapidly increase. Considering the steady-state balance of momentum flux and pressure force imbalance implies that the pressure force must rapidly decrease over the submerged caisson. But in the 3D RANS model the pressure is already much less than the hydrostatic pressure due to the vertical accelerations thus the pressure force imbalance may only require a small change in free surface level to match the momentum flux imbalance. Figure 5.15 shows how the change in free-surface level is on the order of 4 m (and Figure 5.20 plots this in more detail). However, consider what will occur in the 2DH NSW model: the only way to match the momentum flux imbalance with the pressure force imbalance is through a large change in free surface (equivalent to the change in pressure force because of the hydrostatic assumption). It is because of this massive change in free surface (illustrated in Figure 5.20) that the depth-averaged velocity over the submerged caissons in the 2DH NSW model becomes much larger than that in the 3D RANS model since the depth becomes so small in the former. This result appears to be consistent with Fujima et al. (2002) which shows that the 2DH NSW model consistently overestimated the velocities over the submerged caisson in comparison to experimental and 3D simulations. The fact that the hydrostatic pressure assumption is the reason for the disparity also implies that consideration of frequency dispersion in the 2DH model can likely improve the result. However, many Boussinesq type models are based on the assumption of slowly varying topography so it should still be difficult to fully represent the problem even using higher-order long wave models.

The next aspect is the jet structure formed onshore or offshore of the submerged caisson depending on the direction of flow. Let's consider the peak onshore flow in particular. As p_d becomes negatively larger near the submerged caisson, the flow becomes accelerated in the downwards direction due to the dynamic pressure gradient. Thus, the jet is accelerated at an angle towards the sea bed. Due to the effect of the rubble mound and the sea bed the vertical momentum is transferred to horizontal momentum. Hence it is the fact that the RANS model calculates the full vertical momentum equation that the jet can be correctly calculated and the

horizontal velocities become much larger in the jet than in the 2DH NSWE model that ignores any vertical effects. The other significant effect present in the RANS model is diffusion which becomes particularly important at the edges of the jet due to the shear with the surrounding comparatively ambient flow. The RANS model can consider full diffusion processes by modelling the turbulent viscosity which may vary in time and space. ν_t is shown to become large in the jet region in Figure D.7. In contrast, the present 2DH NSWE model ignores any mixing processes. Horizontal mixing may be included to improve its performance in these regions however vertical mixing is also non-trivial in this example. On that note it is mentioned here that the Boussinesq assumption made to relate the Reynolds stresses with ν_t in the RANS model assumes that the mixing is isotropic (same in the horizontal and vertical direction). This is generally not considered to be physically correct in many real geophysical problems and is thus a potential weakness of this type of turbulence modelling. Careful validation with experiments are required to investigate this issue in future work.

The comparison of the bed stresses shown in Figure 5.19 highlights how 2DH NSWE models may under or overestimate the bed stresses depending on the location. This may be because of its poor estimation even of the depth-averaged velocities (comparing Figure 5.19(a) and (b)). The difference is further exaggerated due to the vertical variation of the velocities and the difference in estimating the bed stresses from the near bed velocity compared with the depth-averaged velocity (comparing Figure 5.19(a) and (c)). Sediment transport processes are highly sensitive to the approximations of the shear stress and the vertical distribution of the velocities so are important to get right in this context. Three-dimensional models provide a clear advantage over 2DH ones when it comes to modelling sediment transport problems.

5.5 Hydrodynamic Forces on the Submerged Breakwater Section

During the 2011 Tohoku-oki Earthquake tsunami all but one of the submerged caissons were washed out (the other tilted) indicating excessive hydrodynamic forces. This section evaluates the velocities, forces and moments on the concrete caissons resulting from the 2CLOWNS-3D model simulation and tests them against the 2DH NSWE simulation and critical values of failure for the breakwater.

5.5.1 Comparisons with 2DH NSWE Simulation

§5.4 has highlighted the importance of vertical accelerations to correctly model the flow over the submerged section. Hence, the flow in the vicinity becomes quite different between the 2DH NSWE and 2CLOWNS-3D model simulations. The forces on the submerged breakwater estimated by models should be strongly linked with the general hydrodynamics of the flow. One of the most important bulk forces on the breakwater is that due to the difference in water level across it since in the hydrostatic limit this is equivalent to the drag force on the caissons that can induce sliding (i.e. the 2DH NSWE model estimates that the drag force is equivalent to the free surface difference multiplied by ρg).

Figure 5.20 plots a comparison of the envelopes of the free surface differences, $\Delta\eta$ over the length of the submerged caissons. While the timing of the variation in $\Delta\eta$ is similar between the simulations, the magnitude is vastly different. According to the 2CLOWNS-3D model the free surface difference only reaches a maximum of $\Delta\eta \approx 4.5$ m indicated by the black shaded region. In comparison, the 2DH NSWE simulation indicated by the red shaded region reaches a free surface difference of $\Delta\eta = 23.2$ m at its peak! This is equivalent to a 415% increase. Furthermore, the 2DH NSWE simulation predicts a large range of $\Delta\eta$ predicted over the length. For example, the minimum estimate at the time of the peak gradient is $\Delta\eta = 10.1$ m which is just 44% of the maximum. The 3D RANS on the other hand indicates much less variation over the length which is far more useful for engineering design purposes since large variation indicates great uncertainty in the estimate. For the interval shown in Figure 5.20 the standard deviation of $\Delta\eta$ over the length of the section has a mean of 0.41 m and maximum value of 0.80 m in the 3D RANS simulation. In contrast the mean of the standard deviation is 1.1 m with a maximum value of 3.4 m in the 2DH NSWE model.

Lastly, another shaded region is indicated in blue in Figure 5.20. It is the actual pressure difference recorded in the 3D RANS simulation converted to $\Delta\eta$ by dividing by ρg . It is noticeable that the red curve indicating $\Delta\eta$ or pressure difference in the 2DH NSWE simulation is on average similar in magnitude to the 3D RANS simulation. This suggests that despite the hydrostatic assumption in the NSWE model, the free surface will adjust so that it may reasonably approximate the actual pressure difference on *average* in order to conserve momentum. However,

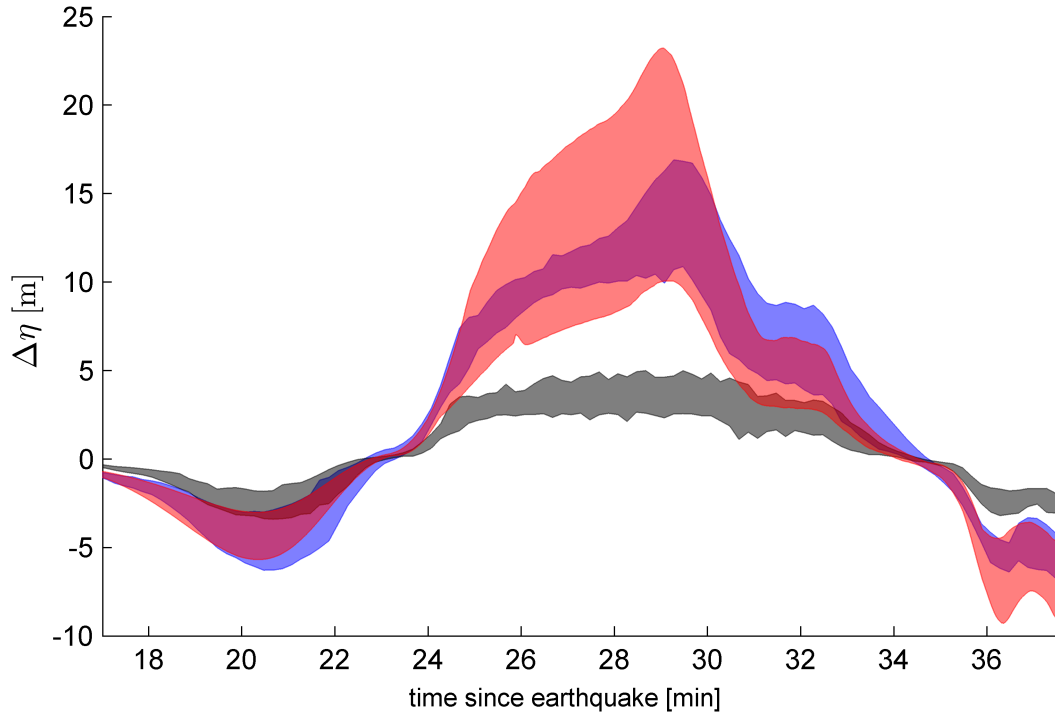


Figure 5.20: Time series of the envelopes of the free surface/pressure difference over the submerged caissons in the 2CLOWNS-3D and 2DH NSWE model simulations due to the incoming tsunami - blue shaded region: 2CLOWNS-3D pressure difference converted to equivalent hydrostatic free surface difference, black shaded region: 2CLOWNS-3D free surface difference, red shaded region: 2DH NSWE free surface difference

as just explained, the uncertainty is very large and the pressure difference at the time of the peak gradient is overestimated. Moreover, from a physical perspective, a free surface gradient of 24 m over a horizontal distance of roughly 20 m is unreasonable, and a non-hydrostatic pressure distribution is required to correctly simulate the flow conditions.

5.5.2 Comparisons with Critical Values

In order to evaluate the hydrodynamic forces on the caissons to indicate probable modes of failure comparisons with critical values of drag force, F_D , overturning moment about the caisson heel, M_D , and punching pressure on the rubble mound, P_e are evaluated.

F_D is determined by summing the pressures on the computational cells normal to the caisson in the horizontal direction multiplied by the surface area. M_D can be found by summing the multiple of each of those forces by the vertical distance to the caisson heel. To determine the critical values for comparison, the caisson weight and lift force, F_L is required. The weight is easily determined using the dimensions and densities shown in Figure 5.1. To get F_L , the pressures on the computational cells normal to the caisson in the vertical direction multiplied

by the surface area are summed. Since the rubble mound is simulated as an impermeable layer in this study, it is assumed that the pressure acting underneath the caissons is just hydrostatic. The critical resistance friction force, F_{Dcrit} is calculated by:

$$F_{Dcrit} = \mu_f(m_c g - F_L) \quad (5.3)$$

where the coefficient of friction between the caisson and rubble mound, μ_f is taken to be 0.6 (Tanimoto and Takahashi, 1994), and m_c is the mass of the concrete caisson. Similarly the critical resisting overturning moment, M_{Dcrit} is equal to:

$$M_{Dcrit} = r_d(m_c g - F_L) \quad (5.4)$$

where r_d is the distance from the center of mass of the caisson to its heel.

The punching pressure acting on the rubble mound is a combination of the vertical force and overturning moment. Firstly, the distance, r_e from the heel of the caisson to the resultant vertical force is given by:

$$r_e = \frac{m_c g - F_L}{m_c g r_d - M_D} \quad (5.5)$$

the punching pressure is then evaluated as (Goda, 2010):

$$P_e = \begin{cases} \frac{2(m_c g - F_L)}{3r_e}, & \text{if } r_e \leq B/3, \\ \frac{2(m_c g - F_L)}{B}(2 - 3\frac{r_e}{B}), & \text{if } r_e > B/3 \end{cases} \quad (5.6)$$

where B is the caisson width. Time series of F_D , M_D and P_e are plotted in Figure 5.21 per unit width showing envelopes of the maximum and minimum values over the length of the submerged section. The hydrostatic component is also shown for comparison, and found to be significantly less than the total simulated quantities as already indicated in §5.5.1. The peak forces and moments correspond to the peak pressure difference shown in Figure 5.20 29.5 minutes after the earthquake rupture.

According to the simulation it is shown that for about half of the length of the submerged caissons, the drag force alone exceeds the resistance friction force, F_{Dcrit} for a duration of up to 2 minutes. The safety factor of the drag force ($= F_{Dcrit}/F_D$) reaches a minimum of 0.77, while the mean along the length is 1.06 with standard deviation equal to 0.12. For comparison a safety factor equal to 0.95 for the partially-submerged caissons in the shallow regions of the south and north sections was estimated in (Port and Airport Research Institute of Japan, 2011b). For the larger partially-submerged caissons in the deep regions the same study estimated the safety factor to be 1.19 and this was confirmed in the overtopping simulations of Bricker (2013) where the drag force was not shown to exceed the resistance force at any time. The overturning moment for both the current study on the submerged caissons and Bricker (2013) for the large partially-submerged caissons was shown not to exceed the resisting moment of the caissons and thus is unlikely to have been a critical factor in the breakwater's failure.

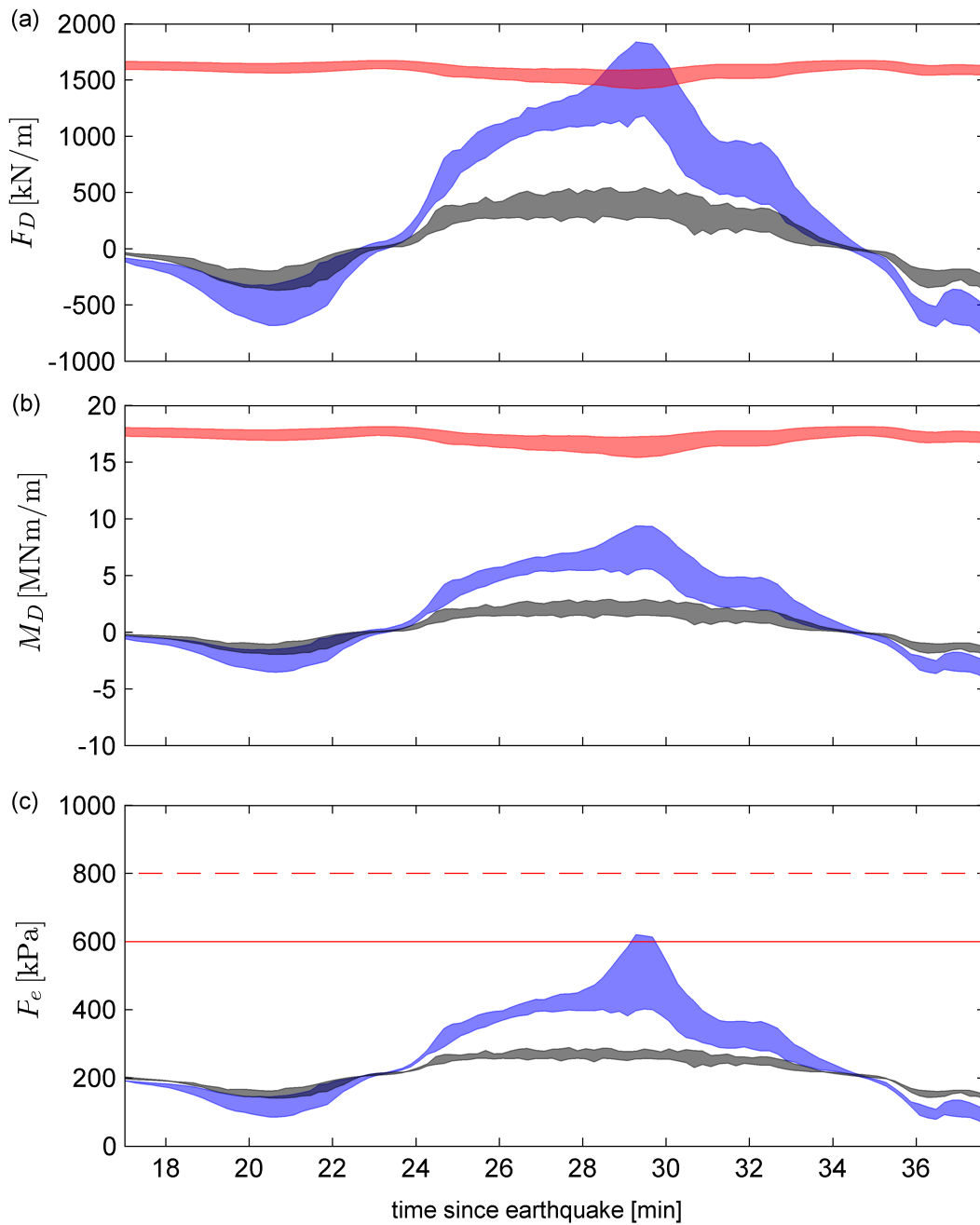


Figure 5.21: Location dependent envelopes of, (a) drag force per unit width, F_D , (b) overturning moment per unit width about the caisson heel, M_D , and (c) punching pressure on the rubble mound, P_e on the submerged caissons and rubble mound due to the incoming tsunami as calculated by 2CLOWNS-3D and compared with critical values - blue shaded region: simulated results, black shaded region: simulated hydrostatic component, red shaded region: critical resistance values, red line: design pressure, red dashed line: critical pressure

We know that in reality almost all the smaller caissons located in the submerged section as well as the shallow regions of the south and north sections were washed out. The drag force calculated in the current study shows that it likely played a significant role in the sliding of these caissons. However, the force alone cannot account for the tilting and sliding of some of the larger caissons that occurred. Bricker (2013) found that the punching failure of the concrete caisson on the rubble mound may have been a significant factor for the larger caissons with overtopping. In this study for the submerged caissons, the punching pressure is shown to slightly exceed the design pressure of 600 kPa (Goda, 2010) for a small part of the length of the section. However, the punching pressure does not exceed the critical one of 800 kPa determined by Uezono and Odani (1987) as was found in Bricker (2013). Hence, it can be concluded that for the smaller caissons with lower resistance, the drag force alone may be large enough to cause sliding in some locations. For the partially-submerged larger caissons this may not be the case, but the extra bearing stress on the rubble mound may induce punching failure that can undermine the stability of the caisson resulting in tilting and a reduction of the friction resistance force between the caisson and the rubble mound.

In addition to the hydrodynamic effects on the caissons, strong flow could have caused significant scour of the rubble mound. Very fast flow at the caisson joints has been identified by Port and Airport Research Institute of Japan (2011b); Arikawa et al. (2012) to cause scour that is an important contribution to the tilting and sliding of the caissons as it undermines their stability. This is likely to be the main reason why even in areas where the drag force is not estimated to exceed the resistance force, caissons were washed out or tilted in addition to possible punching failure of the rubble mound foundation. Unfortunately in this study the estimate of the shear stresses at the joints cannot be reliably determined because the rubble mound is assumed impermeable and the cell size is too large. Future work needs to find ways to reduce the cell size so that the RANS model can properly capture the fine-scale effects of the flow while maintaining the accurate boundary conditions and manageable computational load that has been achieved in this study, i.e. reduction of the size of the RANS model domain without negatively affecting the exchange between the models at the boundary.

5.6 Conclusions

The 2011 Tohoku-oki Earthquake Tsunami caused extensive damage along the Japanese coastline including that of coastal structures that were meant to protect harbours and towns in behind. One case was the 63 m deep offshore tsunami breakwater in Kamaishi Bay that has been shown to attenuate some of the height into the bay. In the process a large number of its concrete caissons were washed out or tilted, and the rubble mound was severely scoured. This study used a fairly novel numerical technique to analyse the hydrodynamics of the tsunami flow on the breakwater and onshore of it, in particular around the submerged section where most of the volume flux passed through.

The numerical technique consisted of two-way coupling a 2DH shallow water model (NSWE) with a 3D Navier-Stokes based (RANS) model, where the final coupled model has been named 2CLOWNS-3D. The 2DH NSWE model propagated the tsunami from the source into Kamaishi Bay as well as accounting for the inundation modelling. The 3D RANS model simulated the hydrodynamics of the flow around the submerged section of the breakwater to provide vertical details of the flow and to properly account for non-hydrostatic and turbulent effects. It was shown that the coupling was successfully achieved where the velocity vectors including rotating currents could pass through the boundaries of the models relatively unaffected. In addition, the pressure distributions were very close to hydrostatic near the east and west boundaries for both the incoming wave and tsunami drawback, allowing for the two-way coupling process to succeed. This was true even though it was possible to allow for a non-uniform vertical distribution of the velocities as was the case during tsunami drawback at the west boundary.

It was found that overall similar volume fluxes through the submerged section and maximum inundation heights were recorded whether or not a 3D RANS model was introduced around the offshore breakwater, although the peak volume flux was shown to be 4.5% larger in the 2CLOWNS-3D simulation. However, either side of the submerged caissons, pressure slightly larger than the non-hydrostatic one and significantly smaller than the hydrostatic one offshore and onshore respectively was generated in the 2CLOWNS-3D simulation that the 2DH NSWE model could not replicate. This resulted in the over estimation of the free surface difference (by up to 415%) in the 2DH NSWE simulation and hence the depth-averaged velocity over this section. However, surprisingly the free surface difference in the 2DH NSWE simulation was on average similar to the actual pressure difference divided by ρg in the 2CLOWNS-3D simulation.

As the the peak tsunami wave flows over the submerged section significant vertical accelerations occur which can be accounted for in the 2CLOWNS-3D model. The jet like flow onshore angled downwards so that it would interact with the sea bed. The conversion of the vertical to horizontal momentum resulted in larger velocities in the jet region in the 2CLOWNS-3D model compared with the 2DH NSWE model. Furthermore, the vertical distribution of the velocities was significant and large bed shear stresses were shown to occur in the jet region between 200 m and 1 km onshore of the breakwater. Bed shear stresses calculated based on the near bed velocity

rather than the depth-average velocity were $\approx 20\%$ larger in the 2CLOWNS-3D model. They were $\approx 110\%$ larger compared with the 2DH NSW E model.

In terms of the hydrodynamic forces simulated on the submerged caissons, it was shown that the drag force was the most severe which reached a minimum safety factor of 0.77. The overturning moment was unimportant and the punching pressure on the rubble mound did exceed the design pressure for a small amount of time in some areas but it did not exceed the estimate of the critical pressure. Due to the lack of sufficient cell resolution and the assumed impermeability of the rubble mound the calculation was not able to estimate the scour around the joints of the caissons. However, such scour has been estimated to have a significant effect on the failure of the breakwater and future studies should develop ways to reduce the cell resolution and introduce permeability of the rubble mound into the 2CLOWNS-3D model.

One of the main goals in the near future is to further validate the 2CLOWNS-3D model with experimental results so that it can be confidently used as a tool for the hydrodynamic simulation around structures such as presented in this study. Finer cell resolution needs to be considered to accurately represent the turbulent characteristics of the flow.

CONCLUSIONS AND RECOMMENDATIONS

This chapter concludes the thesis and makes recommendations for future work. Firstly, the main findings of the work are presented in §6.1. With these results in mind, voids still unfilled, and roads still untrekked are highlighted in §6.2. The author sincerely hopes that the readers have gained even a small amount of knowledge that can be applied to help coastal communities deal with potential disasters as severe as mega-tsunamis - just as this “Lone Miracle Pine” (Figure 6.1) was able to.



Figure 6.1: The Lone Miracle Pine located in Rikuzentakata City, Iwate Prefecture now stands as a symbol of hope for the region after surviving the 2011 Tohoku-oki Earthquake Tsunami (photo: courtesy of my colleague, Hiroshi Nagashima)

6.1 Conclusions

The objective of this study has been to develop, investigate, validate, and apply a two-way coupled multiscale tsunami model capable of simulating the detailed hydrodynamics of tsunamis (particularly during wave breaking and around structures) while computing the propagation of the tsunami from its source towards the coastal zone. This has required the two-way coupling of different grid scales, and governing equations so that a seamless approach is possible where both grid systems and/or models influence each other by passing information in both directions. The coupled model has been named, 2CLOWNS-3D where the “3D” part is omitted in the 2DV case. Conclusions relating to the various aspects of the study are summarised below.

Chapter 3: Numerical Methodology

The two models coupled together in this study as described in Chapter 3 are based on the (1) NSWE and, (2) RANS equations. The NSWE model uses staggered leap-frog discretization with the ability to include linear frequency dispersive effects implicitly if required. It is able to consider tsunami behaviour over a wide-area from the source to the coastal zone inclusive of inundation due to its computationally efficient numerical scheme. A multi-grid nesting technique was developed for the NSWE model in order to consider computation over a range of scales: e.g. coarse grids and time steps offshore and fine grids and time steps nearshore. The RANS based model is discretized on a staggered grid using the non-iterative SMAC algorithm for pressure-velocity coupling. It can accurately model the free surface evolution through the PLIC implementation of the VOF method. The effect of the turbulence on the mean flow is modelled through a turbulent viscosity approach. The $k - \epsilon$ model is used to calculate the transport of turbulent kinetic energy and the rate of turbulent dissipation which can be related to give the turbulent viscosity at any point in space and time. A technique was developed to couple the NSWE and RANS models together. It was found that the multi-grid nesting approach developed for the NSWE model could be simply adapted to consider the coupling of different grid sizes and time steps between the two separate models. One of the additional difficulties is to convert the vertically-integrated volume flux from the NSWE model into a vertical distribution of the velocities as a lateral boundary condition for the RANS model (and vice-versa). A method was introduced to consider an arbitrary velocity profile based on the RANS calculation itself. This should allow non-uniform profiles of the horizontal velocities and vertical vorticities that may develop due to reflections in the RANS model to be more easily passed out through the coupling interface.

Chapter 4: Basic Validation, Range of Applicability, and Coupling Characteristics

A study on solitary wave transformation and breaking on plane beaches was conducted and presented in Chapter 4. A range of offshore wave heights ($0.05 < A'_0 < 0.3$) and slopes (1:20, 1:35, 1:60, 1:100) were tested. All waves could be categorized as plunging breakers. A FNBM model was used as a control model for wave shoaling to determine suitable coupling

positions where deviation from the NSW model occurs, and to estimate errors at the coupling interface. Validation of the two-way coupling scheme and its sensitivity to the vertical distribution of the velocities as an input to the RANS model, the coupling depth, and the slope and wave height was shown. Results from a FNPF model and experiments were used to verify wave breaking characteristics (water depth at breaking, h'_b and wave breaking index A_b/h_b). The following major conclusions were found:

- The NSW model generally described wave shoaling accurately in the zone of gradual shoaling, however it could not match the required shoaling rate in the rapid shoaling zone. This implies that the edge of the zone of gradual shoaling is an optimal location for coupling to the RANS model which can correctly replicate the rapid shoaling process. Since the FNBM model has also been shown to replicate the initial rapid shoaling process, the local depth where the NSW and FNBM models diverge, h'_c was determined for all the experimental combinations. A combination of S_0 and A'_0 was used to collapse the combinations into a single variable, $S_0A'^{-0.5}_0$ and the following equation was derived for h'_c :

$$h'_c = 0.16 - 0.25 \ln(S_0A'^{-0.5}_0)$$

- The two-way coupling algorithm was tested by reflecting waves off a vertical wall over a flat bed. It was found that both the incident and reflected waves could seamlessly pass through the NSW and RANS domains in both directions. Two-way coupling on a steep slope was found to affect the computation of the volume fluxes entering the RANS domain that occurs in order to balance the wave energy during solitary wave shoaling. This balancing effect is not possible in one-way coupling simulations.
- The sensitivity to the vertical distribution of the velocities as a boundary condition to the RANS model during coupling was investigated. It was found that the use of a linear assumption on the vertical velocities gave very different results to a no gradient assumption. In contrast, the effect of the distribution of the horizontal velocities was small. A no gradient condition on both the vertical velocity and the difference in the depth-averaged horizontal velocities was found to give the best results overall.
- Sensitivity to the coupling depth was tested. If coupling occurs in depths much smaller than the optimal depth prescribed by the derived equation, accurate wave transformation could not be achieved. Comparatively, the differences between coupling at the optimal depth and a larger one was small but better performance was generally achieved when coupling in larger depths. However, small reductions in accuracy must be offset against a rapid increase in computational time as the coupling depth increases.

- Using the optimised coupling location, 2CLOWNS simulations were conducted for all experimental combinations. As the slope and offshore wave height increased the relative errors in the form of a deviation in the local wave height at the coupling interface compared with the FNBM model approached approximately 3% at the maximum values of slope and wave height. An equation was derived to describe the deviation in the local wave height, A_{RE} as a function of $S_0s^{-1.095}$:

$$A_{RE} = 0.132 \exp(-0.410S_0s^{-1.095})$$

This indicates that the coupling performance is far more sensitive to the offshore wave height in comparison to the slope. Deviations at the coupling interface are smaller than 1% for offshore wave heights, $A'_0 \leq 0.10$ on any slope.

- The computational time of 2CLOWNS simulations was between 6.2% and 22% that of the computational time using the singular RANS model under the same conditions. In real 2DH/3D large-scale simulations the effect on computational time will be even more dramatic and important. An example result was discussed in detail for a beach slope, $s = 1/60$ with offshore wave height, $A'_0 = 0.05$. The entire wave transformation and breaking process could be accurately described when compared to FNPF, experiments, and theoretical reference shoaling rates.
- The following equations were found to predict the water depth at breaking, h'_b and the wave breaking index, A_b/h_b . The equations are especially suitable for plunging breakers over the range indicated.

$$h'_b = \frac{0.138}{(S_0/A'_0)^{0.664}}, \quad S_0/A'_0 < 4$$

$$\frac{A_b}{h_b} = 0.872 \exp(5.258S_0), \quad S_0 < 0.25$$

- In addition to the prediction of wave transformation and breaking characteristics, the RANS model is able to simulate post-breaking behaviour such as the touchdown of the plunging jet, splashup, bore formation and runup. Snapshots were presented that qualitatively agree with FNFP simulations and high-quality photographs of physical experiments.
- All models have similar vertical profiles of velocity in the zone of gradual shoaling but the NSWE produces drastically different profiles in the rapid shoaling and decay regions. The FNBM also predicts very different velocity profiles during gradual decay to those in 2CLOWNS. These results help to explain the different wave transformation and breaking behaviour overall.

Chapter 5: Real-Scale Application Validation

2CLOWNS-3D was applied to model the hydrodynamics of the flow around the Kamaishi Bay offshore tsunami breakwater during the 2011 Tohoku-oki Earthquake Tsunami in Chapter 5. At first, results from Chapter 4 were used to guide appropriate coupling locations and to determine the suitability to the problem at hand. Second, verification of the setup to the real-scale application was achieved by comparing measured survey values of the maximum inundation heights along the Kamaishi coast and evaluating the effect of the offshore tsunami breakwater. Lastly, the hydrodynamics on and around the offshore tsunami breakwater computed using the 2CLOWNS-3D were analysed in detail with comparisons to the 2DH NSWE simulation and the following conclusions were made:

- The offshore tsunami breakwater was shown to have a significant effect on the tsunami and inundation heights around Kaimaishi Bay through the NSWE model simulations. An estimation in this study was that the reduction in inundation heights due to the breakwater was on the order of 50%. The reduction in inundation area was equivalent to 36%. In reality the breakwater was damaged which explains why the surveyed inundation heights were on average 1.7 m greater than the calculated ones using the pre-tsunami undamaged breakwater condition.
- Overall, similar volume fluxes through the submerged section and maximum inundation heights were recorded whether or not a 3D RANS model was introduced around the offshore breakwater. The average overall difference in inundation heights between the NSWE and 2CLOWNS-3D model simulations was shown to be just 0.20 m. This can be explained by the fact that the peak volume flux was shown to be 4.5% larger in the 2CLOWNS-3D simulation.
- At the time of attack of the maximum positive tsunami wave travelling towards the coastline through the offshore tsunami breakwater, the pressure distribution became significantly smaller than the hydrostatic one over the submerged caissons in the 2CLOWNS-3D simulation. This had the effect of allowing a large pressure force imbalance acting on the caissons to match the momentum flux imbalance. In contrast, the hydrostatic NSWE model could only represent the pressure force imbalance through an extremely large reduction of the free surface over the submerged caissons that was at maximum, 415% larger than that recorded in the 2CLOWNS-3D model simulations.
- Vertical accelerations over the submerged caissons directed the jet formed onshore down into the seabed in the 2CLOWNS-3D model. After interaction with the sea bed and rubble mound this had the effect of increasing the horizontal momentum flux and hence velocities in the jet than those in the 2DH NSWE simulation. Furthermore, the velocities at the seabed were very large for a distance of approximately 1.3 km

onshore of the breakwater which resulted in very large bed shear stresses over an extended region. Bed shear stresses calculated based on the depth-averaged velocity underestimated the bed stresses calculated using the near bed velocity.

- Regarding the hydrodynamic forces on the submerged caissons calculated in 2CLOWNS-3D, the drag force was found to be most severe with the safety factor reaching as low as 0.77. This most likely led to the sliding of the caissons that occurred in reality. Overturning moment and punching pressure were determined to be unlikely causes of failure for the submerged caissons. It has been found in other studies however, that scour at the joints of the caissons was also significant for their failure but the current model could not consider this effect due to limitations on cell resolution and the assumption of impermeability of the rubble mound.

6.2 Recommendations for Future Work

This study has introduced two-way coupling between NSWE and RANS equations based models for multiscale tsunami simulation from the source to the coastal zone. With regards to this type of model (2CLOWNS), equations for the coupling positions and ranges of application to long wave transformation on plane beaches were found. In addition, an application to the flow hydrodynamics through a submerged offshore breakwater section was shown. However, there are a number of avenues that require further study with regards to this model:

1. Often the nearshore may be represented best as a composite beach with more than one slope leading up to the shoreline. It would therefore make sense to extend the equations developed in Chapter 4 to consider composite beaches as well.
2. One verification with an experiment and application to the real-scale situation in 3D was shown. However, further verifications with 3D problems (particularly physical experiments) are desired in order to fully understand the capabilities of 2CLOWNS-3D, suitable coupling locations, and coupling effects.
3. The preponderant application of the 2CLOWNS-3D model is to consider the hydrodynamic response with structures. This inevitably introduces reflections and other possibly relatively high frequency, non-hydrostatic, and rotational effects into the domain of the RANS model. These effects may propagate reasonably far from the structure. Such cases cause significant difficulty for the coupling in 2CLOWNS-3D, because it assumes only long waves, hydrostatic, and irrotational phenomena are present (or at least those complicated effects are very small) at the interface so that the NSWE assumptions remain valid. As was found in Chapter 5, in order to couple effectively, 2CLOWNS-3D may require a very large RANS domain. Hence, computational costs increase and very fine grid sizes are almost impossible to adopt. A reasonable calculation was still possible in the case of Chapter 5 but for best results, finer resolution is desired in order to accurately represent the turbulent characteristics of the flow. In order to achieve this there are two options which may in fact be combined:
 - Introduction of an intermediate model that is capable of modelling weakly non-hydrostatic, turbulent and rotational flow but with comparatively faster computational times than the RANS model. The intermediate model would allow the RANS model domain size to decrease and the cell resolution to increase. In fact such a model was used for the analysis in Chapter 4 (COULWAVE - a weakly dispersive, rotational, and turbulent FNBM). An inviscid, irrotational version of the model has already been coupled with a RANS one in Sitanggang and Lynett (2010). Hence, it would appear possible to use this sort of model as an intermediate. Other possibilities include quasi-3D solvers such as non-hydrostatic versions of ROMS, and SELFE.

- Development of a dynamic coupling mechanism. Based on the local conditions of the flow it may be possible to determine suitable reductions, enlargements and translation of the RANS domain. For example when the wave is small or not present it is unlikely that the RANS calculation needs to be considered (in fact due to the simplicity of the problem, this technique was adopted in Chapter 4). Furthermore, a tsunami wave train alternates between positive flow towards the shoreline and drawback which would likely result in the change of size and movement of important complex regions of the flow with time.



MULTI-GRID TEMPORAL NESTING SUBROUTINE - NUMERICAL CODE

Multi-grid nesting often requires that the time step size is different between each grid (layer). In this case the order of calculation of each layer is important in order to be able to exchange the necessary information at the right time. A recursive subroutine was written in the numerical code to achieve this goal. A simplified version of it is shown below:

recursive subroutine inner_loop_recursive (LN,DT_RATIO)

use leapfrog_mod, only: L, LNUM, ONE

implicit none

integer,intent(in) LN , DT_RATIO

integer LNN , DT_COUNT, DT_RATIO_UP

real*8 DT_CF

!THIS SUBROUTINE LOOPS OVER THE INNER LAYERS IN A RECURSIVE MANNER
!WHEN THE TIME STEPS BETWEEN EACH LAYER ARE DIFFERENT

Layer_Iter: do DT_COUNT = 1, max(DT_RATIO - 1,1)

 DT_CF = real(DT_COUNT) / real(DT_RATIO)

 Layer_loop_Up: do LNN = LN , LNUM

```

!----- Momentum Flux Calc. at n+1 -----
      call leapfrog_flux(L(LNN))

!----- Linearly interpolate the fluxes at outer layer
!along inner layer boundary spatially and in time -----
      if (LNN.gt.1) then
        if (LNN.eq.LN) call interp_outer_flux(L(LNN-1),L(LNN),DT_CF)
        if (LNN.gt.LN) call interp_outer_flux(L(LNN-1),L(LNN),ONE)
      endif

!----- If LNN is not in the innermost layer... -----
      if (LNN.lt.LNUM) then
        !Find ratio of DT between outer and inner layer
        DT_RATIO_UP = int( L(LNN)%DT / L(LNN+1)%DT )
        if (DT_RATIO_UP.gt.1) then
          !When the time steps are different between inner and outer regions
          !we need to calc continuity and flux again in a recursive manner
          call inner_loop_recursive(LNN+1,DT_RATIO_UP)
        endif
      endif
    enddo Layer_loop_Up
  do LNN = LNUM,LN,-1
    !Interpolate the flux from the inner layer to current layer -----
      if (LN.lt.LNUM) call interp_inner_flux(L(LN),L(LN+1),LN)
    !Get the adjustment coefficient to ensure water level is
    !at correct time inside the coupling region
      if (LN.eq.LNUM) CF = 0.0d0          ! No inside region
      if (LN.lt.LNUM) CF = 0.50d0 * (1d0 - L(LN+1)%DT / L(LN)%DT) ! 0 ≤ CF < 0.5
    !Use continuity to calculate new water level at n+1/2
      call leapfrog_cont(L(LN),LN,CF)
    enddo
  enddo Layer_Iter
end subroutine inner_loop_recursive

```

FINITE-DIFFERENCES IN RANS MODEL

Finite-difference formula for use in the RANS model are presented below, as referred from §3.4.3 and §3.4.5.

Third-order upwind (QUICK) Difference

For the nonlinear advection terms in the momentum equation of the RANS model (see §3.4.3), the third-order upwind (QUICK) difference formula is adopted.

$$\left(u \frac{\partial u}{\partial x}\right)_c^n = u_c^n (\lambda_1(u_E^n - u_c^n) + \lambda_2(u_e^n - u_c^n) + \lambda_3(u_w^n - u_c^n) + \lambda_4(u_W^n - u_c^n)) / \text{Det}(A) \quad (\text{B.1})$$

$$\left(v \frac{\partial u}{\partial y}\right)_c^n = v_A^n (\lambda_1(u_N^n - u_c^n) + \lambda_2(u_n^n - u_c^n) + \lambda_3(u_s^n - u_c^n) + \lambda_4(u_S^n - u_c^n)) / \text{Det}(A) \quad (\text{B.2})$$

$$\left(w \frac{\partial u}{\partial z}\right)_c^n = w_A^n (\lambda_1(u_T^n - u_c^n) + \lambda_2(u_t^n - u_c^n) + \lambda_3(u_b^n - u_c^n) + \lambda_4(u_B^n - u_c^n)) / \text{Det}(A) \quad (\text{B.3})$$

where, $v_A^n = 0.25(v_n^n + v_s^n + v_{ne}^n + v_{se}^n)$, and $w_A^n = 0.25(w_t^n + w_b^n + w_{te}^n + w_{be}^n)$ are the averaged values of v and w at the position of u_c . The coefficients of the third-order upwind difference are some combination of the grid sizes:

$$\begin{cases} \lambda_1 = 0, & \lambda_2 = a_{2,2}^+ a_{3,3}^+ - a_{3,2}^+ a_{2,3}^+ & \text{if } u_c^n / v_A^n / w_A^n \geq 0 \\ \lambda_3 = a_{3,2}^+ a_{1,3}^+ - a_{1,2}^+ a_{3,3}^+, & \lambda_4 = a_{1,2}^+ a_{2,3}^+ - a_{2,2}^+ a_{1,3}^+ \\ \lambda_1 = a_{1,2}^- a_{2,3}^- - a_{2,2}^- a_{1,3}^-, & \lambda_2 = a_{3,2}^- a_{1,3}^- - a_{1,2}^- a_{3,3}^- & \text{if } u_c^n / v_A^n / w_A^n < 0 \\ \lambda_3 = a_{2,2}^- a_{3,3}^- - a_{3,2}^- a_{2,3}^-, & \lambda_4 = 0 \end{cases} \quad (\text{B.4})$$

where $a_{i,j}^+$ is the (i,j) element of the following matrix, A^+ :

$$A^+ = \begin{pmatrix} \Delta h_2 & (\Delta h_2)^2 & (\Delta h_2)^3 \\ \Delta h_3 & (\Delta h_3)^2 & (\Delta h_3)^3 \\ \Delta h_4 & (\Delta h_4)^2 & (\Delta h_4)^3 \end{pmatrix} \quad (\text{B.5})$$

and $a_{i,j}^-$ is the (i,j) element of the following matrix, A^- :

$$A^- = \begin{pmatrix} \Delta h_3 & (\Delta h_3)^2 & (\Delta h_3)^3 \\ \Delta h_2 & (\Delta h_2)^2 & (\Delta h_2)^3 \\ \Delta h_1 & (\Delta h_1)^2 & (\Delta h_1)^3 \end{pmatrix} \quad (\text{B.6})$$

with,

$$\begin{cases} \Delta h_1 = \Delta x_E, & \Delta h_2 = \Delta x_e, & \Delta h_3 = \Delta x_c, & \Delta h_4 = \Delta x_w, & \text{for } \left(u \frac{\partial u}{\partial x}\right)_c^n \\ \Delta h_1 = 0.5(\Delta y_N + \Delta y_n), & \Delta h_2 = 0.5(\Delta y_n + \Delta y_c), & & & \text{for } \left(v \frac{\partial u}{\partial y}\right)_c^n \\ \Delta h_3 = 0.5(\Delta y_c + \Delta y_s), & \Delta h_4 = 0.5(\Delta y_s + \Delta y_S) & & & \\ \Delta h_1 = 0.5(\Delta z_T + \Delta z_t), & \Delta h_2 = 0.5(\Delta z_t + \Delta z_c), & & & \text{for } \left(w \frac{\partial u}{\partial z}\right)_c^n \\ \Delta h_3 = 0.5(\Delta z_c + \Delta z_b), & \Delta h_4 = 0.5(\Delta z_b + \Delta z_B) & & & \end{cases} \quad (\text{B.7})$$

and $\text{Det}(A)$ is the determinant of A^+ if $u_c^n / v_A^n / w_A^n \geq 0$ and $\text{Det}(A)$ is the determinant of A^- if $u_c^n / v_A^n / w_A^n < 0$. Note that for uniform grid size, Δx , the equation will reduce to the following for $\left(u \frac{\partial u}{\partial x}\right)_c^n$ with $u_c^n \geq 0$:

$$\left(u \frac{\partial u}{\partial x}\right)_c^n = \frac{u_c^n}{6\Delta x} (2u_e^n + 3u_c^n - 6u_w^n + u_W^n) \quad (\text{B.8})$$

Second-order Derivatives for Viscous terms

For the viscous terms in the momentum equation of the RANS model (see §3.4.3), the second-order central difference is adopted.

$$\left(\frac{\partial^2 u}{\partial x^2}\right)_c^n = \frac{(u_e^n - u_c^n)/\Delta x_e + (u_c^n - u_w^n)/\Delta x_c}{0.5(\Delta x_c + \Delta x_e)} \quad (\text{B.9})$$

$$\left(\frac{\partial^2 u}{\partial y^2}\right)_c^n = \frac{2(u_n^n - u_c^n)/(\Delta y_n + \Delta y_c) + 2(u_c^n - u_s^n)/(\Delta y_c + \Delta y_s)}{0.5[\Delta y_c + 0.5(\Delta y_n + \Delta y_s)]} \quad (\text{B.10})$$

$$\left(\frac{\partial^2 u}{\partial z^2}\right)_c^n = \frac{2(u_t^n - u_c^n)/(\Delta z_t + \Delta z_c) + 2(u_c^n - u_b^n)/(\Delta z_c + \Delta z_b)}{0.5[\Delta z_c + 0.5(\Delta z_t + \Delta z_b)]} \quad (\text{B.11})$$

First-order Derivatives for Production Term

For the first-order derivatives in the production term, P_k used in the $k - \epsilon$ equations (see §3.4.5), second-order central differences are adopted. This is straight forward for the normal derivatives. But, for the cross-derivatives, e.g. $(\frac{\partial u}{\partial z})_c$, the velocities must first be averaged from the cell boundaries to the cell centre before calculating the derivative. In addition the grid non-uniformity must be taken into account.

$$\left(\frac{\partial u}{\partial x}\right)_c = \frac{u_c - u_e}{\Delta x_c} \quad (\text{B.12})$$

$$\left(\frac{\partial v}{\partial y}\right)_c = \frac{v_n - v_s}{\Delta y_c} \quad (\text{B.13})$$

$$\left(\frac{\partial w}{\partial z}\right)_c = \frac{w_t - w_b}{\Delta z_c} \quad (\text{B.14})$$

$$\left(\frac{\partial u}{\partial y}\right)_c = \frac{0.5 \frac{\Delta y_e + \Delta y_s}{\Delta y_c + \Delta y_n} (u_n + u_{nw} - u_c - u_w) + 0.5 \frac{\Delta y_c + \Delta y_n}{\Delta y_c + \Delta y_s} (u_c + u_w - u_s - u_{sw})}{\Delta y_c + 0.5(\Delta y_s + \Delta y_n)} \quad (\text{B.15})$$

$$\left(\frac{\partial u}{\partial z}\right)_c = \frac{0.5 \frac{\Delta z_e + \Delta z_b}{\Delta z_c + \Delta z_t} (u_t + u_{tw} - u_c - u_w) + 0.5 \frac{\Delta z_c + \Delta z_t}{\Delta z_c + \Delta z_b} (u_c + u_w - u_b - u_{bw})}{\Delta z_c + 0.5(\Delta z_b + \Delta z_t)} \quad (\text{B.16})$$

$$\left(\frac{\partial v}{\partial x}\right)_c = \frac{0.5 \frac{\Delta x_c + \Delta x_w}{\Delta x_c + \Delta x_e} (v_{se} + v_{ne} - v_s - v_n) + 0.5 \frac{\Delta x_c + \Delta x_e}{\Delta x_c + \Delta x_w} (v_s + v_n - v_{sw} - v_{nw})}{\Delta x_c + 0.5(\Delta x_w + \Delta x_e)} \quad (\text{B.17})$$

$$\left(\frac{\partial v}{\partial z}\right)_c = \frac{0.5 \frac{\Delta z_c + \Delta z_b}{\Delta z_c + \Delta z_t} (v_{st} + v_{nt} - v_s - v_n) + 0.5 \frac{\Delta z_c + \Delta z_t}{\Delta z_c + \Delta z_b} (v_s + v_n - v_{sb} - v_{nb})}{\Delta z_c + 0.5(\Delta z_b + \Delta z_t)} \quad (\text{B.18})$$

$$\left(\frac{\partial w}{\partial x}\right)_c = \frac{0.5 \frac{\Delta x_c + \Delta x_w}{\Delta x_c + \Delta x_e} (w_{be} + w_{te} - w_b - w_t) + 0.5 \frac{\Delta x_c + \Delta x_e}{\Delta x_c + \Delta x_w} (w_b + w_t - w_{bw} - w_{tw})}{\Delta x_c + 0.5(\Delta x_w + \Delta x_e)} \quad (\text{B.19})$$

$$\left(\frac{\partial w}{\partial y}\right)_c = \frac{0.5 \frac{\Delta y_c + \Delta y_s}{\Delta y_c + \Delta y_n} (w_{bn} + w_{tn} - w_b - w_t) + 0.5 \frac{\Delta y_c + \Delta y_n}{\Delta y_c + \Delta y_s} (w_b + w_t - w_{bs} - w_{ts})}{\Delta y_c + 0.5(\Delta y_s + \Delta y_n)} \quad (\text{B.20})$$

Second-order Derivatives for Turbulent Diffusion Term

For the diffusion terms in the k and ϵ transport equations (see §3.4.5), the second-order central difference is adopted.

$$\left(\frac{\partial}{\partial x} \left[\gamma_x^\alpha \left(v + \frac{v_t}{\sigma_\phi} \right) \frac{\partial \phi}{\partial x} \right]\right)_c = \frac{2\gamma_{xc}^\alpha \left(v + \frac{v_{te} + v_{tc}}{2\sigma_\phi} \right) \frac{\phi_e - \phi_c}{\Delta x_e + \Delta x_c} - 2\gamma_{xw}^\alpha \left(v + \frac{v_{tw} + v_{tc}}{2\sigma_\phi} \right) \frac{\phi_c - \phi_w}{\Delta x_c + \Delta x_w}}{0.5[\Delta x_c + 0.5(\Delta x_e + \Delta x_w)]} \quad (\text{B.21})$$

$$\left(\frac{\partial}{\partial y} \left[\gamma_y^\alpha \left(v + \frac{v_t}{\sigma_\phi} \right) \frac{\partial \phi}{\partial y} \right]\right)_c = \frac{2\gamma_{yn}^\alpha \left(v + \frac{v_{tn} + v_{tc}}{2\sigma_\phi} \right) \frac{\phi_n - \phi_c}{\Delta y_n + \Delta y_c} - 2\gamma_{ys}^\alpha \left(v + \frac{v_{ts} + v_{tc}}{2\sigma_\phi} \right) \frac{\phi_c - \phi_s}{\Delta y_c + \Delta y_s}}{0.5[\Delta y_c + 0.5(\Delta y_n + \Delta y_s)]} \quad (\text{B.22})$$

$$\left(\frac{\partial}{\partial z} \left[\gamma_z^\alpha \left(v + \frac{v_t}{\sigma_\phi} \right) \frac{\partial \phi}{\partial z} \right]\right)_c = \frac{2\gamma_{zt}^\alpha \left(v + \frac{v_{tt} + v_{tc}}{2\sigma_\phi} \right) \frac{\phi_t - \phi_c}{\Delta z_t + \Delta z_c} - 2\gamma_{zb}^\alpha \left(v + \frac{v_{tb} + v_{tc}}{2\sigma_\phi} \right) \frac{\phi_c - \phi_b}{\Delta z_c + \Delta z_b}}{0.5[\Delta z_c + 0.5(\Delta z_t + \Delta z_b)]} \quad (\text{B.23})$$



RANS MODEL GRID CONVERGENCE AND ACCURACY FOR SOLITARY WAVE TRANSFORMATION

The RANS model can be quite sensitive to the grid size. This is particularly true in some areas than others. An additional issue that does not appear for 1DH/2DH models is that the vertical grid size, $\Delta z'$ and its ratio with the horizontal grid size, $\Delta x'$ also becomes important. Thus, the grid convergence study should investigate each grid size independently. In this convergence study we choose $s = 1/35$ and $A'_0 = 0.3$ to investigate. This is because good data exists from a FNPF model (Grilli et al., 1997) on the $1/35$ slope to compare against. Also, $A'_0 = 0.3$ is fairly large, thus potentially sensitive to the grid size.

Firstly, it is common to choose $\Delta x'$ based on the wavelength. Thus, we choose values of $\Delta x' \mu_0$ where μ_0 is a measure of the offshore dispersion parameter which is set equal to $1/(2X'_s)$ for a solitary wave. The selected values to investigate effects on the variation of the horizontal grid size are: $\Delta x' \mu_0 = 1/200, 1/400, 1/800$ which are kept constant through the entire domain. Here, $\Delta z' = \Delta x'/2$ in each case and is also unchanging in the entire domain. The result of the calculation is plotted in Figure C.1. The local wave height, A' and snapshots of the waveform at four different times are shown. Most of the shoaling process is largely unaffected by the horizontal grid size offshore. In fact if one were to observe very closely, A' is very slightly larger in this region for larger $\Delta x'$. However, beyond $x' \approx 20$, effects of the grid size become more apparent and smaller $\Delta x'$ results in the largest peak value of A' which is closest to the breaking point (BP) for the FNPF model (Grilli et al., 1997). Hence, it would be appear that a smaller value of $\Delta x'$ does in fact give a better result near the BP. However, the peak value of A' is still underestimated according to the Grilli et al. (1997) result.

Secondly, since it has been shown that the effects of the horizontal grid size are unimportant offshore and over the initial shoaling region (up to $x' \approx 20$), in order to reduce computational

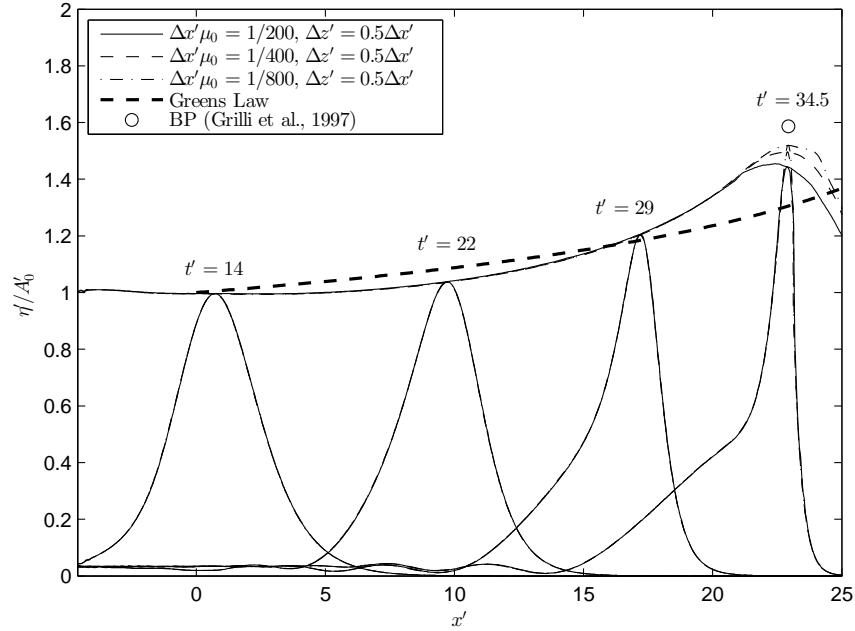


Figure C.1: Effect of horizontal grid size, $\Delta x'$ for solitary wave transformation on slope, $s = 1/35$ with offshore wave height, $A'_0 = 0.30$. The local wave height, A' and snapshots of the waveform are shown at four different values of t' . Green's law and the BP in the FNPF of Grilli et al. (1997) is included for comparison

time it makes sense to vary the grid sizes from a large value offshore (e.g. $\Delta x'\mu_0 = 1/200$) to a small value (e.g. $\Delta x'\mu_0 = 1/800$) beyond where the grid size becomes important ($x' \approx 20$ in this case). The grid variation can be achieved using the method described in §3.4.9. Thus, the next computation compares this variation ($\Delta x'\mu_0 = 1/200 \rightarrow \Delta x'\mu_0 = 1/800$), with the unvaried cases of $\Delta x'\mu_0 = 1/800$ and $1/200$. For the varied case $\Delta z'\mu_0 = 1/1600$ so that it is equal to $\Delta x'/2$ in the rapidly shoaling region where $\Delta x'\mu_0 = 1/800$. The result of the calculation is plotted in Figure C.2. As expected, little difference is shown between the solutions before $x' \approx 20$, but on close inspection A' is smallest in the gradually varied case. Beyond $x' \approx 20$, both the varied solution and the $\Delta x'\mu_0 = 1/800$ solution show good agreement as hoped for, demonstrating that it is not necessary to have such a fine grid size for $x' < 20$, and gradually varying the grid size from a larger size, e.g. $\Delta x'\mu_0 = 1/200$, offshore at the boundary does not adversely affect the solution.

Thirdly, the effect of changing $\Delta z'$ is investigated. In this case, $\Delta x'\mu_0 = 1/400$ is kept constant while the vertical grid is varied: $\Delta z' = \Delta x'$, $\Delta x'/2$, $\Delta x'/4$. The result of the calculation is plotted in Figure C.3. For the propagation offshore and in the initial part of shoaling little influence of $\Delta z'$ is clear. When observing very closely, a slightly larger value A' for the smaller $\Delta z'$ is noticeable in this region. However, beyond $x' \approx 15$, the larger value of $\Delta z'$ induces more rapid shoaling. It is in fact the case where $\Delta z' = \Delta x'$, that gives the best solution closest to the BP of Grilli et al. (1997). This gives the funny situation where increasing the grid size generates a “better” solution.

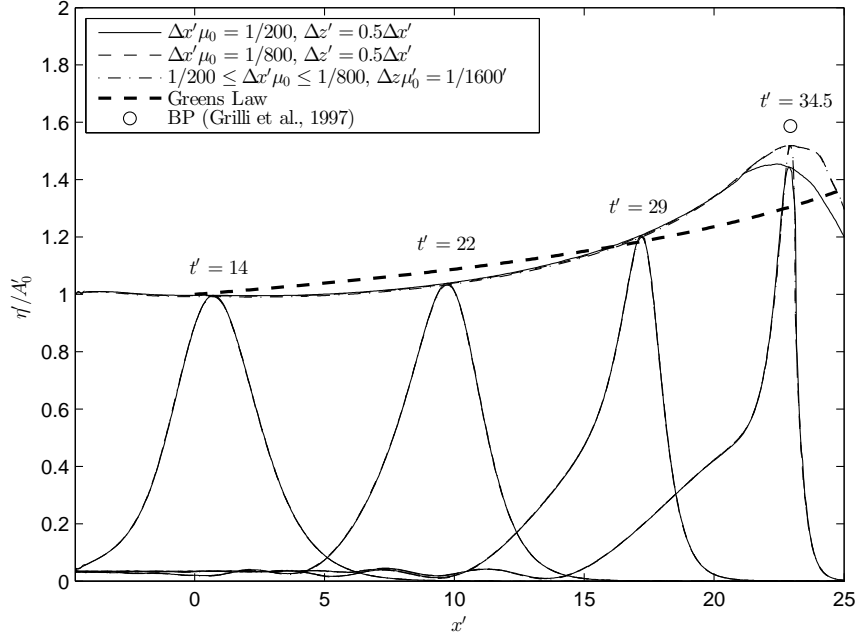


Figure C.2: Effect of gradually varying the horizontal grid size, $\Delta x'$ offshore of $x' = 20$ for solitary wave transformation on slope, $s = 1/35$ with offshore wave height, $A'_0 = 0.30$. The local wave height, A' and snapshots of the waveform are shown at four different values of t' . Green's law and the BP in the FNPF of Grilli et al. (1997) is included for comparison

However, it can be viewed from an opposite perspective: for a small $\Delta z'$, reducing $\Delta x'$ (rather than increasing $\Delta z'$) will give a better solution as has already indicated.

Lastly, similarly to the horizontal grid size, since offshore and over the initial shoaling region the vertical grid size is not shown to be important, computational time can be reduced by varying $\Delta z'$ below the initial free surface. $\Delta z' = \Delta x'$ may be adopted at the offshore sea bed, and increased to $\Delta z' = \Delta x'/4$ just below and above the free surface. This varied case is compared with the unvaried cases of $\Delta z' = \Delta x'$ and $\Delta z' = \Delta x'/4$. Here, $\Delta x'\mu_0 = 1/400$ in each case. The result of the calculation is plotted in Figure C.4. Offshore before $x' \approx 15$, the solutions are in good agreement and the varied case is shown to be in between the other solutions with $\Delta z' = \Delta x'/4$ give the greatest value of A' here. Beyond $x' \approx 15$ the solutions diverge with $\Delta z' = \Delta x'$ giving the solution closest to the BP of Grilli et al. (1997), while the varied case and $\Delta z' = \Delta x'/4$ give very similar solutions as expected since the same value of $\Delta z'$ from just below the free surface is defined in both these cases. This implies that varying $\Delta z'$ from just below the free surface has little effect on the solution and thus can be used to reduce computational time where possible.

Note it may seem strange that since $\Delta z' = \Delta x'$ gives the better result in the rapid shoaling region we bothered to adopt $\Delta z' = \Delta x'/4$ from the initial free surface in the previous investigation. Indeed that was the case here, but variation in $\Delta z'$ can be combined with the variation in $\Delta x'$ to give an overall optimised setup. Such a setup is illustrated in Figure 4.2. Setting $\Delta z' = \Delta x'$

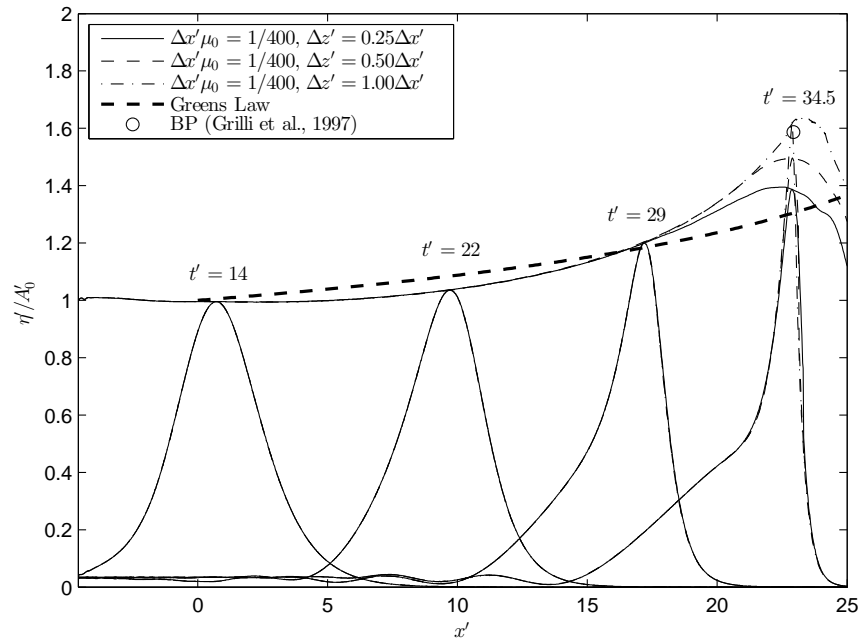


Figure C.3: Effect of vertical grid size, $\Delta z'$ for solitary wave transformation on slope, $s = 1/35$ with offshore wave height, $A'_0 = 0.30$. The local wave height, A' and snapshots of the waveform are shown at four different values of t' . Green's law and the BP in the FNPF of Grilli et al. (1997) is included for comparison

offshore at the sea bed where $\Delta x' \mu_0 = 1/200$ allows $\Delta z'$ to become large here. Further, it has been shown that $\Delta z' = \Delta x'$ is important in the rapid shoaling region near breaking (beyond $x' \approx 15$) so this is also adopted above the free surface where $\Delta x' \mu_0 = 1/800$ here. Eqn. (4.12) can be used to estimated the location to vary $\Delta x'$ until from offshore for some combination of s and A'_0 . This setup has been tested for a range of A'_0 on the $s = 1/35$ slope versus Green's law and Boussineq's shoaling laws in Figure C.5. Also the FNPF BP data (Grilli et al., 1997) is included for comparison. The BP in this study has been calculated directly by searching for the maximum value of the free surface normal in the horizontal direction, $(n_c)_{x,max}$ within the calculation domain. BP is thus defined when $(n_c)_{x,max} > 0.999$. Mostly, the results of the RANS calculation are shown to be accurate compared with the FNPF model. Breaking is predicted a bit later than the FNPF model for all cases except $A'_0 = 0.10$ where breaking is predicted earlier. The FNPF result however doesn't fit the trend of the other previous cases very well. It is unknown why this might be the case.

A final point that must be mentioned is while scaling $\Delta x'$ by μ_0 has meaning offshore and for gradual shoaling, during rapid shoaling any breaking solitary wave tends to become very narrow whether A'_0 is fairly large (e.g. $A'_0 = 0.30$) or small (e.g. $A'_0 = 0.05$). As a result, $\Delta x' \mu_0 = 1/800$ for some of the smaller values of A'_0 tend to be too coarse to approximate the breaking wave shape with any accuracy. If one is concerned about correctly modelling wave overturning and

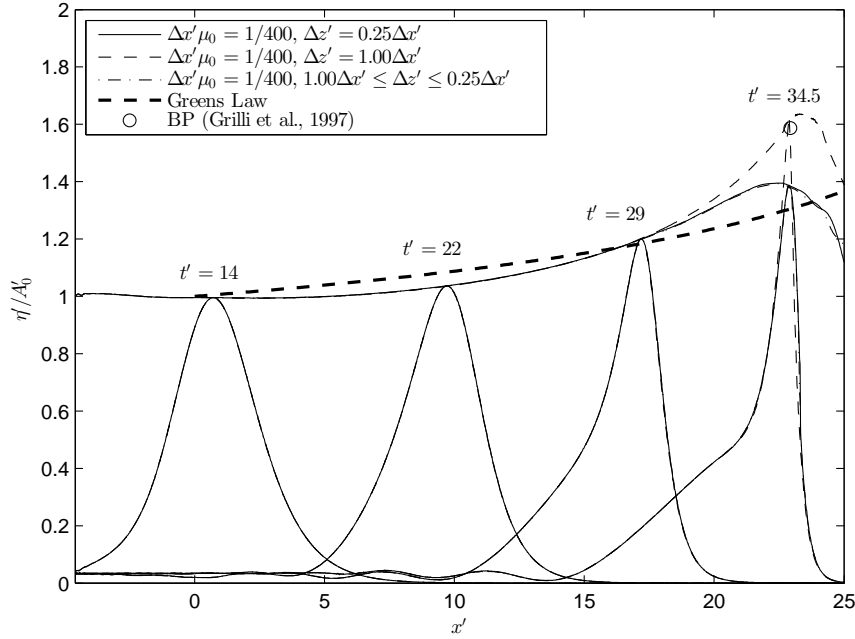


Figure C.4: Effect of gradually varying vertical grid size, $\Delta z'$ from the bed to just below the free surface for solitary wave transformation on slope, $s = 1/35$ with offshore wave height, $A'_0 = 0.30$. The local wave height, A' and snapshots of the waveform are shown at four different values of t' . Green's law and the BP in the FNPF of Grilli et al. (1997) is included for comparison

other turbulent effects, it is likely superior and simpler to chose $\Delta x'$ irrespective of μ_0 in the rapid shoaling region and beyond. $\Delta x'\mu_0 = 1/800$ for $A'_0 = 0.30$ is equivalent to $\Delta x' = 0.012$ which has been found to give a good representation of the breaking wave. Thus, it is suggested that $0.010 < \Delta x' < 0.015$ (with $\Delta z' = \Delta x'$) is a suitable choice for any A'_0 to correctly model wave overturning and post-breaking turbulent effects.

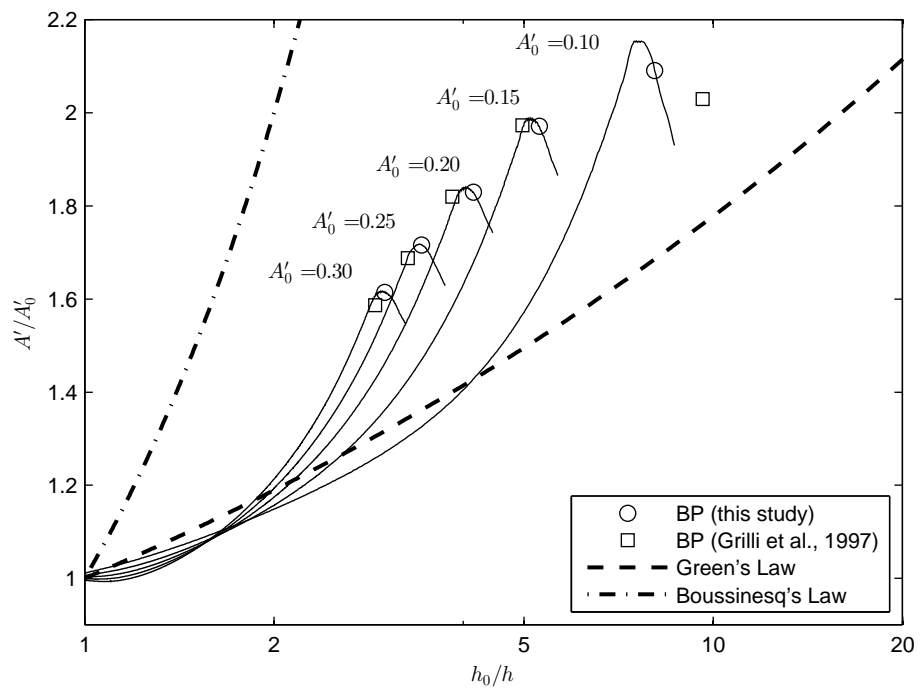


Figure C.5: Performance of RANS model for shoaling and prediction of breaking point versus the FNPF model (Grilli et al., 1997) on a slope, $s = 1/35$ using the optimised grid setup (c.f. Figure 4.2)

APPENDIX 

**EXTRA FIGURES FOR CHAPTER 5:
2CLOWNS-3D SIMULATION IN KAMAISHI BAY**

This appendix includes extra figures for the 2CLOWNS-3D simulation in the vicinity of the Kamaishi Bay offshore tsunami breakwater during the 2011 Tohoku-oki Earthquake Tsumami (Chapter 5).

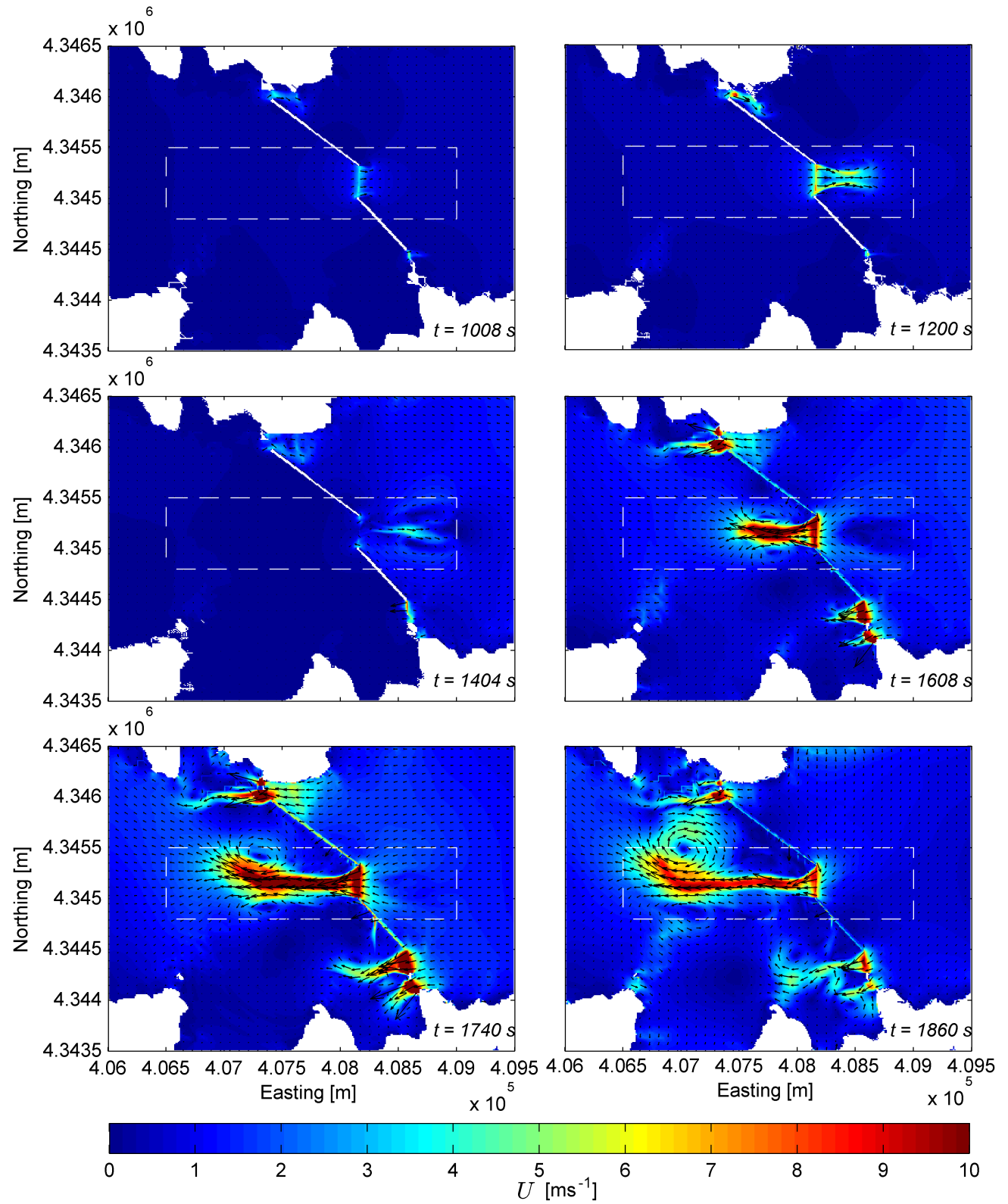


Figure D.1: Colour plot of the magnitudes of the depth-averaged velocities, U and the vector field during 2CLOWNS-3D model simulations on the 10 m 2DH NSWE mesh at various snapshots for $1000 < t < 2000$ s after the earthquake rupture. White dashed rectangle indicates location of the 3D RANS domain

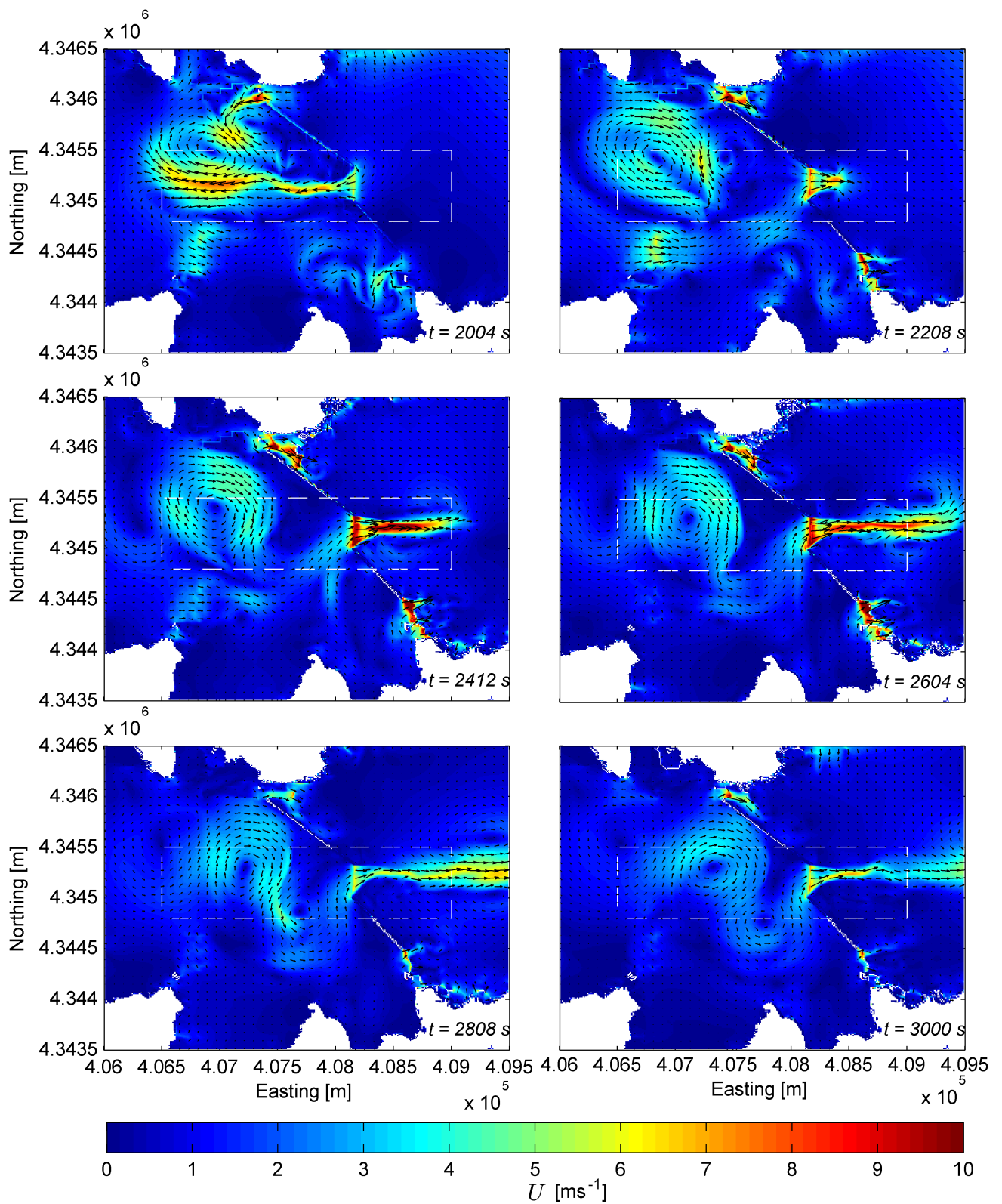


Figure D.2: Colour plot of the magnitudes of the depth-averaged velocities, U and the vector field during 2CLOWNS-3D model simulations on the 10 m 2DH NSWE mesh at various snapshots for $2000 < t \leq 3000 \text{ s}$ after the earthquake rupture. White dashed rectangle indicates location of the 3D RANS domain

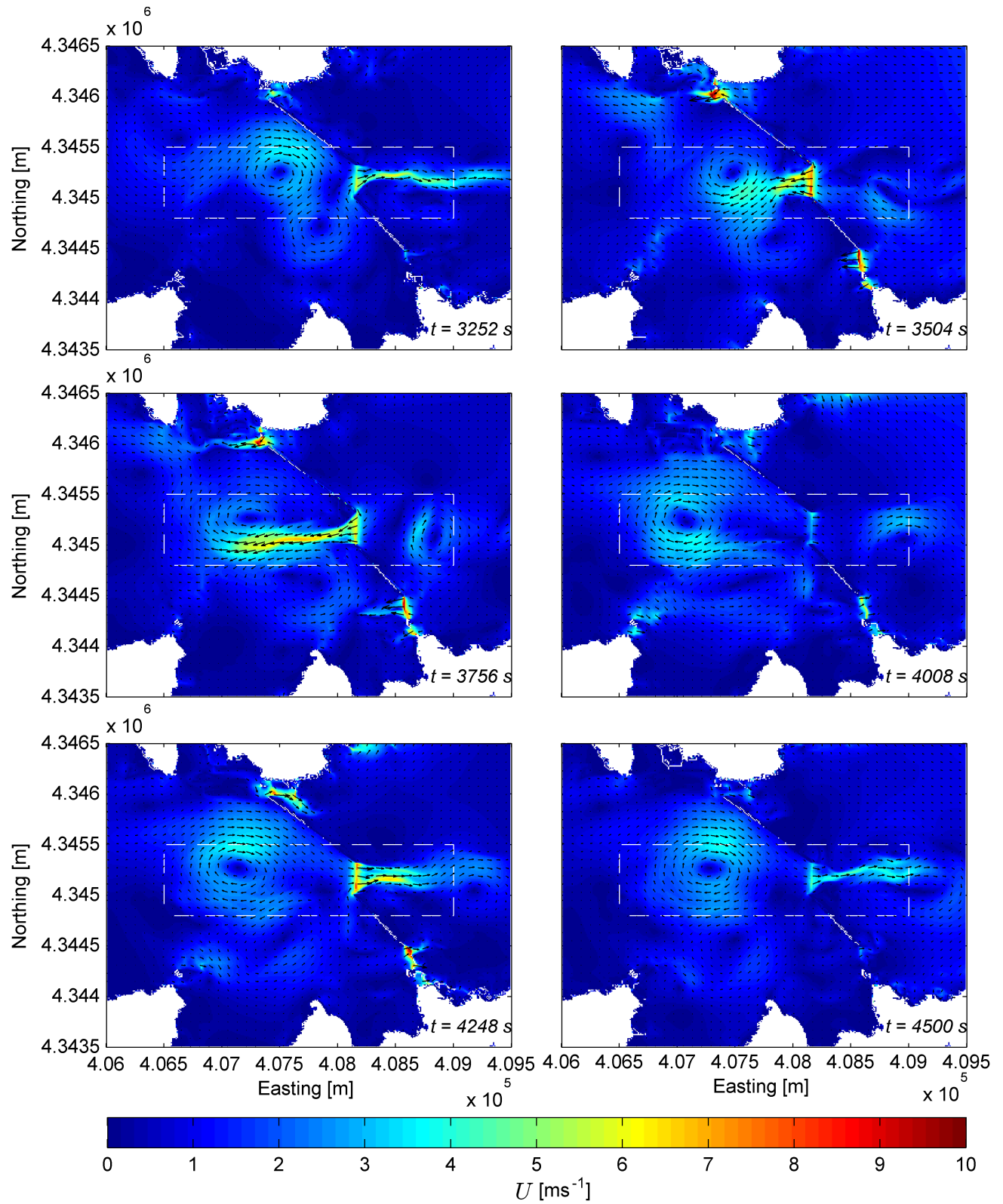


Figure D.3: Colour plot of the magnitudes of the depth-averaged velocities, U and the vector field during 2CLOWNS-3D model simulations on the 10 m 2DH NSWE mesh at various snapshots for $3000 < t \leq 4500$ s after the earthquake rupture. White dashed rectangle indicates location of the 3D RANS domain

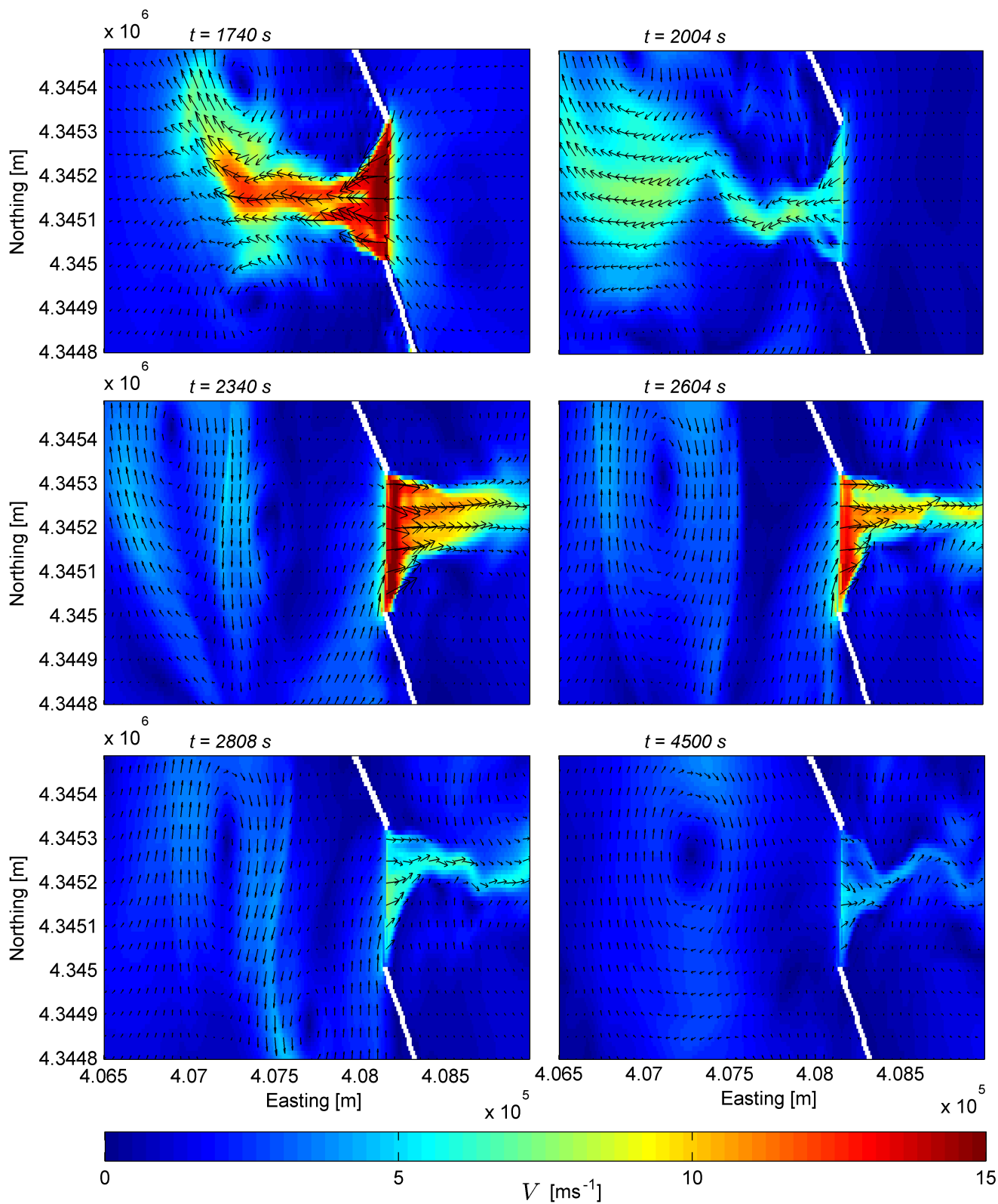


Figure D.4: Colour plot of the magnitudes of the horizontal velocities, V and the vector field in the 3D RANS domain during 2CLOWNS-3D model simulations on the $z = -20.8 \text{ m}$ contour at various times ($1740 \leq t \leq 4500 \text{ s}$) after the earthquake rupture

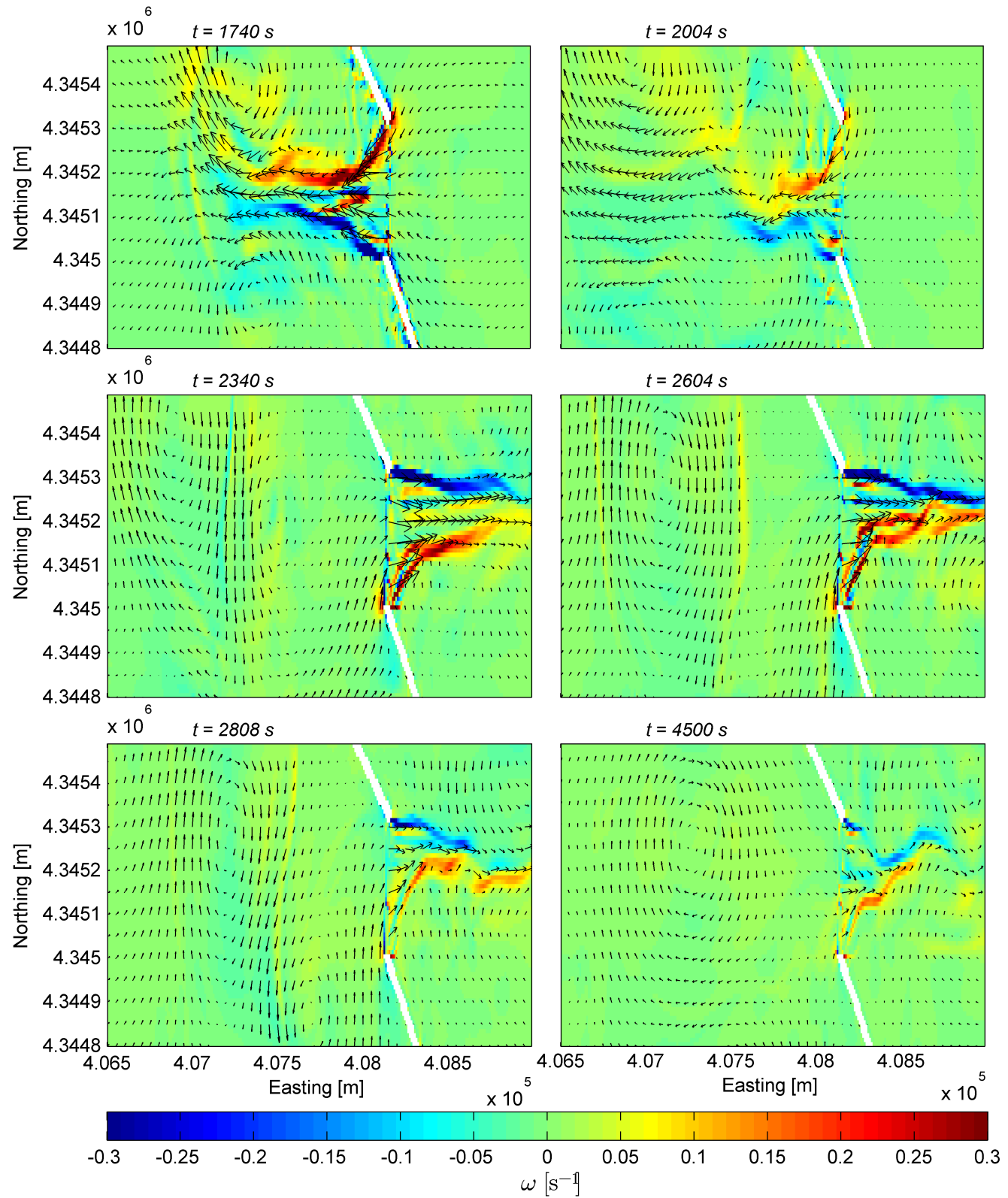


Figure D.5: Colour plot of the vorticities, ω and the vector field in the 3D RANS domain during 2CLOWNS-3D model simulations on the $z = -20.8$ m contour at various times ($1740 \leq t \leq 4500$ s) after the earthquake rupture

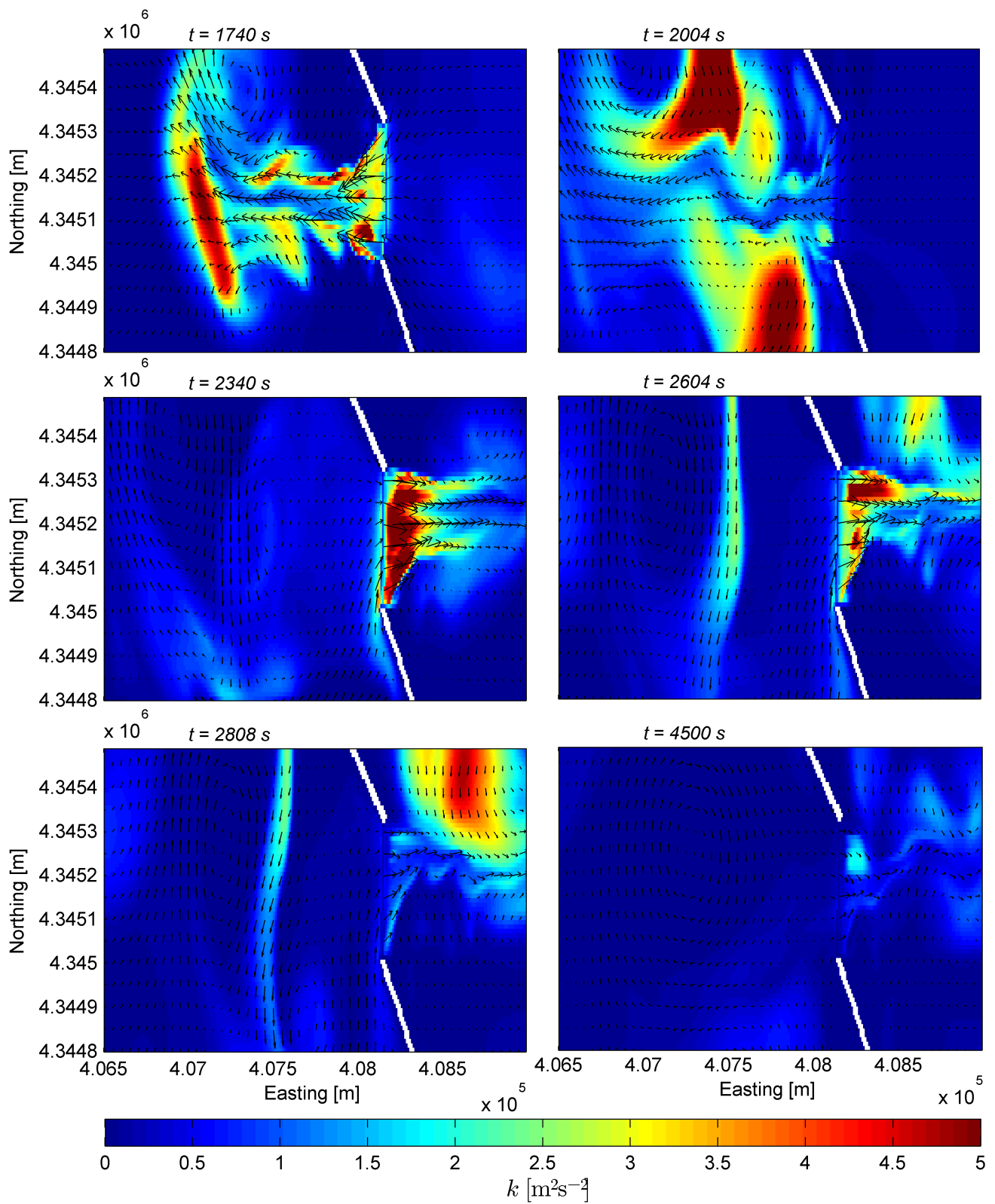


Figure D.6: Colour plot of the turbulent kinetic energy, k and the vector field in the 3D RANS domain during 2CLOWNS-3D model simulations on the $z = -20.8 \text{ m}$ contour at various times ($1740 \leq t \leq 4500 \text{ s}$) after the earthquake rupture

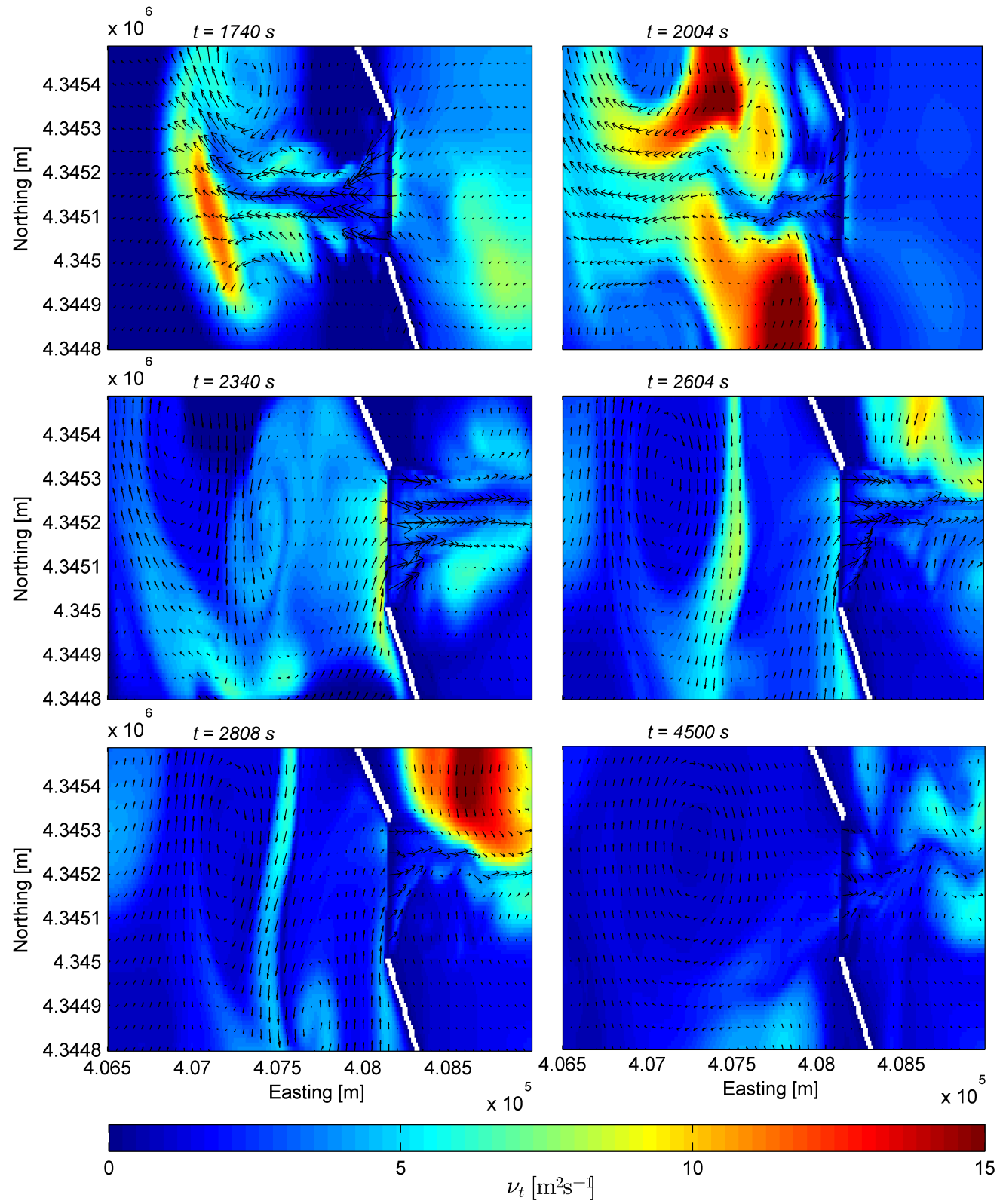


Figure D.7: Colour plot of the turbulent viscosity, ν_t and the vector field in the 3D RANS domain during 2CLOWNS-3D model simulations on the $z = -20.8$ m contour at various times ($1740 \leq t \leq 4500$ s) after the earthquake rupture

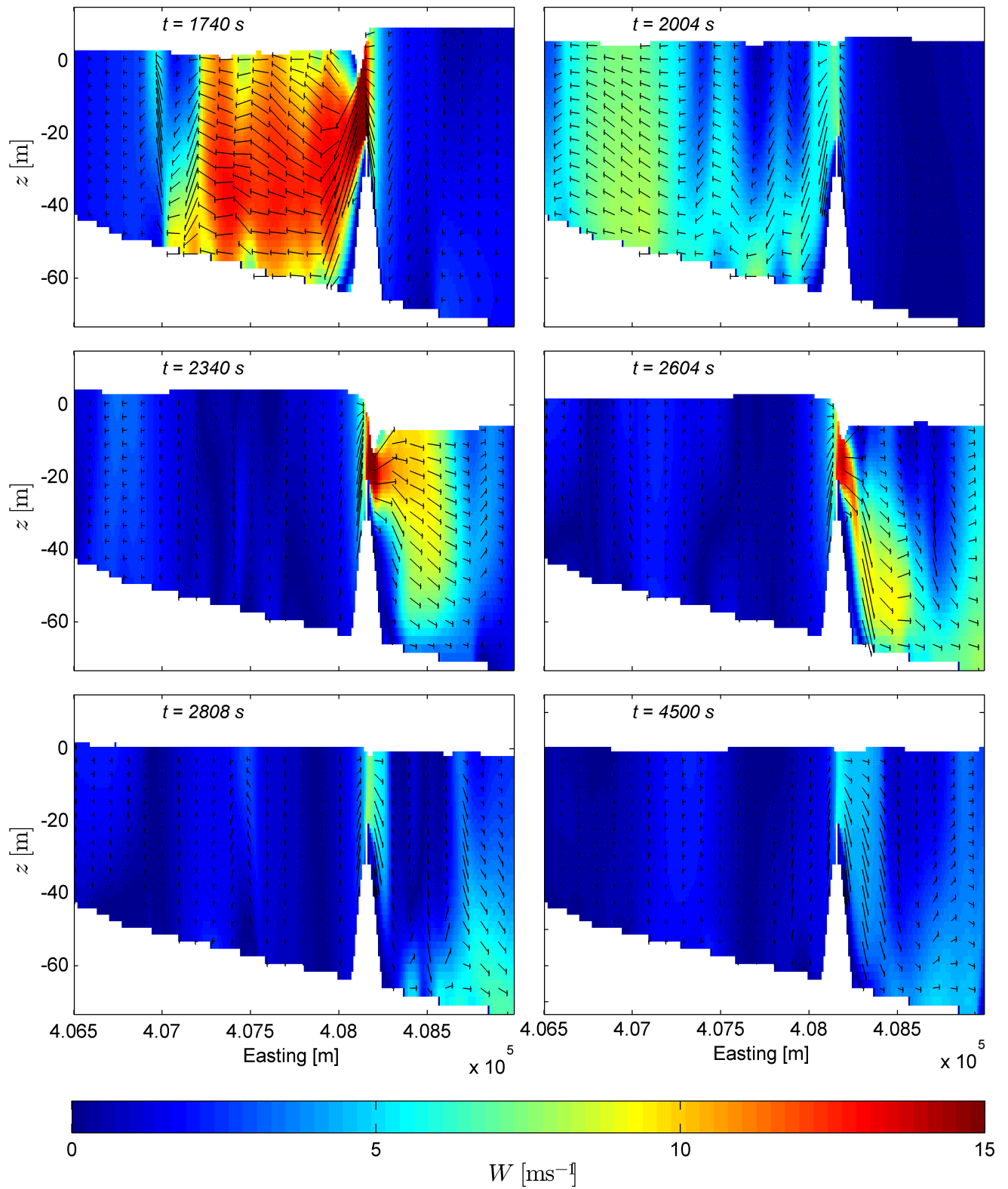


Figure D.8: Colour plot of the magnitudes of the velocities in the $x-z$ plane, W and the vector field in the 3D RANS domain during 2CLOWNS-3D model simulations along the $y = 4,345,175$ m northing cross-section at various times ($1740 \leq t \leq 4500$ s) after the earthquake rupture

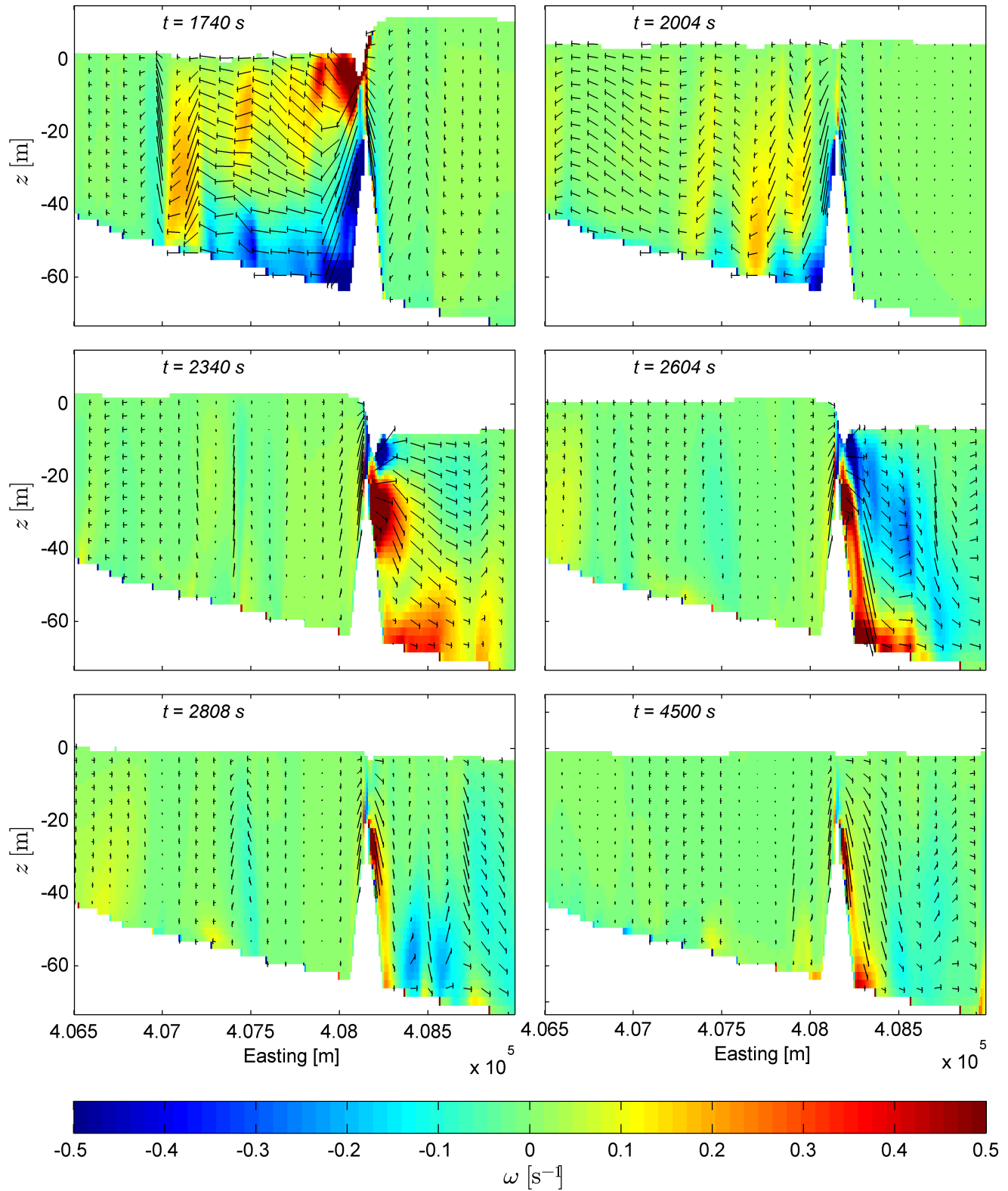


Figure D.9: Colour plot of the magnitudes of the vorticities in the $x-z$ plane, ω and the vector field in the 3D RANS domain during 2CLOWNS-3D model simulations along the $y = 4,345,175$ m northing cross-section at various times ($1740 \leq t \leq 4500$ s) after the earthquake rupture

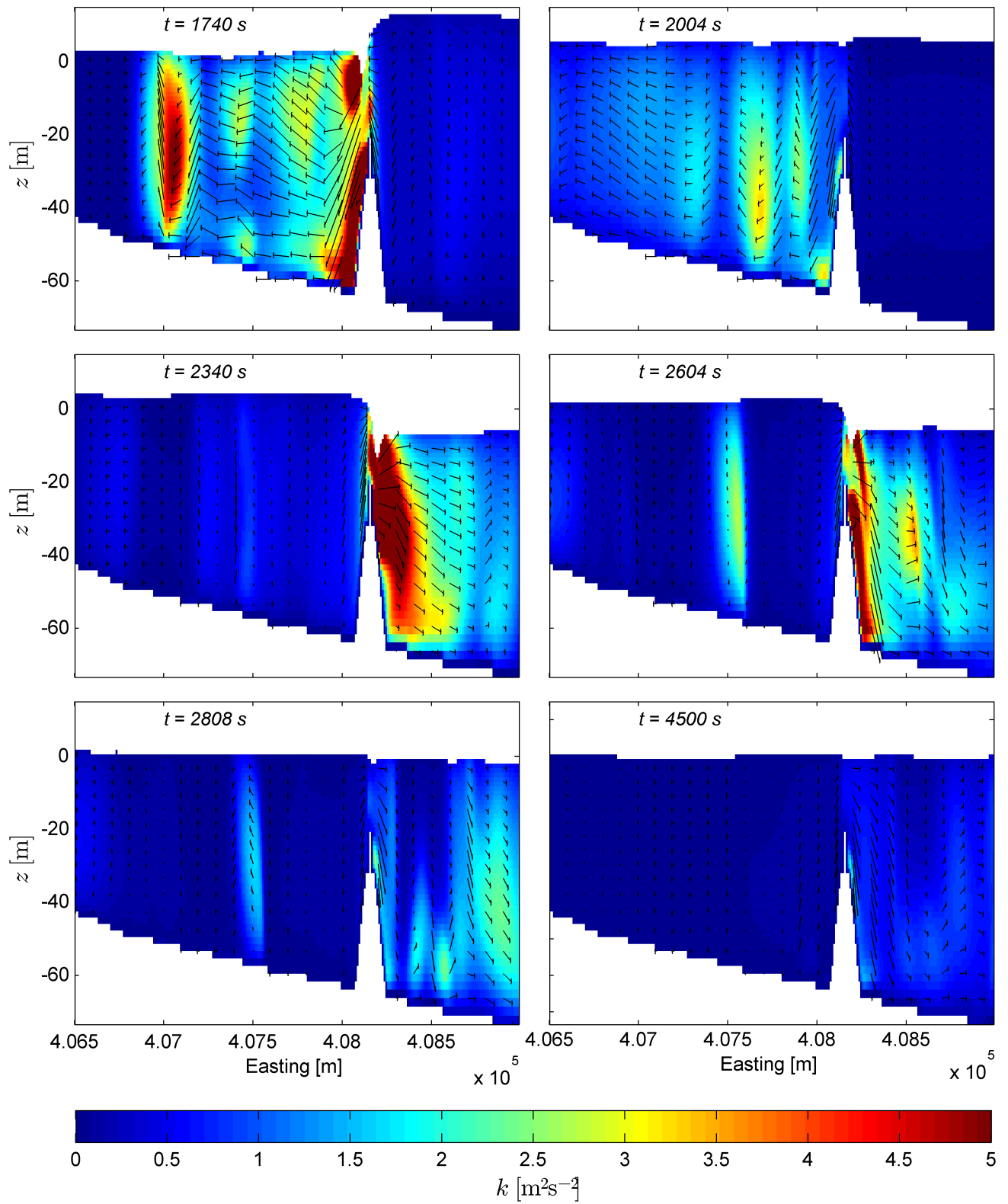


Figure D.10: Colour plot of the magnitudes of the turbulent kinetic energy, k and the vector field in the $x-z$ plane of the 3D RANS domain during 2CLOWNS-3D model simulations along the $y = 4,345,175$ m northing cross-section at various times ($1740 \leq t \leq 4500$ s) after the earthquake rupture

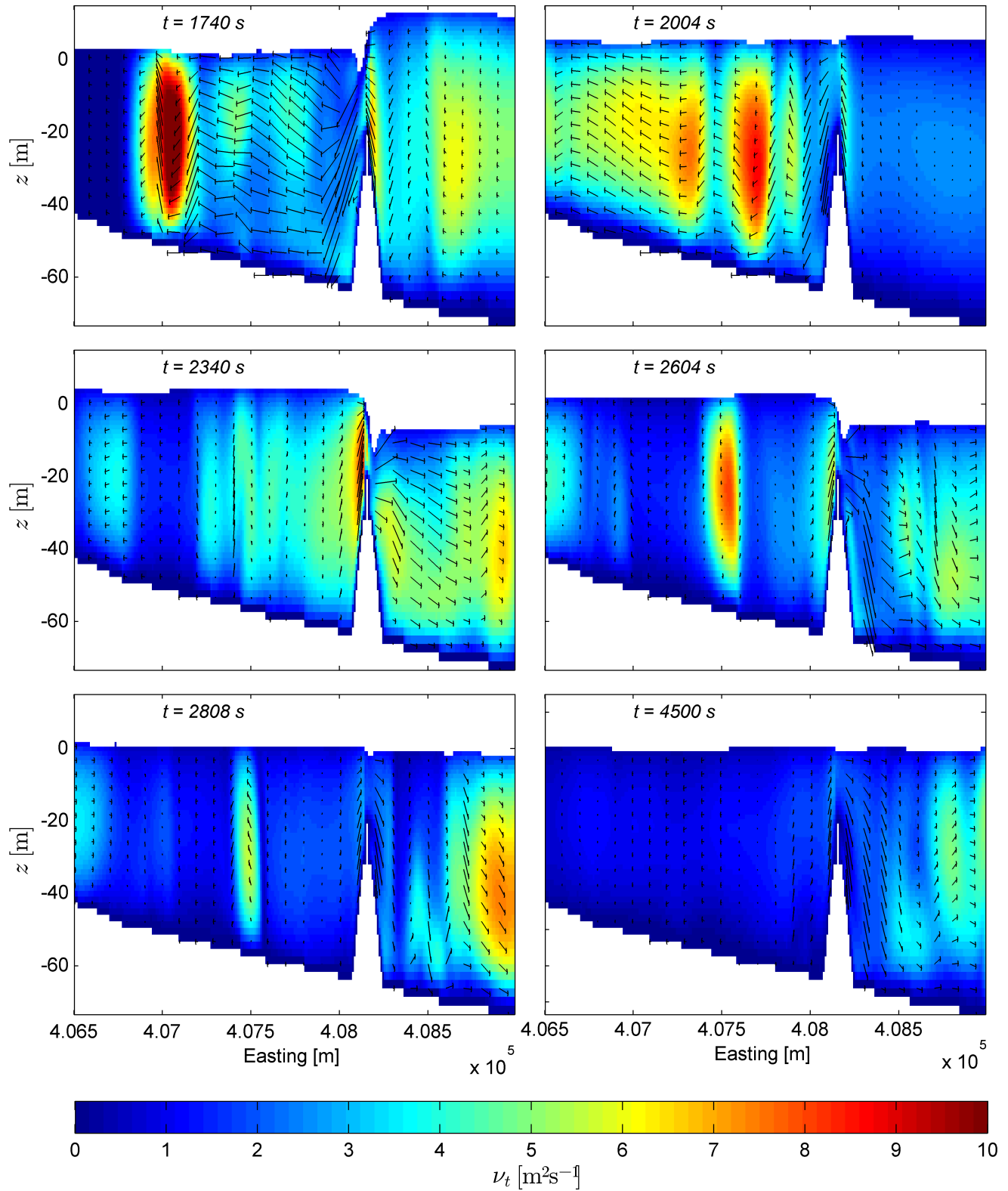


Figure D.11: Colour plot of the magnitudes of the turbulent viscosity, ν_t and the vector field in the $x-z$ plane of the 3D RANS domain during 2CLOWNS-3D model simulations along the $y = 4,345,175$ m northing cross-section at various times ($1740 \leq t \leq 4500$ s) after the earthquake rupture

REFERENCES

- Abe, S., Thangavelu, S.M., 2012. Natural Disasters and Asia: Introduction. *Asian Economic Journal* 26, 181–187. doi:10.1111/j.1467-8381.2012.02081.x.
- Aida, I., 1969. Numerical Experiments for the Tsunami Propagation : the 1964 Niigata Tsunami and the 1968 Tokachi-oki Tsunami. *Bulletin of the Earthquake Research Institute, Tokyo University* 47, 673–700.
- Aida, I., 1977. Numerical experiments for inundation of tsunamis - Susaki and Usa, in Kochi Prefecture. *Bulletin of the Earthquake Research Institute, Tokyo University* 52, 441–460 (in Japanese).
- Ammon, C.J., Ji, C., Thio, H.K., Robinson, D., Ni, S., Hjorleifsdottir, V., Kanamori, H., Lay, T., Das, S., Helmberger, D., Ichinose, G., Polet, J., Wald, D., 2005. Rupture process of the 2004 Sumatra-Andaman earthquake. *Science* 308, 1133–9. doi:10.1126/science.1112260.
- Amsden, A.A., Harlow, F.H., 1970. A simplified MAC technique for incompressible fluid flow calculations. *Journal of Computational Physics* 6, 322–325. doi:10.1016/0021-9991(70)90029-X.
- Arikawa, T., Sato, M., Shimosako, K., Hasegawa, I., Yeom, G.S., Tomita, T., 2012. Failure Mechanism of Kamaishi Breakwaters due to the Great East Japan Earthquake Tsunami. *Coastal Engineering Proceedings* 1, 13. doi:10.9753/icce.v33.structures.16.
- Athukorala, P.c., 2012. Indian Ocean Tsunami: Disaster, Generosity and Recovery. *Asian Economic Journal* 26, 211–231. doi:10.1111/j.1467-8381.2012.02083.x.
- Bakhtyar, R., Barry, D., Yeganeh-Bakhtiary, A., Ghaheri, A., 2009. Numerical simulation of surf-swash zone motions and turbulent flow. *Advances in Water Resources* 32, 250–263. doi:10.1016/j.advwatres.2008.11.004.
- Behrens, J., Dias, F., 2015. New computational methods in tsunami science. *Philosophical Transactions of the Royal Society A: Mathematical, Physical and Engineering Sciences* 373, 20140382. doi:10.1098/rsta.2014.0382.

REFERENCES

- Borrero, J.C., Synolakis, C.E., Fritz, H., 2006. Northern Sumatra Field Survey after the December 2004 Great Sumatra Earthquake and Indian Ocean Tsunami. *Earthquake Spectra* 22, 93–104. doi:10.1193/1.2206793.
- Bradford, S.F., 2005. Godunov-Based Model for Nonhydrostatic Wave Dynamics. *Journal of Waterway, Port, Coastal, and Ocean Engineering* 131, 226–238. doi:10.1061/(ASCE)0733-950X(2005)131:5(226).
- Bricker, J.D., 2013. Turbulence Model Effects on VOF Analysis of Breakwater Overtopping during the 2011 Great East Japan Tsunami, in: 35th IAHR World Congress, Chengdu, China. p. 10.
- Camfield, F.E., Street, R.L., 1969. Shoaling of Solitary Waves on Small Slopes. *Journal of the Waterways and Harbors Division* 95, 1–22.
- Chan, I.C., Liu, P.L.F., 2012. On the runup of long waves on a plane beach. *Journal of Geophysical Research* 117, C08006. doi:10.1029/2012JC007994.
- Chanson, H., 1999. *The Hydraulics of Open Channel Flow: An introduction*. 1st ed., Arnold Publishers, London.
- Chen, M.H., 1986. Numerical Simulation of 1964 Tsunami across the Pacific Ocean, in: *Coastal Engineering Proceedings*, Taipei, Taiwan.
- Cho, Y.S., Sohn, D.H., Lee, S.O., 2007. Practical modified scheme of linear shallow-water equations for distant propagation of tsunamis. *Ocean Engineering* 34, 1769–1777. doi:10.1016/j.oceaneng.2006.08.014.
- Cho, Y.S., Yoon, S.B., 1998. A modified leap-frog scheme for linear shallow-water equations. *Coastal Engineering Journal* 40, 191–205. doi:10.1142/S0578563498000121.
- Choi, B.H., Kim, D.C., Pelinovsky, E., Woo, S.B., 2007. Three-dimensional simulation of tsunami run-up around conical island. *Coastal Engineering* 54, 618–629. doi:10.1016/j.coastaleng.2007.02.001.
- Chorin, A.J., 1968. Numerical solution of the Navier-Stokes equations. *Mathematics of Computation* 22, 745–745. doi:10.1090/S0025-5718-1968-0242392-2.
- Cox, D.T., Kobayashi, N., Okayasu, A., 1994. Vertical Variations of Fluid Velocities and Shear Stress in Surf Zones, in: *Coastal Engineering Proceedings*.
- Dawson, C., Mirabito, C.M., 2008. *The Shallow Water Equations - Lecture Notes*. Institute for Computational Engineering and Sciences, University of Texas, Austin. URL: http://users.ices.utexas.edu/~arbogast/cam397/dawson_{_}v2.pdf.

- Dowell, M., Jarratt, P., 1971. A modified regula falsi method for computing the root of an equation. *BIT Numerical Mathematics* 11, 168–174. doi:10.1007/BF01934364.
- Fritz, H.M., Hager, W.H., Minor, H.E., 2001. Lituya Bay case: rockslide impact and wave run-up. *Science of Tsunami Hazards* 29, 3–23.
- Fritz, H.M., Phillips, D.a., Okayasu, A., Shimosono, T., Liu, H., Mohammed, F., Skanavis, V., Synolakis, C.E., Takahashi, T., 2012. The 2011 Japan tsunami current velocity measurements from survivor videos at Kesennuma Bay using LiDAR. *Geophysical Research Letters* 39, L00G23. doi:10.1029/2011GL050686.
- Fuhrman, D.R., Madsen, P.A., 2009. Tsunami generation, propagation, and run-up with a high-order Boussinesq model. *Coastal Engineering* 56, 747–758. doi:10.1016/j.coastaleng.2009.02.004.
- Fujii, Y., Satake, K., Sakai, S., Shinohara, M., Kanazawa, T., 2011. Tsunami source of the 2011 off the Pacific coast of Tohoku Earthquake. *Earth, Planets and Space* 63, 815–820. doi:10.5047/eps.2011.06.010.
- Fujima, K., 2006. Effect of a submerged bay-mouth breakwater on tsunami behavior analyzed by 2D/3D hybrid model simulation. *Natural Hazards* 39, 179–193. doi:10.1007/s11069-006-0022-x.
- Fujima, K., Achmad, F., Shigihara, Y., Mizutani, N., 2009. Estimation of Tsunami Force Acting on Rectangular Structures. *Journal of Disaster Research* 4, 404–409.
- Fujima, K., Masamura, K., Goto, C., 2002. Development of the 2D/3D Hybrid Model for Tsunami Numerical Simulation. *Coastal Engineering Journal* 44, 373–397. doi:10.1142/S0578563402000615.
- Fukazawa, S., Tosaka, H., 2014. Seamless and Mass-Conservative Numerical Simulation of Tsunami and Inundation with Infiltration of Water into Underground, in: *Proceedings of the 1st International Conference on Computational Engineering and Science for Safety and Environmental Problems*, Sendai, Japan. pp. 703–706.
- Geospatial Information Authority of Japan, 2009. 5 m mesh Digital Elevation Measurements of Japan (JGD2000). Geospatial Information Planning Office, Tsukubashi, Ibaraki Prefecture Office, Japan.
- Geospatial Information Authority of Japan (GSI), 2011. Inundation Area Approximation Including Division of Land Use. URL: <http://www.gsi.go.jp/chirijoho/chirijoho40025.html>.
- Goda, Y., 2010. Design of Vertical Breakwaters, in: *Random Seas and Design of Maritime Structures*. 3 ed.. World Scientific Publishing Company. chapter 4, pp. 161–209. doi:10.1142/9789814282413{_}0004.

REFERENCES

- Godunov, S.K., 1959. A difference method for numerical calculation of discontinuous solutions of the equations of hydrodynamics. *Matematicheskii Sbornik* 89, 271–306.
- Goto, C., Ogawa, Y., Shuto, N., Imamura, F., 1997. IUGG/IOC Time Project: IOC Manuals and Guides No.35 - Numerical Method of Tsunami Simulation with the Leap-frog Scheme. UNESCO.
- Goto, C., Shuto, N., 1983. Numerical simulation of tsunami propagations and run-up, in: Iida, K., Iwasaki, T. (Eds.), *Tsunamis: their science and engineering*. Terra Science Publishing Company, Tokyo, Japan, pp. 439–451.
- Grilli, S.T., Harris, J.C., Tajalli Bakhsh, T.S., Masterlark, T.L., Kyriakopoulos, C., Kirby, J.T., Shi, F., 2012. Numerical Simulation of the 2011 Tohoku Tsunami Based on a New Transient FEM Co-seismic Source: Comparison to Far- and Near-Field Observations. *Pure and Applied Geophysics* 170, 1333–1359. doi:10.1007/s00024-012-0528-y.
- Grilli, S.T., Subramanya, R., Svendsen, I.A., Veeramony, J., 1994. Shoaling of Solitary Waves on Plane Beaches. *Journal of Waterway, Port, Coastal, and Ocean Engineering* 120, 609–628. doi:10.1061/(ASCE)0733-950X(1994)120:6(609).
- Grilli, S.T., Svendsen, I.A., Subramanya, R., 1997. Breaking Criterion and Characteristics for Solitary Waves on Slopes. *Journal of Waterway, Port, Coastal, and Ocean Engineering* 123, 102–112. doi:10.1061/(ASCE)0733-950X(1997)123:3(102).
- Hammack, J.L., 1973. A note on tsunamis: their generation and propagation in an ocean of uniform depth. *Journal of Fluid Mechanics* 60, 769–799. doi:10.1017/S0022112073000479.
- Harlow, F.H., Welch, J.E., 1965. Numerical Calculation of Time-Dependent Viscous Incompressible Flow of Fluid with Free Surface. *Physics of Fluids* 8, 2182. doi:10.1063/1.1761178.
- Harten, A., 1983. High resolution schemes for hyperbolic conservation laws. *Journal of Computational Physics* 49, 357–393. doi:10.1016/0021-9991(83)90136-5.
- Harten, A., Engquist, B., Osher, S., Chakravarthy, S.R., 1987. Uniformly high order accurate essentially non-oscillatory schemes, III. *Journal of Computational Physics* 71, 231–303. doi:10.1016/0021-9991(87)90031-3.
- Harten, A., Osher, S., 1987. Uniformly High-Order Accurate Nonoscillatory Schemes. I. *SIAM Journal on Numerical Analysis* 24, 279–309. doi:10.1137/0724022.
- Hibberd, S., Peregrine, D.H., 1979. Surf and run-up on a beach: a uniform bore. *Journal of Fluid Mechanics* 95, 323–345. doi:10.1017/S002211207900149X.

- Higuera, P., Lara, J.L., Losada, I.J., 2013. Realistic wave generation and active wave absorption for Navier-Stokes models. *Coastal Engineering* 71, 102–118. doi:10.1016/j.coastaleng.2012.07.002.
- Higuera, P., Lara, J.L., Losada, I.J., 2014. Three-dimensional interaction of waves and porous coastal structures using OpenFOAM. Part I: Formulation and validation. *Coastal Engineering* 83, 243–258. doi:10.1016/j.coastaleng.2013.08.010.
- Hirt, C., Nichols, B., 1981. Volume of fluid (VOF) method for the dynamics of free boundaries. *Journal of Computational Physics* 39, 201–225. doi:10.1016/0021-9991(81)90145-5.
- Hirt, C.W., Sicilian, J.M., 1985. A Porosity Technique for the Definition of Obstacles in Rectangular Cell Meshes, in: *International Conference on Numerical Ship Hydrodynamics*, 4th, pp. 1–19.
- Honma, H., 1940. Coefficient of flow volume on low overflow weir. *Civil Engineering - JSCE* 26, 635–645 (in Japanese).
- Hsiao, S.C., Hsu, T.W., Lin, T.C., Chang, Y.H., 2008. On the evolution and run-up of breaking solitary waves on a mild sloping beach. *Coastal Engineering* 55, 975–988. doi:10.1016/j.coastaleng.2008.03.002.
- Hwang, K.S., Chang, Y.H., Hwung, H.H., Yi-Syuan, L., 2007. Large Scale Experiments On Evolution And Run-Up Of Breaking Solitary Waves. *Journal of Earthquake and Tsunami* 1, 257–272. doi:10.1142/S1793431107000158.
- Hwang, L.S., Butler, H.L., Divoky, D., 1972. Tsunami model: Generation and open-sea characteristics. *Bulletin of the Seismological Society of America* 62, 1579–1596.
- Hwang, L.S., Divoky, D., 1970. Tsunami generation. *Journal of Geophysical Research* 75, 6802–6817. doi:10.1029/JC075i033p06802.
- Ichiye, T., 1958. A Theory on the Generation of Tsunamis by an Impulse at the Sea Bottom. *Journal of the Oceanographical Society of Japan* 12, 41–44. doi:10.5928/kaiyou1942.14.41.
- Imamura, F., Goto, C., 1988. Truncation Error in Numerical Simulation by the Finite Difference Method. *Coastal Engineering in Japan* 31, 245–263.
- Imamura, F., Koshimura, S., Mabuchi, Y., Oka, T., Okada, K., 2012. Implementation of tsunami simulation intended for the Tohoku off the coast of the Pacific Earthquake - Tohoku University model version1.2. Technical Report.
- Imamura, F., Shuto, N., Goto, C., 1990. Study on Numerical Simulation of the Transoceanic Propagation of Tsunami. *Zisin (Journal of the Seismological Society of Japan. 2nd ser.)* 43, 389–402 (in Japanese).

REFERENCES

- Imamura, F., Yalciner, A.C., Ozyurt, G., 2006. Tsunami Modelling Manual (TUNAMI model). Technical Report.
- Isobe, M., Takahashi, S., Yu, S.P., Sakakiyama, T., Fujima, K., Kawasaki, K., Jiang, Q., Akiyama, M., Ohyama, H., 1999. Intermin Development of a Numerical Wave Flume for Maritime Structure Design, in: Proceedings of Civil Engineering in the Ocean, JSCE, pp. 321–326 (in Japanese). doi:10.2208/prooe.15.321.
- Issa, R., 1986. Solution of the implicitly discretised fluid flow equations by operator-splitting. *Journal of Computational Physics* 62, 40–65. doi:10.1016/0021-9991(86)90099-9.
- Iwasaki, T., Mano, A., 1979. Two-dimensional simulation of tsunami runup in the Eulerian frame of reference, in: 26th Coastal Engineering Conference, JSCE, pp. 70–74 (in Japanese).
- del Jesus, M., Lara, J.L., Losada, I.J., 2012. Three-dimensional interaction of waves and porous coastal structures. *Coastal Engineering* 64, 57–72. doi:10.1016/j.coastaleng.2012.01.008.
- Kajiura, K., 1963. The Leading Wave of a Tsunami. *Bulletin of the Earthquake Research Institute, Tokyo University* 41, 535–571.
- Kanamori, H., 2006. Seismological Aspects of the December 2004 Great Sumatra-Andaman Earthquake. URL: <http://authors.library.caltech.edu/6714/1/KANes06.pdf>.
- Kanoglu, U., 2004. Nonlinear evolution and runup-rundown of long waves over a sloping beach. *Journal of Fluid Mechanics* 513, 363–372. doi:10.1017/S002211200400970X.
- Kazolea, M., Delis, A., 2013. A well-balanced shock-capturing hybrid finite volume-finite difference numerical scheme for extended 1D Boussinesq models. *Applied Numerical Mathematics* 67, 167–186. doi:10.1016/j.apnum.2011.07.003.
- Kennedy, A.B., Chen, Q., Kirby, J.T., Dalrymple, R.A., 2000. Boussinesq Modeling of Wave Transformation, Breaking, and Runup. I: 1D. *Journal of Waterway, Port, Coastal, and Ocean Engineering* 126, 39–47. doi:10.1061/(ASCE)0733-950X(2000)126:1(39).
- Kihara, N., Fujii, N., Matsuyama, M., 2012. Three-dimensional sediment transport processes on tsunami-induced topography changes in a harbor. *Earth, Planets and Space* 64, 787–797. doi:10.5047/eps.2011.05.036.
- Kim, D.H., Lynett, P.J., Socolofsky, S.A., 2009. A depth-integrated model for weakly dispersive, turbulent, and rotational fluid flows. *Ocean Modelling* 27, 198–214. doi:10.1016/j.ocemod.2009.01.005.
- Kim, S.H., Yamashiro, M., Yoshida, A., 2010. A simple two-way coupling method of BEM and VOF model for random wave calculations. *Coastal Engineering* 57, 1018–1028. doi:10.1016/j.coastaleng.2010.06.006.

- Kim, S.W., Benson, T., 1992. Comparison of the SMAC, PISO and iterative time-advancing schemes for unsteady flows. *Computers & Fluids* 21, 435–454. doi:10.1016/0045-7930(92)90048-Z.
- Kotani, M., Imamura, F., Shuto, N., 1998. Tsunami runup calculations and damage estimation method using GIS, in: *Proceedings of Coastal Engineering, JSCE*, pp. 356–360.
- Lara, J.L., Ruju, A., Losada, I.J., 2010. Reynolds averaged Navier-Stokes modelling of long waves induced by a transient wave group on a beach. *Proceedings of the Royal Society A: Mathematical, Physical and Engineering Sciences* 467, 1215–1242. doi:10.1098/rspa.2010.0331.
- Lauder, B., Spalding, D., 1974. The numerical computation of turbulent flows. *Computer Methods in Applied Mechanics and Engineering* 3, 269–289. doi:10.1016/0045-7825(74)90029-2.
- Lay, T., Kanamori, H., Ammon, C.J., Nettles, M., Ward, S.N., Aster, R.C., Beck, S.L., Bilek, S.L., Brudzinski, M.R., Butler, R., DeShon, H.R., Ekström, G., Satake, K., Sipkin, S., 2005. The great Sumatra-Andaman earthquake of 26 December 2004. *Science* 308, 1127–1133. doi:10.1126/science.1112250.
- van Leer, B., 1974. Towards the ultimate conservative difference scheme. II. Monotonicity and conservation combined in a second-order scheme. *Journal of Computational Physics* 14, 361–370. doi:10.1016/0021-9991(74)90019-9.
- LeVeque, R.J., George, D.L., Berger, M.J., 2011. Tsunami modelling with adaptively refined finite volume methods. *Acta Numerica* 20, 211–289. doi:10.1017/S0962492911000043.
- Li, Y., Raichlen, F., 2002. Non-breaking and breaking solitary wave run-up. *Journal of Fluid Mechanics* 456, 295–318. doi:10.1017/S0022112001007625.
- Li, Y., Raichlen, F., 2003. Energy Balance Model for Breaking Solitary Wave Runup. *Journal of Waterway, Port, Coastal, and Ocean Engineering* 129, 47–59. doi:10.1061/(ASCE)0733-950X(2003)129:2(47).
- Liang, Q., 2010. Flood Simulation Using a Well-Balanced Shallow Flow Model. *Journal of Hydraulic Engineering* 136, 669–675. doi:10.1061/(ASCE)HY.1943-7900.0000219.
- Liang, Q., Borthwick, A.G., 2009. Adaptive quadtree simulation of shallow flows with wet-dry fronts over complex topography. *Computers & Fluids* 38, 221–234. doi:10.1016/j.compfluid.2008.02.008.
- Lin, P., Chang, K.A., Liu, P.L.F., 1999. Runup and Rundown of Solitary Waves on Sloping Beaches. *Journal of Waterway, Port, Coastal, and Ocean Engineering* 125, 247–255. doi:10.1061/(ASCE)0733-950X(1999)125:5(247).

REFERENCES

- Lin, P., Liu, P.L.F., 1998. A numerical study of breaking waves in the surf zone. *Journal of Fluid Mechanics* 359, 239–264. doi:10.1017/S002211209700846X.
- Liu, P.L.F., Cho, Y.S., Briggs, M.J., Kanoglu, U., Synolakis, C.E., 1995. Runup of solitary waves on a circular Island. *Journal of Fluid Mechanics* 302, 259–285. doi:10.1017/S0022112095004095.
- Liu, P.L.F., Woo, S.B., Cho, Y.S., 1998. Computer Programs for Tsunami Propagation and Inundation. Technical Report. Cornell University. Ithaca, New York.
- Liu, X.D., Osher, S., Chan, T., 1994. Weighted Essentially Non-oscillatory Schemes. *Journal of Computational Physics* 115, 200–212. doi:10.1006/jcph.1994.1187.
- Løvholt, F., Pedersen, G., Gisler, G., 2008. Oceanic propagation of a potential tsunami from the La Palma Island. *Journal of Geophysical Research* 113, C09026. doi:10.1029/2007JC004603.
- Lynett, P., 2005. A numerical study of the run-up generated by three-dimensional landslides. *Journal of Geophysical Research* 110, C03006. doi:10.1029/2004JC002443.
- Lynett, P., Liu, P., 2011. Numerical Simulation of Complex Tsunami Behavior. *Computing in Science & Engineering* 13, 50–57. doi:10.1109/MCSE.2011.22.
- Lynett, P.J., Borrero, J., Son, S., Wilson, R., Miller, K., 2014. Assessment of the tsunami-induced current hazard. *Geophysical Research Letters* 41, 1–8. doi:10.1002/2013GL058680.
- Lynett, P.J., Borrero, J.C., Weiss, R., Son, S., Greer, D., Renteria, W., 2012. Observations and modeling of tsunami-induced currents in ports and harbors. *Earth and Planetary Science Letters* 327-328, 68–74. doi:10.1016/j.epsl.2012.02.002.
- Lynett, P.J., Wu, T.R., Liu, P.L.F., 2002. Modeling wave runup with depth-integrated equations. *Coastal Engineering* 46, 89–107. doi:10.1016/S0378-3839(02)00043-1.
- Ma, G., Shi, F., Kirby, J.T., 2012. Shock-capturing non-hydrostatic model for fully dispersive surface wave processes. *Ocean Modelling* 43-44, 22–35. doi:10.1016/j.ocemod.2011.12.002.
- Madsen, P.A., 1997. Surf zone dynamics simulated by a Boussinesq type model. Part I: Model description and cross-shore motion of regular waves. *Coastal Engineering* 32, 255–287. doi:10.1016/S0378-3839(97)00028-8.
- Madsen, P.A., Murray, R., Sorensen, O.R., 1991. A new form of the Boussinesq equations with improved linear dispersion characteristics. *Coastal Engineering* 15, 371–388. doi:10.1016/0378-3839(91)90017-B.
- Madsen, P.A., Schaffer, H.A., 1998. Higher-order Boussinesq-type equations for surface gravity waves: derivation and analysis. *Philosophical Transactions of the Royal Society A: Mathematical, Physical and Engineering Sciences* 356, 3123–3181. doi:10.1098/rsta.1998.0309.

- Madsen, P.A., Schaffer, H.A., 2010. Analytical solutions for tsunami runup on a plane beach: single waves, N-waves and transient waves. *Journal of Fluid Mechanics* 645, 27. doi:10.1017/S0022112009992485.
- Madsen, P.A., Sorensen, O.R., 1992. A new form of the Boussinesq equations with improved linear dispersion characteristics . Part 2 . A slowly-varying bathymetry. *Coastal Engineering* 18, 183–204. doi:10.1016/0378-3839(92)90019-Q.
- Mansinha, B.L., Smylie, D.E., 1971. The displacement fields of inclined faults. *Bulletin of the Seismological Society of America* 61.
- McCowan, J., 1891. On the solitary wave. *Philosophical Magazine Series 5* 32, 45–58. doi:10.1080/14786449108621390.
- Moimoi, T., 1964. Tsunami in the Vicinity of a Wave Origin [I]. *Bulletin of the Earthquake Research Institute, Tokyo University* 42, 133–146.
- Mori, N., Takahashi, T., Group, T.T.E.T.J.S., 2012. Nationwide Post Event Survey and Analysis of the 2011 Earthquake Tsunami. *Coastal Engineering Journal* 54, 1250001. doi:10.1142/S0578563412500015.
- Mori, N., Takahashi, T., Yasuda, T., Yanagisawa, H., 2011. Survey of 2011 Tohoku earthquake tsunami inundation and run-up. *Geophysical Research Letters* 38, 1–6. doi:10.1029/2011GL049210.
- Mori, N., Yoneyama, N., Pringle, W.J., 2015. Effects of the Offshore Barrier Against the 2011 Off the Pacific Coast of Tohoku Earthquake Tsunami and Lessons Learned, in: Santiago-Fandiño, V., Kontar, Y., Kaneda, Y. (Eds.), *Post-Tsunami Hazard: Reconstruction and Restoration*. Springer International Publishing, pp. 121–132. doi:10.1007/978-3-319-10202-3.
- Munk, W.H., 1949. The Solitary Wave Theory And Its Application To Surf Problems. *Annals of the New York Academy of Sciences* 51, 376–424. doi:10.1111/j.1749-6632.1949.tb27281.x.
- Murata, S., Imamura, F., Katoh, K., Kawata, Y., Takahashi, S., Takayama, T., 2009. *Tsunami: to survive from tsunami (advanced series on Ocean Engineering vol. 32)*. World Scientific Publishing Company.
- Nagashima, H., Sasaki, S., Pringle, W.J., Yoneyama, N., 2015. Numerical Assessment of Critical Locations for Tsunami Inundation. *Journal of Japan Society of Civil Engineers, Ser. B3 Ocean Engineering* 71, I_509–I_514 (in Japanese). doi:http://doi.org/10.2208/jscejoe.71.I_{\ }509.
- Naito, C., Cercone, C., Riggs, H.R., Cox, D., 2014. Procedure for Site Assessment of the Potential for Tsunami Debris Impact. *Journal of Waterway, Port, Coastal, and Ocean Engineering* 140, 223–232. doi:10.1061/(ASCE)WW.1943-5460.0000222.

REFERENCES

- Nakamura, S., 1983. Numerical Tsunami Model in Osaka Bay. *Bulletin of the Disaster Prevention Research Institute*search Institute, Kyoto University 33, 1–14.
- Nakamura, S., 1984. A numerical tracking of the 1883 Krakatau tsunami, *Science of Tsunami Hazards*. *Science of Tsunami Hazards* 2, 41–54.
- National Police Agency of Japan, 2015. Damage situation and police countermeasures. URL: <http://www.npa.go.jp/archive/keibi/biki/higaijokyo.pdf>.
- National Tsunami Hazard Mitigation Program, 2015. NTHMP - 2015 Annual Meeting, Portland, Oregon. URL: <http://nws.weather.gov/nthmp/2015annualmeeting/index.html>.
- Nokes, R., 2008a. ENCI341: Basic Fluid Mechanics - Lecture Notes. College of Engineering, University of Canterbury, Christchurch, New Zealand.
- Nokes, R., 2008b. ENCI638: Environmental Fluid Dynamics - Lecture Notes. College of Engineering, University of Canterbury, Christchurch, New Zealand.
- Norio, O., Ye, T., Kajitani, Y., Shi, P., Tatano, H., 2011. The 2011 eastern Japan great earthquake disaster: Overview and comments. *International Journal of Disaster Risk Science* 2, 34–42. doi:10.1007/s13753-011-0004-9.
- Nwogu, O., 1993. Alternative Form of Boussinesq Equations for Nearshore Wave Propagation. *Journal of Waterway, Port, Coastal, and Ocean Engineering* 119, 618–638. doi:10.1061/(ASCE)0733-950X(1993)119:6(618).
- Ogawa, T., 1924. Notes on the volcanic and seismic phenomena in the volcanic district of Shimabara, with a report on the earthquake of December 8th, 1922. *Memoirs of the College of Science, Kyoto Imperial University*, Ser. B 1.
- Okada, Y., 1985. Surface deformation due to shear and tensile faults in a half-space. *Bulletin - Seismological Society of America* 75, 1135–1154.
- Palermo, D., Nistor, I., Al-Faesly, T., Cornett, A., 2013. Impact of tsunami forces on structures. *Science of Tsunami Hazards* 32, 58–76.
- Park, H., Cox, D.T., Lynett, P.J., Wiebe, D.M., Shin, S., 2013. Tsunami inundation modeling in constructed environments: A physical and numerical comparison of free-surface elevation, velocity, and momentum flux. *Coastal Engineering* 79, 9–21. doi:10.1016/j.coastaleng.2013.04.002.
- Patankar, S., Spalding, D., 1972. A calculation procedure for heat, mass and momentum transfer in three-dimensional parabolic flows. *International Journal of Heat and Mass Transfer* 15, 1787–1806. doi:10.1016/0017-9310(72)90054-3.

- Pedersen, G., Løvholt, F., 2008. Documentation of a global Boussinesq solver. Technical Report. Dept. of Math, University of Oslo. URL: <https://www.duo.uio.no//handle/10852/10184>.
- Peregrine, D.H., 1967. Long waves on a beach. *Journal of Fluid Mechanics* 27, 815. doi:10.1017/S0022112067002605.
- Port and Airport Research Institute of Japan, 2011a. GPS Wave Buoy Measurements of the Tohoku off the Coast of the Pacific Earthquake Tsunami. URL: <http://nowphas.mlit.go.jp/nowphasdata/sub301.htm>.
- Port and Airport Research Institute of Japan, 2011b. Technical note of the port and airport research institute No. 1231 (in Japanese). Technical Report. URL: <http://www.pari.go.jp/files/3643/345903759.pdf>.
- Pringle, W.J., Yoneyama, N., 2013. The Application of a Hybrid 2D/3D Numerical Tsunami Inundation-Propagation Flow Model to the 2011 off the Pacific Coast of Tohoku Earthquake Tsunami. *Journal of Japan Society of Civil Engineers, Ser. B2 Coastal Engineering* 69, I_306–I_310 (in Japanese). doi:http://doi.org/10.2208/kaigan.69.I{_}306.
- Pringle, W.J., Yoneyama, N., 2014. Solitary wave runup on a plane beach using a two-way coupled depth-averaged shallow water - RANS VOF model, in: 19th IAHR-APD Congress, Hanoi, Vietnam. p. 8.
- Pringle, W.J., Yoneyama, N., 2015. Analysis of Flow Behaviour around the Kamaishi Bay Offshore Tsunami Breakwater during the 2011 Tohoku Earthquake Tsunami, in: Australasian Coasts and Ports Conference, Auckland, New Zealand. p. 6.
- Pringle, W.J., Yoneyama, N., Mori, N., . Two-Way Coupled Long Wave - Rans Model: Solitary Wave Transformation And Breaking On A Plane Beach. *Coastal Engineering* , submitted to.
- Reynolds, O., 1895. On the Dynamical Theory of Incompressible Viscous Fluids and the Determination of the Criterion. *Philosophical Transactions of the Royal Society A: Mathematical, Physical and Engineering Sciences* 186, 123–164. doi:10.1098/rsta.1895.0004.
- Roe, P.L., 1983. Some contributions to the modelling of discontinuous flows, in: *Large computations in Fluid Mechanics: Proceedings of AMS/SIAM Summer Seminar, San Diego*.
- Roeber, V., Cheung, K.F., 2012. Boussinesq-type model for energetic breaking waves in fringing reef environments. *Coastal Engineering* 70, 1–20. doi:10.1016/j.coastaleng.2012.06.001.
- Roeber, V., Cheung, K.F., Kobayashi, M.H., 2010. Shock-capturing Boussinesq-type model for nearshore wave processes. *Coastal Engineering* 57, 407–423. doi:10.1016/j.coastaleng.2009.11.007.

REFERENCES

- Rueben, M., Cox, D., Holman, R., Shin, S., Stanley, J., 2014. Optical Measurements of Tsunami Inundation and Debris Movement in a Large-Scale Wave Basin. *Journal of Waterway, Port, Coastal, and Ocean Engineering*, 04014029doi:10.1061/(ASCE)WW.1943-5460.0000267.
- Saito, Y., Soma, T., Sagawa, R., Matsushita, Y., H, A., Daikoku, M., Shiota, M., Inamura, T., 2012. Comparison of Solution Algorithm for Flow around a Square Cylinder, in: Ninth International Conference on CFD in the Minerals and Process Industries, Melbourne.
- Sanders, B.F., 2002. Non-reflecting boundary flux function for finite volume shallow-water models. *Advances in Water Resources* 25, 195–202. doi:10.1016/S0309-1708(01)00055-0.
- Sato, S., 1996. Numerical Simulation of 1993 Southwest Hokkaido Earthquake Tsunami around Okushiri Island. *Journal of Waterway, Port, Coastal, and Ocean Engineering* 122, 209–215. doi:10.1061/(ASCE)0733-950X(1996)122:5(209).
- Schember, H.R., 1982. A new model for three-dimensional nonlinear dispersive long waves. Ph.D. thesis. California Institute of Technology. URL: http://thesis.library.caltech.edu/3729/1/Schember_{_}HR_{_}1982.pdf.
- Schlichting, H., Gersten, K., 2000. *Boundary-Layer Theory*. 8 ed., Springer-Verlag Berlin Heidelberg.
- Shi, F., Kirby, J.T., Harris, J.C., Geiman, J.D., Grilli, S.T., 2012a. A high-order adaptive time-stepping TVD solver for Boussinesq modeling of breaking waves and coastal inundation. *Ocean Modelling* 43, 36–51. doi:<http://www.sciencedirect.com/science/article/pii/S1463500311002010>.
- Shi, F., Kirby, J.T., Ma, G., Tehranirad, B., 2012b. Non-Hydrostatic Wave Model NHWAVE User's Guide for Modeling Submarine Landslide Tsunami (Version 1.1) - Research Report No. CACR-12-04. Technical Report. University of Delaware.
- Shibayama, T., Esteban, M., Nistor, I., Takagi, H., Thao, N.D., Matsumaru, R., Mikami, T., Aranguiz, R., Jayaratne, R., Ohira, K., 2013. Classification of Tsunami and Evacuation Areas. *Natural Hazards* 67, 365–386. doi:10.1007/s11069-013-0567-4.
- Shigihara, Y., Fujima, K., 2007. Adequate numerical scheme for dispersive wave theory for tsunami simulation and development of new numerical algorithm. *Doboku Gakkai Ronbunshu B/JSCE Journal of Hydraulic, Coastal and Environmental Engineering* 63, 51–66. doi:10.2208/jscejb.63.51.
- Shuto, N., 1991. Numerical simulation of tsunamis - Its present and near future. *Natural Hazards* 4, 171–191. doi:10.1007/BF00162786.

- Shuto, N., Suzuki, T., Hasegawa, K., Inagaki, K., 1986. A study of numerical techniques on the tsunami propagation and run up. *Science of Tsunami Hazards* 4, 111–124.
- Sitanggang, K.I., Lynett, P.J., 2010. Multi-scale simulation with a hybrid Boussinesq-RANS hydrodynamic model. *International Journal for Numerical Methods in Fluids* 62, 1013–1046. doi:10.1002/flid.2056.
- Son, S., Lynett, P.J., Kim, D.H., 2011. Nested and multi-physics modeling of tsunami evolution from generation to inundation. *Ocean Modelling* 38, 96–113. doi:10.1016/j.ocemod.2011.02.007.
- Sondak, D.L., 1992. Wall functions for the k-[epsilon] turbulence model in generalized nonorthogonal curvilinear coordinates. Ph.D. thesis. Iowa State University. URL: <http://lib.dr.iastate.edu/rtd/9954/>.
- Suppasri, A., Shuto, N., Imamura, F., Koshimura, S., Mas, E., Yalciner, A.C., 2013. Lessons Learned from the 2011 Great East Japan Tsunami: Performance of Tsunami Countermeasures, Coastal Buildings, and Tsunami Evacuation in Japan. *Pure and Applied Geophysics* 170, 993–1018. doi:10.1007/s00024-012-0511-7.
- Sweby, P.K., 1984. High Resolution Schemes Using Flux Limiters for Hyperbolic Conservation Laws. *SIAM Journal on Numerical Analysis* 21, 995–1011. doi:10.1137/0721062.
- Synolakis, C.E., 1986. The runup of long waves. Ph.D. thesis. California Institute of Technology. URL: http://thesis.library.caltech.edu/3506/1/Synolakis{}_ce{}_1986.pdf.
- Synolakis, C.E., 1987. The runup of solitary waves. *Journal of Fluid Mechanics* 185, 523–545. doi:10.1017/S002211208700329X.
- Synolakis, C.E., Bardet, J.P., Borrero, J.C., Davies, H.L., Okal, E.A., Silver, E.A., Sweet, S., Tappin, D.R., 2002. The slump origin of the 1998 Papua New Guinea Tsunami. *Proceedings of the Royal Society A: Mathematical, Physical and Engineering Sciences* 458, 763–789. doi:10.1098/rspa.2001.0915.
- Synolakis, C.E., Bernard, E.N., Titov, V.V., 2007. Standards, Criteria, and Procedure for NOAA Evaluation of Tsunami Numerical Models. NOAA OAR Special Report, Contribution No. 3053, NOAA/OAR/PMEL. Technical Report. Seattle, Washington.
- Synolakis, C.E., Bernard, E.N., Titov, V.V., Kanoglu, U., González, F.I., 2009. Validation and Verification of Tsunami Numerical Models. *Pure and Applied Geophysics* 165, 2197–2228. doi:10.1007/s00024-004-0427-y.
- Synolakis, C.E., Kong, L., 2006. Runup Measurements of the December 2004 Indian Ocean Tsunami. *Earthquake Spectra* 22, 67–91. doi:10.1193/1.2218371.

REFERENCES

- Synolakis, C.E., Skjelbreia, J.E., 1993. Evolution of Maximum Amplitude of Solitary Waves on Plane Beaches. *Journal of Waterway, Port, Coastal, and Ocean Engineering* 119, 323–342. doi:10.1061/(ASCE)0733-950X(1993)119:3(323).
- Tanimoto, K., Takahashi, S., 1994. Design and construction of caisson breakwaters - the Japanese experience. *Coastal Engineering* 22, 57–77. doi:10.1016/0378-3839(94)90048-5.
- Tehranirad, B., Kirby, J.T., Ma, G., Shi, F., 2012. Tsunami benchmark results for non-hydrostatic wave model NHWAVE version 1.1 - Research Report No. CACR-12-03. Technical Report. University of Delaware.
- Titov, V.V., González, F.I., 1997. Implentation and testing of the method of splitting tsunami (MOST) model. Technical Report 1927. NOAA.
- Titov, V.V., Synolakis, C.E., 1995. Modeling of Breaking and Nonbreaking Long-Wave Evolution and Runup Using VTCS-2. *Journal of Waterway, Port, Coastal, and Ocean Engineering* 121, 308–316. doi:10.1061/(ASCE)0733-950X(1995)121:6(308).
- Titov, V.V., Synolakis, C.E., 1998. Numerical Modeling of Tidal Wave Runup. *Journal of Waterway, Port, Coastal, and Ocean Engineering* 124, 157–171. doi:10.1061/(ASCE)0733-950X(1998)124:4(157).
- Tonelli, M., Petti, M., 2009. Hybrid finite volume-finite difference scheme for 2DH improved Boussinesq equations. *Coastal Engineering* 56, 609–620. doi:http://www.sciencedirect.com/science/article/pii/S0378383909000027.
- Tonkin, S., Yeh, H., Kato, F., Sato, S., 2003. Tsunami scour around a cylinder. *Journal of Fluid Mechanics* 496, 165–192. doi:10.1017/S0022112003006402.
- Toro, E.F., 2001. *Shock-Capturing Methods for Free-Surface Shallow Flows*. John Wiley & Sons Ltd., Chichester.
- Uezono, A., Odani, H., 1987. Planning and construction of the rubble mound for a deep water breakwater: the case of the Kamaishi bay mouth breakwater, in: *Coastal and Ocean Geotechnical Engineering*. Japanese Geotechnical Society, Tokyo, Japan. chapter 4.1, pp. 69– (in Japanese).
- United States Geological Survey, 2011. Magnitude 9.0 - Near the east coast of Honshu, Japan. URL: <http://earthquake.usgs.gov/earthquakes/eqinthenews/2011/usc0001xgp/>.
- Versteeg, H., Malalasekera, W., 2007. *An introduction to computational fluid dynamics: the finite volume method*. 2 ed., Prentice Hall, Harlow.

- Wei, G., Kirby, J.T., 1995. Time-Dependent Numerical Code for Extended Boussinesq Equations. *Journal of Waterway, Port, Coastal, and Ocean Engineering* 121, 251–261. doi:10.1061/(ASCE)0733-950X(1995)121:5(251).
- Wei, G., Kirby, J.T., Grilli, S.T., Subramanya, R., 1995. A fully nonlinear Boussinesq model for surface waves. Part 1. Highly nonlinear unsteady waves. *Journal of Fluid Mechanics* 294, 71–92. doi:10.1017/S0022112095002813.
- Wilson, R.I., Admire, A.R., Borrero, J.C., Dengler, L.A., Legg, M.R., Lynett, P., McCrink, T.P., Miller, K.M., Ritchie, A., Sterling, K., Whitmore, P.M., 2012. Observations and Impacts from the 2010 Chilean and 2011 Japanese Tsunamis in California (USA). *Pure and Applied Geophysics* 170, 1127–1147. doi:10.1007/s00024-012-0527-z.
- Witting, J.M., 1984. A unified model for the evolution nonlinear water waves. *Journal of Computational Physics* 56, 203–236. doi:10.1016/0021-9991(84)90092-5.
- Yamazaki, Y., Cheung, K.F., Kowalik, Z., 2011a. Depth-integrated, non-hydrostatic model with grid nesting for tsunami generation, propagation, and run-up. *International Journal for Numerical Methods in Fluids* 67, 2081–2107. doi:10.1002/flid.2485.
- Yamazaki, Y., Kowalik, Z., Cheung, K.F., 2009. Depth-integrated, non-hydrostatic model for wave breaking and run-up. *International Journal for Numerical Methods in Fluids* 61, 473–497. doi:10.1002/flid.1952.
- Yamazaki, Y., Lay, T., Cheung, K.F., Yue, H., Kanamori, H., 2011b. Modeling near-field tsunami observations to improve finite-fault slip models for the 11 March 2011 Tohoku earthquake. *Geophysical Research Letters* 38, L00G15. doi:10.1029/2011GL049130.
- Yeh, H., 2006. Maximum Fluid Forces in the Tsunami Runup Zone. *Journal of Waterway, Port, Coastal, and Ocean Engineering* 132, 496–500. doi:10.1061/(ASCE)0733-950X(2006)132:6(496).
- Yoneyama, N., Matsuyama, M., Tanaka, H., 2002. Numerical analysis for locally high runup of the 1993 Hokkaido Nansei-oki tsunami. *Journal of Hydraulic, Coastal and Environmental Engineering, JSCE* 705, 139–150 (in Japanese). doi:10.2208/jscej.2002.705_139.
- Yoneyama, N., Moriya, S., 1995. Numerical Analysis of 2-dimensional Fluid Flow with Free Surface using VOF technique. *Proceedings of Hydraulic Engineering (JSCE)* 39, 373–378 (in Japanese). doi:10.2208/prohe.39.373.
- Yoneyama, N., Nagashima, H., Toda, K., 2012. Three-dimensional numerical analysis to predict behavior of driftage carried by tsunami. *Earth, Planets and Space* 64, 965–972. doi:10.5047/eps.2011.11.010.

REFERENCES

- Youngs, D., 1982. Time-dependent multi-material flow with large fluid distortion, in: Morton, K.W., Baines, M.J. (Eds.), Numerical methods for fluid dynamics. Academic Press. volume 24, pp. 273–285.
- Zelt, J., 1991. The run-up of nonbreaking and breaking solitary waves. Coastal Engineering 15, 205–246. doi:10.1016/0378-3839(91)90003-Y.
- Zhang, Y.J., Baptista, A.M., 2008. An Efficient and Robust Tsunami Model on Unstructured Grids. Part I: Inundation Benchmarks. Pure and Applied Geophysics 165, 2229–2248. doi:10.1007/s00024-008-0424-7.